Phase-Field Modeling of Relaxor Ferroelectrics and Related Composites

Zur Erlangung des akademischen Grades Doktor-Ingenieur (Dr.-Ing.)
genehmigte Dissertation von Shuai Wang aus Xiaoxian, Anhui, China
Tag der Einreichung: 16.11.2018, Tag der Prüfung: 16.01.2019
Darmstadt — D 17

1. Gutachten: Prof. Dr. Bai-Xiang Xu
2. Gutachten: Prof. Dr. Wolfgang Kleemann

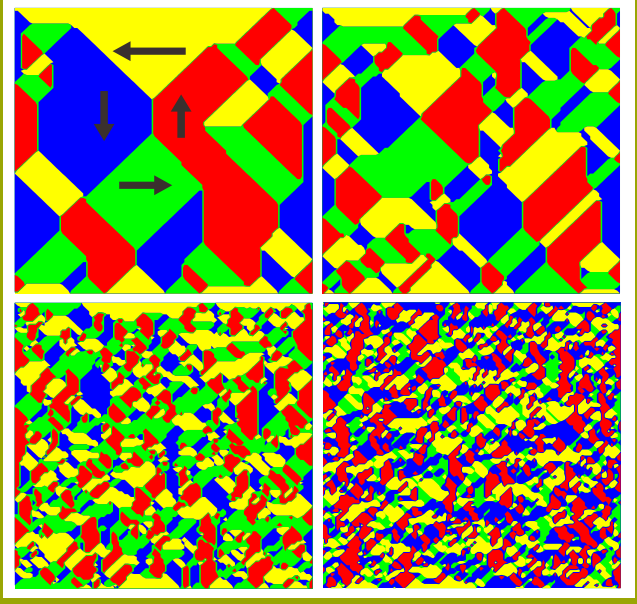

TECHNISCHE UNIVERSITÄT DARMSTADT

MECHANICS of FUNCTIONAL MATERIALS

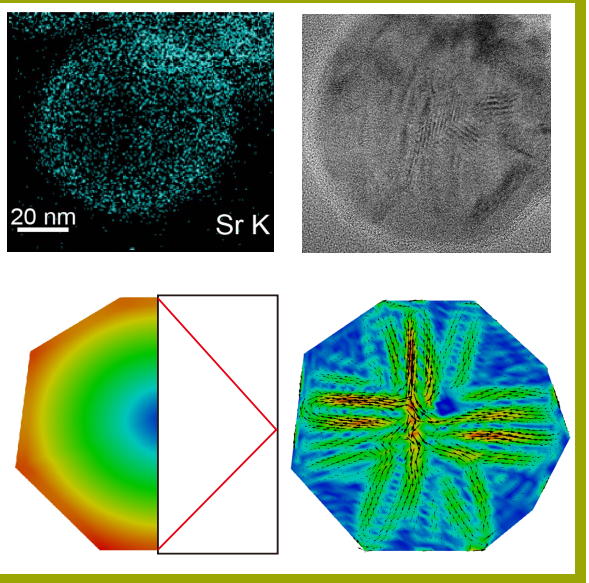

Phase-Field Modeling of Relaxor Ferroelectrics and Related Composites

Genehmigte Dissertation von Shuai Wang aus Xiaoxian, Anhui, China

1. Gutachten: Prof. Dr. Bai-Xiang Xu
2. Gutachten: Prof. Dr. Wolfgang Kleemann

Tag der Einreichung: 16.11.2018
Tag der Prüfung: 16.01.2019

Darmstadt — D 17

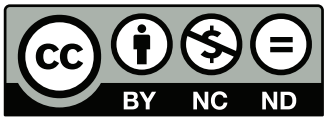

Erklärung zur Dissertation

Hiermit versichere ich, die vorliegende Dissertation ohne Hilfe Dritter nur mit den angegebenen Quellen und Hilfsmitteln angefertigt zu haben. Alle Stellen, die aus Quellen entnommen wurden, sind als solche kenntlich gemacht. Diese Arbeit hat in gleicher oder ähnlicher Form noch keiner Prüfungsbehörde vorgelegen.

Darmstadt, den Wednesday 30th January, 2019

(S. Wang)

Acknowledgments

First and foremost, I would like to express my sincere gratitude to my advisor Prof. Bai-Xiang Xu for her help and support during the whole time of my Ph.D. career in Darmstadt. In my four years research period, she devotes many efforts to guide me with my research project, provides me with high freedom in my research interest, engages me in new ideas, and demands high-quality work. I have benefited and learned a lot from her, especially from her rigorous attitude towards the research and her creative intuition in science. I am proud to be one of the Ph.D. students under her supervision.

I would also like to acknowledge Prof. Jürgen Rödel and Prof. Kyle G. Webber to give me the opportunity to join in the project of "Excellence Initiative" of the German Federal and State Governments and the Graduate School of Computational Engineering (GSC CE) at Technische Universität Darmstadt. Without their support, I would never have a chance to work on such an interesting topic. Moreover, the weekly seminar led by Prof. Jürgen Rödel in the group of Nichtmetallische-Anorganische Werkstoffe (NAW) expanded my knowledge in ferroelectrics. I will never forget the active and fruitful discussions. My special thanks go to Dr. Nikola Novak and Dr. Lalitha Venkataraman for the informative discussions on relaxor ferroelectrics. I am pleased to be together with all the NAW members.

My sincere thanks also go to Prof. Wolfgang Kleemann and Prof. Herbert De Gersem for their kindness to be the members of my examination committee. The discussion with Prof. Kleemann on the random field theory inspired me a lot for the modeling. Prof. De Gersem always keeps track of my research progress. I thank both of you sincerely for your valuable time.

I would also like to acknowledge my colleagues in the research group of Mechanics of Functional Materials (MFM). I thank Dr. Min Yi for keeping encouraging me during my Ph.D. career. The discussion with him always brings me fresh ideas and new perspectives in researches. I thank Dr. Ying Zhao for her support when I was a beginner of programming. I thank Dr. Yangbin Ma for the continuous discussion in ferroelectrics. I thank Yangyiwei Yang for the vivid discussion in science, especially for the time going back home from office together. I would also like to thank all the help from Yang Bai and other members in MFM. Though working on different topics, we always help each other. The four years precious memory in MFM will always stay in my mind. The kind help from Dr. Markus Lazanowski, Birgit Seibert and Carina Schuster for the support on the financial issues in GSC CE is acknowledged.

I would also like to acknowledge my collaborators. I thank Dr. Na Liu, Dr. Christian Dietz and Prof. Robert Stark from the group Physics of Surfaces for the fruitful discussion on the characterization of core-shell relaxors. I thank Dr. Matias Acosta for providing the initial samples for my simulation. Your profound understanding on ferroelectric materials gives me a deep

impression. I thank Dr. Nikola Novak, Prof. Rahul Vaish, Dr. Peng Lv for the discussion on the antiferroelectrics. Although this part of the work is not presented in the thesis, the idea is used to constitute part of the thesis. I thank Prof. Kyle G. Webber and Azatuhi Ayrikyan for the discussion and the experiments on the relaxor composites. Special thanks to Dr. Leopoldo Molina-Luna and Alexander Zintler for the collaboration on the flexoelectricity. The nearly one-year's intensive work was finally rewarded. Thank you so much!

I would like to show my greatest appreciation to my friends Taiyang Wang and Ying Li. Though thousands of miles away, you always make me feel at home when we talk together through the Internet. I also thank "Darmstädter Lauftreff" for having a great time running every Monday and Thursday!

Last but not least, I would like to thank my parents for their love and support. With their understanding, I could concentrate on my research without worrying about other issues. I express my gratitude to my girlfriend Jinxiu. Her love and support have always been my strength. Her patience and sacrifice are and will remain in my mind throughout my life. Without her help, I would not have been able to complete much of what I have done and become who I am. Sorry for not having time being with you and thank you for your understanding.

Shuai Wang

Darmstadt, October 2018

Abstract

In the 1950s, relaxor ferroelectrics or relaxors were discovered and have lately received a renewed interest in condensed matter physics. Despite the fact that the physical interpretation of the relaxors remains the subject of controversy, their extraordinary electromechanical properties and the resultant potential applications in industries have motivated a vast amount of theoretical studies on different aspects.

In this thesis, based on the random field theory, an electromechanically fully coupled phase-field model is proposed to simulate the peculiar behavior of the relaxor ferroelectrics. The model introduces a quenched local random field to characterize the effect of the chemical disorder. By treating the spontaneous polarization as an independent order parameter and the random field as an internal microforce, a thermodynamic analysis is performed. The deduced nonlinear constitutive and evolution equations are further discretized by the finite element method. Numerical examples show that the model can reproduce typical relaxor features, such as the miniaturization of domain size, the reduction of remanent polarization, and the enhancement of large-signal piezoresponse. The influence of the random field strength on the domain structure and the hysteresis loops is also revealed and validated with the related experimental results.

Subsequently, the phase-field model of relaxors, in combination with the conventional ferroelectric model is applied to analyze the large-signal piezoresponse for relaxor-based composites. More specifically, a series of simulations are presented for the relaxor/ferroelectric layer composites with different types of interfaces. The results confirm that the lateral strain coupling, in addition to the polarization coupling, contributes considerably to the large-signal piezoelectric coefficient. The lateral strain mismatch lowers the remanent strain in the ferroelectric layer and thus increases the macroscopic piezoelectric response. It is worth to be highlighted that the composition ratio of the relaxor constituent is optimized for different electric loadings. The composites with higher relaxor content are inclined to obtain higher large-signal piezoresponse with the increase of the applied electric field. These results can be referred in the future design of high-performance relaxor-based composites.

Finally, the core-shell structures in relaxors, as well as the associated microscale features and mechanisms are explored by the combined ferroelectric-relaxor-flexoelectric phase-field simulations. For BNT-25ST at room temperature, it is found that the increased electric potential beneath the core is responsible for the in-plane domain evolution. The resultant field-induced domains at the coherent core-shell interface play an important role in enhancing the polarization in the non-polar shell region and thus promoting the giant strain. Moreover, at an extreme temperature of 800 °C, the domain-like nanoregions found in BNT-25ST core-shell nanoparticle are attributed to the flexoelectric effect, where the strain gradient is believed to originate from

the Vegard effect. This hypothesis is verified by the comparison between the simulation and experimental results on the electric field mediated redistribution of the polarization.

Zusammenfassung

Relaxor-Ferroelektrika (Relaxoren) wurden in den 1950er Jahren entdeckt und haben erneut Interesse in der Physik der kondensierten Materie erhalten. Trotz der Tatsache dass die physikalische Deutung der Relaxoren ein Streitgegenstand bleibt, motivierten die außergewöhnlichen elektro-chemischen Eigenschaften sowie die sich daraus ergebenden potenziellen Anwendungsgebiete in der Industrie eine Vielzahl an Studien zu verschiedenen Aspekten.

Auf der Zufallsfeldtheorie basierend wird in der vorliegenden Arbeit erstmalig ein voll elektromechanisch gekoppeltes Phasenfeldmodell vorgestellt, um das sonderbare Verhalten der Relaxoren zu simulieren. Dabei wird ein lokales Zufallsfeld eingeführt, um den Effekt der chemischen Fehlordnung zu charakterisieren. Desweiteren wird eine thermodynamische Analyse unternommen, bei der die spontane Polarisierung als ein unabhängiger Ordnungsparameter und das Zufallsfeld als eine interne Mikrokraft behandelt werden. Die resultierenden nichtlinearen Material- und Evolutionsgleichungen werden anschließend mit der Finite-Elemente-Methode diskretisiert. Numerische Simulationen zeigen, dass dieses Modell die Merkmale von Relaxoren wiedergeben kann, beispielsweise die Miniaturisierung der Domänengröße, die Reduzierung der remanenten Polarisierung und die Verstärkung der Großsignal-Piezo-Antwort. Es wird insbesondere der Einfluss der Zufallsfeldstärke auf die Domänenstruktur und die Hysteresen diskutiert und durch Versuchsergebnisse validiert.

Im nächsten Schritt wird das Phasenfeldmodell zusammen mit dem Modell für herkömmliche Ferroelektrika auf die Analyse und das Design der Relaxor-basierten Verbundwerkstoffe angewandt. In diesem Zusammenhang wird eine Reihe von Simulationen für die ferroelektrischen Verbundwerkstoffe mit verschiedenen Typen der Grenzschicht ausgeführt. Die Ergebnisse bestätigen, dass zusätzlich zur Polarisierungskopplung, die laterale Verzerrungskopplung einen beachtlichen Beitrag zum GroÃ§signal-Deformationskoeffizienten liefert. Die laterale Verzerrungsfehlanpassung senkt die remanente Verzerrung in der ferroelektrischen Schicht und erhöht dadurch die makroskopische piezoelektrische Reaktion.

Erwähnenswert ist die Optimierung der Zusammensetzungsverhältnise der Relaxoren in Bezug auf verschiedene elektrische Ladungen. Besonders die Verbundwerkstoffe mit einem höheren Gehalt an Relaxor sind geneigt, erhöht Großsignalige-Piezo-Antwort für höhere elektrische Felde zu erhalten. Diese Erkenntnisse können in die weitere Entwicklung von Relaxoren und ferroelektrische Verbundwerkstoffe mit verbesserter Leistung einfließen.

Abschließend werden die core-shell-Strukturen in Relaxoren sowie die assoziierten mikroskaligen Merkmale und Mechanismen durch kombinierte ferroelektrisch-relaxor-flexoelektrische Phasenfeldsimulationen untersucht. Bei Raumtemperatur wird für BNT-25ST festgestellt, dass das erhöhte elektrische Potenzial unterhalb des Kerns für die Domänenentwicklung in der

Ebene verantwortlich ist. Die resultierenden Feld-induzierten Domänen am kohärenten Core-Shell-Interface spielen eine wichtige Rolle für die Steigerung der Polarisation in der nonpolaren Schalenregion und damit für die Erzeugung großer Verzerrungen. Für die extrem hohen Temperaturen von 800 °C lassen sich die domänenartigen Nanoregionen in BNT-25ST core-shell-Nanopartikeln zurückführen auf den flexoelektrischen Effekt, wobei der Verzerrungsgradient seinen Ursprung wohl im Vegard-Effekt besitzt.

Contents

List of Figures

List of Tables

List of symbols

Table 0.1: *Symbols and notations*

Symbol	Units and/or value	Meaning
k_b	$1.38064852(79)\times 10^{23}\ \mathrm{J\,K^{-1}}$	Boltzmann constant
T	K	Temperature
T_c	K	Curie Temperature
T_f	K	Freezing Temperature
ϵ	$\mathrm{F\,m^{-1}}$	Permittivity
ϵ_0	$8.854187817\times 10^{-12}\ \mathrm{F\,m^{-1}}$	Vacuum permittivity
ε_{ij}	-	Strain
σ_{ij}	Pa	Stress
E_i	$\mathrm{V m^{-1}}$	Electric field
f_{ijkl}	V	Flexocoupling coefficient
μ_{ijkl}	$\mathrm{C\,m^{-1}}$	Flexoelectric coefficient
q	C	Charge
ϱ	$\mathrm{C\,m^{-3}}$	Charge density
p_i	C m	Dipole moment
P_i	$\mathrm{C\,m^{-2}}$	Polarization
χ_{ij}	-	Susceptibility
$\mathscr{H}$	$\mathrm{J\,m^{-2}}$	Helmholtz energy/electric enthalpy density
$\mathscr{F}$	$\mathrm{J\,m^{-2}}$	Free energy density
D_i	$\mathrm{C\,m^{-2}}$	Electric displacement
ϕ	V	Electric potential
π_i	-	Internal microforce
γ_i	-	External microforce
e_{ijk}	$\mathrm{C\,m^{-2}}$	Piezoelectric charge tensor
d_{ijk}	$\mathrm{m\,V^{-1}}$	Inverse piezoelectric charge tensor
g_{ijk}	$\mathrm{m^2\,C^{-1}}$	Piezoelectric voltage tensor
h_{ijk}	$\mathrm{V\,m^{-1}}$	Inverse piezoelectric voltage tensor
d_{33}	$\mathrm{m\,V^{-1}}$	Piezoconstant
d^*_{33}	$\mathrm{m\,V^{-1}}$	Large-signal piezoresponse

Table 0.2: *Abbreviations*

Abbrivation	Full name and/or chemical formula
PZT	$PbZr_{1-x}Ti_xO_3$ / lead zirconate titanate
PbO	lead(II) oxide
ZrO	zinc oxide
BNT	$Bi_{1/2}Na_{1/2}TiO_3$ / bismuth sodium titanate
KDP	KH_2PO_4 / dihydrogen phosphate
BT/BTO	$BaTiO_3$ / barium titanate
PMN-PT	$xPbMg_{1/3}Nb_{2/3}O_3 - (1\text{-}x)PbTiO_3$
MD	molecular dynamics
BNT-BT	$xBi_{1/2}Na_{1/2}TiO_3 - (1\text{-}x)BaTiO_3$
BNT-25ST	$0.75Bi_{1/2}Na_{1/2}TiO_3 - 0.25SrTiO_3$
FE	ferroelectrics
RE	relaxor ferroelectrics
BNT-BT-KNN	$(0.94\text{-}x)Bi_{1/2}Na_{1/2}TiO_3 - 0.06BaTiO_3 - xK_{1/2}Na_{1/2}NbO_3$
BNT-7BT	$0.93Bi_{1/2}Na_{1/2}TiO_3 - 0.07BaTiO_3$
BNT-6BT-3AN	$0.91Bi_{1/2}Na_{1/2}TiO_3 - 0.06BaTiO_3 - 0.03AgNbO_3$
XRD	X-ray crystallography
RF	random field
PNR	polar nanoregion
BNKT-6BA	$0.94Bi_{1/2}(Na_{3/4}K_{1/4})_{1/2}TiO_3 - 0.06BiAlO_3$
PE	paraelectric
ER	ergodic relaxor
MPB	morphotropic phase boundary
BZCT	$Ba(ZrTi)O_3$-$(BaCa)TiO_3$
MEMS	microelectromechanical system
STO/ST	$SrTiO_3$ / strontium titanate
BST	$(Ba_{1-x}Sr_x)TiO_3$ / barium strontium titanate
TDGL	time-dependent Ginzburg–Landau equation
FEM	finite element method
FEAP	Finite Element Analysis Program
SBN	$Sr_xBa_{1-x}Nb_2O_6$ / strontium barium niobate
KNN	$(K_{1/2}Na_{1/2})NbO_3$ / potassium sodium niobate
CP	critical point
ROI	region of interest
PFM	piezo force microscope
dc	direct current

TEM	transmission electron microscope
STEM	scanning transmission electron microscopy
PDE	partial differential equation
BVP	boundary value problem
SGE	strain gradient elasticity
DLNRs	domain-like nanoregions
EDS	energy dispersive X-ray spectroscopy
FFT	fast Fourier transformation
GPA	geometrical phase analysis

Chapter 1

Motivation

Ferroelectric materials are of great importance in modern society with a wide spectrum of applications. This category of material shows a number of distinctive properties. [1] For instance, the property of high/non-linear permittivity makes the ferroelectrics as excellent material candidates for high performance/tunable [2, 3] capacitors. The switchable spontaneous polarization enables the applications of ferroelectrics in memory devices. [4] Many applications for ferroelectrics do not make use of the ferroelectricity itself, but of their piezoelectric effect. In contrast to other piezoelectric materials (*e.g.*, ZrO), ferroelectrics are not required to be single crystal. This allows the production of polycrystalline piezoelectric and inverse piezoelectric devices with a lower price and a more flexible design. Nowadays, ferroelectric-based actuators have dominated the market with the market share of over 97 % according to the survey by Innovative Research and Products *Inc.* in 2010. [5]

Among all the piezoceramics, lead-containing piezoceramics, more specifically lead zirconate titanates (PZT) are most widely used materials in the world due to their high piezoelectric constants. However, the production of lead-containing ceramics and films is harmful to the environment and health, owing to, *e.g.*, the evaporation of PbO during the synthesis process. [6] Hence, their lead-free alternatives receive more attention. Although no single compound can replace PZT in the whole application range by current research, the perovskite-structured compounds, such as bismuth sodium ($Bi_{1/2}Na_{1/2}TiO_3$, BNT) based materials can serve as one of a few promising candidates with competitive electromechanical coupling effects. These solid solution-based systems exhibit strong relaxor features, and they are categorized as relaxor ferroelectrics, or relaxors. Understanding the physics of relaxors is essential for further applications.

Compared with normal ferroelectrics which have been intensively studied in the last century, the study of relaxors seems distressful. The terminology of relaxor ferroelectrics first appeared in Ref. [9], while the relaxor behavior in ferroelectrics was discovered much earlier. Table 1.1 compares the normal ferroelectrics with relaxor ferroelectrics. The relaxor nature is believed to be originated from the site randomness. [7] Till now there are many models to describe the relaxor features during the phase transition. Most of them can be generally subdivided into two categories: the random field scenario, originated from the idea of Imry and Ma [10] and applied to relaxors by Westphal *et al.* [11], and the dipole glass scenario in analogy to spin glass model in ferromagnets [12]. Either of the two scenarios receives experimental supports.

	ferroelectric	relaxor ferroelectric
First discovered	1920's	1950's
Order/disorder	long-range order	short-range order
Phase transition	1st or 2nd order	frequency dependent
Microstructure	domain/domain wall	PNRs/nanodomains
Typical material	KDP, BTO	PMN-PT, BNT-BT

Table 1.1: *Comparison between normal ferroelectric and relaxor ferroelectrics, taken from Refs. [7, 8]*

Although extensive efforts have been made to explore the physical origin of relaxors, there are limited works on the discussion of the electromechanical couplings in relaxors, which are more important in applications. Phase-field model has been proved to be an efficient tool to study the evolution of domain structure in ferroelectrics, [13, 14, 15, 16] and the order parameter can be fully coupled with electrical and mechanical quantities. Recently, the phase-field methods have also been employed in the field of relaxors, see Refs. [17, 18]. Rather than generic relaxor models, these works regards the relaxor features are the results of either point defects or localized nanoscale polar volumes inside a different phase. Moreover, the piezoresponse cannot be directly simulated from these models. Therefore, a generic fully coupled phase-field relaxor model which can reproduce and predict relaxor characteristics found in experiments is required.

There are many important issues which could be investigated with the phase-field relaxor model. Here more attention is paid to the following two topics. (1) The role of relaxors in the relaxor/ferroelectric composite structure. Experimentally, the relaxor/ferroelectric composites show excellent large-signal piezoresponse. Understanding the role of relaxors in such composites is important for the designing of relaxor-based piezoelectric devices. (2) The role of relaxors in the core-shell structure. The core-shell structures have been found in some relaxor systems, for instance, $0.75Bi_{1/2}Na_{1/2}TiO_3$-$0.25SrTiO_3$ (BNT-25ST). The phase-field relaxor model will help in understanding the coupling effect at the core-shell interface and the abnormal macroscopic electromechanical behaviors in such core-shell structured relaxors. In the following, these two questions are elaborated in detail.

The first question originates from the searching for a piezoelectric device with better performance at different loading conditions. The relaxors usually need a large electric field to reach high strain, while the ferroelectrics have a high remanent strain at null field due to their strong hysteresis. To overcome this problem, the concept of ferroelectric/relaxor(FE/RE) composite is introduced. Dausch *et al.* [19, 20] first attempted to synthesize the FE/RE composites and fit the polarization hysteresis (P-E) of the composite using the P-E loop of the end-members. This method is not capable of characterizing the piezoresponse nor reflecting the influence of internal stress between different phases. Since 2014, a series of experimental work has

been carried out, focusing on synthesizing lead-free FE/RE composites. Groh *et al.* found an optimized large-signal response with a specific FE/RE ratio in (0.94-x)$Bi_{1/2}Na_{1/2}TiO_3$ -0.06BT-x$K_{1/2}Na_{1/2}NbO_3$ (BNT-BT-KNN) [21] and (1-x)(0.92BNT-0.06BT-0.02KNN)-x(0.93BNT-0.07BT) (matrix: BNT-BT-KNN, seed: BNT-7BT) [22]. The method is extended by replacing 92BNT-6BT-2KNN with 0.91$Bi_{1/2}Na_{1/2}TiO_3$ -0.06BT-0.03$AgNbO_3$ (91BNT-6BT-3AN) by Zhang *et al.* [23]. They further investigated the coupling effect in the composite structures. By designing two types of multilayer composites with interfaces perpendicular and parallel to the electrode surfaces, the polarization coupling effect can be separated from the mechanical coupling. The results showed that both mechanical coupling and polarization coupling play an important role in the enhancement of the large-signal response. [23] Ayrikyan *et al.* [24, 25] analyzed the influence of composite type (0-3 or 2-2 type), porosity, residual stress on the large-signal piezoresponse. The study of the coupling mechanism of RE/FE composite can help us optimize the large-signal piezoresponse in devices. Optimizing methods, such as choosing RE/FE end-members, tuning RE/FE ratios and engineering interfaces can be directed by the combined phase-field ferroelectric/relaxor models.

The second question originated from the investigation of the core-shell structure in the relaxor solid solutions. The observation of core-shell structure in ceramics can date back to the early 1980's. [26] Recently, Rödel and coworkers found the excellent electromechanical performance in BNT-25ST. [27] Further investigation showed that the core-shell structures within a single grain in BNT-25ST have a strong influence on the strain output and the hysteresis. [28] Understanding the functions of the core-shell structure will help in designing better actuator devices. On the other hand, there could be large strain inhomogeneity within the core-shell structure in the relaxors. The strain-gradient may take a role in the polarization response (*i.e.*, flexoelectricity). The flexoelectric model in cooperation with the state-of-the-art ferroelectric model is needed to study some specific phenomenon where the ferroelectric model alone cannot explain.

In short, to study the macroscopic response of relaxors and relaxor-related composite/core-shell structures, a suitable model is required. Phase-field model can characterize the domain configuration, at the same time reflect the electromechanical coupling effect. The state-of-the-art phase-field ferroelectric model needs to be reviewed and further extended to the field of relaxors.

Chapter 2

Basics of ferroelectric materials

The generic relaxor ferroelectric model should cover some of the key features in relaxors. To establish such a model, the basic concepts of material properties are reviewed. Ferroelectrics and relaxor ferroelectrics are introduced in Sec. 2.1 and Sec. 2.2, respectively. Ferroelectrics and relaxors intrinsically have flexoelectric effect. It plays an important role in the electromechanical coupling, especially at the nanoscale. The introduction to flexoelectricity is presented in Sec. 2.3.

2.1 Ferroelectrics

Introduction to the general topic of ferroelectric can be found in the classical textbooks, *e.g.*, Refs [29, 30, 31]. The history of the research in ferroelectricity and representative works can be found in Ref. [32]. The review of recent progress was collected in Ref. [1]. The basic principles of ferroelectric material and ferroelectricity are mostly covered in these books or collections. For those readers who are familiar with ferroelectricity and ferroelectric materials, this section serves as a brief introduction. The following discussion is restricted only to the insulating materials.

A crystal is said to be *ferroelectric* when it has two or more orientation states in the absence of an electric field and can be shifted from one to the other of these states by an applied electric field. Any two of the orientation states are identical with respect to the crystal structure and differ only in electric field polarization vector at a null electric field [29, 30]. The polarization vector at a null electric field is defined as the *spontaneous polarization*. The spontaneous polarization thus creates a direction in the crystal, which is invariant under any symmetrical operation. This specific direction defines the polar axis of the crystal. The above discussion indicates that the spontaneous polarization only exists in certain point groups. Hence the understanding of ferroelectricity needs the consideration of symmetry in the crystal structure.

From the point group theory, there are 32 crystallographic point groups when applying the crystallographic restriction theorem in the 3-dimensional case. All the crystals can be classified as one of those 32 point groups. Since all materials belong to one of those 32 point groups possess atoms or ions with charges, the application of an electrical excitation leads to the redistribution of the charges, and the polarization is generated. The displacement of the ions is reflected macroscopically to the elastic strain. This strain is always positive and originates from the opposite shift of charged ions with different signs in the lattice. This electromechanical

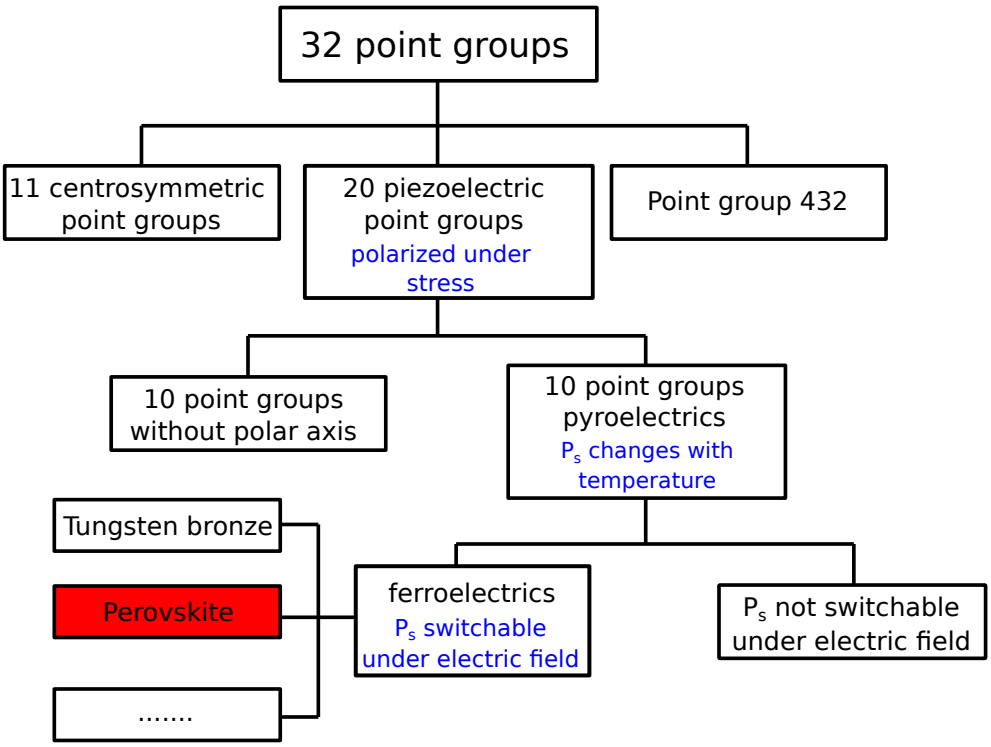

Figure 2.1: *The relationship between the symmetry and the properties of dielectric crystals. The 20 non-centrosymmetry point groups possess a polar axis and therefore show the piezoelectric effect. If this polar axis is unique, the material exhibits a spontaneous polarization (P_s). The temperature-dependent P_s results in pyroelectric effect. A crystal is called "ferroelectric" if an electric field can switch this spontaneous polarization, and these two stable states are equivalent with respect to the crystal structure.*

coupling property is called *electrostriction*, and the electrostrictive strain is quadratically related to the applied field. The above discussion indicates that, Electrostriction applies to all crystal symmetries. Of the 32 point groups, 11 point groups are centrosymmetric. A crystal having a symmetric center does not possess any polarity at a null field, thus holds no ferroelectricity. For the remaining 21 point groups which do not have centrosymmetry, apart from point group (4 3 2), all of them exhibit *piezoelectricity*. This linear electromechanical effect is responsible for the accumulated electric charge in response to the applied mechanical stress. As an inverse effect, the application of an electric field results in the change of elastic strain. This effect is also linear and called the *inverse piezoelectric effect*. Of the remaining 20 point groups, 10 of them possess a spontaneous polarization along the polar axis. Since the configuration of the crystal structure is a function of temperature, this spontaneous polarization is also temperature dependent. As a result, upon heating or cooling, the spontaneous polarization will change, and a voltage can be generated. This effect is called the *pyroelectric* effect.

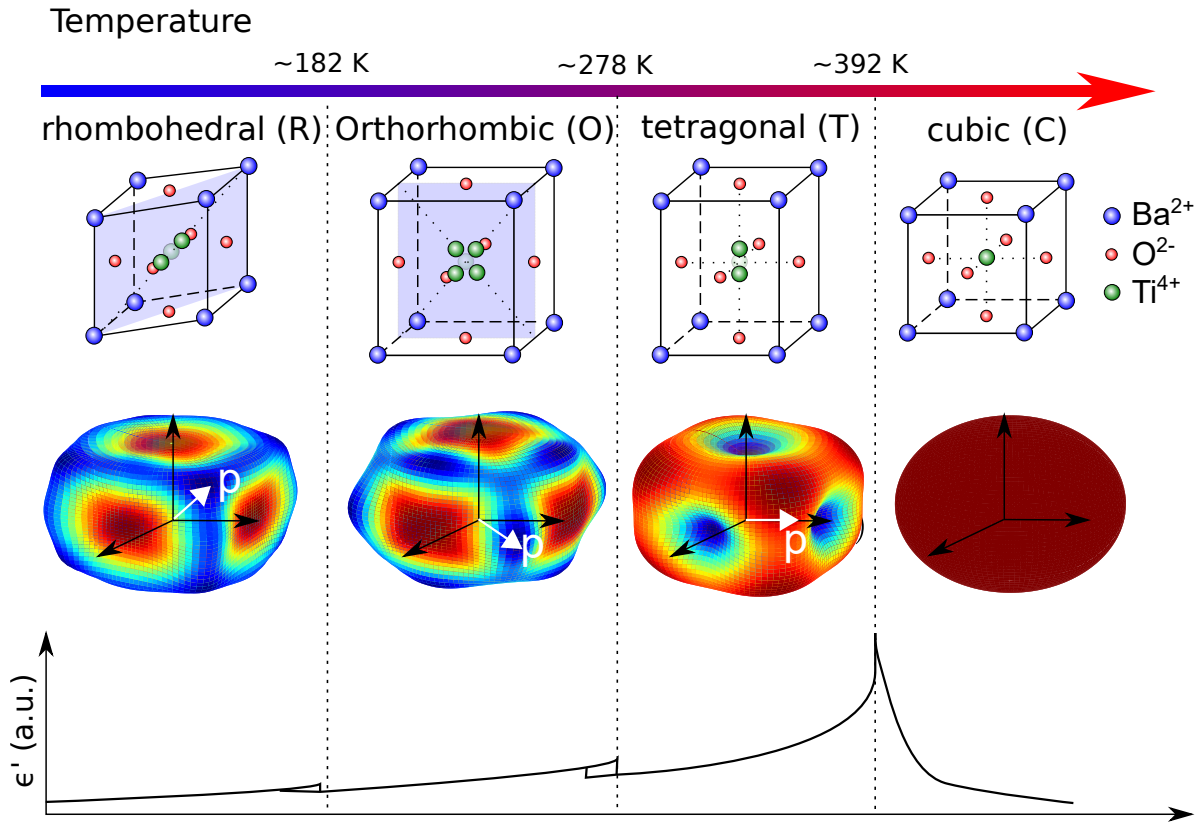

FIGURE 2.2: *Crystal structure and the Landau energy landscape of each phase of barium titanate. From left to right: Rhombohedral, Orthorhombic, Tetragonal, and Cubic. Blue regions indicate lower free energy, while dark red regions for higher free energy. The spontaneous polarization always points in the direction with lower free energy. The permittivity graph is measured along the spontaneous polarization direction [33].*

For most of the crystals belong to these 10 point groups (there are some exceptions such as tourmaline and zinc oxide), the direction of the spontaneous polarization of the crystal can be switched by an external electric field, and these two states are stable and identical at null field.

Such crystals are called ferroelectric crystals. In the thesis, this definition is accepted, although it is doubted by few scientists. They argue that in the defination of ferroelectricity, "it is not the crystal but only a crystal plate, with certain indices, of it" has two stable states of different spontaneous polarization at null field [34]. Figure 2.1 summarizes the relations between the crystal symmetry (point group) and the properties of dielectric crystals.

Ferroelectricity was first discovered in 1921 by Valasek in Rochelle salt [35]. Some of the most used and studied ferroelectric crystals belong to perovskite-type, including lead-contained PZT and lead-free BTO. Ferroelectrics always have a non-polar cubic phase above a certain temperature. Upon cooling, the crystal structure is transferred into the phase with lower symmetry, and the spontaneous polarization appears. Figure 2.2 illustrate the change of the crystal structure and the Landau energy of BTO, with respect to the temperature. As the temperature decreases, the crystal structure of BTO changes from Cubic (C) phase, Tetragonal (T) phase, Orthorhombic (O) phase to Rhombohedral (R) phase (R-O-T-C path). The last three phases are often referred to as polar phases. The temperature above which the materials lose their polarity is called Curie temperature (T_c). For BTO, T_c locates around 392 K. For a tetragonal crystal structure, there are three possible directions of the spontaneous polarization, *i.e.*, [1 0 0], [0 1 0] and [0 0 1]. Each of them has two equivalent states (positive and negative). For an orthorhombic crystal structure, the number of the possible directions increases to 12, and for rhombohedral phase the number is 8.

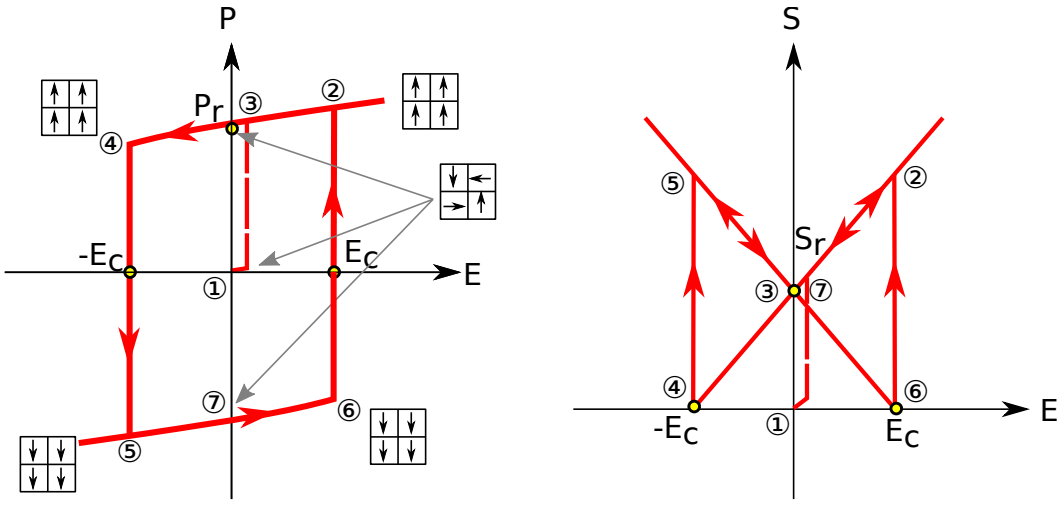

Figure 2.3: *Typical dielectric and strain hysteresis loops of an ideal ferroelectric material under uniaxial bipolar electric field loading.*

The polarization distribution within a ferroelectric crystal has a great impact on the macroscopic behavior. Considering the two neighboring lattices, the interaction between adjacent lattices results in a uniform alignment of the dipole. In general, the uniform alignment of electric dipoles only occurs in certain regions of a crystal, while in other regions of the crystal spontaneous polarization may be in the opposite direction. Such regions with uniform polariza-

tion are called *ferroelectric domains*. The first observation of domains is demonstrated in a study of spontaneous birefringence. [36, 37] The interface between two domains is called the *domain wall*. The existence of the domain wall is a result of the energy minimization. The domain structures can be influenced by the factors, including but not limited to the crystal structure, electric field, temperature, stress, and defects. Domain wall can be categorized by the angle between two domain orientations. For example in BTO, depending on different crystal structures, 90° (for T-phase and O-phase), 60° (O-phase), 120° (O-phase), 71° (R-phase) 109° (R-phase) and 180° (for both R-phase O-phase and T-phase) domain walls may exist. The domain wall in ferroelectrics is often considered as a diffusive one, which means that the polarization within the domain wall changes gradually. Different from ferromagnetic materials, the anisotropy of most ferroelectric material is high. It indicates that the spontaneous polarization can hardly rotate from the polar axis and the domain wall is thus an Ising-type. A recent study by Gu *et al.* [38] shows that the domain wall also contains both Bloch- and Néel-type domain wall components.

Multidomains can be formed in the single crystal as long as it is synthesized. Under a strong external field, a single domain can be obtained. A field reversal may switch the direction of the domain, and the phenomenon is called *domain switching*. The bipolar loading can induce a 180° domain switching. The switching process indicates a hysteresis shape of the field dependent polarization loop (P-E loop). The response of the polarization is non-linear. The application of external field also induces strain, and the strain response (S-E loop) is also non-linear and with a butterfly shape. The schematic P-E and S-E loops of an ideal ferroelectric single crystal are depicted in Fig. 2.3. The state at point ① represents the virgin state with randomly polarized domains. Above certain external field, the monodomain forms (point ②) and the polarization increases linearly with the external field, which represents the pure dielectric response to the external field. Different from the spontaneous one, this contribution to the total polarization is reversible. When the external field is removed (point ③), the polarization for this state is called remanent polarization. Similarly, the strain at this state is called remanent strain. For a perfect single crystal, this value is usually equivalent to the spontaneous ones. If an external field is applied in the opposite direction and exceeds a specific threshold value, the polarization changes its sign (from point ④ to point ⑤). This critical field is referred to as the coercive field E_c. If a reverse field is applied again, the state goes back to point ② and the whole hysteresis loop completes.

Not only the external field but also the mechanical stress can induce domain switching. This effect is called *ferroelastic switching*. In the tetragonal phase, the domain switching can be either 90° or 180° by the electric field, while it can be only 90° switching by the mechanical loading. (Fig. 2.4) It implies that the polarization and strain response under the mechanical loading is also non-linear. This effect is called *ferroelasticity*. The schematic polarization and strain responses of an ideal ferroelectric material under unipolar stress loading are depicted in Fig. 2.5. When above some stress threshold, the monodomain state is transferred to a multidomain state.

The domain cannot be switched back by pure mechanical loading. The linear part of the P-σ loop represents the piezoelectric effect, which can be characterized by the piezoelectric coefficients. The linear parts of the ε-σ loop represent the typical elasticity region governed by Hooke's law.

The above discussion mainly focuses on the properties in single crystal ferroelectrics. Due to the cost and process complexity, single crystals are rarely used for industrial piezoelectric applications, while polycrystalline with multigrains provides a fair solution. Considering that nonferroelectric piezoelectric ceramics are macroscopically isotropic with negligible piezoelectric coefficient due to random orientation of grains, ferroelectric ceramics seems to be the best candidate for piezoelectric applications. After the initial poling process, the grains are aligned to the polar axis close to the direction of the external field and the ceramic becomes polar. Therefore, the prepoled samples can be utilized for piezoelectric applications. The strain response under external field contains three parts, *i.e.*, the spontaneous part, the inverse piezoelectric part, and the electrostrictive part. The spontaneous part is irreversible when the field is removed and is related to the spontaneous polarization. The inverse piezoelectric part is linear to

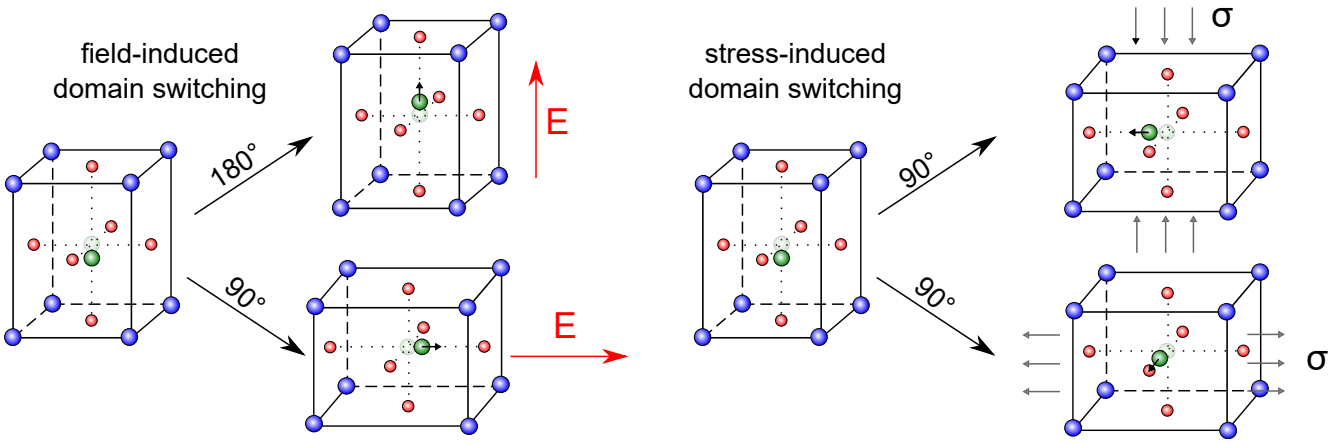

Figure 2.4: *Ferroelectric domains can be induced by either electric field or mechanical stress. The latter one can make the domain switching in four possible equivalent stats in tetragonal phase.*

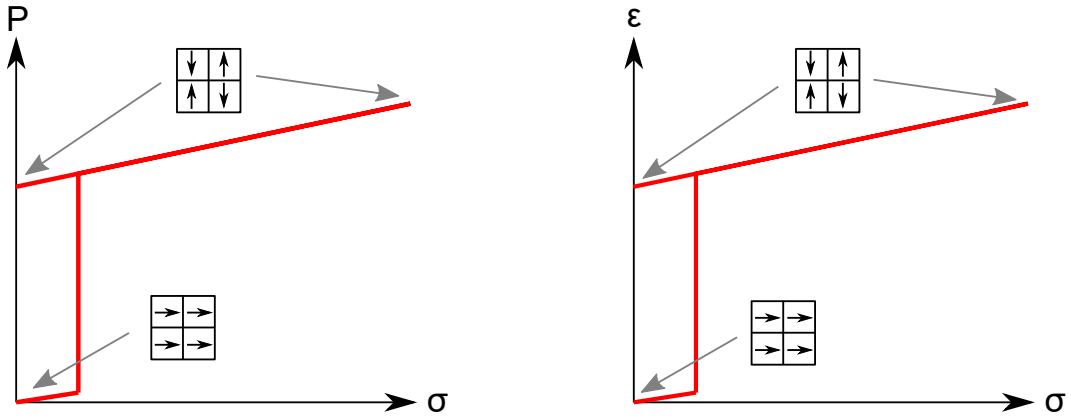

Figure 2.5: *Polarization and strain response of an ideal ferroelectric single crystal under unipolar mechanical loading. The response is not necessarily linear.*

the external field and the process is reversible. The relation between the mechanical components (stress and strain) and the electric parts (electric field and electric displacement) is represented by a couple of piezoelectric tensors, which will be introduced in the Chap. 4. The electrostrictive part is quadratically related to the external field. Despite the region near the phase transition temperature (*e.g.*, T_c), the electrostrictive effect in ferroelectrics is usually weak compared with piezoelectricity. In some ferroelectric models, the electrostrictive effect is ignored. In Sec. 2.3, another contribution to the electromechanical coupling effect, *i.e.*, flexoelectric effect is introduced. With this effect considered, the polarization gradient (or the electric field gradient) can also contribute to the total strain response.

Till now, there are numerous models on ferroelectrics in different aspects. In sub-lattice scale, electron behaviors can be captured by utilizing the quantum mechanic theory (*ab initio* calculation). At the atomic scale, molecular dynamics (MD) and lattice-based Ising-model provide a possibility to study the problem in the range of a few nanometers. For the behaviors of ferroelectric single crystal and piezoceramics, the continuum theory is an appropriate tool. Different continuum theories on the nonlinear ferroelectric and ferroelastic behaviors have been established in the last 30 years and they can be categorized into different types. In micro-electromechanical models, the switching of the domain variants (*e.g.*, spontaneous strain) occurs if the work done by the applied stress and applied electric field achieves a critical level. [39] This theory assumes that the single crystal is comprised of only one domain variant. This model is further modified to allow the contribution of multidomains by introducing the volume fractions of different domain variants. [40] In phenomenological constitutive models, the electromechanical hysteresis effects are reflected by a set of internal history dependent variables. [41, 42] In this approach, the free energy consists two parts, *i.e.*, the reversible part and irreversible part. In thermodynamically consistent macroscopic constitutive models, the irreversible part of the free energy is assumed as a function of a set of internal variables while the reversible part of the free energy is responsible for the piezoelectric effect. [43] Recently, phase-field models have been employed to study the polarization switching and the nonlinear behavior of ferroelectrics. Phase-field models distinguish themselves from other models in the following aspects. First, rather than domain variants, the evolution of ferroelectric domain structures is reflected by a set of order parameters. The order parameter represents the ordering or the symmetry within the system. Second, rather than sharp interface assumption, the order parameter changes its magnitude at the interface. Therefore, the phase-field models offer the possibility to introduce the domain wall energy into the free energy terms by directly providing the gradient of the order parameter. Moreover, the electric and mechanical properties can be coupled with the order parameters. By a proper choice of the free energy, a electromechanically fully coupled model can be established within the phase-field framework. This thesis mainly focuses on the domain, domain walls and their interaction with the electric field and mechanical loading in

relaxors by the phase-field model. The model is further extended to study the relaxor-based ceramics by some additional treatment.

2.2 Relaxors

Relaxors are a class of ferroelectrics with unique properties. It is first discovered by Smolenskii [44] where he found, in his words, "ferroelectrics with a diffuse phase transition" in PMN. Since then, new material systems are discovered, which show similar relaxation features to PMN. In the vital review articles by Cross [9, 7], the relaxors are distinguished from normal ferroelectrics by three characteristics. First, the dielectric response of relaxor is diffusive and frequency-dependent. The temperature of the permittivity peak is shifted to a lower value with the increase in frequency. A strong dispersion in the imaginary part of the permittivity is also a key feature of relaxors. Second, the ferroelectric hysteresis response slowly decays with the increase in temperature. Unlike the ferroelectrics with first-order phase transition, the spontaneous polarization is gradually reduced as the temperature increases, and the hysteresis behavior becomes weaker. Third, relaxor shows no evidence of optical anisotropy or x-ray line splitting at lower temperature. In other words, there is no distinct macroscopic structural phase transition when the temperature decreases to a lower value.

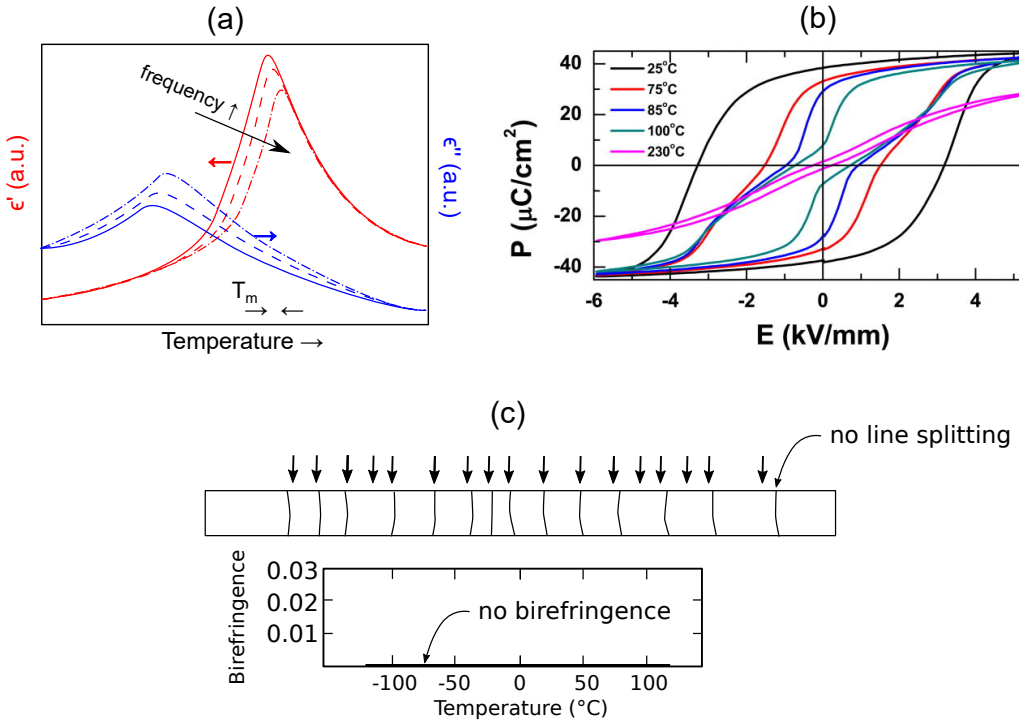

Figure 2.6: *Three features of relaxors: (a) Temperature-dependent permittivity in relaxors shows a diffusive and frequency dependent behavior. [45] (b) The P-E loop gradually lose its hysteresis property with the increase in temperature. [46] (c) XRD and optic evidence of no macroscopical symmetry change in relaxors. [9]*

The relaxor behaviors found in some ferroelectric materials are, for a long time confusing to the ferroelectric community. Taking PMN as an example, one can find the spontaneous polarization, typical hysteresis loop, and domain structure in such a material system. These typical ferroelectric properties indicate a strong dipole correlation. However, the dielectric relaxation process usually related to the weak polarization correlation. This contradiction triggers the development of new models to explain such an abnormal phenomenon. In the following parts, the current understanding of relaxors is reviewed. Some good reviews on relaxor models can be found in the work by Bokov and Ye [47], Kleemann [48] and Ahn *et al.* [8].

The debating on the physical mechanism in relaxors' behaviors lasts for more than half a century. However, the consensus on the origin and the underlying mechanism for the features in the relaxors do not seem to be reached. The established model included but not limited to the diffuse phase transition model [49, 50], the super-paraelectric model [9], the dipolar glass model [51], the WKG model [11], the random-site model [52], the bi-relaxation model [53], and the spherical-random-bond and random-field model (SRBRF model) [54]. All of these models can be roughly categorized into two scenarios, the dipole-glass model which originates from the idea of spin-glass theory in magnet alloys [55] and the random field (RF) model which originates from the idea of Imry and Ma [10]. The two theories show discrepancy on the picture of the crystal symmetry breaking under the cooling process which is shown in Fig. 2.7. Both of them receive a vast amount of experimental and theoretical supports.

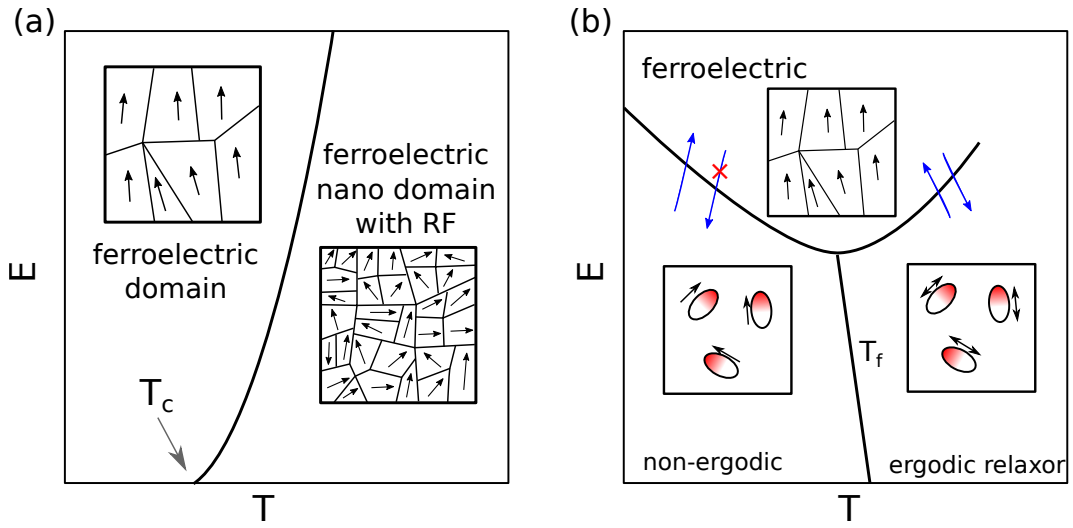

Figure 2.7: *Schematic phase diagram of two relaxor models. (a) RF-type model; (b) dipolar glass-type model. Adopted from Ref. [56]. The matrix surrounding the PNRs are centrosymmetric.*

A good example for the first category of relaxor models is the superparaelectric model. In superparaelectric model, one believes that the energy barrier for polarization switching in ferroelectrics decreases with the size reduction. When the size decreases to some threshold value (k_bT), the thermal disruption becomes critical, and the clusters of polarization become unstable. [49, 57] Cross seems to accept this picture, and in 1987 he pointed out that analogy to

magnetism, “small polar micro-volumes postulated to existing in the relaxor ferroelectric could over some range of sizes, be unstable in a similar manner, giving rise to analogous superparaelectric properties.” [9] Therefore, one can easily expect that the dielectric relaxation is slowing down and finally frozen during cooling. The further theoretical analysis found that the Arrhenius equations fail to characterize this relaxation rate. Instead, a so-called Vogel-Fulcher (VF) relation can successfully describe measurement *ac* frequency f and temperature T_m where the relaxor reaches its maximum dielectric permittivity [58],

$$f = f_0 exp\Big[-\frac{E_A}{k_b(T_m - T_f)}\Big] \tag{2.1}$$

where f_0, E_A, and T_f are constants. Moreover, it is demonstrated that T_f is called the freezing temperature. Viehland *et al.* [51] gave a clear physical “picture” of T_f. Ferroelectric long-range order “thaws” at T_f forced by an electric-field-cooling procedure. From Eq. (2.1), the measurement frequency is infinite small when $T = T_f$, indicating the relaxation time becomes infinite. This equation is reduced to the Arrhenius equation if $T_f = 0$. The permittivity in the range between T_f and T_b can be fitted by some empirical relations, generally with a Lorenz-type,

$$\frac{\epsilon_0}{\epsilon'} - 1 = \frac{(T - T_A)^2}{2\delta^2}, \tag{2.2}$$

where ϵ_0, T_A, and δ are constants. Furthermore, recent studies on the heat capacity of PMN or PMN-PT single crystals revealed that a glass-like behavior really exists in the nonergodic relaxor phase, which can be removed by the application of the external electric field, strongly supporting the dipole-glass model [59, 56].

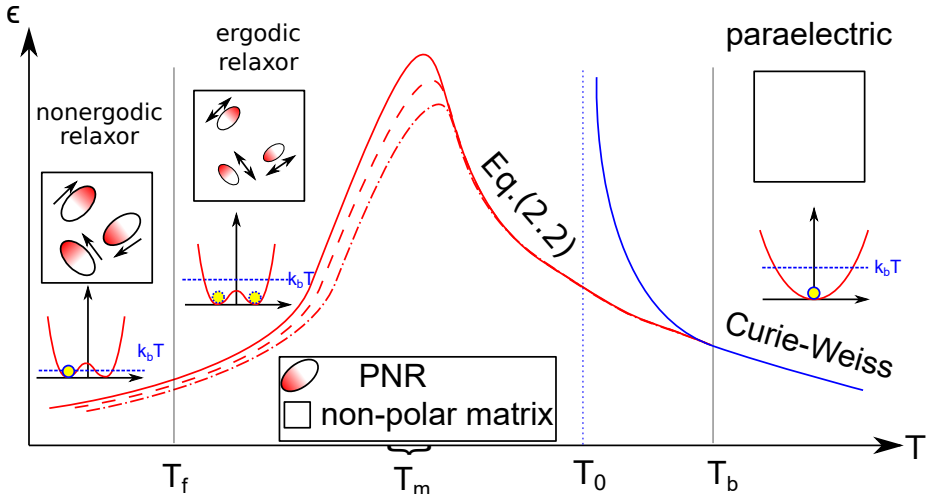

Figure 2.8: *Phase diagram of the canonical relaxor with the interpretation of dipole glass or polar nanoregion scenario. The insert Landau energy shows the idea of the superparaelectric model. Adapted from Refs. [47, 56, 8].*

With such a model, one can get the picture of the different phases in relaxors separated by some characteristic temperatures. Starting from the higher temperature, there is a paraelectric

(PE) or cubic phase, which is similar to that of ferroelectrics. Upon cooling, they transform into the ergodic relaxor (ER) state, in which PNRs with randomly distributed directions of dipole moments appear. This temperature is the so-called Burns temperature (T_b). This relaxor phase is named "ergodic" for the reason that the PNRs in this phase are dynamic, and hence the field-induced phase transition is reversible. As the temperature further decreases from T_b, PNRs become less dynamic. At a low enough temperature, or frozen temperature (T_f) (typically hundreds of degrees below T_b), the relaxation time of the PNRs is unlimited, and the state is called nonergodic state. In this state, the material behaves more like a normal ferroelectric, although the dielectric response is still frequency dependent. A critical phenomenon for nonergodic relaxors which distinguishes them from typical dipole glasses is that they can be irreversibly transformed into a ferroelectric state by a strong enough external electric field. For some relaxors (*e.g.*, PMN-xPT with large x), this phase transition to the ferroelectric state is spontaneous. This phase transition is not a ergodic-nonergodic one, but an ergodic-ferroelectric one.

In the other approach first proposed by Westphal, Kleemann and Glinchuk (known as WKG model), the physical picture is completely different. They questioned the "static freezing" at T_f, and arguing that dielectric relaxation continuously slows down even below the so-called "freezing" temperature. The relaxor behavior is rather driven by the quenched RF. This idea comes from the classical work by Imry and Ma [10], where they point out the ordered state of an extensive system can be unstable against an arbitrarily small static (or "quenched") RF. The original object of Imry and Ma is to answer whether the symmetric is still stable with small disruption by the random field. Considering an isotropic n-component model for phase transition with an order parameter[1] field p_i coupled with a RF $f_i(\mathbf{x})$, the Hamiltonian of the system is

$$\mathscr{H} = -\int (dx)^d p_i(\mathbf{x}) f_i(\mathbf{x}) \tag{2.3}$$

where d is the dimension of the system. The RF $f(\mathbf{x})$ has two properties, *i.e.*, zero mean value and short-range spatial correlation. When the system is split into domains of size L, the system will gain bulk energy of $\mathscr{O}(L^{d/2})$, and lose surface energy (due to the existence of domain wall) of $\mathscr{O}(L^{d-2})$ [60] per domain. Thus if

$$d/2 \leq d-2 \quad \text{or} \quad d \leq 4, \tag{2.4}$$

for an arbitrarily small RF, there will always exist a large enough L, so that the system is energetically favorable to break into the domains with the size of L. This result theoretically supports the splitting of the domains with small RFs. One may note that the above calculation takes

[1] Here, an "order parameter" is a measure of the degree of order across the boundaries in a phase transition system. It usually reflects the symmetry of a system. This concept will be in detailed discussed in Sec. 4.5.)

into account the energy contribution from the domain wall. In a simple Ising model where the domain wall energy is ignored, the value on the right-hand side of Eq. (2.4) is 2. It means that in the RF Ising model [61], the RF can disturb long-range order only for 1-dimensional case.

Following the idea of Imry and Ma, Westphal *et al.* [11] proposed a random-field-induced nanodomain state in relaxors, see Fig. 2.7. They give four arguments in their original paper against the dipolar glass interpretation: (i) The presence of slow relaxation (longer than 10^3 s) during a field cycling well-below T_f. While the dipolar glass model believes the relaxation vanishes at such low temperature. (ii) The presence of Barkhausen jumps implying discontinuous domain rearrangements. While in dipolar glass model, the depinning of the nanodomains takes place on submicrometer length, and hence the linear birefringence should be continuous. (iii) The electric field induces an additional peak in both ϵ' and ϵ''. The broadness and the position of the peak decrease with an increasing electric field. They believe the additional peak is the sign of the percolating cluster of the RF nanodomain structure. [62, 63] (iv) The presence of a power-law decay of the isothermal remanent polarization that signifies the reconstruction of a nanodomain state at zero fields.

The existence and the functionality of the RF are also supported by other experimental observations. By piezoresponse force microscopy (PFM) [64, 65, 66], the miniaturization of the domain structure evidences the correlation between the RF and the order parameter. The random field can stabilize polar nanoregions against thermal fluctuations. The evidence of quenched RF is presented by Kalinin *et al.* using switching spectroscopy PFM [67].

One of the most notable achievements of the RF model is its successful explanation for the ferroelectric-to-relaxor alternating during isovalent substitution, in the systems such as $BaTi_{1-x}Sn_xO_3$ (BST) [68, 45] and $BaTi_{1-x}Zr_xO_3$ [69, 70]. The charge disorder resulting from a chemical inhomogeneity has long been considered essential for the formation of PNRs. However in this case, there is no charge disorder expected due to the isovalent substitution. The responsible mechanism for the induced relaxor state by isovalent substitution can be attributed to the development of "random local strain" fields that may originate from "ferroelastic domain states".

Based on the above theories, numerical simulations are presented focus on different aspects of the relaxor behaviors. In Monte-Carlo simulation, Ma *et al.* proposed a lattice-based relaxor model by introducing the random field to the existing of ferroelectric Hamiltonian. [71] Wang *et al.* established a relaxor model based on a phase-field ferroelectric model by introducing point defects. [72] Li *et al.* proposed a phase-field relaxor model by introducing of an orthorhombic second phase (regarded as PNRs) into the tetragonal ferroelectric phase in a PMN-PT system. [18] Calculations based on quantum mechanics, *e.g.*, *ab initio* calculation are also adopted to study the origin of the mechanism of relaxor behaviors in atomic or even subatomic scale. For these contents, the readers can refer to the works, *e.g.*, by Gröting *et al.* [73] Akbarzadeh *et al.* [74] and Hinuma *et al.* [75].

The above discussion is more focused on the physical origin of relaxor behaviors. In addition to that, the large strain response found in relaxors have received considerable attention in the scientific and industrial community, especially in lead-free community. The review of the current status can be found in Ref. [8, 46, 76, 77] or the review of more recent progress by Rödel *et al.* [78]. The electric-field-induced large unipolar strain was first reported in a BNT-based lead-free piezoceramic by Zhang *et al.* [79, 80, 81]. The unipolar strain performance can be evaluated by the large-signal response

$$d_{33}^{*} = \frac{\varepsilon_{\max} - \varepsilon_{\min}}{E_{\max}}, \tag{2.5}$$

where $\varepsilon_{\max}$ is the maximum strain, $\varepsilon_{\min}$ is the minimum strain, and $E_{\max}$ is the applied electric field, respectively. The strain response of BNT-based piezoceramics can be as large as 0.4 %, and d_{33}^{*} of around 900 pm/V, which makes them competitive to commercially favored soft PZT-based piezoceramics. The reason for the large strain response was initially assumed to the reversible phase transition between paraelectric and field-induced ferroelectric phase during each unipolar cycle. The experiments showed that this assumed paraelectric phase was actually an ergodic relaxor phase [82]. Taking into account the expression of d_{33}^{*} in Eq. (2.5), the key to obtain large strain response appears to be the generation of the macroscopically paraelectric phase at the null field (this will lead to a reduction of $\varepsilon_{\min}$), and the controlling of the phase transition properties (*e.g.*, increase the $\varepsilon_{\max}$ with lower $E_{\max}$). The generation of the macroscopically paraelectric phase can be achieved by, *e.g.*, aging in hard ferroelectrics, introducing antiferroelectric phase, paraelectric phase, relaxor phase or designing composite. The increase of $\varepsilon_{\max}$ or the decrease of the poling field can be achieved by introducing an easier phase transition to the ferroelectric phase. It requires the free energy of the system to be close to its ferroelectric counterpart. These kinds of piezoelectric ceramics is called “incipient” piezoceramics. Among the aforementioned methods, the design of relaxors and relaxor related composites are of practical importance due to their exceptional thermal and cyclic stability.

There are a large number of lead-free relaxor families. [77] One of the most important family is BNT-based relaxors. BNT itself shows typical features of relaxor ferroelectrics. By forming the solid solution, for instance, with BTO of 7% mol, the material favors unique properties, *e.g.*, large piezoresponse and large dielectric permittivity. Such compositional intermediate state between two different structures (*e.g.*, for BNT-xBT, it is the intermediate state between R-phase and T-phase) is called morphotropic phase boundaries (MPB). [83, 84] Other examples with the utilization of MPB include, BNT-based bicomponent (1-x)BNT-x$SrTiO_3$ (x>0.25) [85, 86], xBNT-(1-x)$NaNbO_3$ [87], (1-x)BNT-x$BiFeO_3$ [88], (1-x)BNT-x$BiLiTiO_3$ [89], BNT-Ba(AlNb)O_3 [90], BNT-PT [91], BNT-BKT [91], tricomponent BNT-BT-$KNaNbO_3$ [92], BNT-BT-$AgNbO_3$ [93], BNT-BT-BKT [94] etc., BT-based BT-$BaSnO_3$ [44], BT-$BiScO_3$ [95], BT-$KNbO_3$ [96], etc., KNN-based KNN-$LiSbO_3$ [97], KNN-$SrTiO_3$ [98], etc., and Ba(ZrTi)O_3-(BaCa)TiO_3 (BZCT) family [99, 100,

101]. More combinations and the phase diagrams can be found in Ref. [102]. Figure 2.9 summarized the large-signal behavior of parts of the lead-free relaxor at room temperature.

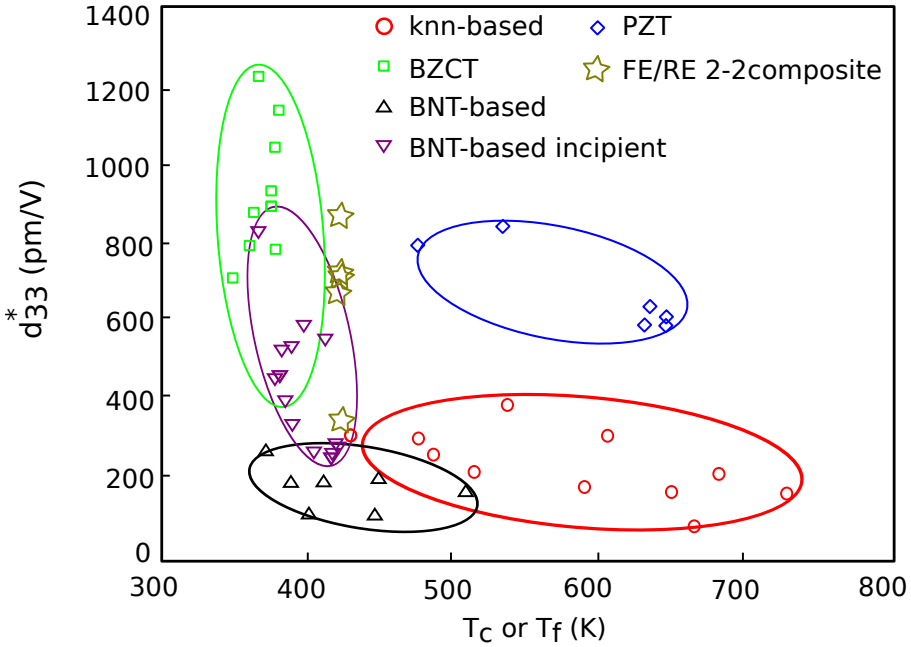

Figure 2.9: *The large signal piezoelectric coefficient (at room temperature) as a function of depolarization temperature for KNN-based, BCZT, BNT-based, BNT-based Incipient piezoelectrics, PZT and FE/RE composite. Data are collected from Refs. [78, 93, 23].*

As mentioned above, the incipient lead-free piezoceramics show great potential in replacing the current market-dominating PZT-type piezoceramics, due to their field-induced giant strain. However, the required electric field for triggering the giant strain in the incipient lead-free piezoceramics is relatively high (for instance, BNT-7BT at 6 $\mathrm{kV\,mm^{-1}}$), and the large hysteresis also restricts their application area. Thus the relaxor/ferroelectric composite is proposed to overcome the disadvantages above. [23, 22, 21, 103] It should be noted that, the temperature-frequency dependent permittivity measurement and other methods prove that, the ferroelectric end-members adopted in most of the ferroelectric/relaxor composites are ergodic relaxors. However, it makes little difference if one views them as normal ferroelectrics, when dealing with the electromechanical response under slow (compared with relaxation time) field loading.

A composite material is a kind of material made from two or more constituent materials with significantly different mechanical, physical, or chemical properties that, when combined, produce a material with characteristics different from the individual components. Different from materials with multi-phases or solid-solutions, the individual components remain separate and distinct within the structure. The idea of designing dielectric composite for better performance can date back to the earlier of the twentieth century. The theories of predicting properties of composites based on the properties of end-member materials are useful and in strong demand. Early attempts to theoretically predict the dependence of the electrical properties of the com-

posite with volume fraction were made by Maxwell and Wagner by a spherical model. [104] Dielectric constants of parallel and series model are in detail discussed in Ref. [105]. Pauer [106] discussed the dielectric properties of piezoelectric ceramics based on serial, parallel, spherical, and cubic models. Banno [107] described the theoretical consideration for the dielectric and piezoelectric constants of 1-3, 0-3, and 3-0 type. The theoretical analysis of ferroelectric composite considering the hysteresis effect is accomplished by Dausch in Refs. [19, 20]. As the simplest and mostly studied composites, *i.e.*, 2-2 type serial ferroelectric composites, they can be in general modeled as two serial connected capacitors. Therefore, the summation of the voltage applied at each phase equals the total applied voltage, while the charges generated (thus the polarization) at the interface are the same between layers. It is the so-called polarization coupled model. Zhang *et al.* [23] experimentally proved that there is an additional mechanical coupling accompanied by polarization coupling in the strain response in ferroelectric/relaxor composite, although the numerical and theoretical analysis are needed. Moreover, this ferroelectric/relaxor structure was also found in the microscopic scale. The so-called "core-shell" structure found in the relaxors ceramics are actually 0-3 type ferroelectric/relaxor "composite" within a grain. [28, 108] The exceptional piezoelectric properties can be ascribed to the interaction between these two distinct phases.

In short, relaxor ferroelectric materials are of great interest for their abnormal relaxation behaviors and exceptional electromechanical properties. The models for the relaxors can be in general categorized into two types, RF model and dipole-glass model. Each model is supported by some experimental arguments. The relaxors show great applicability in giant strain actuators. The ferroelectric/relaxor composite/core-shell structures can overcome some disadvantages usually found in relaxor materials themselves.

2.3 Flexoelectricity

For all dielectrics, including ferroelectrics and relaxors, there exists an electromechanical coupling effect called flexoelectricity, which does not depend on any symmetry of the crystal structure in the materials. It is a generic effect for any insulators and even semiconductors. The basic concepts of flexoelectricity are briefly introduced in this section, and a more comprehensive discussion will be shown in Sec. 7.3.

The flexoelectric effect is an electromechanical effect in which the dielectric polarization exhibits a linear response to a gradient of mechanical strain. [109] Different from ferroelectricity or piezoelectricity, flexoelectricity is a universal property exist in the non-conductive material irrespective of the crystal symmetry.

Flexoelectricity was first observed in liquid crystals [110], while it is rarely mentioned in piezoelectric ceramics owning to its relatively small magnitude, compared with other electromechanical coupling effects. This situation is changed after a series of systematic experi-

mental investigations on the flexoelectric effect in the ferroelectric ceramics reported by Ma and Cross in the early 2000s, see *e.g.*, Refs. [111, 112]. The researchers are intrigued to study flexoelectricity and its applications for several reasons. First, there are no symmetry requirements (unlike non-centrosymmetry limitation for piezoelectricity) for flexoelectricity. Therefore, this effect provides more choices for materials in electromechanical coupling applications. Second, the flexoelectric effect is positively correlated with strain gradient, and the strain gradient is more pronounced in smaller length-scale. [113] Hence, the design of nanoscale devices particularly needs the consideration of flexoelectricity. Third, for some materials with large strain inhomogeneity, *e.g.*, relaxors, flexoelectricity can help us explain some abnormal phenomena.

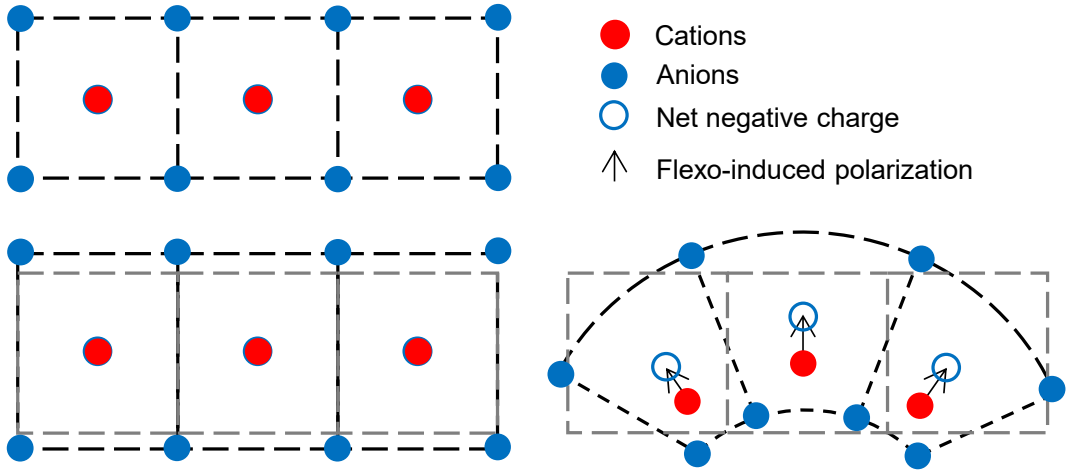

Figure 2.10: *Schematic figure of flexoelectricity. For a material with centrosymmetric crystal structure (e.g., m3m for perovskites), the application of a uniform strain does not generate polarization, while a strain gradient does.*

Figure 2.10 shows the microscopic mechanism of flexoelectricity. Uniform strain does not break inversion symmetry and hence cannot generate polarization in a centrosymmetric material. However, a strain gradient (here in Fig. 2.10 due to bending) can break the inversion symmetry, and therefore lead to relative displacements of the centers of both negative and positive charges. The black arrows Fig. 2.10 represent the resultant polarization, which is referred to as the flexoelectric-induced polarization. Similarly, the inhomogeneity of polarization can also generate strain, which is called *inverse flexoelectricity*. The flexoelectric effect is conventionally expressed by a fourth-rank *flexoelectric tensor* μ_{ijkl}, which was offered by Kogan in 1964 [114]. In 1968, a phenomenological framework for the flexoelectric effect was proposed by Mindlin *et al.* [115]. By an energy minimization process, the electric field can be related to the strain gradient by a *flexocoupling tensor* f_{ijkl}. The flexocoupling tensor can be transformed into flexoelectric tensor by the dielectric susceptibility tensor χ_{km} through the following equation:

$$\mu_{ijkl} = \chi_{km} f_{ijml}. \tag{2.6}$$

The detailed discussion on these coefficients will be presented in Sec. 7.3.

When one of the following situations appears, the role of the flexoelectric effect becomes significant:

- Flexocoupling coefficients are large, *e.g.*, for ferroelectrics and some complex oxide ceramics [116]. For barium titanate ceramics above the Curie temperature, the experimentally measured flexocoupling tensor can be as large as 560 V [109].
- The other forms of electromechanical coupling effects are absent. One example is the paraelectric phase of ferroelectric material above the Curie temperature. Another example is the material which is intrinsically centrosymmetric, *e.g.*, NaCl crystal.
- The strain-gradient is large, which is usually the case when considering larger polar molecules, soft materials, [117] and biomaterials [118]. For example, there is a postulation that flexoelectricity may take a role in the energy transformation in inner mitochondrial. [119]
- The critical length of the system is small. The strain gradient is inversely proportional to the size. That is the reason why there are a lot of abnormal phenomena and applications attributed to the nanoscale flexoelectricity. [113] In nanoscale devices, such as microelectromechanical systems (MEMS), there have been some attempts of flexoelectric-based applications [120, 121].

There are plenty of numerical simulations of flexoelectric effect focusing on different scales. Using first principle calculations, Hong *et al.* calculated the flexoelectric coefficients of BTO and STO [122], and other materials [123, 124]. Ponomareva *et al.* [125] calculated the flexoelectric tensor for BST solid solutions. Based on strain-gradient elasticity theory, Mao *et al.* developed a flexo-electro-elastic model and presented the analytical and numerical solutions with different loadings, geometries, and defects. [126, 127, 128] Other flexoelectric continuum models include but not limited to the following works, *e.g.*, Sharma *et al.* [129], Abdollahi *et al.* [130]. These models are the extension to the piezoelectric model. In the phase-field approach, Gu *et al.* [38] calculated the influence of flexoelectricity on the domain wall in ferroelectrics. Chen *et al.* modeled the flexoelectric effect in ferroelectric epitaxial thin films [131] and bulk materials [132]. Though plenty of flexoelectric models have been developed, there are still some challenges. For example, the experimentally determined flexoelectricity tensor and first principle calculations are incompatible, sometimes different with one order of magnitude. The underline mechanism should be extensively studied. Moreover, there are limited finite element implementations of the phase-field ferroelectric-flexoelectric model. Blanks in this field still need to be filled.

Chapter 3

Objectives of the thesis and outline

3.1 Objectives

The research objective of this thesis is to establish a generic phase-field relaxor model and apply the model to different problems. Considering the state-of-the-art development of the theory of the relaxor model, there is still a debate on the physical origins of relaxor features in relaxors. Nevertheless, to build a generic phase-field model, a proper theory should be selected. On the other hand, the relaxors have been made use of in a variety of fields. The numerical study on the relaxors, especially in terms of the electromechanical response, is needed in industry. Based on the above considerations, this study pursues answers to the following research questions:

1) Which relaxor theory can generally reflect the domain miniaturization in relaxors?

2) What is the influence of the random field on the domain structure? How?

3) What is the influence of the random field on the hysteresis loops and strain response? How?

4) How to model different kinds of relaxor materials, for instance, relaxors with small hysteresis and the relaxors with nonpolar-polar phase transition?

5) What is the strain response of the relaxor/ferroelectric composite under unipolar loading?

6) What is the role of the coupling effect between different layers in relaxor/ferroelectric composite. How do they influence on the large-signal piezoresponse?

7) How can we design relaxor/ferroelectric composites for a better performance?

8) In the core-shell relaxor/ferroelectric structure, how does the core-shell interface influence the polarization distribution, and therefore, the overall performance?

9) In the core-shell relaxor/ferroelectric nanoparticle, will the strain-gradient be large enough to generate the flexoelectric-induced polarization? Can we make use of the flexoelectric effect within the core-shell nanoparticle?

3.2 Outline

The thesis is outlined in the following.

Chapter 2 gives a brief introduction to the ferroelectrics (in Sec. 2.1) and relaxors (in Sec. 2.2). It is followed by a brief introduction of flexoelectricity (Sec. 2.3).

Chapter 4 offers an overview of the basic theory of electrostatics, continuum mechanics and electromechanical coupling, which will be used in the next chapter when developing the phase-field relaxor model. The Landau-Devonshire theory (Sec. 4.4) and phase-field theory (Sec. 4.5) are introduced thereafter.

In Chap. 5, a generic phase-field relaxor model based on random field theory is proposed, in which the microforce theory is utilized. It is followed by a few simulation examples, including the domain configuration, hysteresis loops, ferroelastic response and the ferroelectric response with the additional mechanical loading.

Chapter 6 focuses on the simulation of the relaxor/ferroelectric layered composite. To simulated the "incipient" relaxor piezoceramics, the previously developed relaxor model in Chap. 5 is modified, through which the field-induced nonpolar-polar phase transition can be reflected. By presenting a series of simulations on the multilayer lead-free ceramic/ceramic relaxor/ferroelectric composites, the large-signal response is optimized. In order to find the mechanism of the coupling effect in the layer composites, three types of interface are introduced.

In Chap. 7, a typical microstructure found in relaxor/ferroelectric solid solutions, *i.e.*, the core-shell structure is investigated. After a brief review of the core-shell structure (Sec. 7.1), the phase-field simulation on the relaxor/ferroelectric core-shell particle is presented to explain the remanent domain structure found in the BNT-ST sample by a piezoresponse force microscopy (Sec. 7.2). After introducing the flexoelectric phase-field model (Sec. 7.3), Sec. 7.4 explains the domain-like nanoregions found in BNT-ST nanoparticle at an extreme temperature by a phase-field flexoelectric-ferroelectric model.

Chapter 4

Basic theories

The phase-field ferroelectric models developed in this thesis involve both the electrical and mechanical quantities. In this chapter, the fundamental equations in electrostatics and mechanics are introduced in Sec. 4.1 and Sec. 4.2, respectively. The coupling between electrical and mechanical quantities can be categorized into piezoelectricity, electrostriction, and flexoelectricity, which are discussed in Sec. 4.3. As a prerequisite for the ferroelectric phase-field model, the Landau-Devonshire theory is introduced in Sec. 4.4. The phase-field theory is eloborated in Sec. 4.5.

4.1 Electrostatics

The classical complete description of the electromagnetic fields can be covered by Maxwell equations [133]. For ferroelectrics, the electrodynamic effect and electro-magnetic effect are usually neglected, and hence the electric properties in ferroelectrics involve only the electrostatics. In this section, The basic concepts of electrostatics are introduced, which can also be found in the classic textbooks of Landau and Lifshitz [134], Morin and Purcell [135]. More attention is paid here for the properties of polarization, since it plays an essential role in ferroelectric behavior.

4.1.1 Charge, electric field, and electric potential

Electrons and protons possess charge. The electric charges are in nature quantized, which means that it comes in integer multiples of individual small units. One unit charge is called the elementary charge, with the magnitude equals to a single electron. This magnitude is denoted by e, with the value of around $1.6021766208(98)\times10^{-19}$ C [136]. The interaction between two stationary electric charges is described by Coulomb's law. The electrostatic force experienced by a charge q_a at position x_i^a in the vicinity of another charge q_b at position x_i^b in vacuum equals to

$$F_i^a = \frac{q_a q_b}{4\pi\epsilon_0}\frac{(x_i^a - x_i^b)}{r^3}, \tag{4.1}$$

where r is the distance between the two positions. Equation 4.1 is called Coulomb's equation. The electrostatic force experienced by charge q_0 from a group of charges (q_a, q_b ...) follows the

simple superposition principle, *i.e.*, the summation of the electrostatic force from all the other charges. For a continuum description, discrete charges q_i is replaced by a charge density $\varrho(x_i)$. A continuous and bounded charge density $\varrho(x_i)$ can be defined using volume average over some representative volume V^R:

$$\varrho = \frac{1}{V^R}\sum_{j=1}^{N} q_j, \tag{4.2}$$

where $(q_1, q_2 \ldots q_N)$ are the individual charges within the representative volume. The representative volume in dielectrics is usually much smaller than the region of interest, and much larger than the charge couriers.

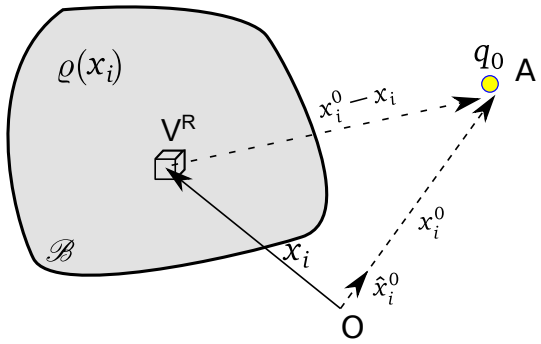

Figure 4.1: *The Coulomb interaction between a test charge q_0 and a continuous charge distribution ϱ within the volume of interest.*

The Coulomb's equation thus can be generalized from point charges q to continuous charge distributions. Considering a continuum body $\mathscr{B}$, the electrostatic force experienced by test charge q_0 at position x_i^0 in the vicinity of a charge density field $\varrho(x_i)$ is

$$F_i = q_0 \int_{\mathscr{B}} \frac{\varrho}{4\pi\epsilon_0}\frac{(x_i^0 - x_i)}{r^3}\mathrm{d}v. \tag{4.3}$$

Here and below, the superscript ^{0} represents the reference position illustrated as "O" in Fig. 4.1. From Eq. (4.3), one can find that the force is proportional to q_0. Dividing out q_0, one obtains a vector field that depends only on the charge distribution of the system, which defines of *electric field* E_i at point x_0:

$$E_i := \frac{F_i}{q_0} = \int_{\mathscr{B}} \frac{\varrho}{4\pi\epsilon_0}\frac{(x_i^0 - x_i)}{r^3}\mathrm{d}v. \tag{4.4}$$

The distribution of the electric field can be calculated directly from Eq. (4.4), but usually it is impossible due to the complex distribution of charges. On the other hand, the Maxwell equations describe the distribution and evolution of the electric field, which converts the calculation of electric field into solving a partial derivative equation (PDE) sets with certain boundary conditions. It provides a solution to describe the complex distribution of the charges in space. By

ignoring the field and assuming that the electric field is static, the Maxwell equations are in a reduced form

$$E_{i,i} = \frac{\varrho}{\epsilon_0}, \tag{4.5a}$$

$$\varepsilon_{ijk} \nabla_j E_k = 0, \tag{4.5b}$$

where $()_{,i}$ is the partial derivative with respect to the Cartesian coordinate i, ε_{ijk} the Levi-Civita symbol, and ∇_j the derivative operator, *i.e.*, $\nabla_j = \partial_j$. Equation (4.5a) is called the Gauss's law, and Eq. (4.5b) is the simplified Faraday's law when the magnetic field is static. For a curl-free vector field in a simple connected space, the field is conservative. It can be expressed as the gradient of a scalar field:

$$E_i = -\phi_{,i}, \tag{4.6}$$

where ϕ is the electrostatic potential or simply the *electric potential*. Combining Eq. (4.6) with Eq. (4.4), the electrostatic potential of a continuous volume charge distribution ϱ can be derived:

$$\phi = \frac{1}{4\pi\epsilon_0} \int_{\mathscr{B}} \frac{\varrho}{r} \mathrm{d}v. \tag{4.7}$$

Combination of Eq. (4.5a) and Eq. (4.6) leads to:

$$\phi_{,ii} = -\frac{\varrho}{\epsilon_0}. \tag{4.8}$$

Equation 4.8 is the famous second-order partial differential equation known as Poisson's equation. It is reduced to Laplace's equation when there is no charge density:

$$\phi_{,ii} = 0. \tag{4.9}$$

4.1.2 Dipole moment and polarization

As shown in the last section, Eq. (4.4) and Eq. (4.7) enables the calculation of the electric field and the potential from the local charge density distribution ϱ. However, the distribution of ϱ within a dielectric material is usually complicated, considering that Avogadro constant is in the order of $10 \times 10^{23}\,\mathrm{mol}^{-1}$. However, the potential distribution can be considered as the superposition of some simple distribution cases, or "modes". It can be realized by the Taylor expansion of Eq. (4.7) with respect to r. According to the calculation in Appx. A, the first expansion term gives rise to the average charge density of within the region. The second term is the moment of the charge with respect to the distance to the reference point. And the third term results in the second-momentum of the charge. Thus the distribution of the potential

can be viewed as the superposition of the average charge density plus its moment, its second-momentum and higher-order momentums. This moment is defined as the *electric dipole*, and its norm is defined as the *dipole moment*.

Figure 4.2 shows the potential distribution of net charge, a dipole and a quadrupole. The solid line indicates the electric field line of the potential field generated. Within this thesis, only charges and dipole moments are taken into account, while moments of higher order are neglected.

Let's now focus on the properties of a dipole. The simplest example of a dipole is a pair of electric charges of equal magnitude but opposite sign, separated by a small distance. The dipole moment can be derived from Eq. (A.5) as

$$p_i = \int_{\mathscr{B}} \left[-q\delta(x_i^1) + q\delta(x_i^2)\right] \mathrm{d}v = q\left[\delta(x_i^2) - \delta(x_i^1)\right] = qd_i, \tag{4.10}$$

where δ is the Dirac function and d_i the distance vector pointed from negative charge to the positive charge. From Eq. (4.10), the dipole moment depends only on the charge distribution, not on the observation point. An idealization of this two-charge system is the electrical point dipole consisting of two infinite charges only infinitesimally separated, *i.e.*, $\|d_i\| \ll \|x_i^0 - x_i^1\|$, where x^0 is the place of interest and r_i is the corresponding displacement vector. (See Fig. 4.3) The potential originated from this pair of electric charges can be calculated by Eq. (A.4):

$$\phi = \frac{1}{4\pi\epsilon_0} \frac{p_i(x_i^0 - x_i^1)}{\|x_i^0 - x_i^1\|^3} = \frac{p_i r_i}{4\pi\epsilon_0 r^3}, \tag{4.11}$$

where r is the distance from the dipole to the place of interest. The electric field generated by this pair of electric charges can be calculated by Eq. (4.6):

$$E_i = -\phi_{,i} = -\frac{1}{4\pi\epsilon_0}\left(\frac{p_j r_j}{r^3}\right)_{,i} = \frac{1}{4\pi\epsilon_0 r^3}\left[\frac{3(p_j r_j) r_i}{r^2} - p_i\right]. \tag{4.12}$$

Polarization density (or *polarization*) is used to describe the local dipole moment in a dielectric material. It is defined as the dipole moment per volume:

$$P_i = \frac{\mathrm{d}p_i}{\mathrm{d}v}. \tag{4.13}$$

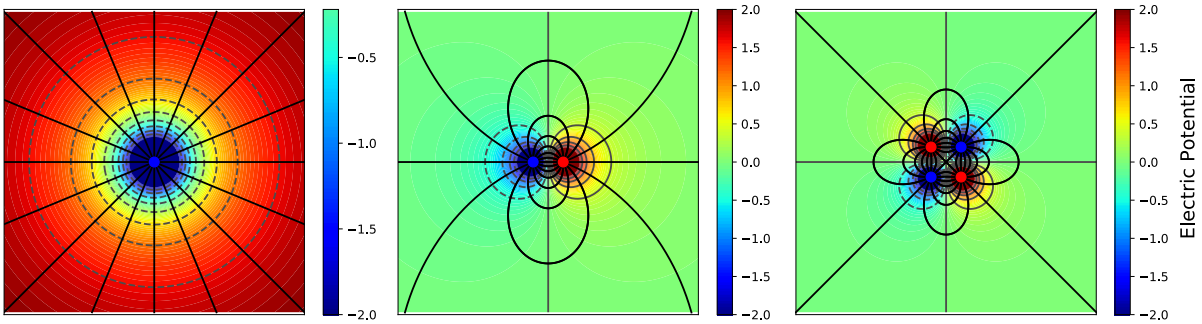

Figure 4.2: *The potential distribution of a net charge, a dipole, and a quadrupole.*

4.1.3 Dielectric displacement

The above discussion enables the description of the system consists of the point charge and charge densities in a vacuum. Consider the charge distribution within the matter. Equation (4.5a) and (4.5b) are still valid in a dielectric medium. However, in a dielectric medium it is usually more convenient to distinguish the charges in the dielectric due to the different behaviors/origins. For the charge which can be added to, or removed from a dielectric (*e.g.*, the plate of a capacitor), it is often called *free charge*. For the charge which are integral parts of the atoms or molecules of the dielectric (*e.g.*, ions in ceramics) is often referred to as a *bound charge*. Thus, Eq. (4.5a) can be rewritten as:

$$\epsilon_0 E_{i,i} = \varrho_{\text{free}} + \varrho_{\text{bound}}. \tag{4.14}$$

For dielectric materials, the cations and anions are bounded to the lattice. Assuming an insulating dielectric material occupying the volume $\mathscr{B}$ with the electric field E_i. The electric field makes the bound charges displaced, thus inducing the local polarization P_i. By using Eq. (A.4) and Eq. (A.5) the potential due to the dipoles can be obtained using superposition over the dielectric volume:

$$\begin{aligned}
\phi(x_i) &= \int_{\mathscr{B}} \frac{x_i^0 P_i}{4\pi\epsilon_0 \|x^0\|^3} \mathrm{d}v \\
&= \frac{1}{4\pi\epsilon_0} \int_{\mathscr{B}} P_i \nabla_i \Big(\frac{1}{\|x^0\|}\Big) \mathrm{d}v \\
&= \frac{1}{4\pi\epsilon_0} \int_{\mathscr{B}} -\nabla_i P_i \Big(\frac{1}{\|x^0\|}\Big) \mathrm{d}v + \frac{1}{4\pi\epsilon_0} \int_{\partial\mathscr{B}} \Big(\frac{1}{\|x^0\|}\Big) P_i n_i \mathrm{d}s \quad \text{(Gauss theorem)}
\end{aligned} \tag{4.15}$$

where n_i is the normal vector to the boundary and $\|x^0\|$ is the distance between the position of interest and the reference position "O". Compare Eq. (4.15) with Eq. (A.3), the divergence of the dipole moment gives the bound charge density:

$$-P_{i,i} = \varrho_{\text{bound}}. \tag{4.16}$$

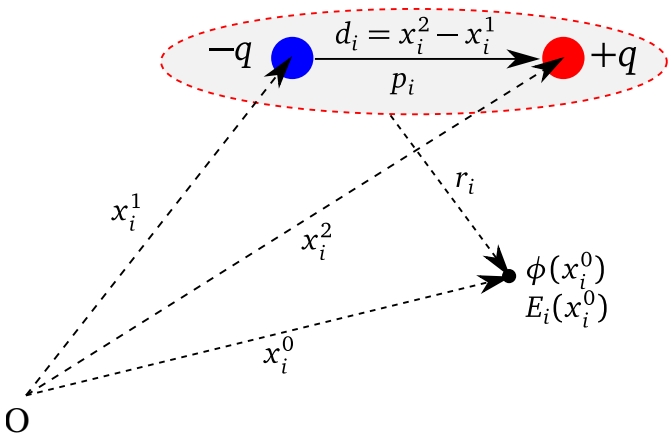

Figure 4.3: *Dipole moment p_i and electric field E_i of a charge pair.*

Inserting Eq. (4.16) into Eq. (4.14) yields

$$(\epsilon_0 E_i + P_i)_{,i} = \varrho_{\text{free}}. \tag{4.17}$$

Here a new field variable *electric displacement* can be naturally introduced,

$$D_i := \epsilon_0 E_i + P_i, \tag{4.18}$$

such that

$$D_{i,i} = \varrho_{\text{free}}. \tag{4.19}$$

The second term on the right-hand side of Eq. (4.15) indicates that, at the material boundary, the dielectric displacement exhibits a discontinuity in the normal direction if there exists a surface charge density ω, *i.e.*,

$$D_i n_i = \omega. \tag{4.20}$$

Overall, the distribution of D_i measures the response of insulating materials on the applying electric field.

For a linear, homogeneous, isotropic dielectric in the electric field, P_i depends linearly on the constant electric field,

$$P_i = \epsilon_0 \chi_{ij} E_j, \tag{4.21}$$

where χ_{ij} is the *electric susceptibility* of the material. Equation 4.18 can be rewritten as

$$D_i = \epsilon_0(\delta_{ij} + \chi_{ij})E_j = \epsilon_0 \epsilon^r_{ij} E_j = \epsilon_{ij} E_j \tag{4.22}$$

where ϵ_{ij} is the material permittivity and ϵ^r_{ij} is the dimensionless relative permittivity. The permittivity ϵ_{ij} in the dielectric material is frequency dependent.

4.2 Continuum mechanics

For the ferroelectric model in the thesis, the electrical properties are fully coupled with mechanical properties, thus a brief introduction of basic concepts in continuum mechanics[137, 138] is necessary.

4.2.1 Deformation and strain

The basic property of a *body* $\mathscr{B}$ in continuum mechanics is the occupation of regions of Euclidean space $\mathscr{E}^3$, or its *configuration*. The configuration of $\mathscr{B}$ may change with a given open time-interval. A *reference configuration* is an arbitrary chosen fixed configuration. The body is referred to as the reference body $\mathscr{B}_r$ with a point vector X_i as a material point. The motion of $\mathscr{B}$ is described by a smooth function χ^d (See Fig. 4.4) that maps each X_i at time t to

$$x_i = \chi^d(X_i, t). \tag{4.23}$$

The smoothness of a function is a property measured by the number of continuous derivatives it has. In this section, the continuity up to the first derivative, *i.e.*, C^1 continuity is required. For a fixed time t, $\chi^d(X,t)$ describes the deformation from its reference configuration and can be denoted by $\chi^d_t(X)$. The *displacement* is defined as

$$u_i(x_i, t) = x_i(X_i, t) - X_i. \tag{4.24}$$

The deformation gradient tensor at a given time is then defined as

$$F_{ij} := \frac{\partial x_i}{\partial X_j} = \frac{\partial u_i}{\partial X_j} - \delta_{ij}. \tag{4.25}$$

The concept of *strain* is used to evaluate how much the displacement differs locally from a rigid body displacement. One kind "measure" of strain at point X can be defined as the difference between the distances of adjacent points in the deformed and undeformed state. The square of the distance between two adjacent points in the deformed state is given by

$$ds^2 = dx_i dx_i = \frac{\partial x_i}{\partial X_j}\frac{\partial x_i}{\partial X_k} dX_j X_k. \tag{4.26}$$

The square of the distance between two adjacent points in the undeformed state is given by:

$$dS^2 = dX_i dX_i = dX_i dX_j \delta_{ij}. \tag{4.27}$$

The difference between Eq.(4.26) and Eq.(4.27) can be reformulated as

$$ds^2 - dS^2 = \left(\frac{\partial x_k}{\partial X_i}\frac{\partial x_k}{\partial X_j} - \delta_{ij}\right) dX_i dX_j = (F_{ki}F_{kj} - \delta_{ij}) dX_i dX_j. \tag{4.28}$$

Replacing x_i with $u_i + X_i$, one obtains

$$ds^2 - dS^2 = \left(\frac{\partial u_i}{\partial X_j} + \frac{\partial u_j}{\partial X_i} + \frac{\partial u_k}{\partial X_i}\frac{\partial u_k}{\partial X_j}\right) dX_i dX_j = 2E_{ij} dX_i dX_j. \tag{4.29}$$

where

$$E_{ij} = \frac{1}{2}\left(\frac{\partial u_i}{\partial X_j} + \frac{\partial u_j}{\partial X_i} + \frac{\partial u_k}{\partial X_i}\frac{\partial u_k}{\partial X_j}\right) \tag{4.30}$$

is the *Green's strain tensor*. For sufficiently small (infinitesimal) displacement gradients ($\frac{\partial u_i}{\partial X_j} \ll 1$), the higher order terms can be ignored:

$$E_{ij} \approx \frac{1}{2}\left(\frac{\partial u_i}{\partial X_j} + \frac{\partial u_j}{\partial X_i}\right) = \varepsilon_{ij}, \tag{4.31}$$

where ε_{ij} is the *Cauchy strain tensor*. In the entire thesis, the discussion is restricted to the infinitesimal strain framework, since the strain of the subject of this thesis, ferroelectrics, is usually below 0.5%.

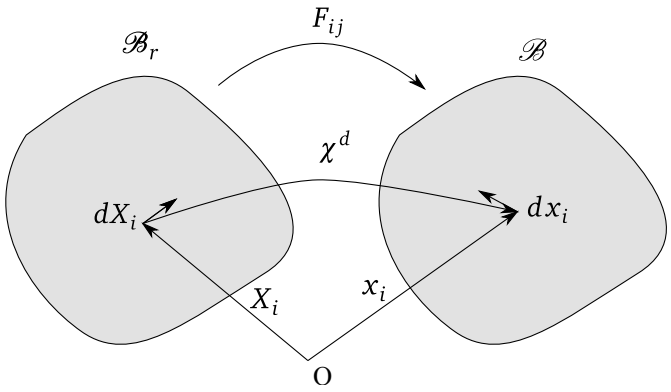

Figure 4.4: *Illustration of reference configuration, current configuration and the mapping of their differentials F_{ij}.*

4.2.2 Force balance and stress

Motions are accompanied by forces. Forces in continuum mechanics can be described by the contacting forces acting on the surface and the body forces on the interior points. The contacting forces and body forces can be measured per unit area and volume in the deformed body $\mathscr{B}$.

The Cauchy's hypothesis deals with the form of the contacting force. Cauchy introduced a surface traction field $t_i(n_i, x_i, t)$ at a subregion $\partial\mathscr{R}$ of $\mathscr{B}$. The force balance can be written as:

$$\int_{\mathscr{R}} \rho \dot{v}_i = \int_{\partial\mathscr{R}} t_i(n, x, t)\mathrm{d}s + \int_{\mathscr{R}} f_i \mathrm{d}v, \tag{4.32}$$

where ρ is the mass density, $\dot{v}_i$ the velocity vector and f_i the body force.

The Cauchy's theorem states (see *e.g.* §19 in [137]), the consequence of balance of forces is that there exists a spatial (second order) tensor field σ_{ij} in $\mathscr{B}$, called the Cauchy stress, such that

$$t_j(n_i) = \sigma_{ij} n_i. \tag{4.33}$$

The Cauchy stress maps one vector field (n_i) to another vector field t_i. Assuming that the force and moment balances are satisfied and inertia contribution can be ignored, the divergence theorem can be utilized to rewrite the force balance equation as

$$\int_{\mathscr{B}} (\sigma_{ij,j} + f_i) \mathrm{d}v = 0. \tag{4.34}$$

Since this must hold for all spatial regions $\mathscr{B}$, the following local force balance holds, *i.e.*,

$$\sigma_{ij,j} + f_i = 0 \quad \text{in} \quad \mathscr{B} \tag{4.35}$$

According to the conservation of angular momentum, at the equilibrium state, the summation of moments with respect to an arbitrary point is zero. It leads to the symmetry of the stress:

$$\sigma_{ij} = \sigma_{ji}. \tag{4.36}$$

For a *continuous linear elastic* material, the stress is linearly related to the strain by Hooke's law:

$$\sigma_{ij} = c_{ijkl}\varepsilon_{kl}, \tag{4.37}$$

where c_{ijkl} is the elastic stiffness tensor. The elastic stiffness tensor of an isotropic material has two independent components. A transverse isotropic material (*e.g.*, a poled ferroelectrics ceramic) can be described by 5 independent elastic constants.

4.3 Electromechanical relations

As mentioned in section 2.1, ferroelectrics are intrinsically piezoelectrics, thus have piezoelectric and inverse piezoelectric effect. At the same time, as an universal property for all dielectrics, the electrostrictive effect and flexoelectric effect also contributes to the electromechanical behaviors in ferroelectrics. To fully describe the electromechanical coupling effects in ferroelectrics, all of these properties needs to be reviewed. The material coefficients for piezoelectricity, electrostriction, and flexoelectricity relate the mechanical properties such as stress and strain elaborated in Sec. 4.2 with the electric properties such as electric field and electric displacement elaborated in Sec. 4.1 in different manners. In the following, they are reinterpreted in the thermodynamic framework.

Depending on the choice of free variables, the piezoelectric constitutive law has different forms. In the following discussion, the electric enthalpy is chosen as the characteristic state function. With the consideration of Eq. (4.22) and Eq. (4.37), the electric enthalpy with piezoelectric effect can be constructed as:

$$\mathscr{H}_2(E_i, \varepsilon_{ij}) = \mathscr{H}^{ela} + \mathscr{H}^{ele} + \mathscr{H}^{piezo} = c_{ijkl}\varepsilon_{ij}\varepsilon_{kl} + \epsilon_{ij}E_iE_j + e_{ijk}\varepsilon_{ij}E_k, \tag{4.38}$$

where the first two terms on the right-hand side represent the elastic energy and electric energy, and the last term represents the piezoelectric contribution. With the expression of $\mathscr{H}_2$, the constitutive relation with the piezoelectric effect can be derived in a stress-charge form:

$$D_i = -\frac{\partial \mathscr{H}_2}{\partial E_i} = \epsilon_{ij} E_j - e_{ijk}\varepsilon_{jk}, \tag{4.39a}$$

$$\sigma_{ij} = \frac{\partial \mathscr{H}_2}{\partial \varepsilon_{ij}} = -e_{kij} E_k + c_{ijkl}\varepsilon_{kl}, \tag{4.39b}$$

where e_{ijk} is a third rank tensor. For a ferroelectric material, this piezoelectric constant is highly dependent on polarization, *i.e.*, $e_{ijk} = e_{ijk}(P_i)$. The piezoelectric constant e_{ijk} can be measured based on the following partial derivatives:

$$e_{ijk} = \Big(\frac{\partial D_i}{\partial \varepsilon_{jk}}\Big)^E \quad \text{or} \quad e_{ijk} = -\Big(\frac{\partial \sigma_{jk}}{\partial E_i}\Big)^\varepsilon. \tag{4.40}$$

The other three types of piezoelectric constants can be defined as:

$$d_{ijk} = \Big(\frac{\partial D_i}{\partial \sigma_{jk}}\Big)^E \quad \text{or} \quad d_{ijk} = \Big(\frac{\partial \varepsilon_{jk}}{\partial E_i}\Big)^\sigma \tag{4.41a}$$

$$g_{ijk} = -\Big(\frac{\partial E_i}{\partial \sigma_{jk}}\Big)^D \quad \text{or} \quad g_{ijk} = \Big(\frac{\partial \varepsilon_{jk}}{\partial D_i}\Big)^\sigma \tag{4.41b}$$

$$h_{ijk} = -\Big(\frac{\partial E_i}{\partial \varepsilon_{jk}}\Big)^D \quad \text{or} \quad h_{ijk} = -\Big(\frac{\partial \sigma_{jk}}{\partial D_i}\Big)^\varepsilon, \tag{4.41c}$$

where the superscript E represents a zero or constant electric field condition or *short circuit* condition, D a zero or constant dielectric displacement condition or *open circuit* condition, σ a zero or constant stress condition or *mechanically free* condition, and ε a zero or constant strain condition or in other words, *mechanically clamped*.

Another kind of electro-mechanical coupling effect, electrostriction, is different from piezoelectric effect. Electrostriction is caused by a slight displacement of ions in the crystal when exposed to an external electric field. This displacement will accumulate and result in an overall strain in the direction of the field. The resulting strain is proportional to the square of the polarization, and hence it represents a quadratic electro-mechanical coupling effect. Electrostriction does not require any specific symmetry of the crystal structure, thus applies to all crystal symmetries.

One can regard the strain due to the electrostriction as an eigenstrain since it is not originated from stress. The contribution to the eigenstrain in ferroelectrics from electrostriction can be written in the following form:

$$\varepsilon_{ij}^{es} = Q_{ijkl} E_k E_l. \tag{4.42}$$

where the superscript $()^{es}$ stands for electrostriction, and Q_{ijkl} is the electrostrictive coefficient. Thus the elastic energy can be modified in the following form:

$$\mathscr{H}^{ela} = c_{ijkl}(\varepsilon_{ij} - \varepsilon_{ij}^{es})(\varepsilon_{kl} - \varepsilon_{kl}^{es}) \tag{4.43}$$

The constitutive equation with only electrostriction considered can be derived:

$$\sigma_{ij} = c_{ijkl}(\varepsilon_{ij} - \varepsilon_{ij}^{es}), \tag{4.44}$$

where ε_{ij}^{es} is regarded as an eigenstrain.

For the flexoelectric coupling effect, as one is expected to see in Sec. 7.3, the express of the flexoelectric energy is (here E_i instead of P_i is treated as the unknown variable, and f_{ijkl} is replaced by μ_{ijkl} accordingly):

$$\mathscr{H}^{flexo} = \frac{1}{2}\mu_{ijkl}(E_{i,j}\varepsilon_{kl} - E_i\varepsilon_{kl,j}). \tag{4.45}$$

The full expression of the electric enthalpy of a dielectric material with the consideration of three kinds of electromechanical coupling effect (*i.e.* piezoelectric effect, electrostrictive effect, and flexoelectric effect) can be obtained:

$$\mathscr{H}_2(E_i, \varepsilon_{ij}) = c_{ijkl}(\varepsilon_{ij} - \varepsilon_{ij}^{es})(\varepsilon_{kl} - \varepsilon_{kl}^{es}) + \epsilon_{ij} E_i E_j + e_{kij}(\varepsilon_{ij} - \varepsilon_{ij}^{es})E_k + \frac{1}{2}\mu_{ijkl}(E_{i,j}\varepsilon_{kl} - E_i\varepsilon_{kl,j}). \tag{4.46}$$

One should note that, in this form, the electrostriction-induced strain does not contribute to the piezoelectric effect, while the total strain is used for the flexoelectric term. This choice of strain is based on the physical origin of different coupling terms: piezoelectric effect and electrostriction are linear and quadratic response of strain with respected to the electric field, therefore these two contributions to the strain should be separated. However, for the flexoelectric effect, the induced polarization is due to the lattice deformation. Considering that the total strain $\varepsilon_{ij} = \frac{1}{2}(u_{i,j} + u_{j,i})$ can reflect the deformation of the lattices, the total strain is used in the flexoelectric term. In some works (*e.g.*, Ref. [139]), the electrostrictive-related energy is expressed as $\tilde{Q}_{ijkl}\varepsilon_{ij}P_kP_l$.

4.4 The Landau-Devonshire theory

The phase transition in ferroelectrics is a kind of structural phase transition. A general theory describing structural phase transitions was developed by Landau in 1937. [140] Ginzburg and Devonshire applied the Landau theory to barium titanate [141] and later to general ferroelectrics [142], where polarization is regarded as the order parameter. In this theory, the thermodynamic potential is expanded as a function of polarization, temperature, and stress.

Following the derivation of Devonshire [141], the Gibbs free energy density F, at zero stress and temperature T can be expanded in the following form:

$$F(P,T) = \frac{1}{2}a(T)P^2 + \frac{1}{4}bP^4 + \frac{1}{6}cP^6, \tag{4.47}$$

where P is the total polarization, a, b and c are the phenomenological Landau coefficients. Here a few assumptions are prescribed. First, the free energy at zero polarization is 0. Second, only the first Landau coefficient is temperature dependent, *i.e.*, $a(T) = a_0(T - T_0)$, where T_0 is the Curie-Weiss temperature. Third, the Landau polynomial is only written to the as a function of P to the power of 6. The coefficient a_0 is always positive, whereas b could be either positive or negative depending on the phase transition type. The coefficient c is always positive to avoid

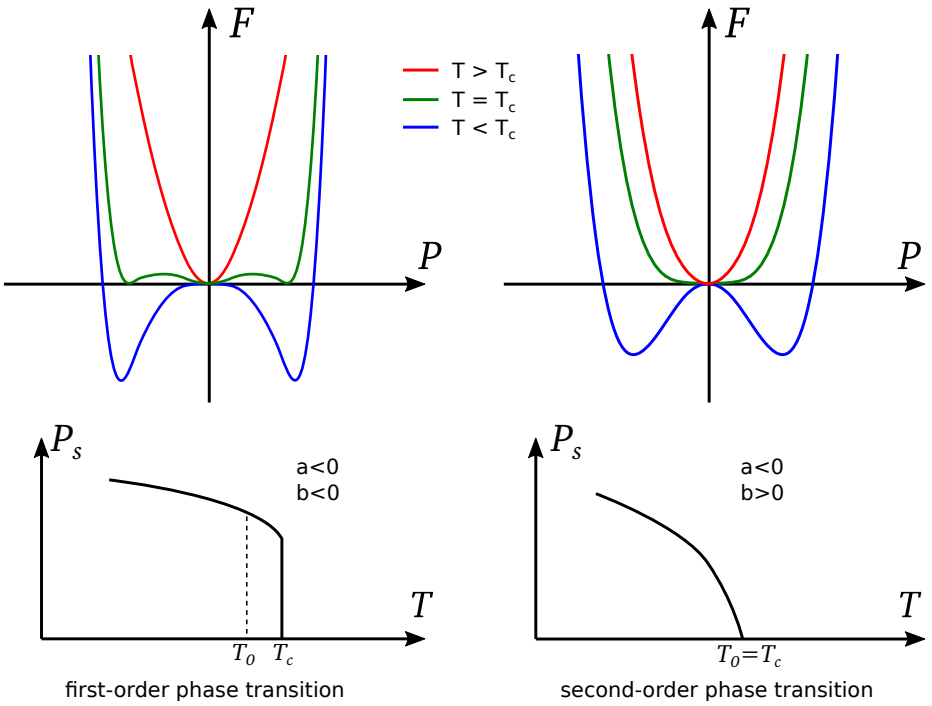

Figure 4.5: *Gibbs free energy F as a function of polarization P at different temperatures and spontaneous polarization P_s as a function of temperature. Left: the first-order phase transition; Right: the second-order phase transition.*

infinitesimal of F when P reaches its two extrema. The spontaneous polarization P_s at null field results from the equilibrium condition:

$$\frac{\partial F}{\partial P} = 0. \tag{4.48}$$

Equation 4.48 has a trivial solution $P_s = 0$ and two nontrivial solutions:

$$P_s^2 = \begin{cases} \dfrac{-b + \sqrt{b^2 - 2a_0(T - T_0)c}}{2c}, & \text{if } b > 0 \\ \dfrac{-b - \sqrt{b^2 - 2a_0(T - T_0)c}}{2c}. & \text{if } b < 0 \end{cases}$$

Figure 4.5 shows the Gibbs free energy as a function of P at different temperatures, and the spontaneous polarization as a function of temperature. As one can observe from the calculation, the first-order phase transition occurs if $b < 0$. In this case, there is a discontinuous drop of the spontaneous polarization to zero at T_c. At the temperature above T_c, there is one minimum in G at $P = 0$, which stands for the cubic or paraelectric state. As the temperature decreases, two local minima appear. At T_c, the free energy for the polarization at these two local minima is equal to the one at $P = 0$. At temperatures below T_c, the two local two local minima at $\pm P_s$ are the stable states, which stands for the ferroelectric phase.

For second-order phase transition, $b > 0$ and P_s continuously decreases to zero. Similar to the first-order phase transition, the free energy function G shows two minima below T_c. However, at $T = T_c$, there is only one minimum at $P = 0$. The change of the order parameter P_s is continuous during the phase transition. One can conclude that there is also no capacity heat reserved during the second-order phase transition.

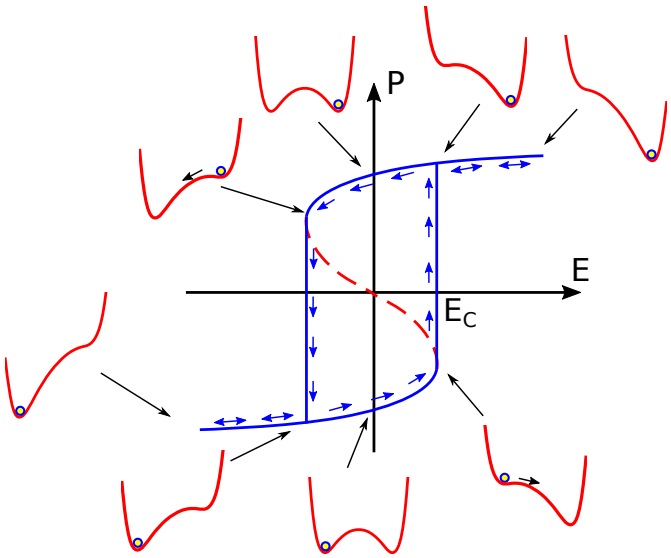

Figure 4.6: *Polarization hysteresis loop in the ferroelectric phase. The yellow point indicates the polarization state. The red curves show the Helmholtz free energy landscape at the corresponding field loading.*

The Helmholtz free energy according to the expression in Eq. (4.47) is:

$$H = F - PE = \frac{1}{2}a_0(T - T_0)P^2 + \frac{1}{4}bP^4 + \frac{1}{6}cP^6 - PE \tag{4.49}$$

The field E is then given by minimizing H:

$$\frac{\partial H}{\partial P} = a_0(T - T_0)P + bP^3 + cP^5 - E = 0. \tag{4.50}$$

With such relation, one can plot the polarization as the function of applied electric field. For the first-order phase transition, at the temperature well above T_c, there is no hysteresis in the P-E curve. At the temperature slightly above T_c, a strong electric field can induce ferroelectric phase, which results in a double hysteresis. The case at the temperature well below T_c is shown in Fig. 4.6. When the external field is not large enough (smaller than E_c shown in Fig. 4.6), H has two minima, corresponding to two polarizations in the hysteresis loop. The polarization state is dependent on its history state. If the external field increases above some specific value (*i.e.*, coercive field E_c), H has only one minimum, and the polarization reaches the saturation state.

The above statements summarized the main concepts of the Landau-Devonshire theory. It can describe a sample with a (spatially) uniformly distributed polarization, or a monodomain state. However, in a realistic case, the polarization usually distributed with some spatial variations, like domains and domain walls. The consideration of the spatial variation of the polarization field involves the Ginzburg-Landau theory. In such case, an additional gradient energy term should be considered:

$$\mathscr{H} = \underbrace{\frac{1}{2}a_0(T - T_0)P^2 + \frac{1}{4}bP^4 + \frac{1}{6}cP^6 - PE}_{\mathscr{H}^{bulk}} + \underbrace{\kappa|\nabla P|^2}_{\mathscr{H}^{grad}}, \tag{4.51}$$

where κ is a coefficient for the gradient energy. Equation. (4.51) can be solved analytically. The solution of the problem with the bulk energy $\mathscr{H}^{bulk}$ extended to the fourth-degree is given by Cahn (1958) [143] and Zhirnov (1959) [144]. The solution of the problem with $\mathscr{H}^{bulk}$ extended to the power of six can be found in Appx. B. As one can see from the analytical solution, the domain wall width

$$\gamma \propto \sqrt{\frac{\kappa}{a}}, \tag{4.52}$$

while the energy stored at the interface (or domain wall) is

$$G \propto \sqrt{a\kappa}. \tag{4.53}$$

From Eq. (4.52) and Eq. (4.53), one obtains

$$a \propto \frac{G}{\lambda} \tag{4.54a}$$

$$\kappa \propto \lambda G. \tag{4.54b}$$

As shown from Eq. (4.52) to Eq. (4.54), there are two sets of parameters. The first set of parameters (a, κ) are model parameters which reflects the energy barrier in $\mathscr{H}^{bulk}$ and the magnitude of $\mathscr{H}^{grad}$, respectively. The second set of parameters (γ, G) are physical parameters related to the domain wall: γ stands for the domain wall width and G stands for the domain wall energy density. In Chap. 5, parameters γ and G are used to formulate separation energy coefficients and gradient energy coefficients for the ferroelectric model. In this approach, the free energy density with only polarization contribution can be formulated in the following form:

$$\mathscr{H} = \frac{G}{\lambda}\tilde{\psi}(P_i) + G\lambda|\nabla P|^2, \tag{4.55}$$

where $\tilde{\psi}$ is the Landau polynomial. Compared to other formulations (*e.g.* Ref. [131]), the models formulated by γ and G have a clearer physical meaning.

It can be seen that the parameter κ has a great influence on the distribution of the order parameter at the equilibrium state. Indeed, the gradient of the order parameter contributing to the free energy is one of the core features for the phase-field theory. In the next section, the basic concepts of phase-field theory is introduced.

4.5 Phase-field theory

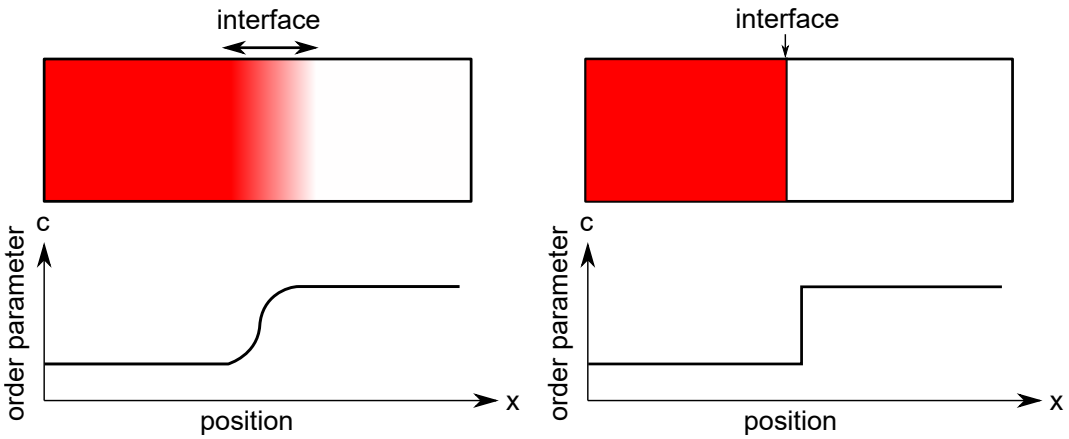

Figure 4.7: *Schematic figure of the diffusive and sharp interfaces. Adapted from Ref. [145].*

Phase-field model is a mathematical model dealing with the diffuse interface problems, which are sometimes also called “diffuse interface models”. This model possesses two characteristic

features. The first feature is that the interface is described by a steep, but continuous transition of the phase-field variable $\rho(\mathbf{x},t)$ between two states.[146] This parameter $\rho(\mathbf{x},t)$, which distinguishes different phases or states of the microstructure is called *order parameter*. The idea of the diffusive interface model first come from Van der Waals, when he tried to give the representation of the surface tension at the interface of two phases. He realized that the equation of surface tension could not be in consistent with observations if the change of the density along the interface is ignored. Thus he proposed the surface tension,

$$\gamma_s \propto \int (\frac{dc}{dx})^2 dx \tag{4.56}$$

where c is the density and x is the direction perpendicular to the surface tension. (See Fig. 4.7) Rayleigh independently gave the same representation to Eq. (4.56). This idea, albeit half century later, inspired Cahn and Hilliard when they considered the free energy at the interface for a nonuniform system. [143] They proposed the local free energy density f in a region of nonuniform composition will depend on not only the local composition, but also local composition *derivatives*,

$$f(c,\nabla c,\nabla^2 c\ldots) = f_0(c) + \kappa_1\nabla^2 c + \kappa_2(\nabla c)^2 + \ldots \tag{4.57}$$

It can be noted that in Eq. (4.57), only terms in even powers of the operator ∇ can appear, by assuming the medium isotropic with respect to c. By integrating it over the whole volume, applying the divergence theorem, and assuming ∇n is zero at the boundary, the total free energy over the volume $\mathscr{B}$ occupied by the material,

$$F = \int_{\mathscr{B}} \left[f_0(c) + \frac{1}{2}\kappa|\nabla c|^2 + \ldots\right] \mathrm{d}v \tag{4.58}$$

where $\kappa = -\dfrac{2\partial\kappa_1}{\partial c} + 2\kappa_2$. Landau and Lifshitz derive the same form of the equation to Eq. (4.58) for superconductors and ferromagnetic materials. [147, 148] The first part in Eq. (4.58) is the local free energy, while the second part in Eq. (4.58) is the gradient energy. In ferroelectrics, Eq. (4.58) results in the form of Eq. (4.51) shown in Sec. 4.4.

The second feature of the phase-field model is that it takes into account the kinetics of the order parameter. For instance, in ferroelectrics, the evolution of the order parameter is subjected to the following equation:

$$\frac{\partial P_i}{\partial t} = -M\frac{\delta F}{\delta P_i}, \tag{4.59}$$

where M is the kinetic coefficient. Equation 4.59 belongs to the type of *Allen–Cahn equation*. In the ferroelectric community, it is referred to as time-dependent Ginzburg–Landau equation (TDGL). The Allen–Cahn model can describe the system with non-conserved order parameters,

e.g., multi-component alloy phase transformations [149], fracture propagation [150], ferroelectric domain evolution [151].

For some specific problems, the order parameter field is conserved. The resultant equation is referred to as the Cahn–Hilliard equation. The Cahn–Hilliard model can describe some systems, *e.g.*, spinodal decomposition [152], complex flow [153] and diffusion problems [154]. For the ferroelectric system, the Allen–Cahn type, or TDGL equation is employed. The Cahn–Hilliard model will not be in detail discussed here.

The phase-field modeling enables a full description of domain structure in ferroelectrics. Till now, there is plenty of work on the modeling of ferroelectric in the phase-field approach. These ferroelectric phase-field ferroelectric models mainly differ in the form of free energy functions and the type of the order parameter (total polarization or spontaneous polarization). They result in different constitutive relations thus reflect different physical mechanisms. The first attempt of applying the phase-field model to the ferroelectric systems seems to be the work by Cao and Barsch [155], where the rotation angle of BX_6 in perovskite structure is chosen as the order parameter. Later, Cao and Cross [156] used the material polarization as the order parameter, in which the 90° domain wall was presented by an analytical solution. Nambu and Sagala [157, 158] simulated the domain-wall structure by the finite difference scheme. Hu and Chen [159] took the long-range dipole-dipole interaction into consideration. In the work of Su and Landis [160], a set of micro-forces are postulated in conjunction with the order parameters, and the model was implemented by a finite element formulation. Other models based on the phase-field concepts includes Li *et al.* [161, 162], Wang and Kamlah [163], Zhang and Bhattacharya [164, 165] along with others. In the work of Skula *et al.* [166], the spontaneous polarization is used as the order parameter, while the piezoelectric effect is ignored.

In the work of Xu *et al.* [15] and others [151], rather than material polarization (shown in Eq. 4.18), the spontaneous polarization is used as the order parameter. By doing so, the electrical and mechanical contribution to the material polarization can be separately considered. Moreover, the elastic, piezoelectric and dielectric tensor can depend on the spontaneous polarization. This choice of the order parameter reflects the fundamental merit of the Landau theory, where the material variable rather than the sum of material and field dependent variable should be chosen to reflect different phases in the material. [167]

In the end of this section, the following remarks to the phase-field theory are drawn:

- The order parameter usually characterizes the main feature of the system. The appropriate chosen of the order parameter for the phase-field modeling can reveal the physical nature, especially the symmetry of the system. For ferroelectric domain evolution, polarization (either spontaneous polarization or total polarization) can be regarded as the order parameter.

- The local bulk energy f_0 reflects the symmetries of the system and is responsible for the phase separation (sometimes f_0 is also referred to as the phase separation energy).

- In different cases, f_0 can be a function of temperature (T), pressure (p), etc. Thus the phase-field model can characterize the phase transition with respect to the above condition changes.
- In ferroelectric phase-field model, f_0 is a series of Taylor expansion from the ground state with only even terms,

$$f_0(P, T, p_0) = \alpha(T, p_0) + \beta(T, p_0)P^2 + \gamma(T, p_0)P^4 + \dots \tag{4.60}$$

  where α, β and γ are coefficients dependent on temperature (T), hydrostatic pressure (p_0) and other variables. With these parameters considered, an electromechanical fully coupled phase-field ferroelectric model could be achieved.
- For ferroelectric phase-field models, choosing different free energy functions and order parameter (total polarization or spontaneous polarization) results in different constitutive relations.

In the next chapter, a generic phase-field relaxor model is built, where the spontaneous polarization is used as the order parameter and the terminology of the microforce [168] is adopted for the implementation of the RF.

Chapter 5

Phase-field relaxor model based on the random field theory

A lot of theoretical [49, 50, 9, 51, 55, 11] and modeling [169, 71, 72, 18] development have been made since the relaxor ferroelectric material first was discovered in 1950s. The main feature of the relaxors compared with normal ferroelectrics is the randomness, regarding both the chemical composition and the local polar/nonpolar properties. For phase-field modeling, different approaches can be attempted. For instance, Wang *et al.* [72] used the point defect to represent such disorder in the "doped ferroelectrics". Li *et al.* [18] considered the disorder in the relaxors originated from the structural inhomogeneity: the orthorhombic PNRs are surrounded by the tetragonal matrix.

In the genius work by Imry and Ma [10], they ascribed the local disorder to the Random Field (RF), and the long-range order is broken by the local RF. The concept of RF provides a direct, at the same time simple way to model the disorder in the relaxor systems.

In this chapter, the phase-field model for relaxors based on the RF theory is introduced. The derivation of the constitutive equations and the evolution equations are based on the Clausius-Duhem inequality, and the microforce balance is utilized for the implementation of the RF within the phase-field framework. The numerical results show that typical relaxor features, such as domain miniaturization and small remanent polarization can be reproduced.

Parts of this chapter are based on the publication "S. Wang *et al.*, A phase-field model of relaxor ferroelectrics based on random field theory. *Int. J. Solid. Struct.* **83**, 142-153 (2016)". Here, I thank Dr. Min Yi for the fruitful discussion on the RF theory. The idea of the comparison between two RF models originated from the discussion with the reviewer of the above mentioned paper, which is also acknowledged here.

5.1 Introduction

As motivated in Chap. 1, relaxors exhibit high permittivity [170], less hysteresis effect [171] and large piezoelectric response [172]. The peculiar behavior of relaxors results from the abnormal domain structures, in which the short-range order dominates. The origin for the short-range order remains controversial. Besides the concept of polar nanoregions [47], the random field model [11, 173] and the spherical random bond-random field model [54] have been used to

explain the properties of relaxors. The RF model was firstly proposed by Westphal *et al.* [11], referring to the original idea of Imry and Ma [10]. It was claimed that the relaxor behavior of PMN is due to the quenched random electric fields. These quenched fields can originate from charged compositional fluctuations. In fact, most of the relaxors with the perovskite structure have heterovalent substitutions on the A- and/or B-site. For instance, in $AB_1B_2O_3$ structure, the differences in the charge and size of B_1 and B_2 cations make the structure asymmetric. When cooling down from high temperature, the concentrations of B_1 and B_2 cation tend to fluctuate and form chemical disorder. It can give rise to a random internal electric field [11, 173]. The experiment in linear birefringence supported this theory [11, 173].

Nevertheless, the exact mechanism, *i.e.*, how the RF influences the domain structure in relaxors, remains unclear. There are very few theoretical attempts in the literature. For instance, Blinc and Pirc assumed Gaussian RF in their spherical random-bond-random-field model [174, 54], and showed analytically that these RFs could prohibit the phase transition from the paraelectric phase into ferroelectric phase. Instead, a long-range disordered phase forms. Using the same model, the authors also explained the dielectric non-linearity in PMN and predict local polarization distribution. Since the model is based on the Landau theory [148] with homogeneous domain assumption, it has no access to the domain structure. More recently, Ma *et al.* [71] proposed a lattice-based Ginzburg-Landau-type Hamiltonian and performed Monte-Carlo simulations on relaxors, by considering the RF theory. They found that the higher the RF is, the lower the freezing temperature will be. The influence of the RF on the hysteresis and domain size were also studied. However, there is few reported literature for the study of the domain structure on a larger scale, at the same time considering the electromechanical coupling effect in relaxors.

Phase-field approaches have been successfully applied to model the polarization switching in conventional ferroelectrics. [175, 139, 13, 176, 151, 177, 178, 179, 16, 180] In particular, Su and Landis [160] proposed a phase-field model for ferroelectrics based on the microforce theory [168]. Thereby the total polarization is treated as the order parameter. Keip *et al.* [181] extended the phase-field [182, 183] simulation of ferroelectric single crystal into composites and polycrystals by homogenization. These models have become a useful tool in the study [184] and designing [185] of domain structures in ferroelectrics. However, due to the complexity of relaxors, the phase-field models on relaxors are very limited in the literature.

In this chapter, an electromechanically fully coupled phase-field model is proposed for the simulation of domain structures in relaxors. A continuum phase-field model is first established in the framework of thermodynamics and the microforce theory. Particularly, the static RF is introduced, and its influence on the electrostatic energy is considered. As a result, the evolution equations of the polarization and the constitutive equations are modified accordingly. Following the random field theory [173], a Gaussian distribution generator is employed to produce the local random electric field. The Gaussian distribution is generated based on the Box-Muller

formula [186]. Similar to our previous phase-field model for ferroelectrics [15, 178], the spontaneous polarization, instead of the total polarization, is taken as the order parameter, so that the spontaneous polarization, electric field-induced polarization and the mechanically induced polarization can be treated independently. Moreover, the physical parameters (domain wall width γ and domain wall energy G) instead of model parameters (energy barrier height a and gradient energy coefficient κ), are used for the as the parameters in the phase-field model. These two features differentiate this phase-field model with other models, (*e.g.* [160]) and make the model more physically sound. This phase-field model is implemented in the finite element method (FEM) for its merit of robustness and flexible boundary condition. The model and its implementation are used to analyze the influence of RF on the macroscopic response and domain evolution under mechanical and/or electrical stimulation.

The phase-field model and FEM implementation are elaborated in Sec 5.2 and Sec. 5.3, respectively, whereas Sec. 5.4 presents the simulation results based on the model, in order to reveal the influence of the RF. In Sec. 5.4.1 the dependency of the equilibrium domain structure on the variance of the RF is first revealed by numerical results. The domain structure evolution under bipolar electric field is demonstrated in Sec. 5.4.2, along with the dielectric and butterfly hysteresis. Section 5.4.3 is concerned with the ferroelastic switching of the domains in relaxors. Finally, the electromechanical loading is considered in Sec. 5.4.4. Results show that the model can predict characteristic features of relaxors, such as domain miniaturization, decreasing of remanent polarization and increased electromechanical effect.

5.2 Phase-field model

5.2.1 Governing equations

Denote the space occupied by a relaxor ferroelectric body and its boundary by $\mathscr{B}$ and $\partial\mathscr{B}$, respectively. At each point in $\mathscr{B}$ the mechanical equilibrium:

$$\sigma_{ij,i} + f_j = 0 \quad \text{in} \quad \mathscr{B} \tag{5.1}$$

must be satisfied, where σ_{ij} is the Cauchy stress in the Cartesian space, and f_i is the body force in the i^{th} direction. Hereafter, the Einstein notation is implied, the Latin symbols i, j, k, l run from 1 to 3, and the comma in the subscript represents the spatial partial derivative. By assuming small deformation, the following strain measures are used:

$$\varepsilon_{ij} = \frac{1}{2}(u_{i,j} + u_{j,i}), \tag{5.2}$$

where u_i the displacement vector. For the point at the boundary surface, displacement or force boundary conditions can be applied:

$$u_i = \bar{u}_i \quad \text{on} \quad \partial\mathscr{B}_u, \tag{5.3a}$$

$$\sigma_{ij} n_i = \bar{t}_j \quad \text{on} \quad \partial \mathscr{B}_\sigma, \tag{5.3b}$$

where n_i is the normal vector on the surface, and t_j the traction vector. Moreover, $\bar{u}_i$ denotes the displacement prescribed on the surface part $\partial \mathscr{B}_u$, while $\bar{t}_j$ denotes the traction on the surface part $\partial \mathscr{B}_\sigma$.

The electric quantities such as electrical displacement D_i and volume charge density q are governed by the quasi-static equilibrium derived from the Maxwell equations, *i.e.*,

$$D_{i,i} = q \quad \text{in} \quad \mathscr{B}. \tag{5.4}$$

The electric field can be given as

$$E_i = -\phi_{,i}. \tag{5.5}$$

in which ϕ is the electric potential. The boundary conditions for the electric quantities can be given as

$$\phi = \bar{\phi} \quad \text{on} \quad \partial \mathscr{B}_\phi, \tag{5.6a}$$

$$D_i n_i = -\bar{\omega} \quad \text{on} \quad \partial \mathscr{B}_D, \tag{5.6b}$$

where $\bar{\phi}$ is the electric potential applied on the surface part $\partial \mathscr{B}_\phi$, and $\bar{\omega}$ is the surface charge density applied on the surface part $\partial \mathscr{B}_D$.

The microforce theory, originally proposed by Gurtin *et al.* [168], is utilized for the derivation of the polarization evolution equation in the following subsection. Thereby the balance law of the microforces is introduced first. In the aimed phase-field, the order parameter is chosen to the spontaneous polarization P_i. The microforce system associated with P_i is characterized by a generalized stress tensor ξ_{ij} together with related body forces π_i and γ_i that represent, respectively, the internal and external forces distributed over the volume $\mathscr{B}$. Given an arbitrary control volume $\mathscr{R}$ (a subregion of $\mathscr{B}$), with n_i the unit normal vector on the surface $\partial \mathscr{R}$, the microforce balance holds,

$$\int_{\partial \mathscr{R}} \xi_{ji} n_j dS + \int_{\mathscr{R}} \pi_i \mathrm{d}v + \int_{\mathscr{R}} \gamma_i \mathrm{d}v = 0. \tag{5.7}$$

By using the Gauss law and noting that Eq. (5.7) should hold for any arbitrary volume, it yields

$$\xi_{ji,j} + \pi_i + \gamma_i = 0. \tag{5.8}$$

On the boundary, there lays

$$\xi_{ji} n_j = \bar{\mu}_i \quad \text{on} \quad \partial \mathscr{R}, \tag{5.9}$$

where $\bar{\mu}_j$ is the surface microforce applied on the surface part $\partial \mathscr{R}$. In the next subsection, these microforces are adopted to derive the constitutive and the evolution equations.

5.2.2 Constitutive and evolution equations

In order to get the constitutive relations and evolution equation, thermodynamic relations are considered. According to the second law of thermodynamics, under the isothermal condition, the change rate in the Helmholtz free energy in the control volume should not be greater than the external power W^{ext} expended on the control volume, *i.e.*,

$$\left\{\int_{\mathscr{B}} \mathscr{H} \mathrm{d}v\right\}^{\cdot} \leq \mathscr{W}^{ext}. \tag{5.10}$$

The free energy $\mathscr{H}$ is a functional of $\varepsilon_{ij}, D_i, P_i, P_{i,j}$ and high order items of these parameters. To simplify the model but not lost generality, one can write $\mathscr{H}$ as

$$\mathscr{H} = \mathscr{H}(\varepsilon_{ij}, D_i, P_i, P_{i,j}). \tag{5.11}$$

Applying the Taylor expansion and retaining only the first order term, one has

$$\left\{\int_{\mathscr{B}} \mathscr{H} \mathrm{d}v\right\}^{\cdot} = \left(\int_{\mathscr{B}} \frac{\partial \mathscr{H}}{\partial \varepsilon_{ij}} \dot{\varepsilon}_{ij} + \int_{\mathscr{B}} \frac{\partial \mathscr{H}}{\partial D_i} \dot{D}_i + \int_{\mathscr{B}} \frac{\partial \mathscr{H}}{\partial P_i} \dot{P}_i + \int_{\mathscr{B}} \frac{\partial \mathscr{H}}{\partial P_{i,j}} \dot{P}_{i,j}\right) \mathrm{d}v. \tag{5.12}$$

The power done by external resources W^{ext} has contributes on the surface and in the body,

$$W^{ext} = \int_{\mathscr{B}} (f_i \dot{u}_i + \phi \dot{q} + \gamma_i \dot{P}_i) \mathrm{d}v + \int_{\partial \mathscr{B}} (\bar{t}_i \dot{u}_i + \phi \dot{\bar{\omega}} + \bar{\mu}_i \dot{P}_i) \mathrm{d}s, \tag{5.13}$$

where the power related to P_i is represented by microforce γ_i and $\bar{\mu}_i$. What should be noticed is that the internal force π_i do not contribute to the external power W^{ext}. After the Legendre transformation, the electric enthalpy $\mathscr{H}_2(\varepsilon_{ij}, E_i, P_i, P_{i,j})$ can be derived as $\mathscr{H}_2 = \mathscr{H} - E_i D_i$. Inserting Eq. (5.12), (5.13), and (5.8) into Eq. (5.10) and applying the divergence theorem, one arrives at

$$\begin{aligned} \int_{\mathscr{B}} \Big\{ (\sigma_{ji} - \frac{\partial \mathscr{H}_2}{\partial \varepsilon_{ij}}) \dot{\varepsilon}_{ij} - (D_i + \frac{\partial \mathscr{H}_2}{\partial E_i}) \dot{E}_i - (\frac{\partial \mathscr{H}_2}{\partial P_i} - \gamma_i - \xi_{ji,j}) \dot{P}_i + \\ (\xi_{ji} - \frac{\partial \mathscr{H}_2}{\partial P_{i,j}}) \dot{P}_{i,j} \Big\} \mathrm{d}v \geq 0. \end{aligned} \tag{5.14}$$

Since Eq. (5.14) should hold for any arbitrary $\dot{\varepsilon}_{ij}$, $\dot{E}_i$, and $\dot{P}_i$, one has

$$\sigma_{ji} = \frac{\partial \mathscr{H}_2}{\partial \varepsilon_{ij}}, \quad D_i = -\frac{\partial \mathscr{H}_2}{\partial E_i}, \quad \xi_{ji} = \frac{\partial \mathscr{H}_2}{\partial P_{i,j}}, \tag{5.15}$$

and one inequality

$$(\frac{\partial \mathscr{H}_2}{\partial P_i} - \gamma_i - \xi_{ji,j})\dot{P}_i \leq 0 \tag{5.16}$$

due to the dissipative process. The detailed calculation shows that using the electric enthalpy or the Helmholtz free energy leads to the same results, see Appx. C.

To ensure the inequality, one can assume that

$$\frac{\partial \mathscr{H}_2}{\partial P_i} - \gamma_i - \xi_{ji,j} = -\beta \dot{P}_i, \tag{5.17}$$

where the non-negative constant β indicates the mobility parameter. Considering that $\xi_{ji} = \frac{\partial \mathscr{H}_2}{\partial P_{i,j}}$, one can rewrite Eq. (5.17) in the following form

$$\beta \dot{P}_i = -\frac{\partial \mathscr{H}_2}{\partial P_i} + \xi_{ji,j} + \gamma_i = -\frac{\partial \mathscr{H}_2}{\partial P_i} + \left(\frac{\partial \mathscr{H}_2}{\partial P_{i,j}}\right)_{,j} + \gamma_i. \tag{5.18}$$

5.2.3 Electric enthalpy

In our model, the electric enthalpy consists of five parts, *i.e.*,

$$\mathscr{H}_2 = \mathscr{H}^{ela} + \mathscr{H}^{ele} + \mathscr{H}^{coup} + \mathscr{H}^{sep} + \mathscr{H}^{grad}, \tag{5.19}$$

in which $\mathscr{H}^{ela}$, $\mathscr{H}^{ele}$, $\mathscr{H}^{grad}$, $\mathscr{H}^{sep}$ and $\mathscr{H}^{grad}$ represent the elastic energy density, the electrical energy density, the electromechanical coupling energy density, the domain separation energy density and the gradient energy density, respectively. These energy terms take the following specific form,

$$\begin{cases} \mathscr{H}^{ela} = \dfrac{1}{2} c_{ijkl} \varepsilon^e_{ij} \varepsilon^e_{kl} \\ \mathscr{H}^{ele} = -\dfrac{1}{2} k_{ij} E_i E_j - P_i E_i \\ \mathscr{H}^{coup} = -b_{ijk} \varepsilon_{ij} E_k \\ \mathscr{H}^{sep} = \beta_1 \dfrac{G}{\lambda} \psi(P_i) \\ \mathscr{H}^{grad} = \beta_2 G \lambda P_{i,j} P_{i,j}. \end{cases} \tag{5.20}$$

The quantities induced in the last equations are explained in the following. Firstly, ε^e_{ij} stands for the elastic strain, which is further given by the difference between the mechanical strain ε_{ij} and

the spontaneous strain ε_{ij}^0, *i.e.*, $\varepsilon_{ij}^e = (\varepsilon_{ij} - \varepsilon_{ij}^0(\boldsymbol{P}))$. The spontaneous strain $\varepsilon_{ij}^0(\boldsymbol{P})$ is caused by the spontaneous polarization. According to [187],

$$\varepsilon_{ij}^0(P_i) = \frac{3}{2}\varepsilon_{sat}\frac{\sqrt{\|\boldsymbol{P}\|}}{P_0}(n_i n_j - \frac{1}{3}\delta_{ij}), \tag{5.21}$$

where δ_{ij} is the Kronecker delta, $\|\boldsymbol{P}\|$ the norm of the vector P_i, n_i the unit vector of P_i, ε_{sat} the maximum remanent strain, and P_0 the maximum remanent polarization. The stiffness tensor c_{ijkl} and the permittivity tensor k_{ij} are assumed to be independent of the polarization. For the piezoelectric tensor b_{ijk}, the following representation is used [188]

$$\begin{aligned} b_{kij}(P_i) = &\frac{\sqrt{\|\boldsymbol{P}\|}}{P_0}\Big\{d_{33}n_i n_j n_k + d_{31}(\delta_{ij} - n_i n_j)n_k \\ &+ \frac{1}{2}d_{15}\big[(\delta_{ki} - n_k n_i)n_j + (\delta_{kj} - n_k n_j)n_i\big]\Big\}, \end{aligned} \tag{5.22}$$

in which d_{33}, d_{31}, d_{15} are the linear piezoelectric constants at the poled state. The parameter G and λ are the specific energy and the width of the 180° domain wall [178], while the coefficients β_1 and β_2 are used to calibrate the two parameters. [189] The function $\psi(P_i)$ is the Landau-Devonshire free energy function with potential wells. Some additional comments on this five terms can be found in Appx. D.

It should be noted that the total electric field has three contributions, *i.e.*,

$$E_i = E_i^d + E_i^{ext} + E_i^{random}, \tag{5.23}$$

where E_i^d represents the depolarization field, E_i^{ext} the applied electric field, and E_i^{random} the RF induced by the chemical disorder. In this model, the first two terms E_i^d and E_i^{ext} are derived from the negative gradient of electric potential ϕ. The random electric field can also be related to the negative gradient of a potential, see ϕ^{random}. This potential is, however, excluded from the electric potential ϕ defined here. The random electric field is assumed to be static and independent from field variables. Therefore, the discussion is restricted only to the random electric field. The only restriction on the random electric fields is the vanishing expectation. To be in accordance with Eq. (5.5), the sum of E^d and E^{ext} is denoted as E^ϕ. It reveals

$$\begin{cases} E_i = E_i^\phi + E_i^{random} \\ E_i^\phi = \phi_{,i} = E_i^d + E_i^{ext} \\ E_i^{random} = \mathcal{N}(\mu, \Delta). \end{cases} \tag{5.24}$$

Here, E_i^{random} is assumed to be static and obeys the Gaussian distribution $\mathcal{N}(\mu, \Delta)$ [190, 54]. The expectation of the RF Gaussian distribution is set to be zero, while the variance of the

distribution is denoted by Δ. The numerical implementation is explained in Sec. 5.3. It should be noted that when introducing the Gaussian random electric fields, the mathematical proof on the existence of a corresponding potential is not discussed, which goes beyond the interest of this paper.

Inserting the expression into Eqs. (5.15) and (5.18) and assuming $\gamma_i = 0$, the constitutive equations and the evolution equation can be rewritten as,

$$\begin{cases} \sigma_{ij} = c_{ijkl}\varepsilon^e_{kl} - b_{jik}E^{\phi}_k - b_{jik}E^{random}_k \\ D_i = k_{ij}E^{\phi}_j + k_{ij}E^{random}_j + b_{ijk}\varepsilon_{jk} + P_i \\ \beta\dot{P}_i = E^{\phi}_i + E^{random}_i - \beta_1\dfrac{G}{\lambda}\dfrac{\partial\psi}{\partial P_i} + 2\beta_2 G\lambda(P_{i,j})_{,j}. \end{cases} \tag{5.25}$$

As it was implied by Imry and Ma [10] that, the RFs should work conjugating to the order parameter. From Eq. (5.12) one can further see that the random electric field E^{random}_i, which is contained inside the term $\dfrac{\partial\mathscr{H}}{\partial P_i}$, is conjugated with the order parameter in an internal sense.

Another approach to consider the relaxor nature is to include RFs as the microforce γ_i, instead of introducing the random electric field in the formulation of the electric enthalpy $\mathscr{H}_2$. Even though this approach can lead to the same form of the polarization evolution equation as the last equation in Eq. (5.25), the corresponding constitutive equations are different from the first two equations in Eq. (5.25). More precisely, the term $-b_{jik}E^{random}_k$ and $+k_{ij}E^{random}_j$ will not be present. In other words, the piezoelectric and dielectric effects induced by the random fields cannot be covered. In fact, both theoretical and experimental work [173, 17, 191] show that RFs in relaxor are rather random electric fields induced by charged hetero lattice ions, defects, and impurities. These RFs will inevitably affect the stress σ_{ij} and electric displacement D_i in the piezoelectric and dielectric sense, along with the influence on polarization.

One can still treat the RF as the external microforce γ_i. To differentiate these two models, the model with RF as the internal microforce is named as model A, and the model with RF as the external microforce is named as model B. For the model B, the constitutive equations are different from model A. By regarding the RF as the external microforce, the constitutive equations and the evolution equation of model B read as follows:

$$\begin{cases} \sigma_{ij} = c_{ijkl}\varepsilon^e_{kl} - b_{jik}E^{\phi}_k \\ D_i = k_{ij}E^{\phi}_j + P_i + b_{ijk}\varepsilon_{jk} \\ \beta\dot{P}_i = E^{\phi}_i + \gamma_i - \beta_1\dfrac{\partial\psi}{\partial P_i} + 2\beta_2(P_{i,j})_{,j}. \end{cases} \tag{5.26}$$

Comparison between these sets of equations with Eq. 5.25 shows clearly that model A includes the piezoelectric and dielectric terms resultant from the random electric field automatically, while these influences cannot be considered by model B. The domain configurations calculated by the two models are compared in the next section.

It is noted once more that the phase-field approach applied in this paper differentiates from those phase-field models based on free energy expansion. See the works, *e.g.*, Chen *et al.* [192], Su and Landis [160], Wang *et al.* [139] and Wang *et al.* [163]. The fundamental difference lies in the choice of the order parameter. In these models mentioned above, the order parameter P_i is the total polarization, as in their models, the relation $D_i = \kappa_0 E_i + P_i$ holds with κ_0 being the vacuum permittivity. However, in our model, only the irreversible part of polarization, *i.e.* the spontaneous polarization, is chosen to the order parameter, as it can be seen in the expression of the electric displacement in Eq. (5.25). By using this type of phase-field approach, the number of parameters is largely reduced, and the physical interpretation of these parameters is more clear. For more details on the difference between these two types of phase-field models, one can refer to the paper by Schrade *et al.* [189].

5.3 Numerical implementation

5.3.1 Weak form

The governing equations for the phase-field model are Eq. (5.1)-Eq. (5.9), Eq. (5.25). To obtain solutions to these equations, the finite element method is adopted. Mechanical displacement, electric potential, and spontaneous polarization are chosen as the degrees of freedom, by following the choice of electric enthalpy as the energy type. The weak form of the field equation can be given as

$$\begin{aligned} &\int_{\mathscr{B}} \beta \dot{P}_i \delta P_i \mathrm{d}v + \int_{\mathscr{B}} (\sigma_{ji}\delta\varepsilon_{ij} - D_i \delta E_i + \eta_i \delta P_i + \xi_{ji}\delta P_{i,j})\mathrm{d}v = \\ &\int_{\mathscr{B}} (f_i \delta u_i - q\delta\phi + \gamma_i \delta P_i)\mathrm{d}v + \int_{\partial\mathscr{B}} (\bar{t}_i \delta u_i - \bar{\omega}\delta\phi + \bar{\mu}_i \delta P_i) ds. \end{aligned} \tag{5.27}$$

The left-hand of the equation represents the generalized virtual strain energy. The first part of the right-hand stands for the virtual work done in the body, and the second part for the virtual work done on the boundary. The stresses, electric displacements, and microforces can be derived from Eqs. (5.25).

By considering that u_i, E_i, P_i are the independent variables, one obtains from Eq. (5.27) the following weak forms,

$$\begin{cases} -\int_{\mathscr{B}} \sigma_{ji}\delta\varepsilon_{ij}\mathrm{d}v + \int_{\mathscr{B}} f_i \delta u_i \mathrm{d}v + \int_{\partial\mathscr{B}} \bar{t}_i \delta u_i \mathrm{d}s = 0 \\ -\int_{\mathscr{B}} D_i \delta E_i \mathrm{d}v + \int_{\mathscr{B}} q\delta\phi \mathrm{d}v + \int_{\partial\mathscr{B}} \bar{\omega}\delta\phi \mathrm{d}s = 0 \\ -\int_{\mathscr{B}} \beta\dot{P}_i\delta P_i \mathrm{d}v - \int_{\mathscr{B}} (\frac{\partial \mathscr{H}_2}{\partial P_i}\delta P_i + \frac{\partial \mathscr{H}_2}{\partial P_{i,j}}\delta P_{i,j})\mathrm{d}v + \int_{\partial\mathscr{B}} \mu_i \delta P_i \mathrm{d}s = 0. \end{cases} \tag{5.28}$$

5.3.2 2-Dimensional case

The Landau-Devonshire free energy function ψ for cubic-to-noncubic take the following form:

$$\psi = a_1 + a_2(P_1^2 + P_2^2 + P_3^2) + a_3(P_1^4 + P_2^4 + P_3^4) + a_4(P_1^2 P_2^2 P_3^2) + a_5(P_1^6 + P_2^6 + P_3^6). \tag{5.29}$$

With a proper choice of the Landau coefficients, ψ can represent different phases transition, for instance, cubic-to-tetragonal (BTO), cubic-to-rhombohedral (PMN). Reads are referred to Fig 2.1 for the landscape of ψ. With such implementation of the Landau-Devonshire free energy, the weak form of the field equation of 3-dimensional case can be derived. However, it is adequate to explore the domain evolution in 2 dimensions, since in this chapter merely qualitative study of the relaxor behavior is intended. Meanwhile, this saves calculation time. It is non-trivial to reduce the 3-dimensional rhombohedral system into a 2-dimensional one, while the tetragonal and the orthorhombic system can be represented in two dimensions by limiting the allowed polarization directions to one principal plane [1 0 0]. For the tetragonal structure, polarization has six possible orientations. In 2-dimensional case, the plane with 4 possible orientations is investigated, through which both 90° and 180° domain switching can be presented. If one only focus on one principal plane [1 0 0], ψ is degraded to following form,

$$\psi = a_1 + a_2(P_1^2 + P_2^2) + a_3(P_1^4 + P_2^4) + a_4(P_1^2 P_2^2) + a_5(P_1^6 + P_2^6). \tag{5.30}$$

The parameters a_1 to a_5 are chosen properly to allow 90°and 180° domain switching. Meanwhile ψ must guarantee that it takes local minima at $(\pm P_0, 0)$ and $(0, \pm P_0)$. The five parameters used in the simulations are derived from the coefficients published in Ref. [193].

The discretization of the 2-dimensional model is achieved by four-node linear elements. The spontaneous polarization $\underline{\mathbf{P}}(P_1, P_2)$, the electric potential ϕ, and mechanical displacement $\underline{\mathbf{u}}(u_1, u_2)$ are taken as independent variables. Therefore, each node has five degrees of freedom:

$$\underline{\mathbf{d}}^{\mathrm{I}} = [P_1^I, P_2^I, \phi^I, u_1^I, u_2^I]^T,$$

in which the superscript I indicates the element nodal number and the underlined bold symbol denotes a matrix. In this section, matrix instead of index notation is used to clearly shows the components of the tensor. A Voigt notation is used in the discretized equations. Detailed components of the matrix can be found in the Appx. E. By introducing the shape functions, the values within the element can be expressed by nodal values,

$$\begin{cases} \underline{\boldsymbol{u}} = \sum_I N_u^I \underline{\boldsymbol{u}}^I; \quad \delta\underline{\boldsymbol{u}} = \sum_I N_u^I \delta\underline{\boldsymbol{u}}^I; \\ \phi = \sum_I N_\phi^I \phi^I; \quad \delta\phi = \sum_I N_\phi^I \delta\phi^I; \\ \underline{\boldsymbol{P}} = \sum_I N_P^I \underline{\boldsymbol{P}}^I; \quad \delta\underline{\boldsymbol{P}} = \sum_I N_P^I \delta\underline{\boldsymbol{P}}^I; \\ \underline{\dot{\boldsymbol{P}}} = \sum_I N_P^I \underline{\dot{\boldsymbol{P}}}^I. \end{cases} \tag{5.31}$$

The strain, the electric field, and the polarization gradient can be calculated by introducing corresponding derivative matrices, and then the stress and the electric displacement can be obtained through Eqs. 5.25,

$$\begin{cases} \underline{\boldsymbol{\varepsilon}} = \sum_I \underline{\boldsymbol{B}}_u^I \underline{u}^I; \quad \underline{\boldsymbol{\varepsilon}}^e = \underline{\boldsymbol{\varepsilon}} - \underline{\boldsymbol{\varepsilon}}^0(\boldsymbol{P}); \quad \underline{\boldsymbol{E}} = -\sum_I \underline{\boldsymbol{B}}_\phi^I \phi^I; \quad \nabla \underline{\boldsymbol{P}} = \sum_I \underline{\boldsymbol{B}}_\nabla^I \underline{\boldsymbol{P}}^I; \\ \underline{\boldsymbol{\sigma}} = \underline{\boldsymbol{C}}\,\underline{\boldsymbol{\varepsilon}} - \underline{\boldsymbol{b}}^T \underline{\boldsymbol{E}}; \quad \underline{\boldsymbol{D}} = \underline{\boldsymbol{b}}\,\underline{\boldsymbol{\varepsilon}} + \underline{\boldsymbol{k}}\underline{\boldsymbol{E}} + \underline{\boldsymbol{P}}. \end{cases} \tag{5.32}$$

From Eqs. (5.28), the element residuals can be given by the integration over the element area $\mathscr{B}^e$:

$$\begin{cases} \underline{\boldsymbol{R}}_u^I = -\int_{\mathscr{B}^e} \underline{\boldsymbol{B}}_u^{I\,T} \underline{\boldsymbol{\sigma}} \mathrm{d}v \\ R_\phi^I = -\int_{\mathscr{B}^e} \underline{\boldsymbol{B}}_\phi^{I\,T} \underline{\boldsymbol{D}} \mathrm{d}v \\ \underline{\boldsymbol{R}}_P^I = -\int_{\mathscr{B}^e} \{\beta N_P^I \dot{\underline{\boldsymbol{P}}} + N_P^I \frac{\partial \mathscr{H}}{\partial \underline{\boldsymbol{P}}} + \underline{\boldsymbol{B}}_\nabla^{I\,T} \frac{\partial \mathscr{H}}{\partial \nabla \underline{\boldsymbol{P}}}\} \mathrm{d}v, \end{cases} \tag{5.33}$$

where

$$\begin{cases} \frac{\partial \mathscr{H}_2}{\partial \underline{\boldsymbol{P}}} = -\frac{\partial \underline{\boldsymbol{\varepsilon}}^{0T}}{\partial \underline{\boldsymbol{P}}} \underline{\boldsymbol{\sigma}} - (\underline{\boldsymbol{\varepsilon}}^{0T} \frac{\partial \underline{\boldsymbol{b}}^T}{\partial \underline{\boldsymbol{P}}} + \underline{\mathbf{1}})(\underline{\boldsymbol{E}}^\phi + \underline{\boldsymbol{E}}^{random}) + \beta_1 \frac{\partial \psi}{\partial \underline{\boldsymbol{P}}} \\ \frac{\partial \mathscr{H}_2}{\partial \nabla \underline{\boldsymbol{P}}} = \beta_2 \nabla \underline{\boldsymbol{P}}. \end{cases} \tag{5.34}$$

The RF $\underline{\boldsymbol{E}}^{random}$ has two independent components, which are subject to the same Gaussian distribution. To generate the RF, the Box-Muller method [186] is used to ensure the interdependency of the random values in each element and direction. Suppose $U_1(0,1)$ and $U_2(0,1)$ are independent samples chosen from the uniform distribution ranged from 0 to 1. Let

$$\begin{aligned} Z_1 &= \sqrt{-2\ln U_1}\cos(2\pi U_2) \\ Z_2 &= \sqrt{-2\ln U_1}\sin(2\pi U_2) \end{aligned} \tag{5.35}$$

Box and Muller [186] proved that Z_1 and Z_2 are independent random variables with a standard Gaussian distribution $\mathscr{N}(0,1)$. Figure 5.1 shows the generated Gaussian random number sets by the Box-Muller equation. With the sampling number $N = 1000$, (Z_1, Z_2) are well fitted to the Gaussian distribution. The statistic variables including the norm μ and the variance Δ^2 of the distribution as a function of sampling number N are also plotted for reference. As the sampling number increases, the norm of the distribution approaches to zero and the variance approaches to 1. One also finds that when the sampling number goes above 10^3, the distribution of the collected points does not improve much with respect to the standard Gaussian distribution.

The interdependency of the two random variable sets Z_1 and Z_2 can be measured by Pearson correlation:

$$Corr(Z_1, Z_2) = \frac{\text{expected value}[(Z_1 - \mu_{Z_1})(Z_2 - \mu_{Z_2})]}{\Delta_{Z_1}\Delta_{Z_2}} \tag{5.36}$$

As the sampling number increases, the correlation between the two random variable sets also approaches to zero.

After obtaining $\mathcal{N}(0,1)$, one can generate the Gaussian distributed numbers with a variance of Δ^2 by

$$\begin{aligned} Z_1'(0,\Delta^2) &= Z_1\Delta^2 \\ Z_2'(0,\Delta^2) &= Z_2\Delta^2 \end{aligned} \tag{5.37}$$

The number sets Z_1' and Z_2' can be inserted into the history variable at the initial step, and be assigned to the vector $\underline{\boldsymbol{E}}^{random}$.

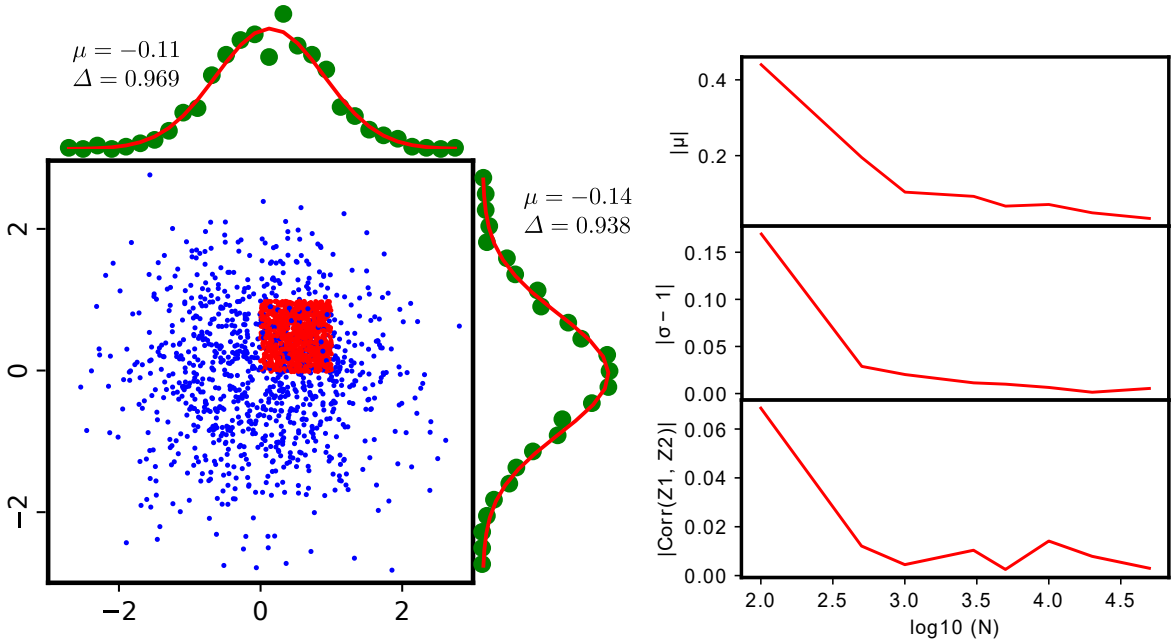

Figure 5.1: *Left: Generation of two independent Gaussian-distributed random variables by Box-Muller equation. Red dots represent initial uniform random samples. Blue dots represent the generated Gaussian distributed number sets. The green dots show the probability distributions in the corresponding direction. The sampling number N = 1000. Right: some featured values of Gaussian distribution as a function of sampling number.*

With the implementation of the RF, the stiffness matrix can be calculated thereafter by

$$\begin{cases} \underline{\boldsymbol{K}}_{uu}^{IJ} = -\dfrac{\partial \underline{\boldsymbol{R}}_u^I}{\partial \underline{\boldsymbol{u}}^J}; & \underline{\boldsymbol{K}}_{u\phi}^{IJ} = -\dfrac{\partial \underline{\boldsymbol{R}}_u^I}{\partial \phi^J}; & \underline{\boldsymbol{K}}_{uP}^{IJ} = -\dfrac{\partial \underline{\boldsymbol{R}}_u^I}{\partial \underline{\boldsymbol{P}}^J}; \\ \underline{\boldsymbol{K}}_{\phi u}^{IJ} = -\dfrac{\partial \underline{\boldsymbol{R}}_\phi^I}{\partial \underline{\boldsymbol{u}}^J}; & \underline{\boldsymbol{K}}_{\phi\phi}^{IJ} = -\dfrac{\partial \underline{\boldsymbol{R}}_\phi^I}{\partial \phi^J}; & \underline{\boldsymbol{K}}_{\phi P}^{IJ} = -\dfrac{\partial \underline{\boldsymbol{R}}_\phi^I}{\partial \underline{\boldsymbol{P}}^J}; \\ \underline{\boldsymbol{K}}_{Pu}^{IJ} = -\dfrac{\partial \underline{\boldsymbol{R}}_P^I}{\partial \underline{\boldsymbol{u}}^J}; & \underline{\boldsymbol{K}}_{P\phi}^{IJ} = -\dfrac{\partial \underline{\boldsymbol{R}}_P^I}{\partial \phi^J}; & \underline{\boldsymbol{K}}_{PP}^{IJ} = -\dfrac{\partial \underline{\boldsymbol{R}}_P^I}{\partial \underline{\boldsymbol{P}}^J}. \end{cases} \tag{5.38}$$

For the only time-dependent term $\dot{P}_i$, implicit backward Euler time integration method can be adopted. The non-zero damping matrix $\underline{\boldsymbol{D}}_{PP}^{IJ}$ can be calculated by

$$\begin{cases} \dot{\underline{\boldsymbol{P}}} = \dfrac{\underline{\boldsymbol{P}}^{t+\tau} - \underline{\boldsymbol{P}}^t}{\tau} \\ \underline{\boldsymbol{D}}_{PP}^{IJ} = -\dfrac{\partial \underline{\boldsymbol{R}}_P^I}{\partial \dot{\underline{\boldsymbol{P}}}^J}, \end{cases} \tag{5.39}$$

where τ is the time step, and t the current time. With stiffness and damping matrix, the element iteration matrix $\underline{\boldsymbol{S}}$ can be assembled, in which $\underline{\boldsymbol{S}}_{PP}^{IJ} = \underline{\boldsymbol{K}}_{PP}^{IJ} + \dfrac{1}{\tau}\underline{\boldsymbol{D}}_{PP}^{IJ}$. For a given set of nodal values at time t, the non-linear algebraic equations can be solved by the Newton-Raphson method. The model is implemented as a user element in the software FEAP [194].

5.4 Simulation results and discussion

Four cases are simulated based on the relaxor model presented above. First, the equilibrium domain configurations of a relaxor single crystal with different RFs are simulated. Second, the ferroelectric response under bipolar loading is analyzed. Domain evolution with various RFs shows different features. Third, pure mechanical loading is applied, and the influence of the RF is demonstrated. Finally, domain evolution under electromechanical loading is discussed. In all the simulations, the body force f_i and charge q are neglected. The parameters used in the simulations are listed in Table 5.1.

5.4.1 Domain configuration in relaxors

In this section, the qualitative study of the influence of the RF on the domain configuration is presented. The simulation parameters are shown in Table 5.1. The size of the simulated sample is 100 × 100 nm^2, with a mesh size of 1 nm. All the boundaries are traction-free and charge-free. Initial polarization distribution is assumed to be random.

The equilibrium state of relaxor single crystal is first investigated. One of the key factors which can influence the domain configuration is the local RF which obeys the Gaussian distribution

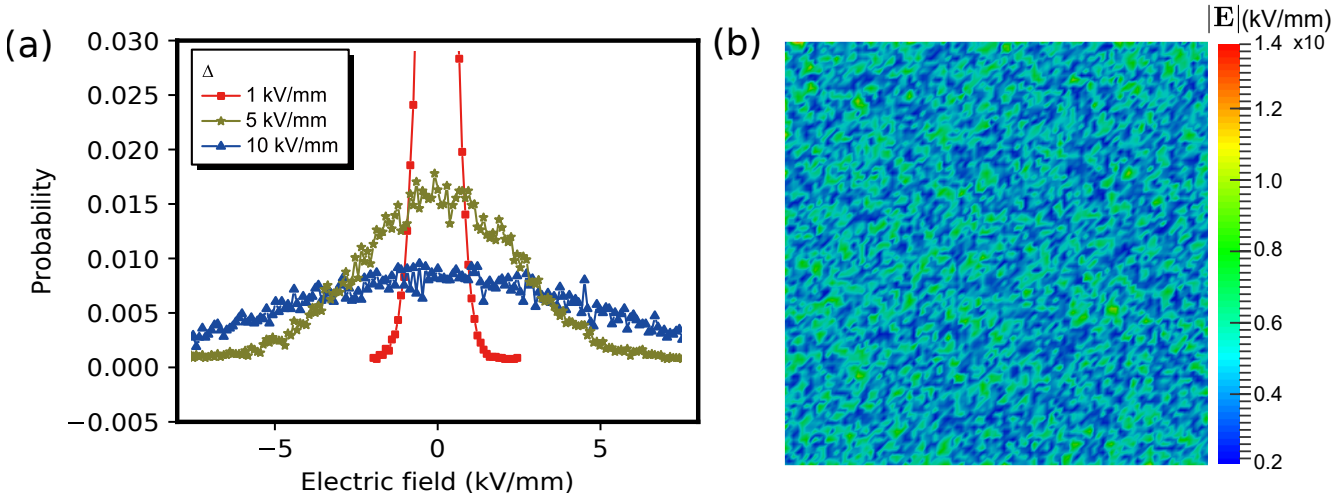

Figure 5.2: *Left: Probability diagram of the local random field distributions with different Δ. Right: Random field distribution within the sample for the case of $\Delta = 5$ kV mm^{-1}. Legend unit: V/m.*

Parameter	Signal	Value	Unit
Elastic stiffness moduli	C_{11}	211	GPa
	C_{12}	107	GPa
	C_{33}	56.2	GPa
Piezoelectric moduli	e_{31}	−3.88	C m^{-2}
	e_{33}	5.48	C m^{-2}
	e_{51}	32.6	C m^{-2}
Dielectric permittivity	ϵ_{11}	1.75×10^{-7}	F m^{-1}
	ϵ_{22}	1.75×10^{-7}	F m^{-1}
Domain wall width coefficient	λ	1	nm
Domain wall energy	G	0.7×10^{-3}	J m^2 C^{-2}
Mobility	β	7×10^{-6}	A V^{-1} m^{-1}
Eigenpolarization	P_0	0.31	C m^{-2}
Eigenstrain	ε_0	0.262	%

Table 5.1: *Parameters used in the benchmark test of the RF relaxor model.*

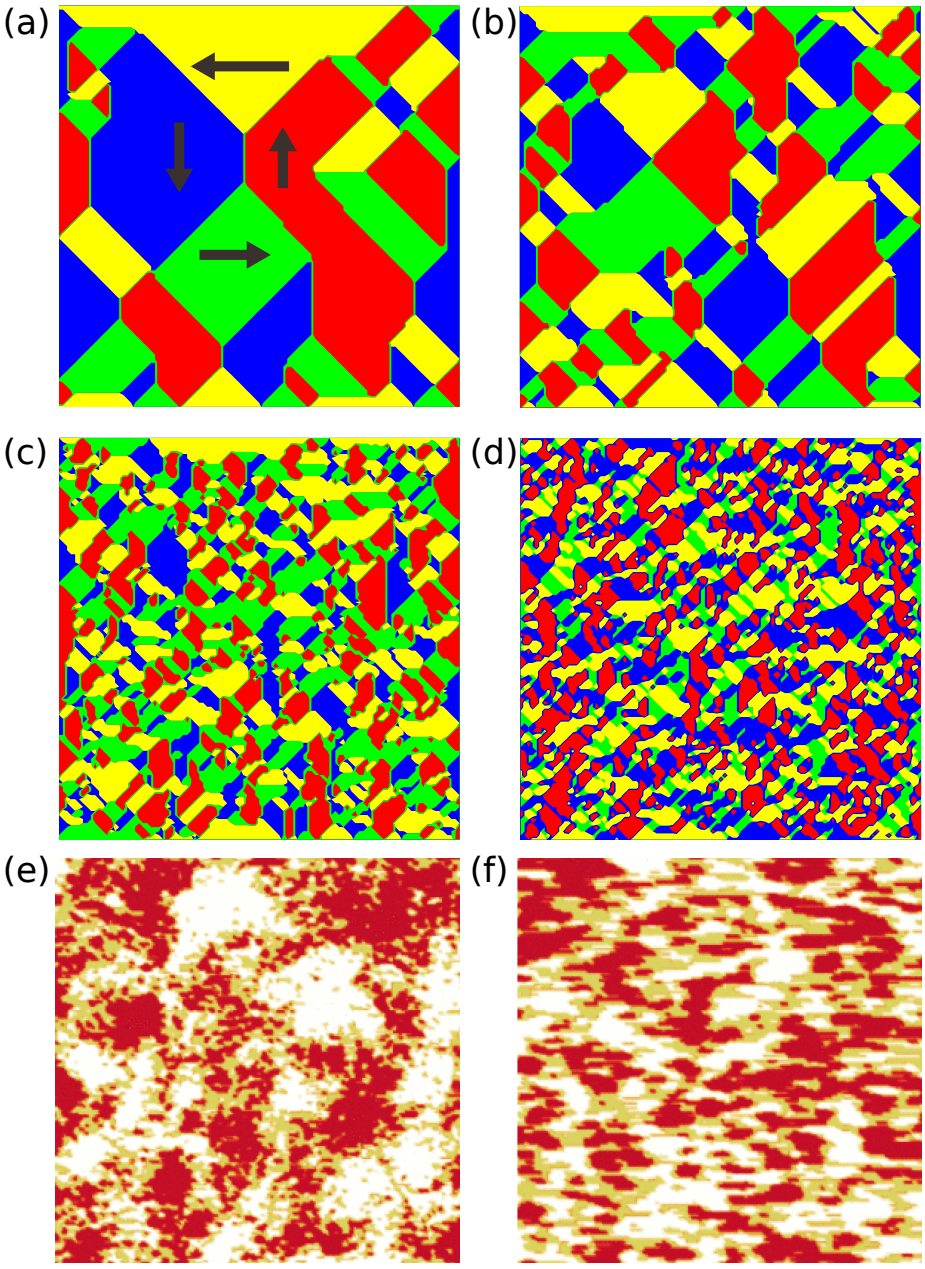

FIGURE 5.3: *(a-d) Equilibrium domain configuration for four cases with different Gaussian distribution variances: (a) $\Delta = 0$ kV mm^{-1}; (b) $\Delta = 1$ kV mm^{-1}; (c) $\Delta = 5$ kV mm^{-1}; (d) $\Delta = 10$ kV mm^{-1}. Four colors represent four polarization orientations of domains: yellow-left; green-right; red-top and blue-down. PFM images observed on a c-cut SBN single crystals with various compositions: (e) SBN61 and (f) SBN75. The PFM images are taken from the paper by [65].*

$\mathcal{N}(0, \Delta)$. In the simulation, the mean value of the RFs is set to be zero, to ensure that there is no macroscopic bias field. Thus, the variance Δ of the Gaussian distribution accounts for the strength of the local RF. Three values of Δ, *i.e.*, 1 kV mm^{-1}, 5 kV mm^{-1} and 10 kV mm^{-1}, are considered. The probability diagram is shown in Fig. 5.2a, while the random field distribution in the sample for the case $\Delta = 5$ kV mm^{-1} is shown in Fig. 5.2b. It can be seen that although Δ is 5 kV mm^{-1}, most elements have the RF below 5 kV mm^{-1}. The maximum value can reach as high as 10 kV mm^{-1}.

The equilibrium domain configuration for different values of Δ can be found in Fig. 5.3. In Fig. 5.3a-d four colors represent four polarization orientations, respectively. Both 90° and 180° domain walls are visible. Due to the force-free boundary condition, polarization at the edge of the body tends to point parallel to the boundary. By comparing Figs. 5.3a-d, it can be concluded that the domain size decreases with increasing Δ. In Fig. 5.3a, the variance of the RF $\Delta = 0$. It is the case representing a conventional ferroelectric material without RF. As the strength of RF increases, the material behavior becomes more relaxor-like. When Δ is increased to 5 kV mm^{-1}, the domain distribution becomes much randomized, as shown in Fig. 5.3d. The size of the domain becomes smaller and the shape becomes more twisted.

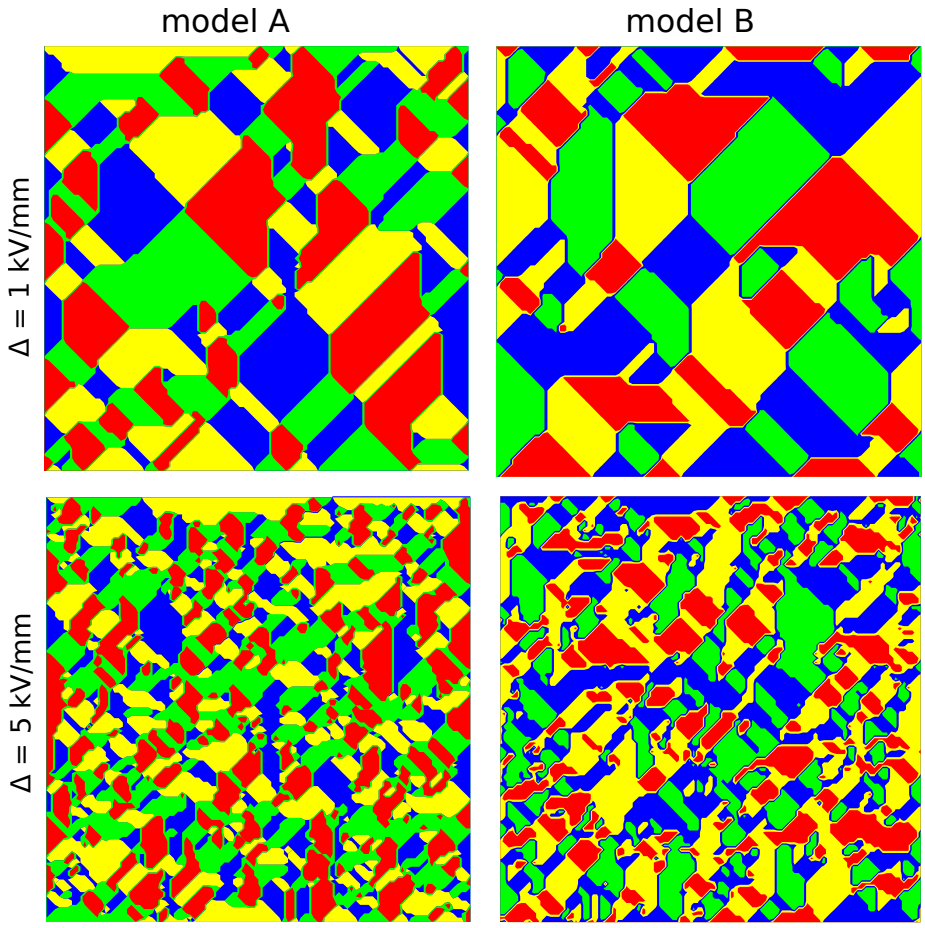

Figure 5.4: *Comparison of two different random field relaxor models. Left: the RF is regarded as the random electric field; Right: the RF is regarded as the external microforce.*

The domain configuration can be compared with experimental results. In the work by Shvartsman *et al.* [65], the surface polarization status of Czochralski-grown relaxor relaxor single crystal $Sr_xBa_{1-x}Nb_2O_6$ (SBNx) at 293 K was studied by Piezoresponse Force Microscopy (PFM). The vertical PFM characterization mode shows the polar structures at the surface of the sample. Fig. 5.3e and 5.3f are two PFM images, which demonstrate different domain structures on the surfaces of the sample SBN61 and SBN75, respectively. Thereby, the tri-modal color code is used: white stands for up, red for down, and yellow for unresolved fine-structured domains. It can be seen that for higher Sr content, the domain size becomes smaller, and the domain boundaries jag more. Comparison between the simulated equilibrium domain structures with the PFM images shows that Fig. 5.3b is close to Fig. 5.3e, while Fig. 5.3c appears similar to Fig. 5.3f. It can thus be suggested that the Sr content is positively correlated to the strength of the RF.

In order to demonstrate the difference between model A and model B discussed in Sec. 5.2.3, the simulations on the equilibrium domain configurations of the cases $\Delta = 1\ \mathrm{kV\,mm^{-1}}$ and $5\ \mathrm{kV\,mm^{-1}}$ are presented. The simulation results of model B are shown in the left, while the corresponding results for model A are shown in the right of Fig. 5.4. It can be seen that the domain size calculated by model A is smaller than that of model B. The reason is that, in model A, the RF has direct effects on the electric displacement and stress. Therefore the influence of the randomness is stronger. It is an interesting topic to compare these two different models, but it is beyond the topic of this thesis.

5.4.2 Hysteresis loop in relaxors

The influence of RF on the macroscopic behavior of relaxor ferroelectrics can be characterized by polarization and strain hysteresis. Here $6\ \mathrm{kV\,mm^{-1}}$ bipolar loading is adopted for simulation. Gaussian distribution variance (Δ) of RF varies from $0\ \mathrm{kV\,mm^{-1}}$ to $50\ \mathrm{kV\,mm^{-1}}$.

In order to reveal the influence of the RF, dielectric hysteresis for the two cases $\Delta = 5\ \mathrm{kV\,mm^{-1}}$ and $10\ \mathrm{kV\,mm^{-1}}$ are compared in Fig. 5.5. For small $\Delta = 5\ \mathrm{kV\,mm^{-1}}$, the hysteresis tends to be rectangular, which is typical for a ferroelectric single crystal. Whereas, for large $\Delta = 10\ \mathrm{kV\,mm^{-1}}$, the hysteresis becomes very slim. Particularly, the remanent polarization P_r almost vanishes. In order to examine this decrease of P_r, snapshots of domain structure and electric potential distribution during the poling are compared in Fig. 5.5. Starting from initially random distribution (Point 1), the polarization is fully poled at maximum field state (Point 2) for both cases. It can be explained by the fact that for both cases the applied electric field is stronger than the local fields at most sites. However, the domain structures at the remanent state (Point 3) are rather different from each other. When the applied field decreases, the influence of RF becomes obvious. Specifically, for $\Delta = 5\ \mathrm{kV\,mm^{-1}}$, the polarization distribution remains almost unchanged, because the potential barrier prevents the domain switching. However, if the local

RF is high enough (*e.g.*, $\Delta = 10\ \mathrm{kV\,mm^{-1}}$), this barrier can be overcome. Thus the polarization distribution becomes randomized again, which explains the trivial remanent polarization.

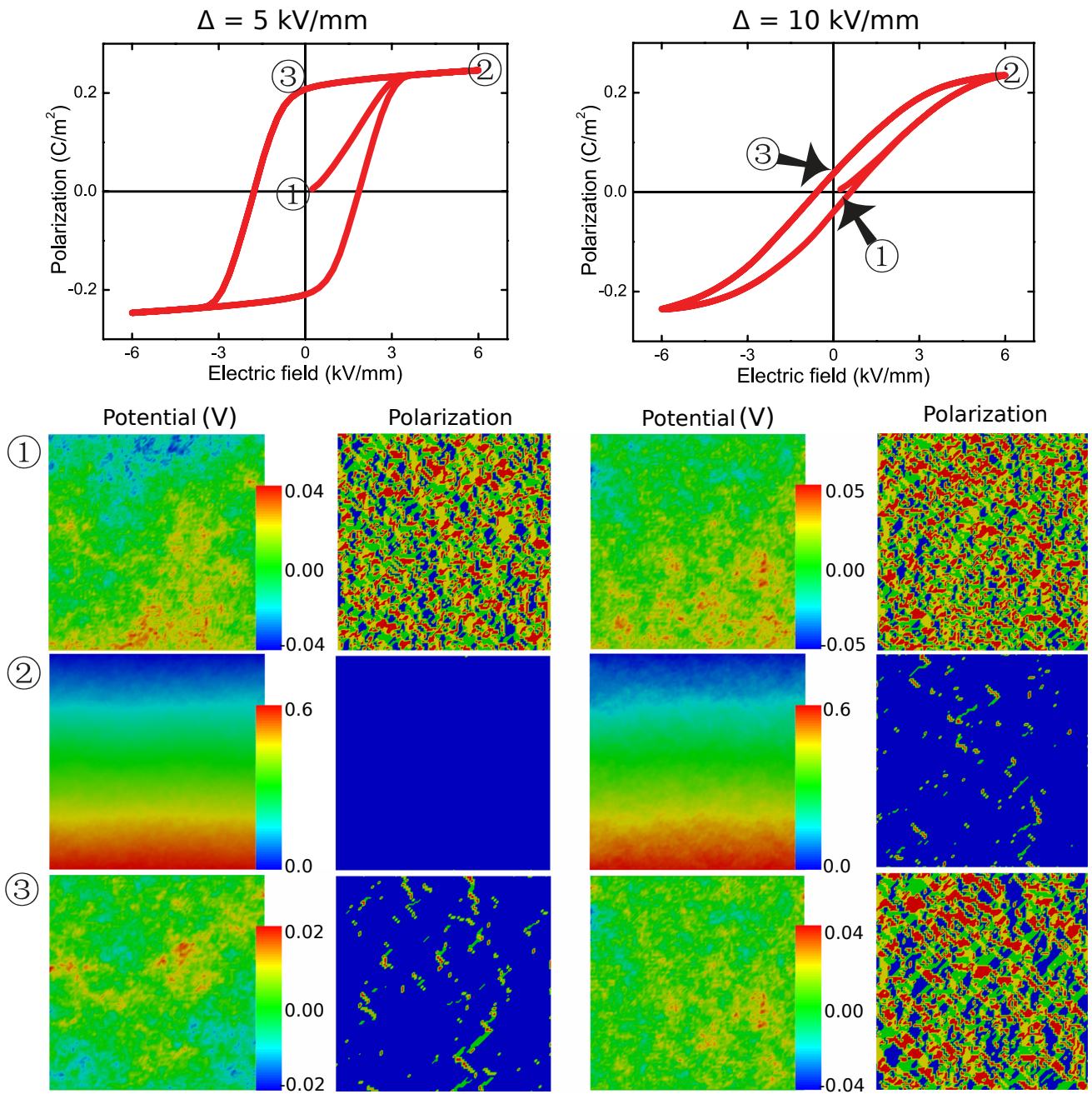

Figure 5.5: *Dielectric hysteresis, snapshots of domain structure and electric potential distribution for two different cases:* $\Delta = 5\ \mathrm{kV\,mm^{-1}}$ *(left) and* $\Delta = 10\ \mathrm{kV\,mm^{-1}}$ *(right).*

In Fig. 5.6, the influence of the RFs on the dielectric and strain hysteresis is demonstrated in detail. The calculated hysteresis can be classified into three types:

- If Δ is less than $5\ \mathrm{kV\,mm^{-1}}$, the remanent polarization (P_r) is close to the maximum polarization, while the coercive field (E_c) has a relatively high value of $4.5\ \mathrm{kV\,mm^{-1}}$. These two

phenomena are commonly found in conventional ferroelectric materials. Moreover, when the external field reaches the critical value for the domain switching, the polarization orientation changed simultaneously, which leads to a steep slope at the switching point. It is one of the typical features for single crystals [170]. After the domain switching process, both polarization and strain are in proportion to the external field.

- For the sample with a moderate RF (*e.g.*, $\Delta = 10\ \mathrm{kV\,mm^{-1}}$ and $\Delta = 15\ \mathrm{kV\,mm^{-1}}$), P_r decreases with the increase of RF. The hysteresis feature is less obvious (*cf.* the cases with a lower RF). Due to the lost of hysteresis, the remanent strain becomes smaller, and the difference between the maximum strain and the remanent strain becomes larger. Hence, the existence of the RF makes the high-field piezoelectric coefficient (maximum strain divided by maximum field) larger.

- For the sample with a very larger RF (*e.g.*, $50\ \mathrm{kV\,mm^{-1}}$), the material shows a dielectric feature and exhibit a nearly linear response to the external field. The RF, in this case, is so high that the external field has little influence on the polarization distribution. The polarization direction is determined by the local RF distribution and stays unchanged during the loading.

From the discussion above, a short conclusion can be drawn that with the increase of the RF, P_r decreases, the hysteresis effect vanishes gradually, and the material behavior changes from conventional ferroelectric to relaxor type.

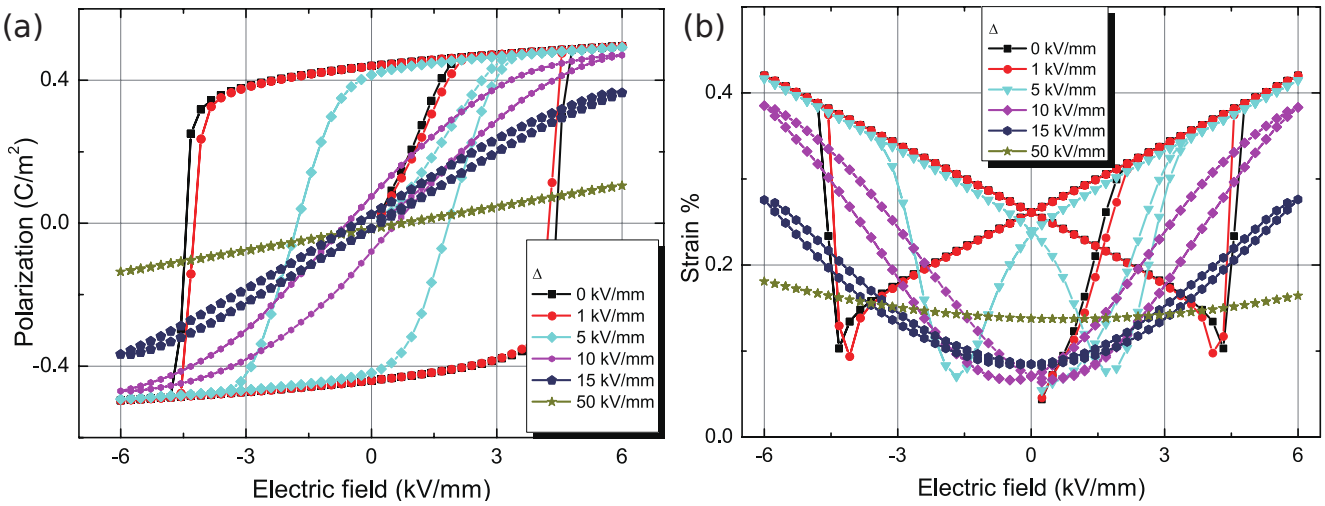

Figure 5.6: *(a) Polarization hysteresis and (b) strain hysteresis under bipolar loading for different cases of RF variance.*

5.4.3 Ferroelastic response

In this subsection, the domain switching induced by pure mechanical loading is studied, and the effect of the RF on this response is revealed. Figure 5.7 shows the evolution of the domain

structure and of the stress distribution in a sample under linearly increased tensile loading up to 0.6% in the vertical direction. Two cases of RFs, *i.e.*, $\Delta = 1\ \mathrm{kV\,mm^{-1}}$ and $5\ \mathrm{kV\,mm^{-1}}$ are considered. Charge-free boundary conditions are prescribed.

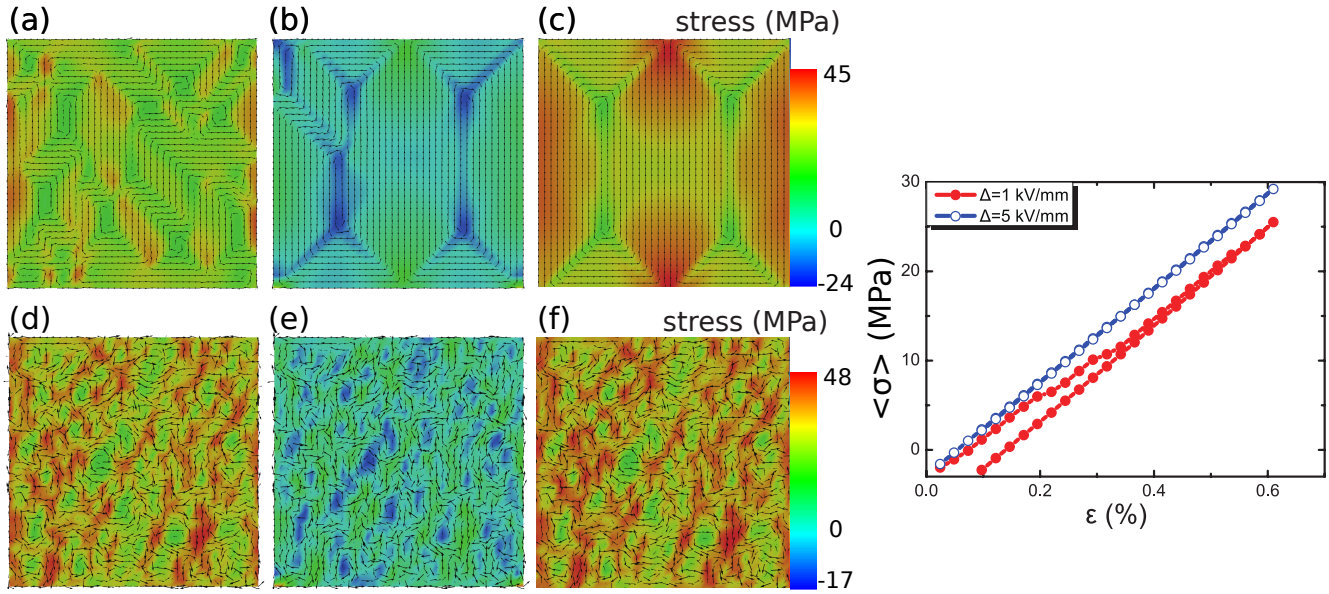

Figure 5.7: *(a-f)Domain structure evolution under uniaxial tensile loading. (g) Mechanical stress v.s. strain curves.*

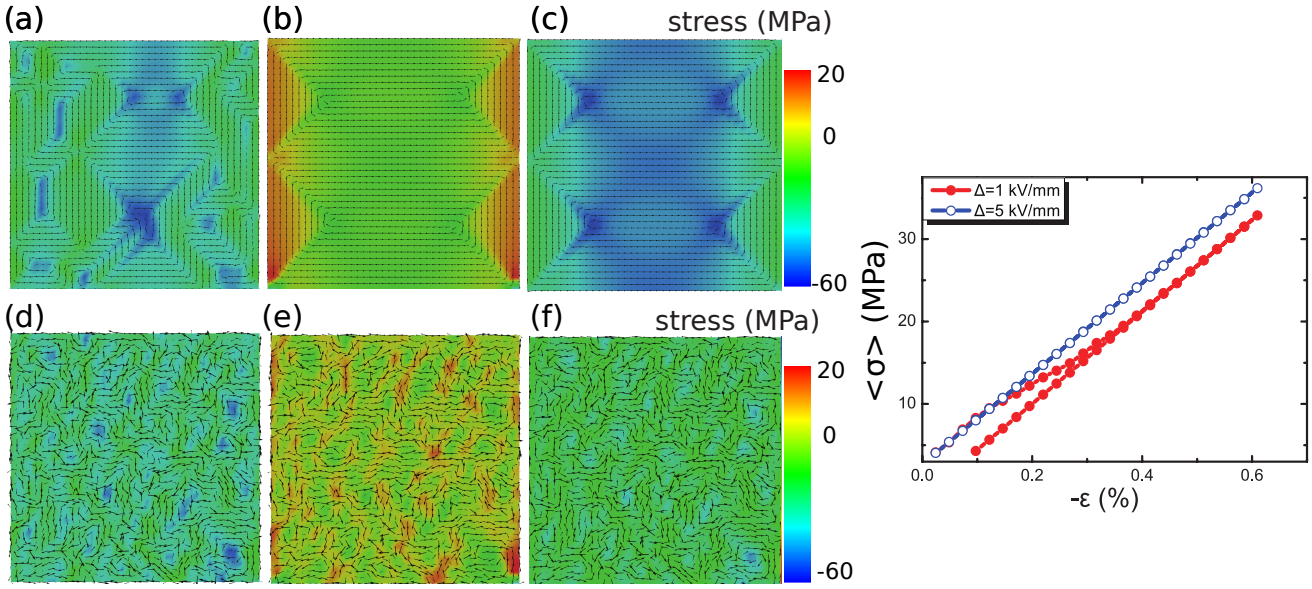

Figure 5.8: *(a-f)Domain structure evolution under uniaxial compression. (g) Mechanical stress v.s. strain curves.*

For the case of low RF $\Delta = 1\ \mathrm{kV\,mm^{-1}}$, the initially random distributed polarization vectors tend to align along the vertical direction, as it is demonstrated in Fig. 5.7a-c. Domains with vertical polarization become larger. Due to the constraint of charge-free boundary conditions, domain structure with multi vertices is formed at the end. This mechanical-induced domain

switching can also be identified by stress-strain relation shown in Fig.5.7g. The slope of the curve decreases during the tensile loading, which indicates that the domain switching happens in this range. The slope then goes back to its original value after the domain switching process. It can be explained by the assumption in the model that the stiffness tensor is independent of polarization state. During the unloading process, the slope of the stress-strain curve remains constant. Hence the remanent strain emerges, with the value of about 0.1%. This result is close to the experimental measurement of the commercial ferroelectric ceramic PIC 151 [195].

For the sample with high RF $\Delta = 5\ \mathrm{kV\,mm^{-1}}$, the coarsening of the domain is not visible, and the tendency of the vertical polarization is not so obvious, as it can be seen in Fig. 5.7d-f. Meanwhile, there is hardly slope change of the S-E curve shown in Fig. 5.7g. It indicates that there is no apparent mechanical-induced domain switching. The RF counteracts the influence of mechanical loading on polarization switching. A similar phenomenon can be found in the case of compression loading, as it can be seen from the simulated domain structures and the stress-strain relation shown in Fig. 5.8.

5.4.4 Relaxor response under electromechanical loading

As the last example, the relaxor behavior under the electromechanical loading is presented in this subsection.

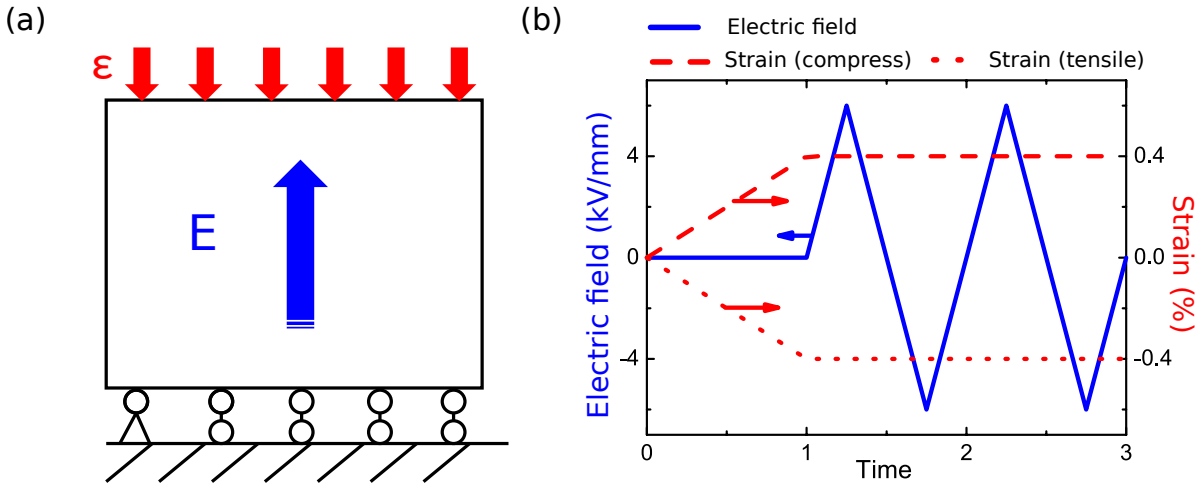

Figure 5.9: *(a)Illustration of the simulation setup; (b) Electric and mechanical loading history.*

The hysteresis behavior of mechanically assisted bipolar poling on relaxors is studied. For each of the two RFs with $\Delta = 2.3\ \mathrm{kV\,mm^{-1}}$ and $7.5\ \mathrm{kV\,mm^{-1}}$, three loading scenarios are simulated: 1) only bipolar electric loading, 2) bipolar electric loading combined with tensile loading, 3) bipolar electric loading combined with mechanical compression. As illustrated in Figs. 5.9a and 5.9b, mechanical loading in the last two scenarios are applied first along the vertical direction. The electric bipolar loading is then applied in the same direction after the

mechanical loading reached a constant. The maximum compression/tension is 0.6%, and the amplitude of the electric field is 6 $\mathrm{kV\,mm^{-1}}$.

The three hystereses of the different loading scenarios shown in Fig. 5.10a are for the RF case $\Delta = 2.3\ \mathrm{kV\,mm^{-1}}$. For this relatively low RF, the polarization at maximum field saturates at all the three loading scenarios, and the polarization is fully poled. However, the remanent states of the compressed and the tensile sample, marked as point 1 and point 2 in Fig. 5.10a, are rather different, after the external field is removed. It can be seen that the remanent polarization of the compressed sample is much less than that of the tensile one. This feature can be well explained by the domain structure at the corresponding remanent states. The domain structure at the remanent state of the compressed sample is shown in Fig. 5.10c, while that of the tensile sample in Fig. 5.10d. It is clear that due to the compressive loading, part of the polarization is switched to the lateral directions, which leads to the drop of the remanent polarization, whereas in the tensile loading, the poled state is maintained. Moreover, E_c of the compressed sample is much smaller than that of the tensile one. It can be simply explained by the switching energy criterion [39]. The positive mechanical work reduces the work needed from the external field for switching. In other words, more energy is needed for the compressed sample than for the tensile sample to switch the polarization. Similar results can be found in the work by [14] on the electromechanical coupling problems of ferroelectrics. Their simulation results show that both E_c and P_r of compressed samples decrease.

For the case of a rather high RF $\Delta = 7.5\ \mathrm{kV\,mm^{-1}}$, different features in this hysteresis are observed, as shown in Fig. 5.10b. The polarization of the compressed sample at the maximum electric field does not reach the saturation, because the imprint effect of the RF and the effect of the compression loading is strong enough to prevent part of the dipoles switching to the vertical direction. On the other hand, in the tensile sample, the driving force induced by the applied field and by the tensile loading overruns the imprint effect of the random electric field, and thus the polarization is fully poled. The domain structures at this state of the tensile and the compressed sample, shown in Fig. 5.10e and Fig. 5.10f, verify this argument. Moreover, not only the compressed sample but also the free sample has a decreased polarization. It implies that the imprint effect of the RF is strong enough so that some of the dipoles are switched back to the lateral directions. In the tensile sample, the imprint effect of RF is counteracted by the mechanical loading. It explains the large remanent polarization.

5.5 Summary

In this chapter, a continuum phase-field model for relaxor ferroelectrics is constructed to simulate the domain structure evolution in relaxor ferroelectrics. Local RFs are introduced according to the RF theory, which can appropriately reflect the influence of chemical disorder in relaxors. The strength of the RF is controlled by the variance of the Gaussian distribution. The simulation

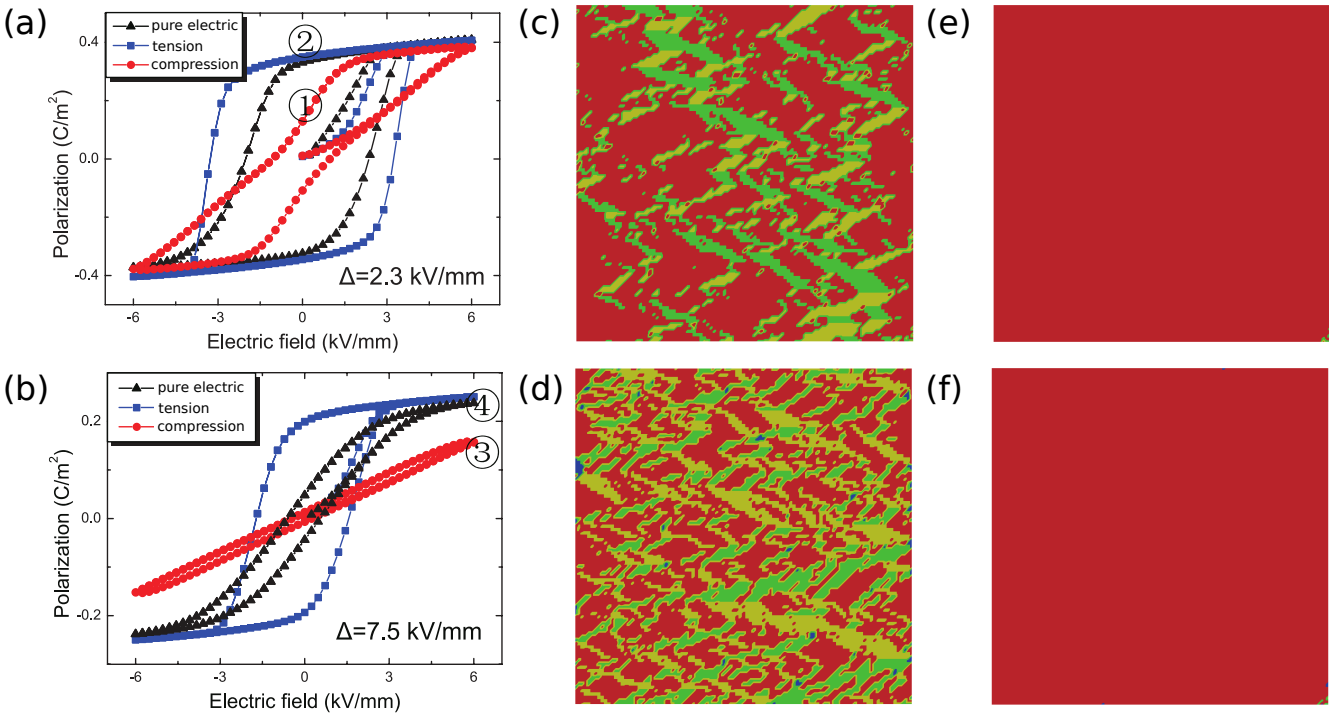

FIGURE 5.10: *Dielectric hysteresis for three loading scenarios for (a) the random field with* $\Delta = 2.3\,\mathrm{kV\,mm^{-1}}$ *and (b) the RF with* $\Delta = 7.5\,\mathrm{kV\,mm^{-1}}$. *(c) Domain structure at the remanent state of the compressed sample (Point 1). (d) Domain structure at the remanent state Point 2 of the tensile sample (Point 2). (e) Domain structure at the maximum field of the compressed sample (Point 3). (f) Domain structure at the maximum field of the tensile sample (Point 4).*

results presented in this section and the comparison with experimental measurements demonstrate that this model can reproduce typical relaxor features, such as domain miniaturization, small remanent polarization, and large piezoelectric response.

Under a pure electric loading, the domain size decreases and the domain configuration is more twisted, as the RF becomes stronger. The remanent polarization decreases with the increase of RFs. Under pure mechanical loading, domains size also become smaller as random field increases, and the strain-induced domain switching can be prevented in the presence of a larger RF. When a bipolar loading is applied on a preloaded sample, the macroscopic properties such as the remanent and the maximum polarization can be modified. These results are consistent with the previous study on ferroelectric materials.

Chapter 6

Enhanced large-signal response in relaxor/ferroelectric layered composites

In this chapter, the phase-field relaxor model developed in Chap. 5 is modified by introducing a new Landau energy polynomial. By doing so, the nonpolar-polar phase transition in some "incipient" relaxor piezoceramics can be simulated. The trilayer composite composed of BNT-7BT and BNT-6BT-3AN is compared to the experimental results. By introducing coherent/soft/charge interfaces, the coupling effect in such lead-free relaxor/ferroelectric composites is investigated. Results show the lateral strain coupling in the serial layer contributes considerably to the large-signal piezoelectric response. The main mechanism is that the lateral mismatch lowers the remanent strain in the ferroelectric layer. Moreover, the charge interphase layers in the composite can introduce an internal electric field, leading to a weaker large-signal response compared with the composite with coherent interfaces.

This chapter are based on the manuscript "S. Wang *et al.*, Phase-Field Study of Electromechanical Coupling in Lead-Free Relaxor/Ferroelectric Layered Composites." Here, I thank Prof. Haibo Zhang and Mrs. Azatuhi Ayrikyan for providing the experimental data. The discussion with Prof. Kyle G. Webber on the coupling mechanism is also acknowledged.

6.1 Introduction

Ferroelectric materials have received considerable attention in both industry and science due to their electromechanical response, which is important for many applications such as sensors, actuators, and data storage. [196] Due to the high strain response of lead-based piezoelectric ceramics, they have dominated the piezoelectric transducer market. [197] Research on lead-free piezoceramics, however, has dramatically increased in response to various international regulations limiting the use of toxic metals in electronics and electric devices. For instance, an early investigation showing electromechanical properties in textured KNN are competitive with lead-based materials. [97] Afterwards, other lead-free material systems were proposed; the readers can refer to the previous reviews for a detailed discussion of the various lead-free ferroelectric materials and their electromechanical responses, see Rödel et al. [76, 78] Hong *et al.* [198] and Shrout *et al.* [98].

One promising lead-free ferroelectric system is BNT-based piezoceramics. A giant unipolar strain of 0.45% at 8 kV mm^{-1} was first observed by Zhang *et al.* [79, 80, 199] in KNN-modified BNT-$BaTiO_3$ system (BNT-BT-KNN). Similar phenomena were found in other BNT-based systems such as 0.72$Bi_{1/2}Na_{1/2}TiO_3$ -0.28$SrTiO_3$ (BNT-28ST) [200] and 0.92$Bi_{1/2}Na_{1/2}TiO_3$ -0.08$KNbO_3$ (BNT-8KN) [102]. The origin of the giant strain was found to be the electric field-induced nonpolar to polar phase transition that is modulated by destabilization elements that enhanced reversibility of the transition. [82] This effect, however, typically requires large electric fields to induce the transition and results in significant hysteresis and frequency dependence. Recently, Zhang *et al.* [93] designed a textured BNT-6BT-3AN, which exhibit superior strain response compared to other BNT-based ceramics. The large signal piezoelectric coefficient d^*_{33} can be as high as 766 pm/V at 5 kV mm^{-1} at room temperature, and it shows excellent frequency stability.

A more recent strategy has been to tailor the macroscopic electromechanical response using FE/RE ceramic composites. [22] It has been proposed that the electrical and mechanical coupling between the constituents results in an enhanced strain response at a reduced electric field. [21] These effects can be difficult to be decoupled in the 0-3 composites, making the determination of their relative contributions non-trivial. In order to differentiate them, Zhang *et al.* [23] designed elegantly two types of multilayer FE/RE ceramics composites with interfaces parallel and perpendicular to the poling direction, respectively. In the parallel case, the strain in the poling direction is coupled through the interface, while in the perpendicular case the polarization charge is deemed to be coupled. The authors reported that both polarization coupling and strain coupling are important to the observed large electrochemical effect. This work provided important insights on the strain and polarization coupling in the poling process. Nevertheless, even in the perpendicular case, the lateral strain coupling is also present, as the authors pointed out. Studies that further differentiate the contribution of lateral strain coupling from the polarization coupling would be helpful. More recent work has also found that internal stresses due to different sintering shrinkages and thermal expansions between constituents can result in changes in microstructure and porosity [25], which are expected to also affect the electromechanical properties. The interface between the constituents can weaken both the mechanical and polarization coupling. The above experimental analyses of electric and mechanical coupling effect in the FE/RE composites are time-consuming and require the careful control of different influential factors, while numerical simulations with designed interfaces can be helpful to reveal their potential impact.

To understand the electromechanical coupling behavior and to provide an improved design strategy for better performance in ferroelectric-based piezoelectric devices, various models have been proposed. For example, Hwang and McMeeking [201], as well as Kamlah *et al.* [202], developed micromechanical models, in which the domain switching is controlled by an energy criterion. Recently, phase-field models based on a time-dependent Ginzburg–Landau equation (TDGL) have been employed to study the evolution of domain structure in conventional FE. [13,

139, 14, 151, 203, 15, 204, 16] In a phase-field model, the thermodynamic energy is described in terms of a set of order parameters, for instance, polarization in FE. The evolution of the microstructure is obtained by a minimization process of the total electric enthalpy of the system, which does not make any prior assumptions about the switching criteria of the order parameter.

There are few phase-field models of relaxors, due to the complexity of their domain structure and its unclear origins. [205] In the work by Wang *et al.* [17], the point defects are regarded as the disorder origin in "doped ferroelectrics". The phase transition temperature is also influenced by the point defects density. Li *et al.* [18] considered the disorder in the RE originated from the structural inhomogeneity: the orthorhombic PNRs are surrounded by the tetragonal matrix. They demonstrated that the rotation of collinear PNRs is responsible for the enhanced di/piezoelectricity at room temperature. Nevertheless, these models have not been applied to study electromechanical coupling. As shown in Chap. 5, mechanically coupled phase-field simulations with the consideration of the RF have been carried out. The Gaussian random electric field [54, 48] which results phenomenologically from various disorder origins in RE, is included in the phase-field free energy functional. Simulation results show that the model can reproduce certain features of relaxors represented by SBNx [65], such as the domain miniaturization and decrease of remanent polarization/strain.

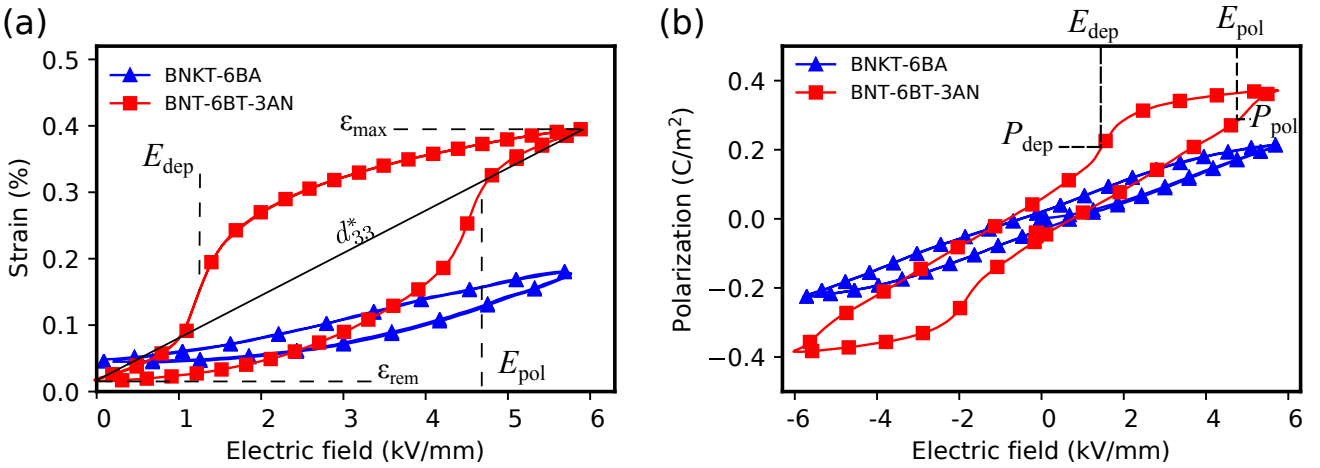

Figure 6.1: *Comparison between measured hysteresis of relaxors BNT-6BT-3AN and BNKT-6BA. Relaxor BNT-6BT-3AN undergoes field-induced nonpolar-polar phase transition (red square), while BNKT-6BA (blue triangle) not. The featuring values (ε_{max}, ε_{rem}, E_{pol}, E_{dep}, P_{pol}, P_{dep} and d^*_{33}) are shown. (a) Strain response under unipolar electric field loading. The E_{pol} for BNT-6BT-3AN is around 4.7* kV mm^{-1}. *(b) Polarization hysteresis under bipolar electric field loading, where P_{pol} and P_{dep} are the polarization at E_{pol} and E_{dep}, respectively.*

Relaxors BNT-6BT-3AN experience, however, a field-induced nonpolar-polar phase transition, and displayed pinched polarization-electric field hysteresis. In Fig. 6.1 the polarization and strain hysteresis loops of two typical lead-free RE materials are contrasted. Relaxors $0.94Bi_{1/2}Na_{3/4}K_{1/4}TiO_3$-$0.06BiAlO_3$ (BNKT-6BA) has trivial dielectric and strain hysteresis,

while BNT-6BT-3AN has a large hysteresis effect. Even though the remanent polarization and strain are small, there is a distinct nonpolar to polar phase transition at E_{pol} and polar to nonpolar phase transition at E_{dep}. E_{pol} for BNT-6BT-3AN is around 4.6 $\mathrm{kV\,mm^{-1}}$. For the study of the electromechanical interface coupling in the composite of BNT-6BT-3AN, a suitable phase-field model should be first developed. In the work of Franzbach [206], a Landau-type polynomial bulk free energy was proposed, and the energy landscape over polarization is illustrated in Fig. 6.2b, in comparison with the conventional double well Landau free energy shown in Fig. 6.2a. As it is demonstrated, the proposed free energy has a single well but with inflection points. The P-E loop has thus two snap-through points, which correspond to the two nonpolar-polar phase transition fields, respectively. However, in that model, the inertia effect of the polarization evolution and the domain-wall energy from the polarization gradient is not considered. Nevertheless, the bulk free energy proposed by Franzbach [206] can be adopted for the phase-field theory, which allows the simulation of the domain structure by adding the gradient term to the bulk one.

In this chapter, a new type of bulk free energy form is introduced inspired by the work of Franzbach. [206] The energy is implemented into the mechanically coupled finite element phase-field framework presented in Chap. 5. It is followed by the simulation of the impact of interface on the electromechanical coupling of the RE/FE/RE trilayer composite, consisting of a RE constitute that displays a field-induced nonpolar-polar phase transition. By designing different interfaces in the simulation, the contribution of lateral strain coupling and the interface charges are revealed. As a representative example, the relaxor BNT-6BT-3AN and the ferroelectric BNT-7BT are regarded as the two composite end-members in the simulations.

Considering that in Chap.5, the phase-field conventional relaxor model is extensively elaborated, brief introduction to the ferroelectric model is given and more attention is paid to the modified relaxor model. The relaxor model with nonpolar-polar phase transition is introduced in Sec. 6.2. By fitting the measured dielectric and strain hysteresis, the parameters of the phase-field models for the RE and FE end-members are determined in Sec. 6.2.2. By using the parameterized phase-field models, finite element simulations are carried out on the layered composites, and results are presented in Sec. 6.3. The large-signal piezoelectric coefficient d^*_{33}, which is the total unipolar strain normalized by the applied maximum electric field, *i.e.*, $\Delta S/E\mathrm{max}$, is calculated for composites with various FE content. An optimal thickness ratio is determined and explained through the simulated domain configuration in Sec. 6.3.1. By introducing coherent/soft interfaces, the cases with/without mechanical coupling are compared in Sec. 6.3.2, and thereby the influence of lateral strain coupling on d^*_{33} is addressed. By assuming external interface charges, the effect of polarization coupling is analyzed in Sec. 6.3.3.

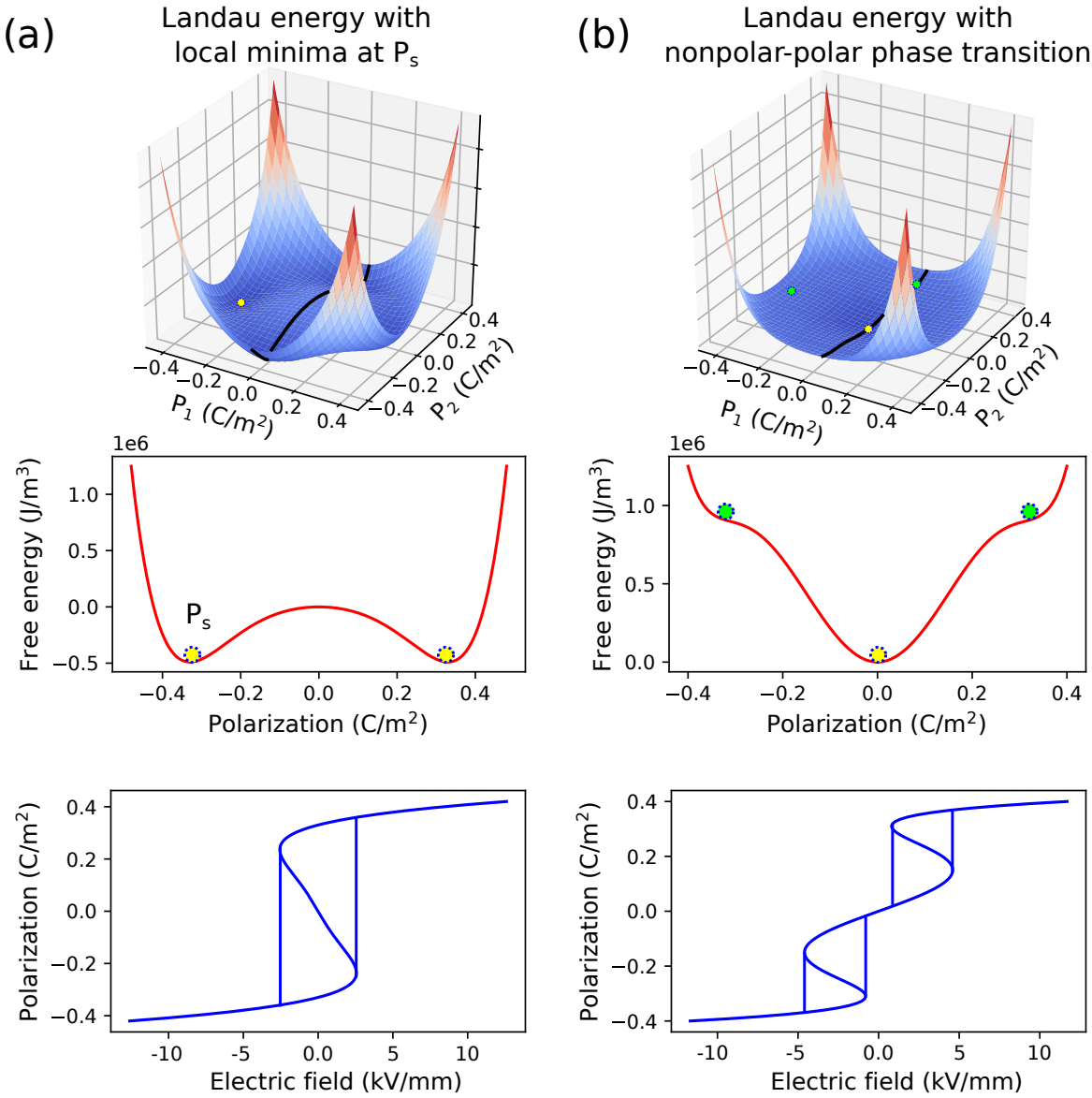

Figure 6.2: *Illustration of the Landau energy and the related P-E loops for (a) FE and for (b) RE with a field-induced nonpolar-polar phase transition. The black lines shown in the 3D Landau landscapes indicate the slice plane for the 1D Landau landscape. The yellow points show the spontaneous polarization while the green points show the polarization at the nonpolar-polar phase transition.*

6.2 Models for the two composite end-members

Phase-field simulations serve as an important tool to reveal the domain structure and the electromechancial coupling in ferroelectrics. As preparation for the simulation of the layered BNT-6BT-3AN/BNT-7BT composites in the next section, the phase-field models for the two end-members and the related parameters are introduced here. While BNT-7BT has conventional FE features, the BNT-6BT-3AN is RE with a distinct field-induced nonpolar-polar phase transition. Therefore, details on the phase-field models are given separately, while the parameterization through fitting the measured hysteresis is presented side by side in the last subsection.

6.2.1 Phase-field model for FE and RE

For BNT-7BT, the previous phase-field models are employed [15], where the spontaneous polarization, instead of the total polarization, is adopted as the order parameter, and physical parameters, such as domain wall thickness and energy, instead of model parameters are used. In the model, the electric enthalpy is expressed by the following independent variables: the mechanical displacement (u_i), the electric potential (ψ), and the spontaneous polarization (P_i). The equations are exactly the same to the Eqs. (5.1-5.25), except that the RF is set to zero, and the separation energy is set as:

$$\mathscr{H}^{sep} = a_1 + a_2(P_1^2 + P_2^2) + a_3(P_1^4 + P_2^4) + a_4 P_1^2 P_2^2 + a_5(P_1^6 + P_2^6) \tag{6.1}$$

The relaxors BNKT-6BT-3AN, among other "incipient" piezoelectrics [46], can experience a nonpolar-polar phase transition during application of the external field, and demonstrates large pinched hysteresis, as shown in Fig. 6.1. The phase-field model presented in the last subsection was therefore modified. More particularly, the single well inflected Landau bulk energy proposed by Franzbach [206] is applied to replace the double well one. The separation energy function is modified to a polynomial of the spontaneous polarization up to the 8th order. In two dimensional case:

$$\mathscr{H}^{sep} = b_1(P_1^2 + P_2^2) + b_2(P_1^2 + P_2^2)^2 + b_3(P_1^2 + P_2^2)^3 + b_4(P_1^2 + P_2^2)^4. \tag{6.2}$$

The coefficients can be calculated by providing the featuring values of P_{pol}, P_{dep}, E_{pol}, and E_{dep}. To be specific, at the transition field E_{pol} (poling process) and E_{dep} (unloading process), the following criteria should be fulfilled.

$$E_{\text{pol}} = \left.\frac{\partial \psi}{\partial P}\right|_{P=P_{\text{pol}}} \tag{6.3}$$

$$E_{\text{dep}} = \left.\frac{\partial \psi}{\partial P}\right|_{P=P_{\text{dep}}} \tag{6.4}$$

$$0 = \left.\frac{\partial^2 \psi}{\partial P_1^2}\right|_{P=P_{\text{pol}}} \tag{6.5}$$

$$0 = \left.\frac{\partial^2 \psi}{\partial P_2^2}\right|_{P=P_{\text{dep}}} \tag{6.6}$$

where P_{pol} and P_{dep} are the polarization at E_{pol} and E_{dep}, respectively. From Eqs. (6.3-6.6), the coefficients in Eq. (6.2) can be determined. With this type of Landau energy, the material remains nonpolar when the applied electric field is below E_{pol}. Above E_{pol}, the polarization is trapped into the local minima of the Landau energy function (shown as green points in Fig. 6.2), which reflects the field-induced nonpolar-polar phase transition. Note that even though the pinched P-E loop resembles that of the antiferroelectrics, the formulation of their free energy differs from each other. In particular, the free energy is assumed to depend on the sub-lattice polarizations in antiferroelectrics [207], while the one used here relies on the spontaneous polarization. In addition, in order to account for the RFs, which originate from the disorder in relaxors, a similar concept to our previous model is adopted. In summary, the relaxor phase-field model differs from the model presented in the last subsection mainly by two points. First, the Landau free energy is replaced by the new form. Second, the electric field E_i is replaced by $E_i + E_i^{random}$. The model framework and the finite element implementation remain similar. By space discretization, a four-node linear element with five degrees of freedom (two displacement components, one electric potential, and two polarization components) at each node is employed.

6.2.2 Parameterization

The phase-field models are able to provide detailed domain evolution at different external loadings, and the traditional simulation was usually restricted to a single grain. [192] However for piezoceramic devices, the critical length scale is on the scale of micrometers. In order to deal with this scale issue, here an average method is introduced to acquire the proper simulation parameters. The adoption of those parameters enables the model to give the correct macroscopic response, *e.g.*, polarization hysteresis loops (P-E loops) and strain loops (S-E loops), while still reflecting the microscopic coupling properties, such as polarization coupling and strain coupling at the layer interfaces. The process is illustrated in Fig. 6.3. using BNT-7BT as an example. This kind of material has been intensively studied, and some of the simulation parameters, such as elastic stiffness and piezoelectric coefficients can be directly obtained from the literature. [208] For the parameters that are not available, *e.g.*, RF, eigenstrain, and eigenpolarization, etc., some test values are used to run the simulation. For ceramics, crystallites of varying orientations coexist. Hence, in our simulation, different angles θ between the external field and the "easy

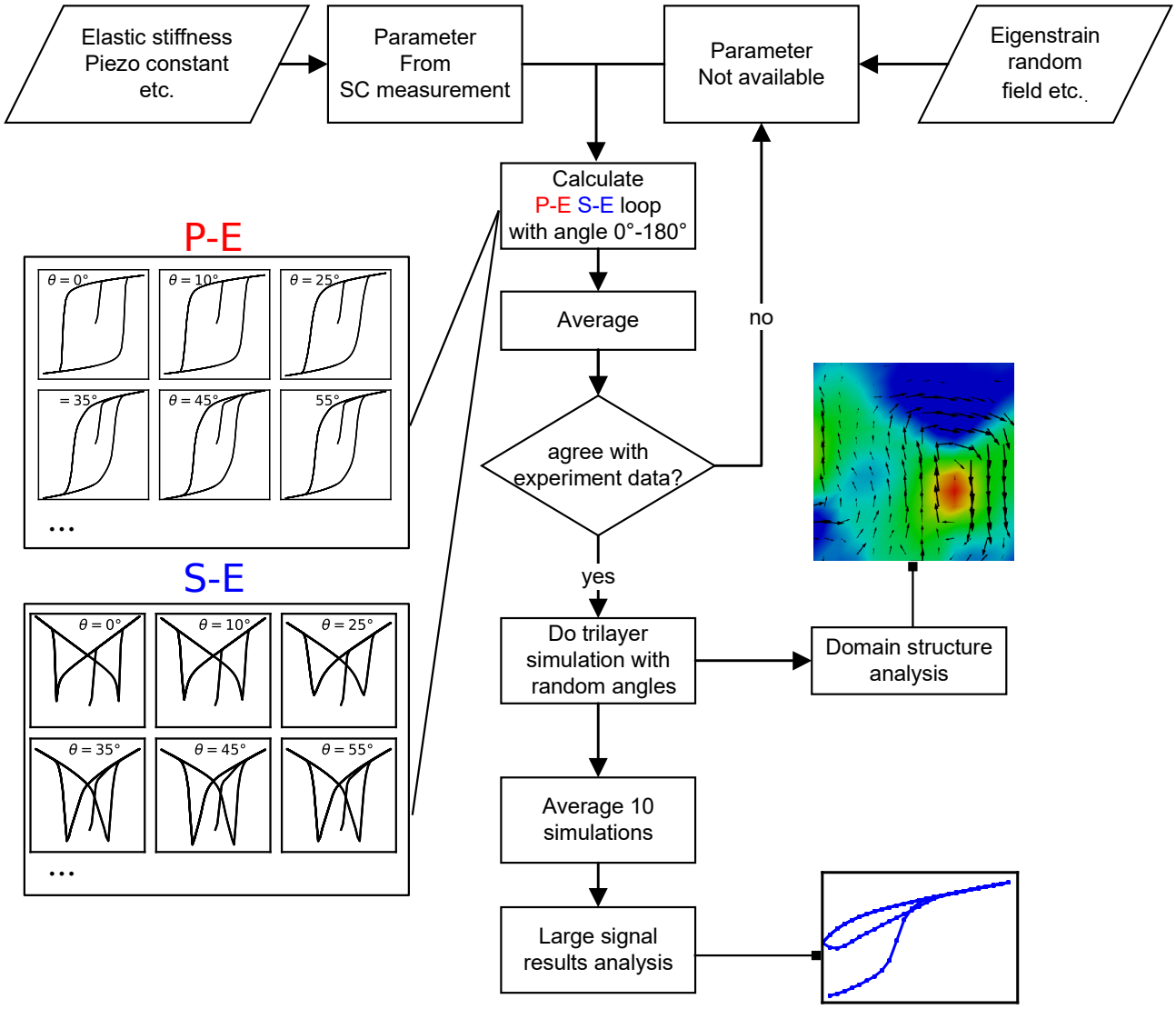

Figure 6.3: *Flowchart of the calculation procedure.*

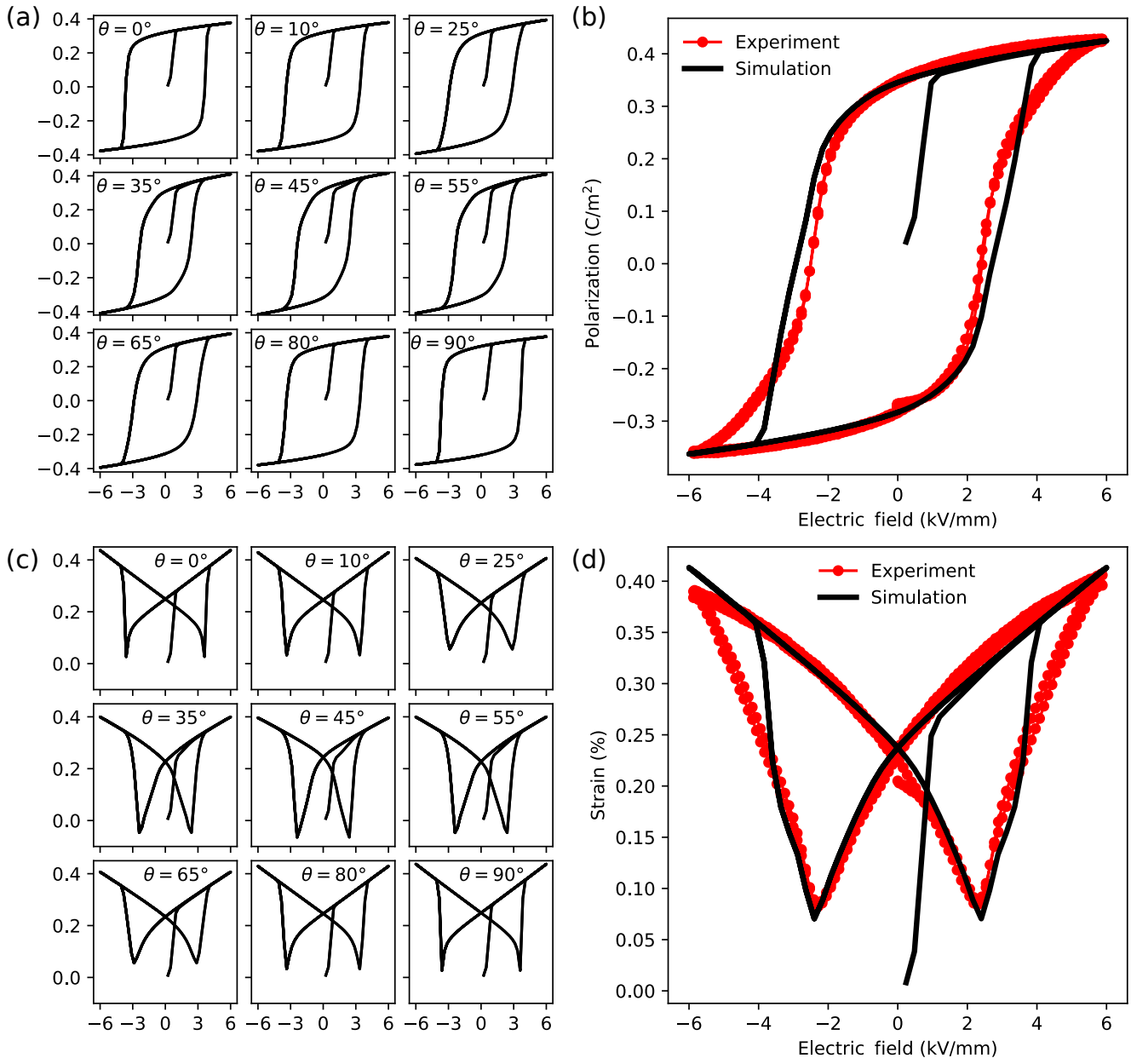

Figure 6.4: *Comparison between the simulation results with experiments for both polarization and strain hysteresis loops of BNT-7BT.*

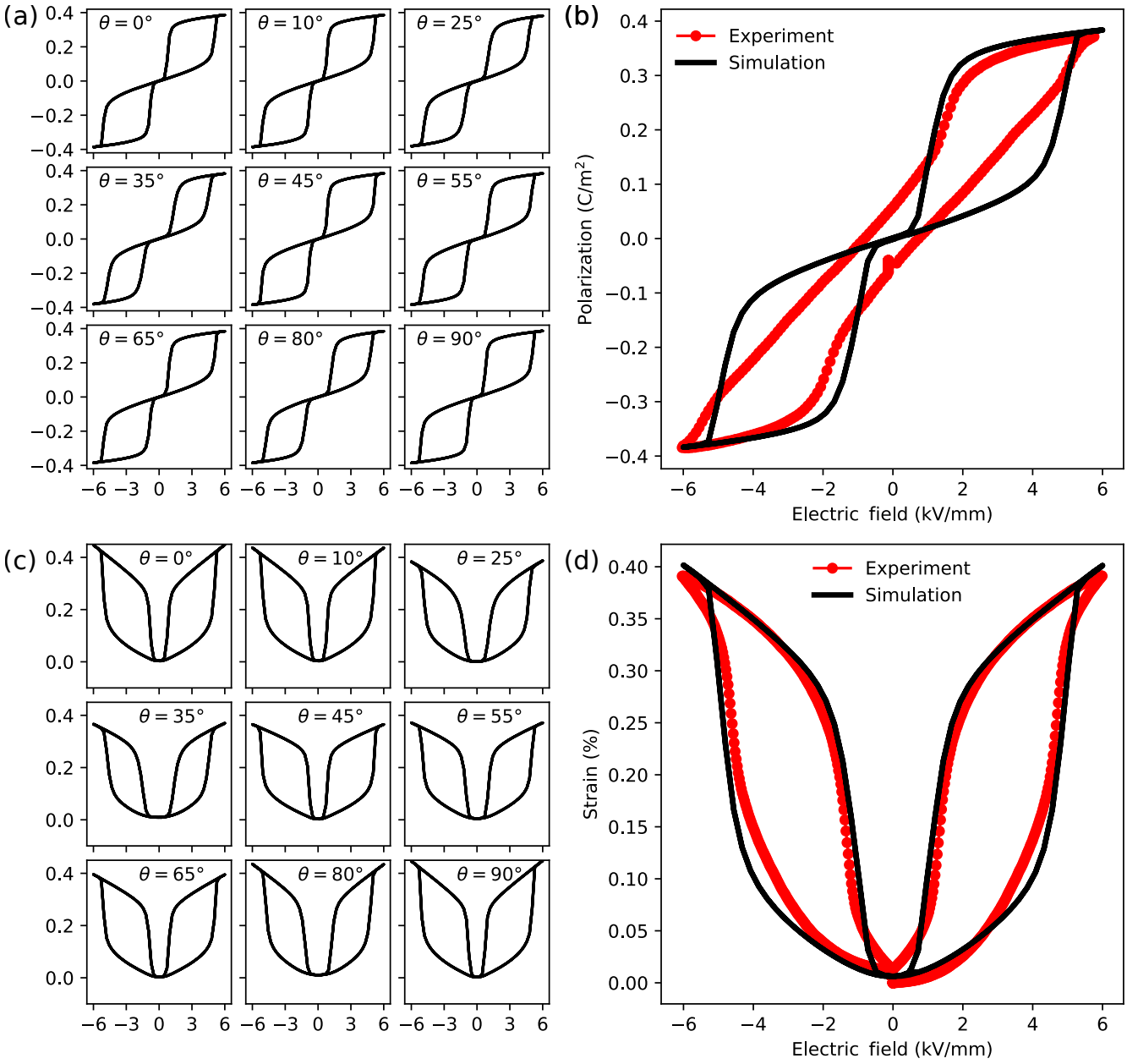

Figure 6.5: *Comparison between the simulation results with experiments for both polarization and strain hysteresis loops of BNT-6BT-3AN.*

Parameter		BNT-7BT	BNT-6BT-3AN	Unit
Piezoelectric coefficient	e_{31}	-1.7	-2.1	$\mathrm{C\,m^{-2}}$
	e_{33}	12	15	$\mathrm{C\,m^{-2}}$
	e_{51}	12.1	15	$\mathrm{C\,m^{-2}}$
Elastic stiffness	c_{11}	159	177	GPa
	c_{12}	95	106	GPa
	c_{44}	75	71.3	GPa
Dielectric constant	k_{11}	6.2	6.2	$10^{-11}\,\mathrm{C V^{-1}\,m^{-1}}$
	k_{22}	6.2	6.2	$10^{-11}\,\mathrm{C V^{-1}\,m^{-1}}$
	k_{12}	0	0	$10^{-11}\,\mathrm{C V^{-1}\,m^{-1}}$
Eigenpolarization	P_0	0.33	0.21	$\mathrm{C\,m^{-2}}$
Eigenstrain	ε_0	0.262	0.12	%
Variance of random field	Δ	0	2.3	$10^6\,\mathrm{V\,m^{-1}}$
Landau coefficient	a_1	1	-	$\mathrm{N\,m^{-2}}$
	a_2	-11.1	-	$\mathrm{Nm^2C^{-2}}$
	a_3	-69.3	-	$\mathrm{N\,m^2\,C^{-2}}$
	a_4	234.3	-	$\mathrm{N\,m^6\,C^{-4}}$
	a_5	803.8	-	$\mathrm{N\,m^6\,C^{-4}}$
	b_1	-	49.1	$\mathrm{N\,m^2\,C^{-2}}$
	b_2	-	-440.8	$\mathrm{N\,m^6\,C^{-4}}$
	b_3	-	1344.7	$\mathrm{N\,m^{10}\,C^{-6}}$
	b_4	-	757.2	$\mathrm{N\,m^{14}\,C^{-8}}$

Table 6.1: *Parameters used for BNT-7BT (FE) and BNT-6BT-3BA (RE).*

axis" (energetically favorable direction of spontaneous polarization) are used in the simulation, from 0° to 180° with the interval of 10°. By a volume averaging of both polarization and strain, the "averaged" P-E loop and S-E loop are obtained, which are further compared with the experimental data. If the experimental data and the simulation diverge, the unknown parameters are updated for a new cycle of calculation, while the parameters from the literature are unchanged. This process is repeated until an acceptable fitting is reached for both P-E and S-E loops between the simulation and the experiment. After obtaining the parameters for both end-members, a trilayer structure was studied. The domain-scale analysis can be operated at this stage. In order to obtain the simulation results for the multigrain composite, a number of simulations are performed on the trilayer structure with a random θ in each layer. An averaging process is presented to get the macroscopic response of the composite. The detailed averaging process can be found in Fig. 6.4 and Fig. 6.5. Note that, by using the method of angle average, the grain boundary effect is ignored. The determined parameters for two end-member materials are listed in Table 6.1.

6.3 Results and discussion of RE/FE/RE trilayer composites

Finite element phase-field simulations were carried out for the BNT-6BT-3AN/BNT-7BT/BNT-6BT-3AN sandwich composites. By varying the thickness ratio, the content of the ferroelectric BNT-7BT, indicated by ω_{FE}, can be changed, and simulations were completed for various FE content, respectively. If not particularly indicated, the Neumann boundary conditions for displacement DOFs are set for all the boundaries. The electric field is applied with a Dirichlet boundary condition for potential DOF at top and bottom. Charge free boundary conditions are set for left and right boundaries. The layered composite is subjected to a triangle potential poling to simulate the unipolar behavior. Based on the work [23], two maximal poling fields $E_{\max}$ are considered: 4 $\mathrm{kV\,mm^{-1}}$ and 6 $\mathrm{kV\,mm^{-1}}$. As an important figure of merit, the large-signal piezoelectric constant d_{33}^{*} is evaluated from

$$d_{33}^{*} = \frac{\varepsilon_{\max} - \varepsilon_{\mathrm{rem}}}{E_{\max}}. \tag{6.7}$$

In this section, three kinds of interfaces between FE and RE layers are used to show the different coupling effects, which are illustrated in Fig. 6.6. In Sec. 6.3.1, coherent interfaces are adopted, which assumes perfect continuity of displacements and charge. Depending on the synthesis process, the interface between the RE and FE layer is not necessarily ideal. Xue *et al.* [209] used a linear combination of parameters such as Landau coefficient and elastic modulus at the interface. In Sec. 6.3.2, the case in which the lateral strain coupling is excluded by introducing soft interphase layers between layers is further regarded. Through comparison with the coherent case, the effect of lateral strain coupling on the large-signal d_{33}^{*} is unveiled. The

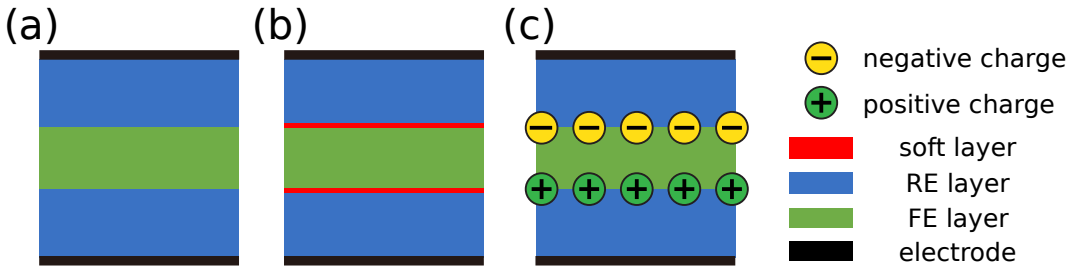

FIGURE 6.6: *Schematic diagram of the simulated trilayer composites with three kinds of interfaces: (a) coherent interface; (b) with soft interphase layers; (c) with charge interphase layers. The simulation results for these three kinds of interfaces will be discussed in Sec, 6.3.1, Sec. 6.3.2 and Sec. 6.3.3, respectively.*

charge continuity across the interface may also be weakened. For the interface between different layers in piezoceramics, Stephanovich *et al.* [210] implemented Robin boundary conditions for polarization at ferroelectric-paraelectric (FE/PE) interface, which was originally developed by Kretschmer *et al.* [211]. In Sec. 6.3.3, two different charged interphase layers are regarded in the finite element simulations, and the change of d_{33}^* is discussed.

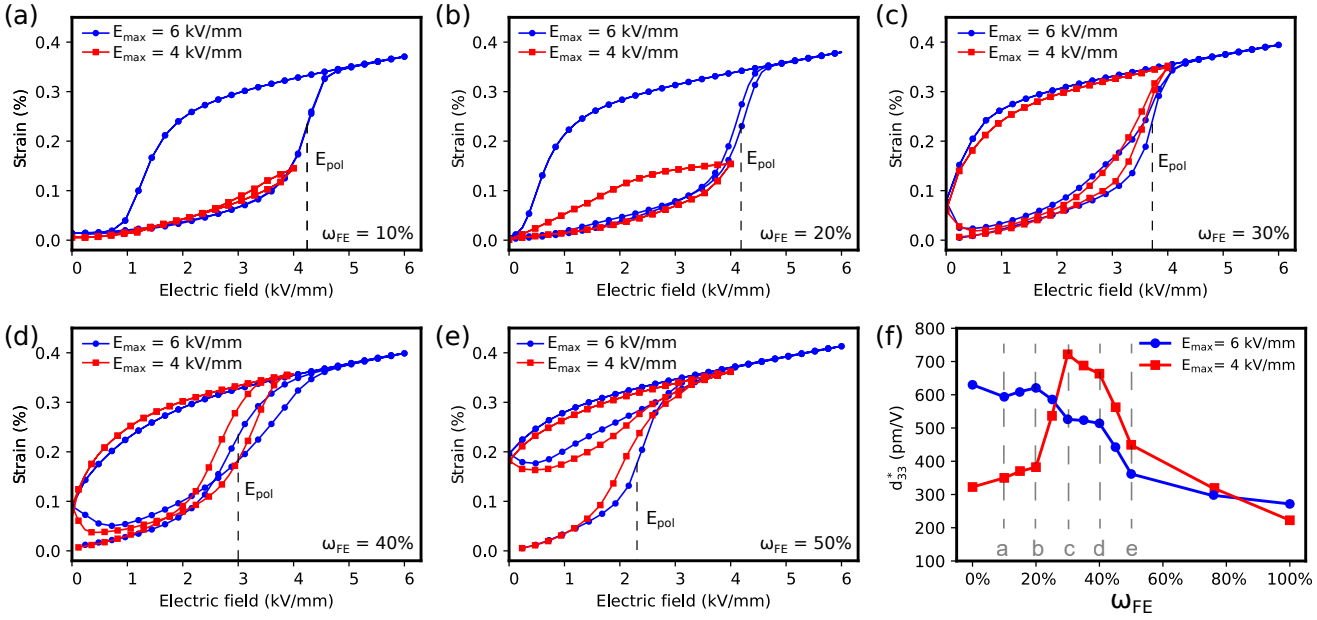

FIGURE 6.7: *(a-e) S-E loop of the BNT-6BT-3AN/BNT-7BT/BNT-6BT-3AN trilayer structure under unipolar loading with different FE volume content ω_{FE} ranged from 10% to 50%. (f) Large-signal response as a function of ω_{FE}.*

6.3.1 Influence of FE content

The unipolar strain-electric field loops of the trilayer composites with different FE content ω_{FE} are shown in Fig. 6.7a-e, along with the variation of the d_{33}^* in Fig. 6.7f. Results are given for both poling fields of $E_{\max} = 4\ \mathrm{kV\,mm^{-1}}$ and $6\ \mathrm{kV\,mm^{-1}}$. It is seen that d_{33}^* shows a peak

value at $\omega_{FE} = 30\%$ in the case of small unipolar loading ($E_{max} = 4\ \mathrm{kV\,mm^{-1}}$), while there is no such peak in the case of large unipolar loading ($E_{max} = 6\ \mathrm{kV\,mm^{-1}}$). This result agrees well with our previous experimental study on the same material system. [23] With full numerical access to the individual quantities related to the definition Eq. (6.7) of d^*_{33}, this observation can be explained.

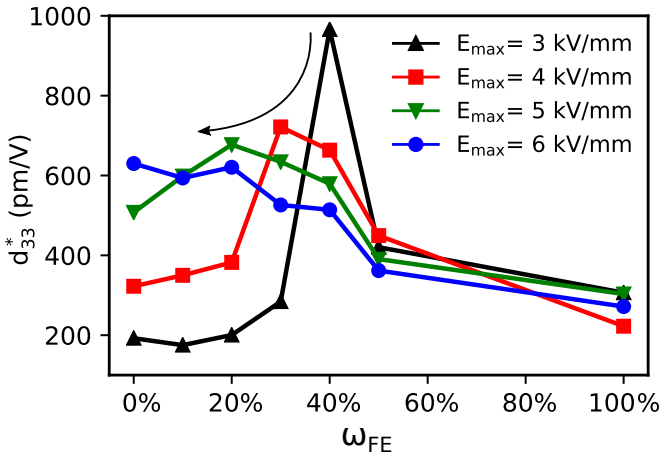

Figure 6.8: *Large-signal response d^*_{33} as a function of FE content with different E_{max}.*

From Fig. 6.7a-e it can be seen that the nonpolar-to-polar transition field E_{pol} decreases with increasing FE content ω_{FE}, while the remanent strain ε_{rem} increases with ω_{FE}. Starting with the case without the FE layer, E_{pol} is equal to the polar transition field of pure BNT-6BT-3AN, *i.e.*, 4.6 $\mathrm{kV\,mm^{-1}}$, and the remanent strain is negligible. If FE content increases up to 100%, E_{pol} approaches the coercive field of the ferroelectric phase BNT-7BT, *i.e.*, around 2 $\mathrm{kV\,mm^{-1}}$, and the remanent strain equals that of the BNT-7BT. Particularly, E_{pol} is slightly above 4 $\mathrm{kV\,mm^{-1}}$ at $\omega_{FE} = 20\%$, while below this value at $\omega_{FE} = 30\%$. Thus there is a significant increase of the maximal strain ε_{max} around $\omega_{FE} = 30\%$ in the case of $E_{max} = 4\ \mathrm{kV\,mm^{-1}}$. At the same time, the remanent strain is still trivial. The resultant d^*_{33} is very large. As the FE content further increases, the maximal strain remains almost unchanged, but the remanent strain increases significantly. It leads hence a decrease of the d^*_{33}. The situation is different in the case of $E_{max} = 6\ \mathrm{kV\,mm^{-1}}$. Due to the large field, the composite can undergo the nonpolar to polar phase transition for all FE contents. In other words, the maximal strain shows little change with FE content, while the remanent strain increases constantly. As a result, d^*_{33} decreases monotonically with the FE content.

Fig. 6.8 shows the large-signal response d^*_{33} as a function of ω_{FE} with different E_{max}. The peak of individual E_{max} case is always found where E_{max} is close to E_{pol}, if one compares Fig. 6.8 with Fig. 6.7a-e. For instance, for the case that $E_{max} = 3\ \mathrm{kV\,mm^{-1}}$, The closest value of E_{pol} is found at $\omega_{FE} = 40\%$ (see Fig. 6.7d). The peak of d^*_{33} is also found at $\omega_{FE} = 40\%$. It indicates that one can determine the best composition ratio for one specific E_{max}. In addition, the peak of d^*_{33} increases with the decrease of E_{max}. And if E_{max} decreases to a very small value (*e.g.*,

2 kV mm^{-1}), the peak of d_{33}^* vanishes. For such small E_{max}, the composites cannot experience nonpolar-polar phase transition, which results in a very small d_{33}^*.

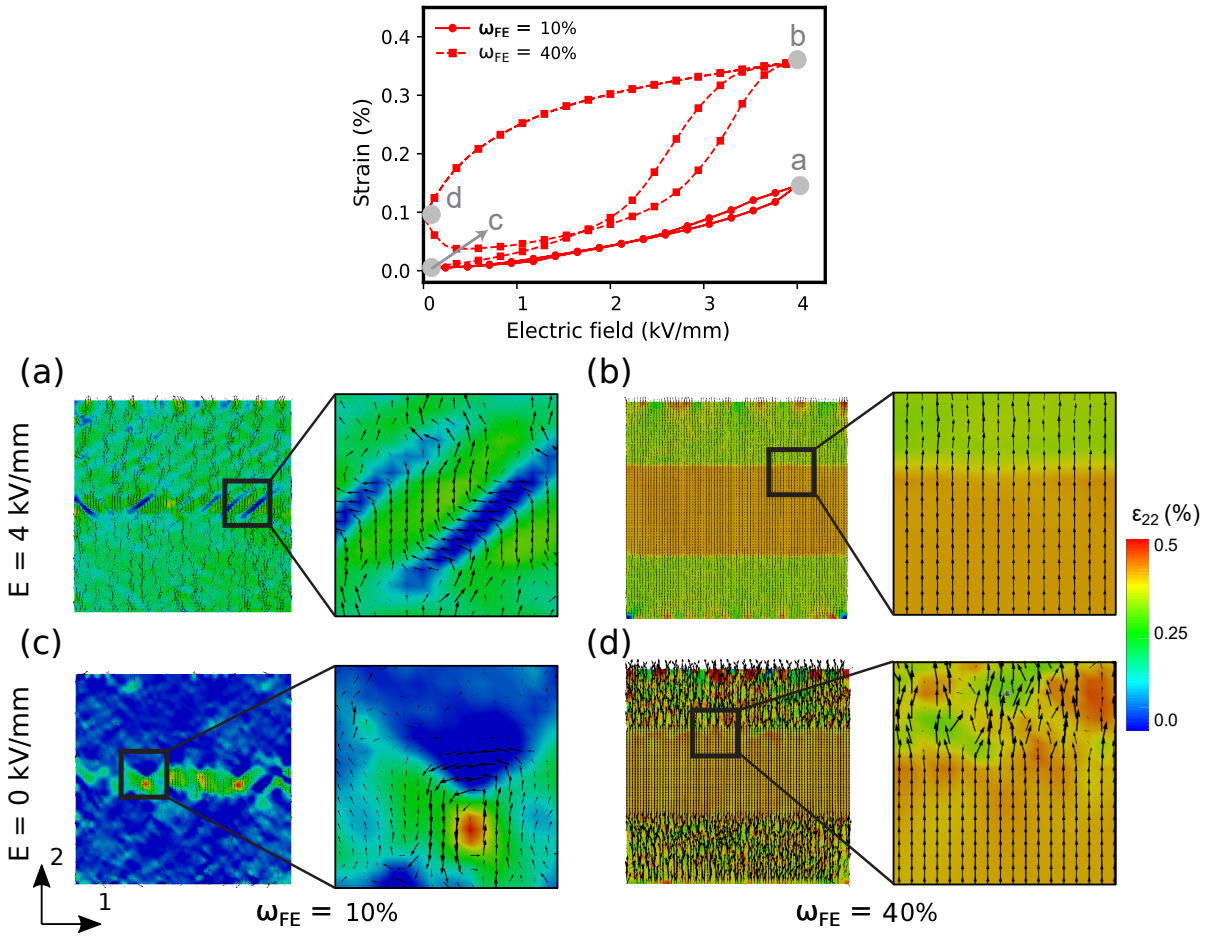

Figure 6.9: *Domain structure for the FE/RE trilayer structure and the polarization distribution at 4* kV mm^{-1}*, with FE content of (a) 10% and (b) 40%, respectively. The black arrows indicate the orientation of the polarization. (c) and (d): Domain structure for the remanent state. The corresponding S-E loops are shown on top for reference.*

Domain structures for different FE content and different states (*i.e.*, poled and remanent state) help also to explain the coupling between the layers. Here, the cases of ω_{FE} are chosen for a better comparison: 10% where RE layer dominates the overall response feature under unipolar loading and 40% where FE layer dominates and focus only on the case where the peak appears, *i.e.*, $E_{max} = 4$ kV mm^{-1}. The domain structures are shown in Fig. 6.9. The domain configuration is the result of the competition between these two phases. For $\omega_{FE} = 10\%$, the FE layer is more influenced by the RE layer. The RF from the RE layer at the interface disturbs the alignment of polarization in the FE layer, thus multi-domains are formed. For $\omega_{FE} = 40\%$, the RE layer is more influenced by the FE layer. Instead of keeping randomized at 4 kV mm^{-1}, the RE layer tends to align to the direction of the poling field, especially at the interface. The FE layer has a positive effect on the poling process in the RE layer, which leads to the decrease of E_{pol} as ω_{FE} increases. The domain structures at zero field for ω_{FE}= 10% and 40% are shown in Fig. 6.9c

and Fig. 6.9d, respectively. For the 10% case, the impact of the RF from RE is non-negligible. Instead of forming a monodomain, several vortices appear. The FE layer cannot contribute much to the vertical strain of the composite. While for the 40% case, the FE phase aligned to the same direction of the poling field. At the interface region, the polarization vectors tend to align to the poling direction, despite the interference of the RF.

6.3.2 Influence of lateral strain coupling

The above discussion is based on the assumption that the interfaces between different layers are coherent. However, in the experimental samples, the interfaces may not be ideally bonded. Moreover, it is also meaningful to exam how significant the contribution of the mechanical coupling is, *i.e.*, the coupling of the lateral strain in the trilayer composite, while still polarization-coupled. To uncouple the mechanical deformation between the layers, a soft layer with a certain thickness can be inserted between the layers in the finite element model. In the simulation, Young's modulus of the soft layer is three orders lower than that of the end-member materials.

With the implementation of the soft interphase layers, a series of simulations are operated. All the other conditions are exactly the same to those of the coherent interface cases shown in Sec. 6.3.1. After removal of the poling field, the FE layer remains the poled state, while the RE layers intend to become nonpolar. Assuming the coherent interfaces, internal lateral stress is expected in all three layers near the interface, in order to compensate the strain mismatch in the horizontal direction. Finite element simulations shown in the Fig. 6.10a demonstrate that the FE layer is under tensile loading in the horizontal direction, while the two RE layers experience compressive stress. The results agree with the prediction made in [93]. If the lateral stress in FE is strong enough, it can even lead to 90 degree polarization switching by ferroelastic effect, as it is demonstrated in Fig. 6.10b. In contrast, if a soft interphase layer is introduced, the layers are mechanically uncoupled, as it is confirmed by the finite element results shown in Fig. 6.10c. The poled state in the FE layer is preserved.

The tensile lateral stress in the FE layer can lower the remanent strain in the FE layer significantly. Since the remanent strain in RE layers is negligible and not sensitive to the internal stress, the effective remanent strain of the composites with coherent interfaces is smaller than that of the composites with soft interphase layers, as it is confirmed by the finite element simulation results shown in Fig. 6.10e. On the other hand, at the maximal field, both FE and RE layers are poled, and thus there is trivial or decreased lateral mismatch. Thus, the lateral mechanical coupling has hardly influence on the maximal strains, as it can be seen in Fig. 6.10e. Based on the definition of the large-signal d^*_{33}, it can be thus expected that the large-signal d^*_{33} of the composite with soft interphase layers should be smaller than that of composites with coherent interfaces, which is well confirmed by the simulation results shown in Fig. 6.11a. Around ω_{FE}

is 30%, the d_{33}^* decreases by almost 27% percent. In the case of 4 kV mm^{-1} unipolar loading, similar results are observed. Additional simulations were performed in which Young's modulus of the soft layer is set to be 20% of the value of the FE layer. These results show values between the two extreme cases, as the black dotted line in Fig. 6.11b shows. These results imply that the lateral strain coupling in the trilayer composite contributes positively to the macroscopic electromechanical coupling.

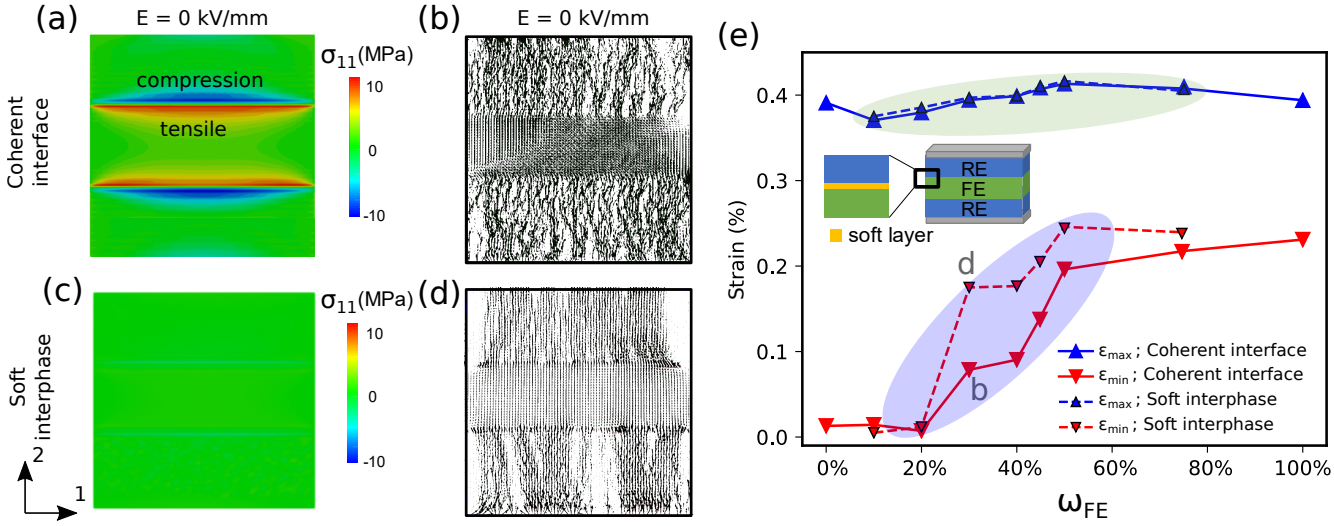

Figure 6.10: *(a)-(d) Stress and polarization distribution of the BNT-6BT-3AN/BNT-7BT/BNT-6BT-3AN trilayer structure at remanent state the FE content ω_{FE} is 30%. (a) and (b) are the results for the coherent interface case, while (c) and (d) are for the case with soft interphase layers. (e) Comparison of the maximum strain ε_{max} and the remanent strain ε_{rem} between coherent and soft interfaces in trilayer composites with different ω_{FE}. The magnitude of the unipolar loading is $E_{max} = 6$ kV mm^{-1}.*

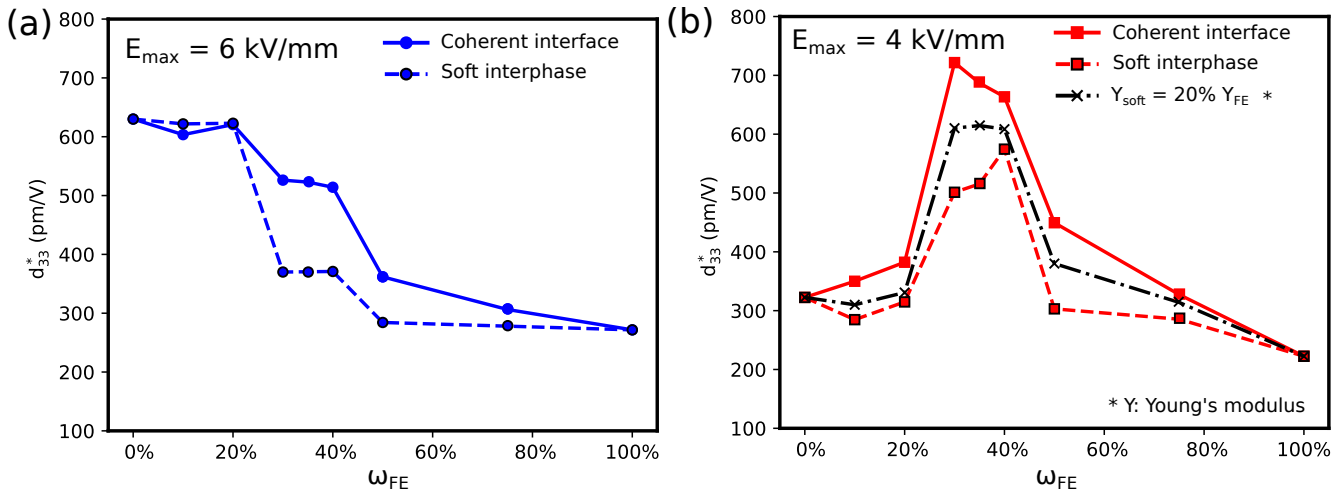

Figure 6.11: *Comparison of the large-signal response d_{33}^* of trilayer composites with and without lateral strain coupling. (a) 6 kV mm^{-1} unipolar loading. (b) 4 kV mm^{-1} unipolar loading.*

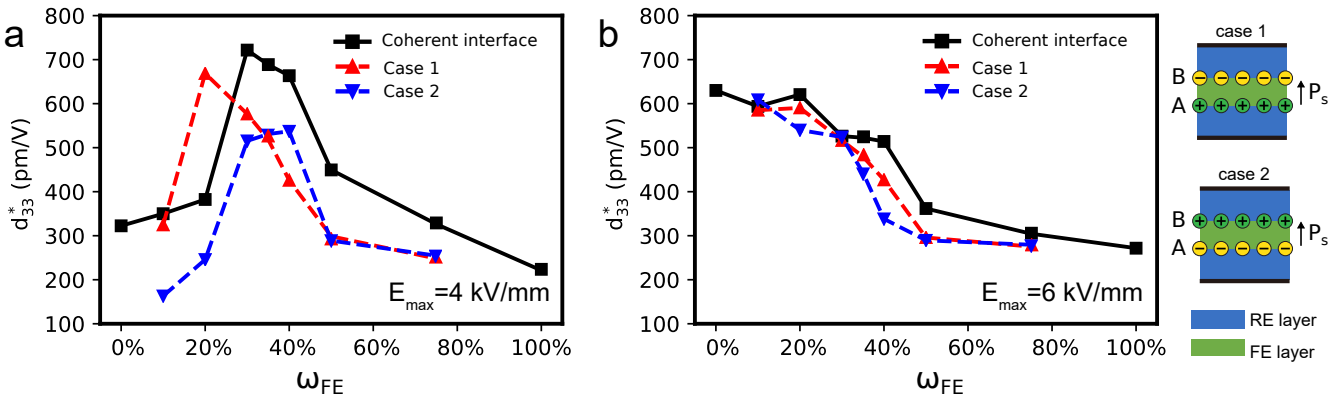

Figure 6.12: *Large-signal response d_{33}^* as a function of FE content ω_{FE} with charged interphase layers. (a) $E_{max} = 4\,\mathrm{kV\,mm^{-1}}$. (b) $E_{max} = 6\,\mathrm{kV\,mm^{-1}}$.*

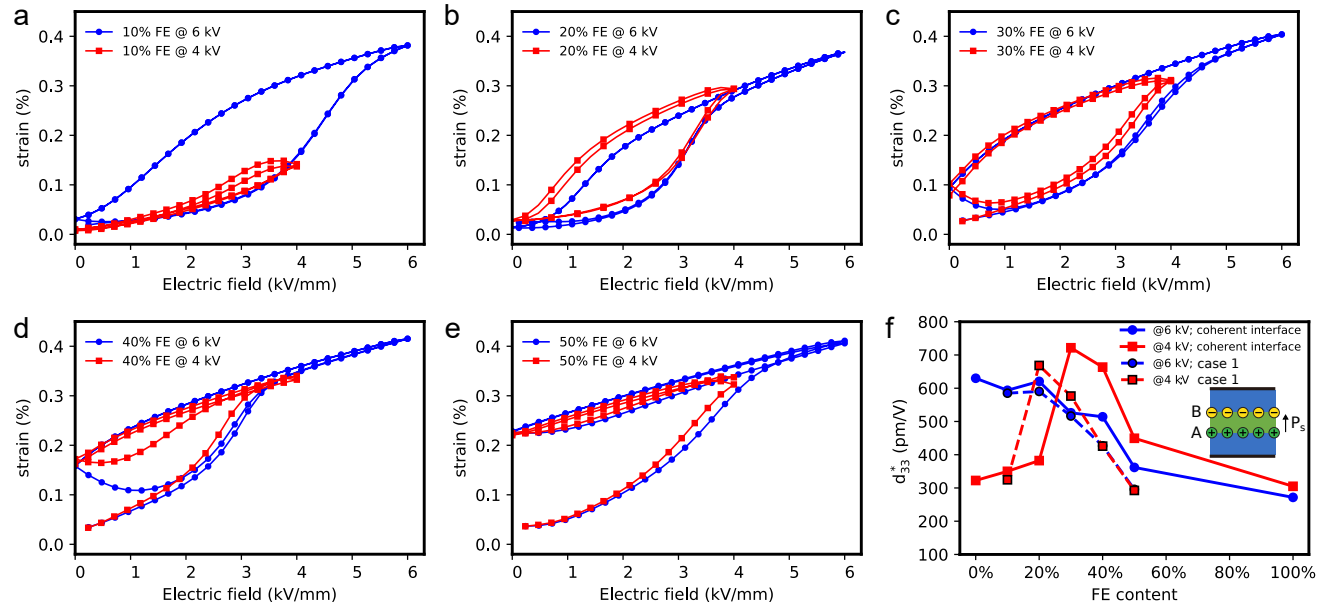

Figure 6.13: *(a-e) S-E loop of the BNT-6BT-3AN/BNT-7BT/BNT-6BT-3AN trilayer structure under unipolar loading with different FE volume content ω_{FE} ranged from 10% to 50%. (f) Large-signal response as a function of ω_{FE}.*

6.3.3 Influence of interface charge

In thin films and layered ferroelectric composites [212], the charge at the interface between different layers can affect its electrical properties significantly. Due to impurity or aging effect, charges can accumulate at the interfaces of the layered composite. [213] Their existence leads to uncoupling of the polarization between the layers. Phase-field simulations have shown that the space charge can influence the stability of the domain structure [214, 215]. Here, the thin charge interphase layers between FE/RE interfaces are introduced in the finite element simulation to investigate the effect of electrical decoupling of layers, viz. layer A and B in Fig. 6.12. In this situation, interphase A is positively charged while interphase B is negatively

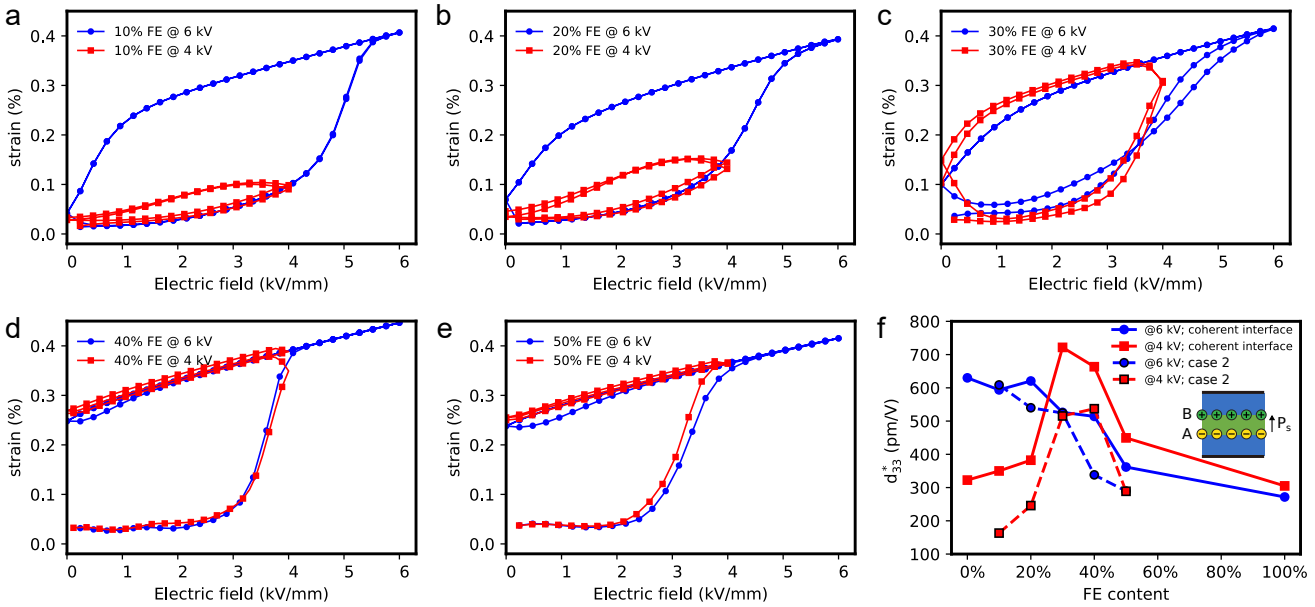

FIGURE 6.14: *(a-e) S-E loop of the BNT-6BT-3AN/BNT-7BT/BNT-6BT-3AN trilayer structure under unipolar loading with different FE volume content ω_{FE} ranged from 10% to 50%. (f) Large-signal response as a function of ω_{FE}.*

charged with the charge density of $0.8 \times 10^6\,\mathrm{C\,m^{-3}}$. The thickness of the charge layer is 1 nm. The induced internal field between the two interphase layers is around $1.25\,\mathrm{kV\,mm^{-1}}$.

The large signal response d^*_{33} is shown in Fig. 6.12 and the detailed P-E loops can be found in Fig. 6.13 and Fig. 6.14. The large-signal performance for this situation does not show any advantage over the coherent interface case. One interesting phenomenon found in Fig. 6.12a is that the peak of d^*_{33} is shifted to the low ω_{FE} region. The reason is that the internal field is in the same direction to the applied field, hence E_{pol} is reduced. For $\omega_{\mathrm{FE}} = 20\%$, E_{pol} is around $4.2\,\mathrm{kV\,mm^{-1}}$, while with such charged interphase layers, E_{pol} is dropped below $4\,\mathrm{kV\,mm^{-1}}$. As a consequence, the peak appears at 20%. If the interface is engineered with the opposite charge state (case 2 in Fig. 6.12), simulations still indicate no improvement of the d^*_{33}. The vertical strain first decreases due to the opposite internal field then increase when the applied field overcomes the internal field. There is no increase of $\varepsilon_{\mathrm{max}}$. As a consequence, d^*_{33} cannot benefit from the modified charged interface.

The accumulation of positive charges in layer A and negative charges in layer B (case 1) can be regarded as the aging effect. [216] Case 2 can be regarded as one type of interface charge engineering. From the above simulation results, it is obvious that there is no apparent advantage in aging or modifying interface of the composite for a better large-signal performance. However, the peak shifting effect found in Fig. 6.12 shows another factor which can influence the optimized ω_{FE} in such layered FE/RE composite.

6.4 Concluding remarks

The interface coupling effect of multilayer lead-free relaxor (RE)/ferroelectric (FE) ceramic/ceramic composite was studied by finite element phase-field simulations. To reflect the field-induced NP-P phase transition in the RE layer, a new relaxor phase-field model is first developed in this work and parameterized by fitting the measured hysteresis loops. The influence of different contributing factors, such as FE content, lateral strain coupling, and interface charge on the large-signal response d_{33}^* is investigated by the simulations of coherent/softer/charged interfaces in RE/FE/RE trilayer composite. Through the analysis of the strain and detailed domain structure under different conditions, *e.g.*, different ω_{FE} and $E_{\max}$ the following conclusions can be drawn:

- For small unipolar loading ($E_{\max} = 4\ \mathrm{kV\,mm^{-1}}$), the enhancement of d_{33}^* can be found at $\omega_{\mathrm{FE}} = 30\%$. which agrees with the experimental observation. The further analysis of the domain structure shows that, for the case with lower ω_{FE}, the RF from RE leads to the vortex domain structure in FE, thus lowers the remanent strain. While for the case with higher ω_{FE}, the polarization vector tends to align to the poling direction, which leads to higher remanent strain.
- The peak of d_{33}^* is always found at the place where $E_{\max}$ is close to E_{pol}. The peak of d_{33}^* increase with the decrease of $E_{\max}$ till some finite value.
- Both lateral strain coupling and charge interfaces between composite layers influence the large-signal response.
  - *Mechanical coupling* The different properties between FE and RE layers result in the lateral strain at the interface. The compensated bias stress at the interface in general has a positive effect on d_{33}^*. Softer interphase layers hinders the stress coupling between layers, thus reduces the large-signal performance.
  - *Charge effect* The charges can accumulate at the interface, which can be regarded as one of the aging effects after long-time unipolar cycling. The resultant charged interfaces can induce an internal field with the same direction to the spontaneous polarization. This results in a weaker large-signal response compared with the composite with a coherent interface.

This model can be further used to predict the electromechanical performance of FE/RE composite with more complex microstructure, *e.g.*, 0-3 composite. Note that the influential factors on the FE/RE composite are more than above-mentioned ones. For instance, the oxygen vacancy may accumulate at the layer interfaces. In addition, previous experimental work has also demonstrated the formation of constrained sintering-induced porosity in such composite structures as well as changes in the mechanical properties. The grain boundaries within each layer

also affect the response of the poling process. The interfaces between layers cannot be ideally polarization-coupled, which is also not intensively discussed in this work. More efforts could be made to investigate coupling effects in such FE/RE composites based on the above discussions.

Chapter 7

Investigation of core-shell structure in relaxors

In this chapter, the abnormal phenomena observed in the core-shell structured relaxor materials are investigated using the phase-field model. This chapter is arranged as follows. The introduction to the core-shell structure in relaxors is shown in Sec. 7.1. Special attention is paid to the $0.75Bi_{1/2}Na_{1/2}TiO_3$ -$0.25SrTiO_3$ (BNT-25ST) material system. It is followed by the study of two specific cases: (i) abnormal domain configuration found in the poled core-shell relaxor, and (ii) abnormal domain-like nanoregions (DLNRs) found in core-shell nanoparticles. In Sec. 7.2, the random field phase-field relaxor model is utilized to explain the abnormal domain observed in a core-shell BNT-25ST. As a prerequisite for Sec. 7.4, the flexoelectric model within the framework of the phase-field ferroelectric model is introduced in Sec. 7.3. In the last section (Sec. 7.4), the flexoelectric-ferroelectric phase-field model is adopted to explain the DLNRs in BNT-ST core-shell nanoparticle at extreme temperature.

Parts of this chapter are based on the publication "Liu *et al.* Revealing the core-shell interactions of a giant strain relaxor ferroelectric $0.75Bi_{1/2}Na_{1/2}TiO_3$-$0.25SrTiO_3$. *Sci. Rep.* **6**, 36910." and "L. Molina-Luna, S. Wang *et al.* Enabling nanoscale flexoelectricity at extreme temperature by tuning cation diffusion. *Nat. Commun.* **9** (1), 4445." Here, I express my special gratitude my collaborator Dr. Na Liu and Dr. Christian Dietz for the operation of PFM, Dr. Matias Acosta for preparing the sample, Dr. Leo Molina-Luna and Mr. Alexander Zintler for the operation of TEM, which are essential for the results presented in this chapter.

7.1 Introduction

The design of the core-shell structure in the material community has been utilized for a long time. One of the pioneers in this field is Rawal *et al.* [26], who designed a grain core-grain shell structure in BTO-based dielectrics in order to improve the material properties, such as increasing the dielectric constant and the breakdown voltage. The core-shell structure is also used in other fields, *e.g.*, superconductor materials [217], lithium-ion battery materials [218], and magnetic materials [219]. Recently, the core-shell structure in relaxor-ferroelectric composite [28, 108] is also designed to modify its physical properties such as large-signal piezoresponse d^*_{33}, relative permittivity, and electric resistance, to name a few. One of the most promising application is the improvement of the electromechanical property, as a result of the interaction between the core and the shell.

On the other hand, global awareness for the environment and sustainability has increased in the past decades. [76, 78] Regulations have been proposed worldwide to minimize the usage of toxic materials in end consumer products. [6] In the piezoelectric community, three main solid solution families have been widely recognized as potential environmentally friendly candidates to replace lead-content ones: KNN-based, BNT-based, and BT-based materials. However, to date, there is no single class of lead-free piezoelectric material that can replace PZT entirely. Recent work has shown that the core-shell structured piezoelectric ceramics possess unique electromechanical properties thus provides another route to replace PZT for large-signal applications. Therefore, a clearer understanding of the role of the core-shell structure is in great demand. [28]

Throughout this chapter, BNT-25ST is used as a representative model system to study the properties of the core-shell structure. The fundamentals of the BNT-25ST system is introduced in the next subsection.

7.1.1 BNT-25ST ceramic and BNT-25ST core-shell structure

BNT-25ST was first studied by Sakata *et al.* [220]. As introduced in Chap. 2, in some solid-solution ferroelectric ceramics, for instance, PMN-xPT and BNT-xBT, tuning the composition x leads to the significant change in their physical properties. It is ascribed to the misfit of different crystal structures, or to the newly introduced crystal structure (*e.g.*, monoclinic phase). [83, 84] For (1-x)$Bi_{1/2}Na_{1/2}TiO_3$-x$SrTiO_3$, the compositional range 25-30 mol% ST features exceptional electromechanical properties. [220, 27, 90]

The schematic phase diagram of (1-x)BNT-xST can be found in Fig. 7.1. The left figure shows the different phases as a function of STO component x and temperature. The morphophonemic phase boundary can be found at around 25 mol% ST at room temperature, which separates the BNT rhombohedral phase to the STO tetragonal one. Upon heating up to a feature temperature T_d, piezoelectricity disappears. Sakata *et al.* [220] regards this phase as an antiferroelectric phase. The maximum permittivity can be reached when the temperature increases to a higher value T_m. In Fig. 7.1, the blue cross marks the state where the case (i) was investigated, while the red cross designates the condition for case (ii). The right figure shows the schematic isothermal E-T phase diagram of (1-x)BNT-xST with x = 0.25. The solid line indicates a first-order field-induced phase transition from relaxor phase to the ferroelectric phase. In the viewpoint of the PNR model, as temperature increases, the barrier for activation and reorientation of PNRs gets lower, which leads to the decrease of transition field. The threshold field increases again with the increase of temperature, due to the rise of the instability of PNRs. [221]. When the field is removed, the material is changed from the ferroelectric state to either nonergodic relaxor or ergodic relaxor depending on the operation temperature. The first-order phase transition is terminated at a higher temperature. This region is marked by the critical point (CP). The CPs are usually related to the enhancement of material properties, such as piezoelectric response.

The phase boundary between the rhombohedral and the pseudocubic phases has a considerable effect on the electromechanical properties of the BNT-xST system. The maximum dynamic piezoresponse $d_{33} = 130\ \mathrm{pC\,N^{-1}}$ was reported to be around 22 mol% ST, followed by a decrease leading to negligible values above 28 mol% ST. The maximum value of large-signal response d^*_{33} is found to be 500 $\mathrm{pC\,N^{-1}}$ at 28 mol% ST. [102]

In the work of Kuroza *et al.* [108] and Acosta *et al.* [28], core-shell structure within the grain can be found and can be tuned with special treatment. The main reason for the formation of the core-shell structure is the diffusion of the Sr^{2+} from the core to the shell. To be specific, during the sintering process, the perovskite BNT phase is first formed at the temperature between 410 °C and 610 °C, while ST is formed approximately 200 °C higher. Further heated above 800 °C, the diffusion between BNT and ST phases results in the formation of an inhomogeneous BNT-ST solid solution. The different reaction temperatures of both phases are therefore suggested to be the origin of the formation of the core-shell microstructure of BNT-ST, consisting of two solid solutions: a BNT-rich core and ST-rich shell. [108] It is expected that the core-shell structure in BNT-ST could potentially lead to a modification of the strain output, hysteresis, temperature stability, and fatigue properties. [28]

The synthesis procedure of the BNT-25ST solid solution can be found in, for example, Refs. [222, 223, 224, 225, 226]. The synthesis of core-shell structure in BNT-25ST needs some special heating treatment which can be found in Refs. [108, 28].

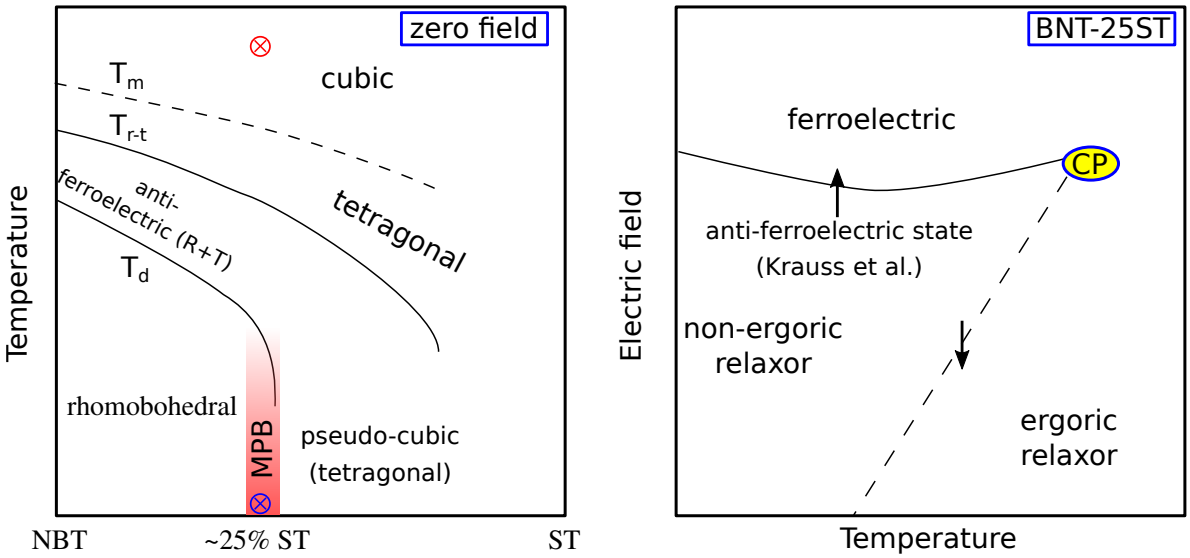

Figure 7.1: *Schematic phase diagram of (1-x)BNT-xST. The information is collected from Ref. [224, 227, 228, 223]. The red and blue cross mark indicates the phases, that will be investigated in Sec. 7.2 and Sec. 7.4, respectively.*

In the following sections, the domain structure in the core-shell BNT-25ST particle is investigated. Section 7.2 mainly focus on the domain structure near the core region at room temperature after field removal. Lateral distributed domains are formed due to the high potential region

beneath the core. These field-induced domains act as pivotal points at the coherent core-shell interface, reinforcing the phase transition in the non-polar shell and thus promoting the giant strain. Section 7.4 focus on the domain-like structure in BNT-ST nanoparticle at extreme temperature (800 °C). At this temperature, the nanoparticle is no longer in the state of ferroelectric or relaxor phase, but rather a pseudocubic phase. The diffusion of the Sr^{2+} is in responsible for the strain inhomogeneity within the nanoparticle. The flexoelectric effect is introduced to explain the observed domain-like nanoregions. It provides a route in design high-temperature flexoelectric nanomaterials.

7.2 Domain configuration of the core-shell structure at room temperature

As mentioned above, core-shell relaxor materials are characterized by an extraordinarily high electric field-induced strain. An in-depth understanding of the interaction between core and shell and the electromechanical coupling at their interface, however, is still lacking. In the following, nanoscale relaxation behavior of field-induced domains is reported in the core-shell specimen BNT-25ST with PFM at room temperature. The utilization of PFM enables the detailed characterization of the domain structure, including the magnitude of the polarization (amplitude mode) and the orientation of the polarization (phase mode). The domain structure near the core-shell interface is of particular interest.

7.2.1 Experimental observation

The synthesis procedure is operated by our collaborator Dr. M. Acosta. The prepared sample is placed onto the PFM holder and scanned by our collaborators Dr. N. Liu and Dr. C. Dietz. A representative core-shell structure of an individual grain is captured by the vertical phase channel shown in Fig. 7.2a. This individual grain exhibits distinctive domain contrasts in the core, whereas there is only a weak contrast in the surrounding areas. In the next step, the response of the material to an external electric field (local poling) and the subsequent relaxation of the tip-induced polarization were investigated. A surface area of 1.5 × 1.5 μm^2 was poled within the region of interest (ROI). After polling, the material is relaxed, and the domain configuration is captured at 15 min 45 min and 90 min, as shown in Fig. 7.2b-e, respectively.

Figure 7.2b shows the virgin domain state, with a sharp image contrast in the core but a negligible image contrast within the shell. Fig. 7.2c reveals that the virgin lateral domain configuration completely disappeared after vertical poling. Moreover, new lateral domains were formed at preferential nucleation spots around the core-shell interface, as indicated by the blue arrows. Remarkably, 45 min after poling, these lateral domains became larger and more pronounced. This observation indicates that lateral domains can be induced by the electrical field and start to nucleate at the core-shell interface. These freshly induced domains continue to grow in the lateral direction and propagate into the adjacent shell to compensate for the mismatch of

stress and polarization between the irreversibly induced ferroelectric state in the core and the ergodic shell, which is the driving force of the lateral domain propagation.

In the next subsection, the explanation for the formation of such domain structure in the core-shelled BNT-ST is elaborated by the phase-field model.

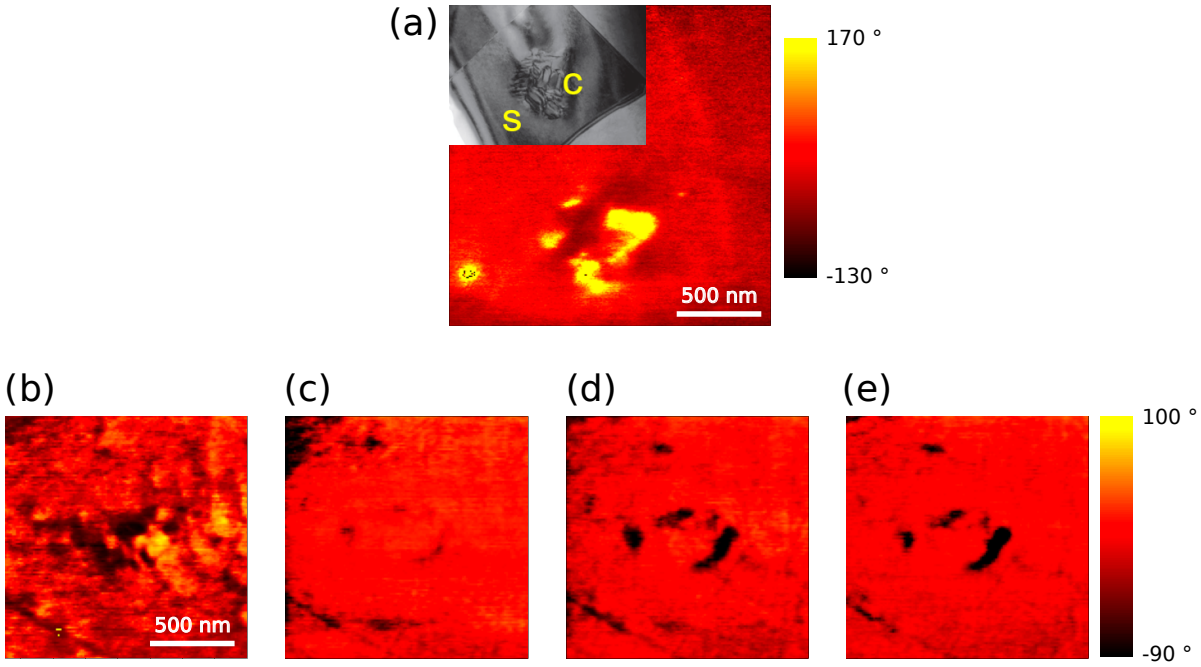

Figure 7.2: *(a) Core-shell structure of individual grains. PFM vertical phase image exhibiting a distinct contrast in the core region. Inset: Typical TEM showing the core-shell microstructure (different location). (b) Evolution of the lateral domain at the core-shell interface after poling. The blue arrows highlight the newly formed lateral ferroelectric domain at the core-shell interface. TEM image ©2015 John Wiley & Sons, Inc. PFM images ©2016 Springer Nature Limited.*

7.2.2 Explanation of the lateral-aligned domains by the phase-field model

As shown above, under an external field, the entire virgin material can be poled. After removing the field, the core remains at the poled state, whereas the shell reversibly relaxes to the initial state. To gain further insights into the evolution of the domain distribution after poling, and particularly at the interface, a continuum phase-field simulation was carried out.

In the simulations, The ergodic relaxor core region is regarded as the ferroelectric phase, and the nonergodic shell region is regarded as a relaxor phase, using the relaxor model developed in Chap. 5. The variance of the RF for the relaxor matrix $\Delta = 2.3\ \mathrm{kV\,mm^{-1}}$. For the ferroelectric phase, there is no RF, *i.e.*, $\Delta = 0\ \mathrm{kV\,mm^{-1}}$.

Based on the measured geometric dimensions of the core-shell microstructure and assuming that the region deeper than 500 nm from the surface was not affected by the biased-tip, a nonergodic spherical core of radius 250 nm surrounded by an ergodic matrix of size 500 nm × 1,000 nm (depth × width) was simulated. A coherent interface was assumed between the core

and the shell. Due to the rotational symmetry, the system could be reduced to a 2-dimensional configuration on the x-z plane for the simulation. The size of the finite elements should be fine enough to resolve the domain structure and to guarantee the precision of the results. Moreover, symmetric boundary conditions were set on the left and right edges of the box to ensure that the simulation represents a periodic case without the boundary effect. The reference potential at the bottom boundary was set to zero, and the electric field was assumed to undergo a linear potential decrease with distance between the top and bottom boundaries. The simulations revealed not only the polarization state of the sample surface but also the domain configuration beneath the surface. For vertical poling, a + 10 V dc voltage difference was applied, similar to the PFM experiment. A triangular potential vs. time distribution was employed for simulating the increase and the subsequent decrease of the electric field. The quasi-static simulation was performed with a potential increment of 0.1 V. Before poling, the equilibrium polarization distribution in the nonergodic core and the ergodic shell was awaited.

The configuration of a core-shell microstructure was included in the model (see Fig. 7.3h). The initial equilibrium state is shown in Fig. 7.3a, in which large domains are present in the nonergodic core and a structure with small-sized domains in the ergodic shell. The corresponding potential distribution (Fig. 7.3b) shows a potential with small variations around zero throughout the x-z plane. The random field distribution caused by the chemical disorder leads to some hot spots with relatively high/low potential. The electric field loading was then applied by a potential difference between the top and bottom boundary. Core and shell regions were fully poled under the peak potential of +10 V (Fig. 7.3c), with the polarization pointing downwards. The corresponding distribution of electric potential difference indicates an almost homogeneous gradient (Fig. 7.3d). After the external potential is switched off, polarization and potential distribution represent the remanent state (Fig. 7.3e,f): the poled polarization state in the shell region relaxes to a random state, whereas the field-induced ferroelectric domains within the core region remain poled. The potential distribution also relaxes to zero, except for the bottom of the core-shell interface (red area). The downward polarization of the ferroelectric domain in the nonergodic core can thus not be compensated for and leads to the presence of a positive charge beneath the core. As a result, the potential beneath the core is higher (red area) than the one in the rests of the simulated areas (see Fig. 7.3f). The remanent domain configuration is symbolized as polarization vectors (see Fig. 7.3g), in which black frames enclose regions with predominantly lateral-oriented domains (red and green arrows), which is consistent with the lateral domain phenomenon observed in the PFM experiment (*cf.* Fig. 7.2). The local poling induced a transition from the relaxor states (ergodic – shell, nonergodic – core) to the ferroelectric state in both regions, which was completely reversible in the shell area but caused the core region to be permanently in the ferroelectric state. These findings and the appearance/growth of a ferroelectric domain with a polarization direction perpendicular to the applied field into the ergodic shell are in good agreement with the results obtained by the phase-field simulation

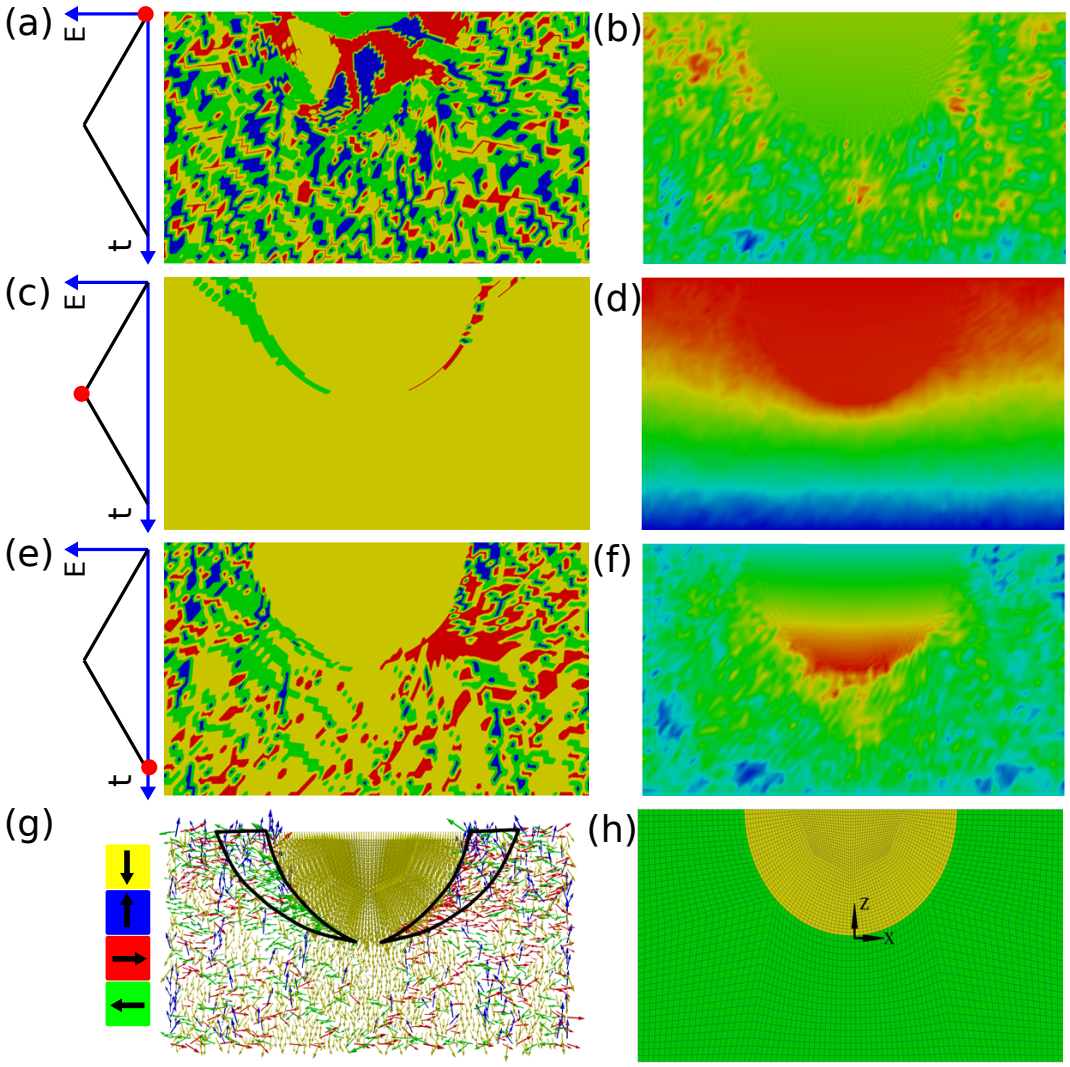

FIGURE 7.3: *Phase-field simulation of a formation of the field-induced polarization.(a,c,e,g) Domain distribution and respective orientation of the polarization. (b,d,f) Corresponding potential distribution. (h) Designed mesh in the x-z plane through the sample volume miming the geometry of a core-shell structure. The simulation evolves from the initial state (a,b) over a maximum potential state (c,d) to the remanent state (e,f,g). The detailed polarization vector distribution at the remanent state is shown in (g). The marked regions (black frames) have a preferential lateral domain orientation. The colours in (a,c,e) and the arrows in (g) represent four polarization orientations of the domains: yellow - down; blue - up; green - left; red - right. The length of the arrows indicates the magnitude of the polarization vector. The three upper charts on the left illustrate the different stages of the simulation, in which red dots denote the current applied field and the y- and x-axis represent the electric potential and the time step, respectively.*

based on a core-shell microstructure model. It revealed a strong gradient in the electric potential at the interfacial area, which causes the nucleation and propagation of an in-plane polarization

The phase-field simulation demonstrated that the observed evolution of field-induced lateral domains via PFM is due to a compensation of polarization charges at the core-shell interface beneath the sample surface. Transferring these local observations within an individual grain to the macroscopic scale offers new insights into the performance and functionality of actuators: actuator applications require materials with large, recoverable, electric field-induced strain outputs executed at low fields. Macroscopically, an actuator based on a relaxor runs from the remanent state (generally negligible) to a state where the entire material is held at the ferroelectric state by a sufficiently strong external electric field and returns back to the remanent state. Interpreting this cycle microscopically implies that the relaxed ergodic state of each shell is switched to a ferroelectric state and back. The core, in contrast, permanently remains in the ferroelectric state. Upon switching on the external field, the alignment of the "pivot points" at the interface from a polarization direction perpendicular to the applied field to a parallel configuration facilitates the domain orientation in the shell. These pivot points originate from the residual high potential at the interface and generate domain nuclei at the adjacent shell. These nuclei aggregate and the surrounding PNRs align with the external electric field. Consequently, the energy barrier for the completion of the phase transition in the shell is reduced. Conversely, upon switching off the external field, the pivot points reduce the mechanical stress at the interface that was established during the relaxation process between the polarized core and the arbitrarily distributed shell polarization. The formation of the lateral polarization thus plays the central role in the compensation of the polarization and strain mismatches between the core and the shell during the poling and relaxation processes.

7.2.3 A short conclusion

Our phase-field simulation provides detailed information of the evolution of the domain configuration in the core-shell structure. Thus it provides theoretical insight into the mechanism behind the macroscopic functionality of core-shell piezoceramics. The interaction of the polarization between the core and the shell results in a local potential plateau beneath the core. Thus change the behavior of the shell domains. It may provide a hint on explaining the unique electromechanical properties found in this core-shell structure. In the next section, the flexoelectric model is introduced within the framework of the phase-field ferroelectric model. It is then utilized for the study of the DLNRs of core-shell BNT-ST nanoparticle at extreme temperature.

7.3 Phase-field flexoelectric-ferroelectric model

The flexoelectric effect is a general property of materials with any crystal symmetry. It is merely discussed in ferroelectric materials until a series of work by Ma and Cross [111, 112,

229, 230, 231]. Some phenomenon (*e.g.*, the twinned domain structure in Ref. [120] and domain switching with mechanical loading in Ref. [232, 233]) in ferroelectrics cannot be explained without the consideration of flexoelectricity, especially in nanoscale. Here briefly the basic concepts of the direct and converse flexoelectric effects are introduced within the framework of thermodynamics.

7.3.1 Thermodynamics

Theoretical work on flexoelectricity dates back to the work by Mashkevich and Tolpygo [234, 235], who first proposed the effect in the study of the liquid crystal. It was further proposed by Kogan [114], the first phenomenological theory on the polarization effect by the strain gradient. The thermodynamic formulation of the flexoelectric effect described in this subsection is based on the work of Maranganti *et. al.* [236] and Tagantsev *et al.* [109, 237]. The thesis focuses on the static bulk flexoelectric effect. The *dynamic flexoelectric effect* and *surface flexoelectricity* are beyond the scope of this thesis.

Within the assumption of the centrosymmetric crystal structure of the dielectrics and energy only involves up to the first derivative of polarization and strain, the most general expression for the internal energy density, can be written as:

$$\mathscr{U} = \frac{1}{2}\tilde{a}_{ij}P_iP_j + \frac{1}{2}\tilde{b}_{ijkl}P_{i,j}P_{k,l} + \frac{1}{2}c_{ijkl}\varepsilon_{ij}\varepsilon_{kl} + \underbrace{\tilde{d}_{ijkl}P_{i,j}\varepsilon_{kl} + \tilde{g}_{ijkl}P_i\varepsilon_{kl,j}}_{\text{flexoelectric contribution}} + \frac{1}{2}\tilde{h}_{ijklmn}\varepsilon_{ij,k}\varepsilon_{lm,n}. \quad (7.1)$$

One may note that $\tilde{a}_{ij}$ is the second order reciprocal dielectric susceptibility, $\tilde{b}_{ijkl}$ is the analogy to the gradient energy coefficient κ shown in Eq. (D.2e), c_{ijkl} is the well-known elasticity tensor. The last term $\frac{1}{2}\tilde{h}_{ijklmn}\varepsilon_{ij,k}\varepsilon_{lm,n}$ represents the strain-gradient energy coefficient[1] commonly appeared in strain gradient elasticity (SGE) theory. [238, 239] The remaining coefficients $\tilde{d}_{ijkl}$ and $\tilde{g}_{ijkl}$ correspond to higher order electro-elastic couplings which do not appear in the classical continuum elastic dielectric theory. The former tensor $\tilde{d}_{ijkl}$, which was first introduced by Mindlin [240] represents the coupling effect between the polarization gradient and strain (or inverse flexoelectricity), while the latter tensor $\tilde{g}_{ijkl}$ represents the coupling effect between the polarization and strain gradient (or direct flexoelectricity). These two coefficients can be measured by a designed experiment. [112].

The flexoelectric-related energy density thus can be written as:

$$\mathscr{H}^{flexo} = \tilde{d}_{ijkl}P_{i,j}\varepsilon_{kl} + \tilde{g}_{ijkl}P_i\varepsilon_{kl,j} \quad (7.2)$$

[1] see Eq. 5.1 in Mindlin [238] the full expression of the elastic energy.

It can be reformulated as:

$$\begin{aligned}\mathscr{H}^{flexo} &= \tilde{d}_{ijkl}P_{i,j}\varepsilon_{kl} + \tilde{g}_{ijkl}P_i\varepsilon_{kl,j} + \frac{1}{2}\left(\tilde{d}_{ijkl}P_i\varepsilon_{kl,j} - \tilde{d}_{ijkl}P_i\varepsilon_{kl,j} + \tilde{g}_{ijkl}P_{i,j}\varepsilon_{kl} - \tilde{g}_{ijkl}P_{i,j}\varepsilon_{kl}\right) \\ &= \frac{1}{2}\underbrace{(\tilde{d}_{ijkl} - \tilde{g}_{ijkl})}_{\text{flexocoupling tensor}}(P_{i,j}\varepsilon_{kl} - P_i\varepsilon_{kl,j}) + \frac{1}{2}(\tilde{d}_{ijkl} + \tilde{g}_{ijkl})(P_i\varepsilon_{kl,j} + P_{i,j}\varepsilon_{kl}) \\ &= \frac{1}{2}f_{ijkl}(P_{i,j}\varepsilon_{kl} - P_i\varepsilon_{kl,j}) + \frac{1}{2}(\tilde{d}_{ijkl} + \tilde{g}_{ijkl})(P_i\varepsilon_{kl})_j\end{aligned} \tag{7.3}$$

The Helmholtz free energy density takes strain and electric displacement (or polarization) as the independent variable:

$$\mathscr{H}(P_i, \varepsilon_{ij}, P_{i,j}, \varepsilon_{ij,k}) = \mathscr{U} - \sigma_{ij}\varepsilon_{ij} \tag{7.4}$$

The stationary solutions $P_i(x_i)$ and $\varepsilon_{ij}(x_i)$ for Eq. (7.3) can be given by:

$$\begin{cases} \dfrac{\delta\int_V \mathscr{H}\,\mathrm{d}v}{\delta P_i} = 0 \\ \dfrac{\delta\int_V \mathscr{H}^{flexo}\,\mathrm{d}v}{\delta\varepsilon_{ij}} = 0 \end{cases} \tag{7.5}$$

The integral of the last terms in Eq. (7.3) yields:

$$\int_v \frac{1}{2}(\tilde{d}_{ijkl} + \tilde{g}_{ijkl})(P_i\varepsilon_{kl})_j \mathrm{d}v = \frac{1}{2}(\tilde{d}_{ijkl} + \tilde{g}_{ijkl})\int_s P_i\varepsilon_{kl}n_j\mathrm{d}s \tag{7.6}$$

It is transformed to the surface of the sample. Thus for the static bulk flexoelectric model, this contribution can be safely neglected. The Euler-Lagrange equation can be applied to solve Eqs. 7.5:

$$\begin{cases} \dfrac{\partial\mathscr{H}}{\partial P_i} - \left(\dfrac{\partial\mathscr{H}}{\partial P_{i,j}}\right)_{,j} = 0 \\ \dfrac{\partial\mathscr{H}}{\partial\varepsilon_{ij}} - \left(\dfrac{\partial\mathscr{H}}{\partial\varepsilon_{ij,k}}\right)_{,k} = 0 \end{cases} \tag{7.7}$$

Replacing the notation $\tilde{a}_{ij}$ by more commonly used notation χ_{ij}^{-1}, and ignoring the polarization gradient and strain gradient energy part, one obtains the following equations:

$$\begin{cases} \chi_{ij}^{-1}P_j - f_{ijkl}\varepsilon_{kl,j} = 0 \\ \sigma_{ij} - c_{ijkl}\varepsilon_{kl} - f_{ijkl}P_{k,l} = 0 \end{cases} \tag{7.8}$$

Compare Eq. (7.8) with the constitutive equations (4.22) and (4.37) for elastic and linear dielectric material, one finds

$$E^{flexo} = f_{ijkl}\varepsilon_{kl,j} \tag{7.9}$$

is the electric field contributed by the strain gradient through the flexoelectric effect and

$$\sigma^{flexo} = f_{ijkl} P_{k,l} \tag{7.10}$$

is the stress contributed by the polarization gradient through the inverse flexoelectric effect. From the above description, one can write one energy term which represents both the direct and inverse flexoelectric effect,

$$\mathscr{H}^{flexo} = \frac{1}{2} f_{ijkl} (P_{i,j} \varepsilon_{kl} - P_i \varepsilon_{kl,j}) \tag{7.11}$$

where $f_{ijkl} = \frac{1}{2}(d_{ijkl} - g_{ijkl})$. In some literatures [241, 130], the coupling coefficient μ_{ijkl} is used which links the strain gradient with the electric field. This coefficient can be related to f_{ijkl} by multiplying the material susceptibility,

$$\mu_{ijkl} = \chi_{km} f_{ijml}. \tag{7.12}$$

Inserting Eq. (7.11) into Eq. 5.19, one obtains the full expression of the electric enthalpy of a ferroelectric material with flexoelectric effect taking into account,

$$\mathscr{H}_2 = \mathscr{H}^{ela} + \mathscr{H}^{ele} + \mathscr{H}^{piezo} + \mathscr{H}^{sep} + \mathscr{H}^{grad} + \mathscr{H}^{flexo}. \tag{7.13}$$

7.3.2 The influence of flexoelectric effect in ferroelectrics

In this subsection, the influence of the flexoelectric effect in the ferroelectric behaviors is discussed analytically, including the hysteresis and the phase transition. In order to simplify the discussion, the above thermodynamics model is reduced to 1-dimensional. The typical ferroelectric material BTO is taken as the example. Hence, only the first order phase transition is discussed here. The parameters are listed in Table 7.1.

The 1-d Landau free energy with flexoelectric effect can be written as:

$$\mathscr{F} = \alpha_1(T)P^2 + \alpha_{11}P^4 + \alpha_{111}P^6 + \alpha_{1111}P^8 - \frac{1}{2} f P \nabla \varepsilon, \tag{7.14}$$

where $\alpha_1(T) = \alpha_0(T - T_c)$ Here the Landau coefficients are adopted from Li *et al.* [242]. The spontaneous polarization P_s takes the value where $\mathscr{F}$ is minimized:

$$\frac{\partial \mathscr{F}}{\partial P}\Big|_{P=P_c} = \alpha_0(T - T_c)P_c + 4\alpha_{11}P^3 + 6\alpha_{111}P^5 + 8\alpha_{1111}P^7 - \frac{1}{2} f \nabla \varepsilon = 0 \tag{7.15}$$

By minimizing the Helmholtz free energy $\mathscr{H} = \mathscr{F} - EP$, one obtains the P-E hysteresis loop:

$$\frac{\partial \mathscr{H}}{\partial P} = \alpha_0(T - T_c)P_c + 4\alpha_{11}P^3 + 6\alpha_{111}P^5 + 8\alpha_{1111}P^7 - \frac{1}{2} f \nabla \varepsilon - E = 0 \tag{7.16}$$

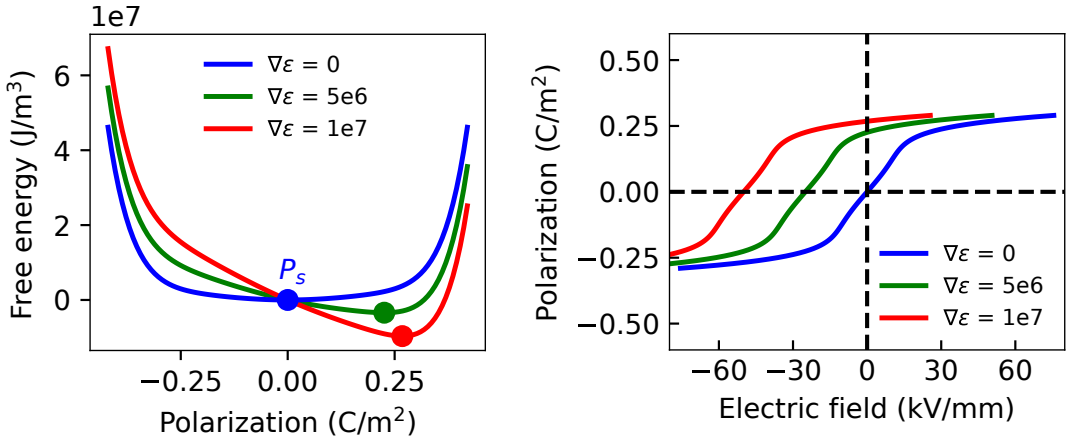

Figure 7.4: *The influence of strain gradient on the Landau energy and P-E loop for BTO in the paraelectric phase.*

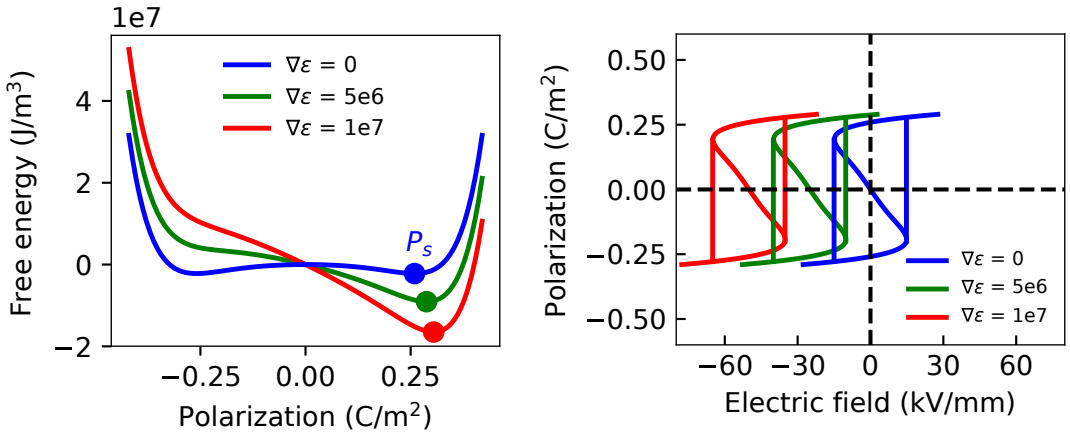

Figure 7.5: *The influence of strain gradient on the Landau energy and P-E loop for BTO in the ferroelectric phase.*

Figure 7.4 shows the Landau energy and the P-E loop of BTO single crystal at 500 K, which is above the Curie temperature. The flexocoupling coefficient f is set to 5 V. The three sets of lines show the results with different strain gradient with the value of 0, 5×10^6 and 1×10^7. As the strain gradient increases, the spontaneous polarization increases from zero to a finite number, and the P-E loop is shifted to the left. It indicates that the flexoelectric effect induces a bias electric field proportional to $f\nabla\varepsilon$.

Figure 7.5 shows the Landau energy and the P-E loop of BTO single crystal at 300 K. BTO is in ferroelectric phase at this temperature with $P_s \approx 0.26\ \mathrm{C\,m^{-2}}$ The flexocoupling coefficient f is also set to 5 V. The three sets of lines show the results with different strain gradient. As the strain gradient increases, the spontaneous polarization slightly increases, and the P-E loop is also shifted to the left. Compared with Fig. 7.4, there is no abrupt change of P_s. In order to better illustrate the temperature and strain gradient influence on the shifting of P_s. The spontaneous polarization P_s as a function of strain gradient at different temperatures are presented in Fig. 7.6. For the temperature below and above T_c, the spontaneous polarization changes roughly linear with the strain gradient. One interesting result is found at the temperature slightly above T_c. The spontaneous polarization abruptly increased to a large value (around $0.2\ \mathrm{C\,m^{-2}}$) at small strain gradient value, which indicates that there is a flexoelectric-induced paraelectric-ferroelectric phase transition.

	Value	Unit
α_1	4.124(T-388) $\times\ 10^5$	$\mathrm{C^{-2}m^2N}$
α_{11}	-209.7 $\times\ 10^6$	$\mathrm{C^{-4}m^6N}$
α_{111}	129.4 $\times\ 10^7$	$\mathrm{C^{-6}m^{10}N}$
α_{1111}	3.863 $\times\ 10^{10}$	$\mathrm{C^{-8}m^{14}N}$

Table 7.1: *Landau parameters for barium titanate from the collective work of Chen [243].*

The above-mentioned phenomenon can be explained by the Landau-Devonshire theory introduced in Sec. 4.4. For the first order phase transition, there is another feature temperature T_1 above T_c, as shown in Fig. 7.6. When the temperature is above T_1, the local free energy minimum for some nonzero polarization state vanishes. Paraelectric phase is the only stable state. While for the temperature between T_1 and T_c, there are local free energy minima besides $P = 0$. This energy is larger than $\mathscr{F}(P = 0)$, which indicates that there is a metastable state besides the paraelectric phase. If there is an external electric field stimulus, the material can be transferred to such metastable state. If there is a strain gradient generated in the material, the flexoelectric-induced field can overcome the energy barrier and induce a ferroelectric phase. This phase transition can thus only occur between T_c and T_1, which indicates that the flexoelectric effect may play an important role near the phase transition temperature.

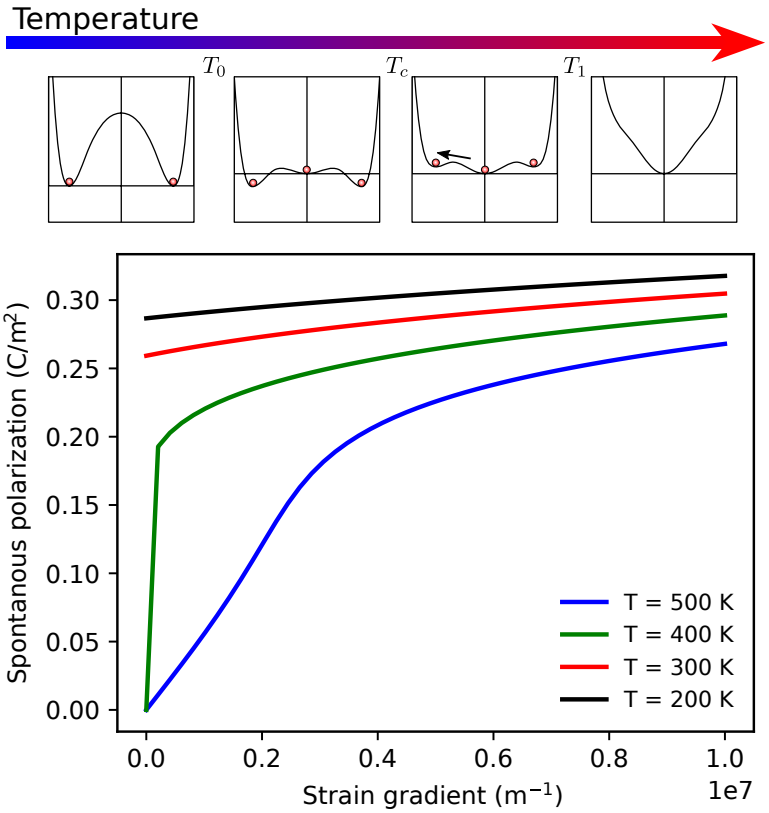

Figure 7.6: *The influence of strain gradient and temperature on the spontaneous polarization.*

7.3.3 Benchmark test of the flexoelectric model

By implementing the flexoelectric energy term Eq. (7.11) into the electric enthalpy, the constitutive equations and the evolution equation can be modified accordingly:

$$\sigma_{ij} = \frac{\partial \mathscr{H}_2}{\partial \varepsilon_{ij}} = c_{ijkl}(\varepsilon_{kl}^{tot} - \varepsilon_{kl}^{0}) - e_{ijk}E_k + f_{klij}P_{k,l} \tag{7.17}$$

$$D_i = -\frac{\partial \mathscr{H}_2}{\partial E_i} = \epsilon_{ij}E_j + e_{jki}(\varepsilon_{jk}^{tot} - \varepsilon_{jk}^{0}) + P_i \tag{7.18}$$

and

$$-\beta \dot{P}_i = -\frac{\partial \mathscr{H}_2^{sep}}{\partial P_i} - G_{ijkl}P_{k,lj} - f_{ijkl}\varepsilon_{kl,j}. \tag{7.19}$$

The above equations can be implemented into the finite element method program. To validate our model, the simulation results are first compared with the analytical solution with a simple boundary value problem. If one set ε_{ij}^{0} (here due to the spontaneous polarization in

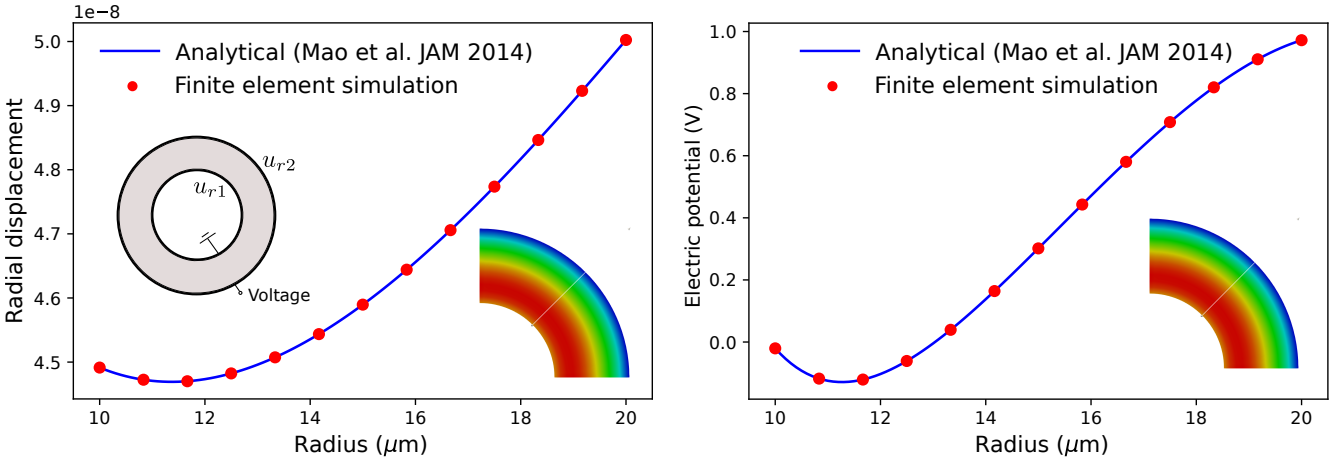

FIGURE 7.7: *Comparison between the analytical solution and the finite element solution of a BVP for a dielectric ring with the consideration of flexoelectric effect.*

ferroelectrics), e_{ijk} (from piezoelectric contribution) and G_{ijkl} to zero, the model is degraded to a linear dielectric model with flexoelectric effect:

$$\begin{cases} \sigma_{ij} = c_{ijkl}\varepsilon_{kl} + \epsilon f_{ijkl}E_{k,l} \\ D_i = \epsilon E_i + \epsilon f_{ijkl}\varepsilon_{kl,j} \end{cases} \tag{7.20}$$

Considering a BVP of a 2-dimensional ring: the inner radius of the sample is 10 μm and 20 of outer radius. The voltage difference between the inner surface and outer surface is 1 V. The radial displacement of the inner surface is 4.5 nm and 5.0 nm of the outer surface. The analytical solution is given by Mao *et al.* [126]. The comparison between the analytical solution and the simulation results are shown in Fig. 7.7. The simulation results agree well with the analytical solution. The minimum values of the potential and radial displacement do not locate at the boundary but within the ring, which differs from the pure dielectric material of which potential and radial displacement increases monotonically.

The next example shows the polarization switching of the ferroelectric thin film under a concentrated force. The example is motivated by the experimental work of Lu *et al.* [233] In 2012, Lu *et al.* successfully accomplished a 180° domain switching of a BTO thin film by pure mechanical loading. The mechanical loading is realized by an insulated AFM tip. The PFM phase image proved the reversal of the ferroelectric polarization. The flexoelectric-based simulation shows that there is a large strain gradient generated in the region near the tip. If the flexoelectric effect is considered, the strain gradient-induced local electric field points out of the surface. This flexoelectric-induced (or strain gradient-induced) electric field acts as the driving force for the 180° domain switching. However, that model is only a mechanical model and there is no electromechanical coupling evolved. The flexoelectric induced field is directed calculated based on the strain distribution.

Here the ferroelectric-flexoelectric phase-field is utilized to calculate the polarization distribution under the same condition shown in the experiment of Lu *et al.* Here the strain distribution

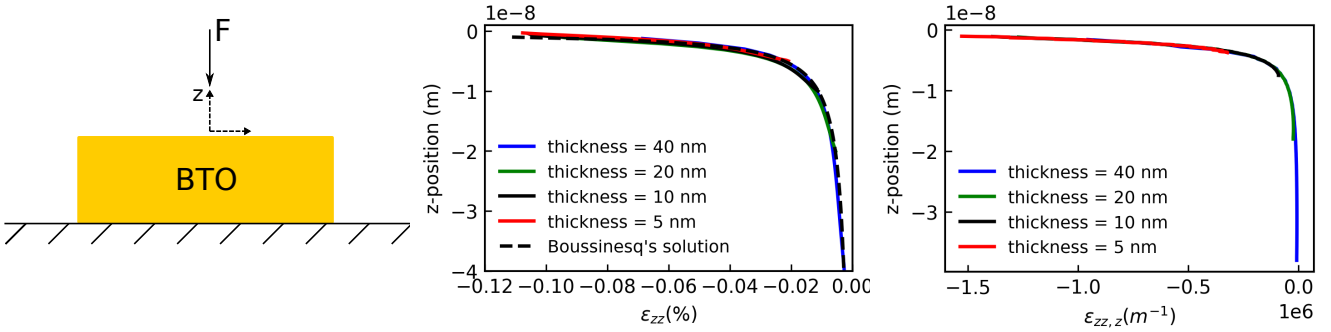

Figure 7.8: *The strain and strain gradient distribution of a BTO thin film under a concentrated force.*

of the elastic thin film under a concentrated force is calculated to see whether the concentrated force can be successfully implemented in our finite element model. The distribution of strain in the z-direction, ε_{zz}, and the corresponding strain gradient $\varepsilon_{zz,z}$ is calculated for the thin films with different thickness. It is compared with the Boussinesq's solution, which provides the distribution of the strain under a concentrated force in a semi-infinite plane. The results are shown in Fig. 7.8. The analytical solution differs with the simulation only at the region near the concentrated force. The reason is that the concentrated force in the finite element method is implemented by a surface integral over a small region. This concentrated force is just an approximation. However, for the rest of the thin film, the simulation agrees well with the analytical solution. In the following step, the same concentrated force is applied to the ferroelectric thin film. As one can see from both the analytical solution and the numerical results, the strain gradient induced by the 20 N loading near the surface is around $-1 \times 10^6\,\mathrm{m}^{-1}$.

Figure 7.9 shows the domain configuration of a BTO thin film under a concentrated force. The initial polarization is set to be $(P_x, P_z) = (0, P_0)$. For the case where the concentrated force is 5 N (Fig. 7.9b), the polarization does not change its direction. In the region near the concentrated force, the magnitude of the polarization decreases, due to both the linear piezoelectric effect and the flexoelectric effect. However, this driving force is not large enough to trigger the domain switching. Fig. 7.9c shows the final domain configuration with the 20 N concentrated force. The flexocoupling coefficient is set to 0, which means that only piezoelectric effect is considered here. From Fig. 7.9c, one finds that the piezoelectric effect can only induce a non-180° domain switching (in this particular case, from z-direction to x-direction). This result agrees with the argument shown in Fig. 2.4. For the case with only flexoelectric effect evolved, (see Fig. 7.9d). The flexoelectric effect induced a 180° domain switching. Considering that the flexocoupling coefficient f_{11} is positive and the strain gradient $\varepsilon_{zz,z}$ is negative, the flexoelectric induced polarization component P_z^{flexo} is therefore negative. The flexocoupling coefficient for BTO varies from different literatures. [112, 244, 122] Here, the experimentally measured flexoelectric coefficient of BTO by Ma *et al.* is adopted. [112] From Eq. 7.9, the flexoelectric-induced polarization with 20 N concentrated force is around $0.27\,\mathrm{C\,m}^{-2}$. ($P^{flexo} = 0.27\mu\mathrm{C\,m}^{-1}$

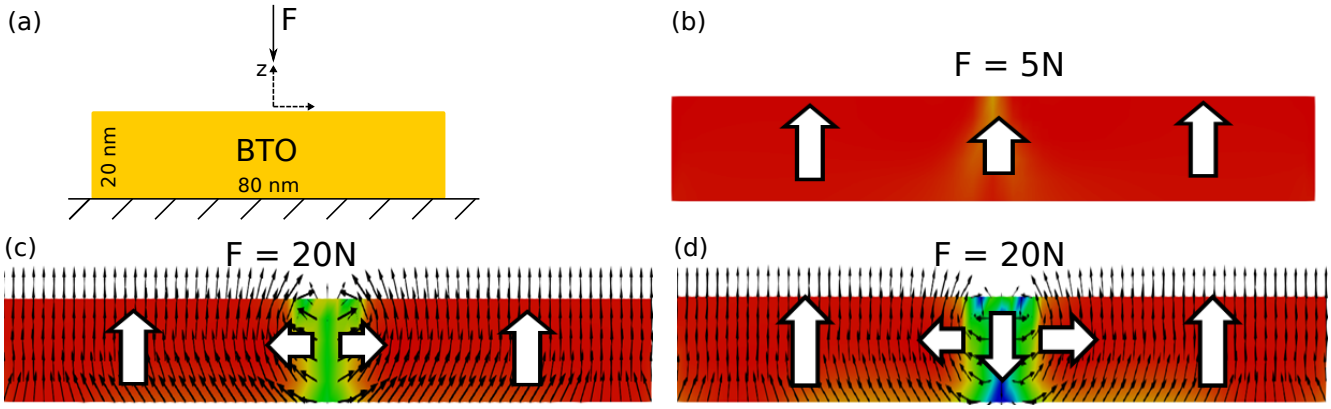

Figure 7.9: *Domain configuration of a BTO thin film under a concentrated force.*

$\times\, 1 \times 10^6\,\mathrm{m}^{-1} = 0.27\,\mathrm{C\,m}^{-2}$) The flexoelectric-induced polarization and the spontaneous polarization of BTO is in the same magnitude. That explains the final domain configuration shown in Fig. 7.9d, which also agree with the pure elastic simulation by Lu *et al.* [233]

The above phase-field flexoelectric model along with the ferroelectric framework is utilized in Sec. 7.4 to explain the abnormal domain-like nanoregions observed at an extreme temperature in a BNT-25ST nanoparticle.

7.4 Flexo-induced domain-like nanoregions in the core-shell structure

In this section, a possible explanation of observed abnormal phenomenon – DLNRs in the BNT-25ST material system is demonstrated. The observed DLNRs is abnormal, in the sense that the operation temperature is extreme (800 °C), and the sample is small (a nanoparticle with a radius of around 50 nm). It cannot be explained by the conventional ferroelectric or relaxor theory. The observed DLNRs is ascribed to the flexoelectric effect, and try to verify it by a designed experiment. The theory and the observed phenomenon are self-consistent.

7.4.1 Introduction

Materials with switchable polarization are indispensable in memory devices [245], sensors [246], actuators [247] and transducers [248]. As mentioned in Sec. 7.3, any dielectric material under a strain gradient presents flexoelectricity [120], which is especially relevant at the nanoscale [113]. Here, the BNT-25ST core-shell nanoparticles are synthesized via a solid-state chemical reaction directly inside a transmission electron microscope (TEM) and observed DLNRs up to an extreme temperature of 800 °C. This abnormal phenomenon is attributed to a chemically induced lattice strain gradient. The strain was generated by controlling the diffusion of Sr^{2+} cations to produce core-shell nanoparticles. By combined electrical biasing and temperature dependent *in situ* TEM together with phase-field simulations, the resulting strain gradient

and local polarization distribution within a single nanoparticle are analyzed. The analysis confirms that a local symmetry breaking, occurring due to a strain gradient (*i.e.*, flexoelectricity), accounts for switchable polarization beyond the conventional temperature range of existing polar materials. These series of experiments and simulations show that the polar nanomaterials can be obtained through flexoelectricity at extreme temperature by tuning the cation diffusion.

7.4.2 Experimental observation

In order to observe and manipulate a strain gradient at the nanoscale, the core-shell BNT-25ST nanoparticles are directly synthesized inside a TEM. The solid-state solution BNT-25ST was chosen as the model system for three reasons. First, BNT-25ST has a high dielectric constant, which gives rise to a high flexocoupling coefficient. Second, the Sr^{2+} diffusion can be accelerated or suppressed dramatically by modifying the A-site stoichiometry [249]. This renders an attractive system to tune cation diffusion and to generate a strain gradient without additional mechanical loading. Last, the nanoscale (∼100 nm) synthesis of particles makes it easier to generate large strain gradients.

A microelectromechanical (MEMS) based electro-thermal nano-chip is used for the *in situ* TEM experiments. The nano-chip consists of an encapsulated microheater and electrical biasing electrodes. A suspension of raw powders with a stoichiometry of 75 mol % $Na_{1/2}Bi_{1/2}TiO_3$-25 mol % $SrTiO_3$ was placed on a silicon nitride electron transparent window. The powders were heated using a defined temperature profile ramp based on the work of Koruza *et al.* [108]. With this approach, core-shell BNT-25ST nanoparticles are directly synthesized inside the TEM. In order to estimate the electric field and temperature distribution generated between the electrical biasing electrodes, a finite element analysis using COMSOL Multiphysics is presented by our colleagues in DENS solutions, Delft. The experimental setup is shown in Fig. 7.10.

Figures 7.10b and 7.10d show that the temperature and the applied electric field between the electrodes are homogeneous at the sample region. Using this experimental setup, it was possible to observe physical processes with atomic resolution while applying a temperature up to 800 °C and simultaneously setting a potential up to 100 V. This bias corresponds to an electric field up to 20 $kV\,mm^{-1}$ for electrodes separated by a 5 μm gap.

By using scanning transmission electron microscopy (STEM) in combination with energy dispersive X-ray spectroscopy (EDS), the core-shell BNT-25ST formation process can be *in situ* controlled at T = 300, 600 and 800 °C. After performing a careful structural analysis at 800 °C on several nanoparticles, the formation of DLNRs is observed. An exemplary single nanoparticle is shown in Fig. 7.11. DLNRs on the scale of few lattice spacings can be clearly recognized (Fig. 7.11a). It can be seen that they are similar to domain patterns commonly observed in ferroelectrics. [250] From a previous study on bulk BNT-25ST [27], it is known that nanodomains cease to exist around 350 °C. Thus, the DLNRs observed at 800 °C cannot be attributed to a

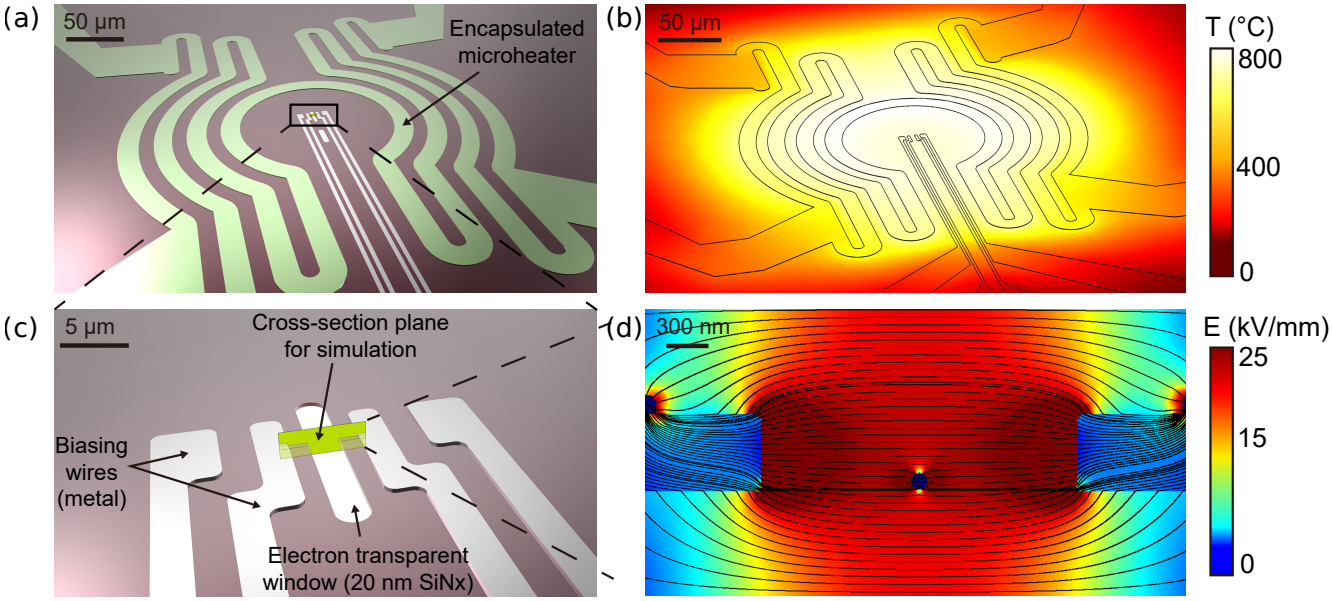

Figure 7.10: *Electro-thermal sample carrier for in situ transmission electron microscopy: (a) Schematics of the electro-thermal chip, including the set of biasing electrodes surrounded by the encapsulated microheater that is temperature controlled by Joule heating. (b) Corresponding simulated temperature distribution profile generated by the microheater. (c) Magnified view of the biasing wires region, showing a close-up of the 20* nm *thick electron transparent window and the four surrounding biasing wires. The green plane represents the cross-section where the sample is placed. (d) Finite element simulation of the electric field strength and the electric field lines over the cross-sectional plane indicated in (c). A nanoparticle was placed in the window area between the electrodes for modeling.*

long-range ferroelectric spontaneous polarization. Moreover, one might assume that they are related to the presence of PNRs in a relaxor state [251, 252]. A recent quantitative analysis demonstrated that the fraction of PNRs in BNT-6BT is negligible above 700 °C. [253] A detailed quantification of the PNRs in BNT-25ST is beyond the scope of this work. However, by comparing the temperature-electric field phase diagrams of BNT-25ST and BNT-06BT [227], t the existence of PNRs above 700 °C in BNT-25ST can be safely neglect due to its lower transition temperatures. The observed DLNRs are thus a consequence of other physical mechanisms.

The mechanical factor (*e.g.* strain distribution) could be one of the explain to the observed phenomenon. In the next step, the strain distribution within the particle is examined. Elemental EDS mapping revealed that the synthesized BNT-25ST nanoparticles exhibit a core-shell structure. The Sr^{2+} concentration increases towards the edge of the nanoparticles (Fig. 7.11b), while the other elements are homogeneously distributed (Fig. 7.11c-f). This is a direct consequence of the slow diffusion of the Sr^{2+} in stoichiometric BNT-25ST. A gradient of Sr^{2+} leads to a chemically induced lattice strain because of the differences in ionic radii of the A-site cations. This effect is usually referred to as the Vegard effect [254, 255]. In this case, the magnitude of the eigenstrain increases from the center to the edge. This eigenstrain influences the total strain distribution in the nanoparticles. As shown in recent work on strontium titanate, atomic scale measurements of local displacements due to the flexoelectric effect have been reported [256]. However, for the BNT-25ST nanoparticle system, the measurement of atomic-displacements for the whole nanoparticle is nontrivial. Nevertheless, a quantitative assessment of the total strain distribution by atomic-displacement mapping in small regions of interest is possible (see Fig. 7.12), which indicates large strain gradients within the single nanoparticle. The value of strain ranges from -0.2% to 0.2 % at the distance of 3.8 nm. By the strain analysis, the conclusion can be made that the DLNRs highlighted in the zoom-in image could either be a result of the non-polar lattice strain mismatch or originate from flexoelectricity as a consequence of the strain gradient.

7.4.3 Flexoelectric-ferroelectric simulation

7.4.3.1 Fitting the Landau parameters of BNT-25ST

In order to reveal the origin of the observed DLNRs, the flexoelectric model shown in Sec. 7.3 can be utilized. However, there is no Landau parameter available for BNT-25ST either from first principle calculation or from the experiments. In this subsection, the Landau parameters of BNT-25ST are derived from the based on the collected data from the published literature. This method can also be applied to other material systems.

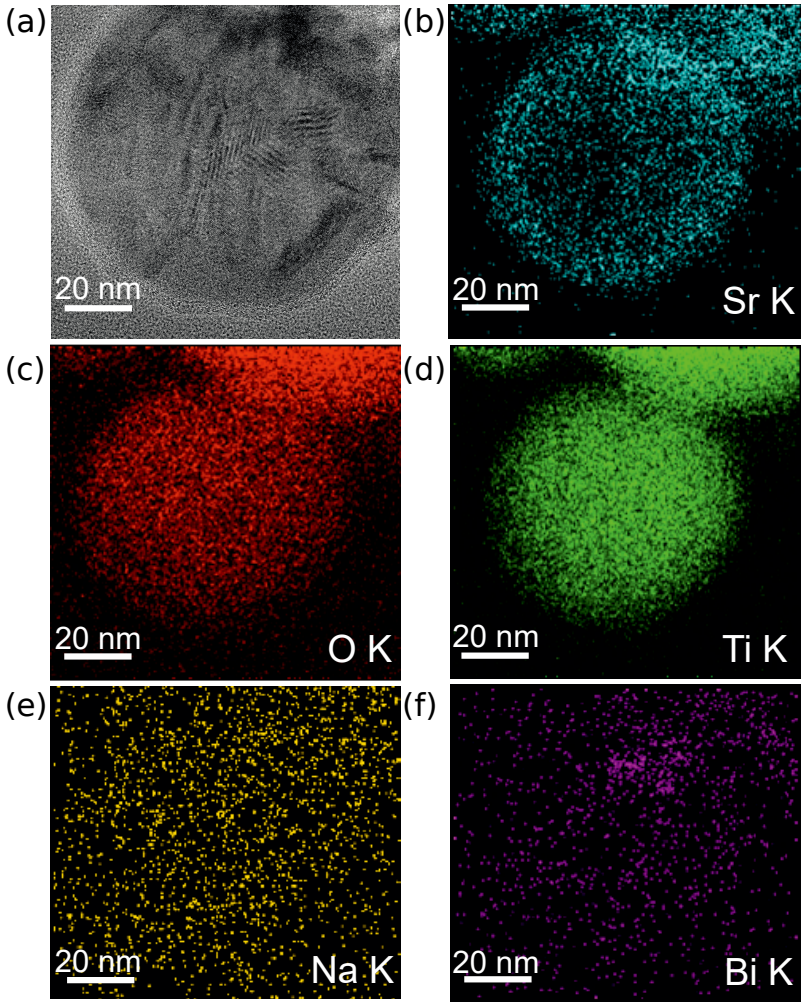

Figure 7.11: *In situ core-shell nanoparticle formation: (a) Bright-field TEM image of a core-shell nanoparticle with DLNRs. (b) Energy-dispersive X-ray spectroscopy elemental mapping shown Strontium ion (Sr^{2+}) diffusion. (c)-(f), Elemental maps of the remaining homogeneously distributed elements.*

Assume the Landau energy under mechanical stress-free boundary condition take the form of a sixth-degree polynomial

$$\mathscr{H}^{\text{sep}} = \alpha_1(P_1^2 + P_2^2) + \alpha_{11}(P_1^4 + P_2^4) + \alpha_{12}(P_1^2 P_2^2) + \alpha_{111}(P_1^6 + P_2^6) + \alpha_{112}(P_1^4 P_2^2 + P_1^2 P_2^4), \quad (7.21)$$

and in such a sixth-degree polynomial only the first coefficient α_1 is temperature dependent. For ferroelectrics, it is related to the permittivity by the Curie-Weiss law. In the paraelectric phase:

$$2\alpha_1 = \frac{\partial^2 \mathscr{H}^{\text{sep}}}{\partial P_1^2} = \frac{\partial E_1}{\partial P_1} = \frac{1}{\epsilon} = \frac{T - T_0}{C} = 2\alpha_0(T - T_0) \quad (7.22)$$

where T_0 is the Curie-Weiss temperature and C is the Curie constant. However, for relaxors (*e.g.*, BNT-25ST), the Curie-Weiss law is no longer valid. Instead, the permittivity follows:

$$\frac{1}{\epsilon} - \frac{1}{\epsilon_m} = \frac{(T - T_m)^\gamma}{C} \quad (7.23)$$

where γ is the diffusion factor which takes the value between 1 and 2. [51, 257] The permittivity-temperature graph is adopted from Gomah-Pettry *et al.* [222] and fit it to the above modified Curie-Weiss law, the results are shown in Fig. 7.13. The diffusion factor $\gamma = 1.004$, which means that the dielectric behavior at high frequency is more like a ferroelectric. As a simplification, γ is set to 1.0. The Landau coefficient is:

$$\alpha_0 = 5.14 \times 10^5 (T - 216). \quad (7.24)$$

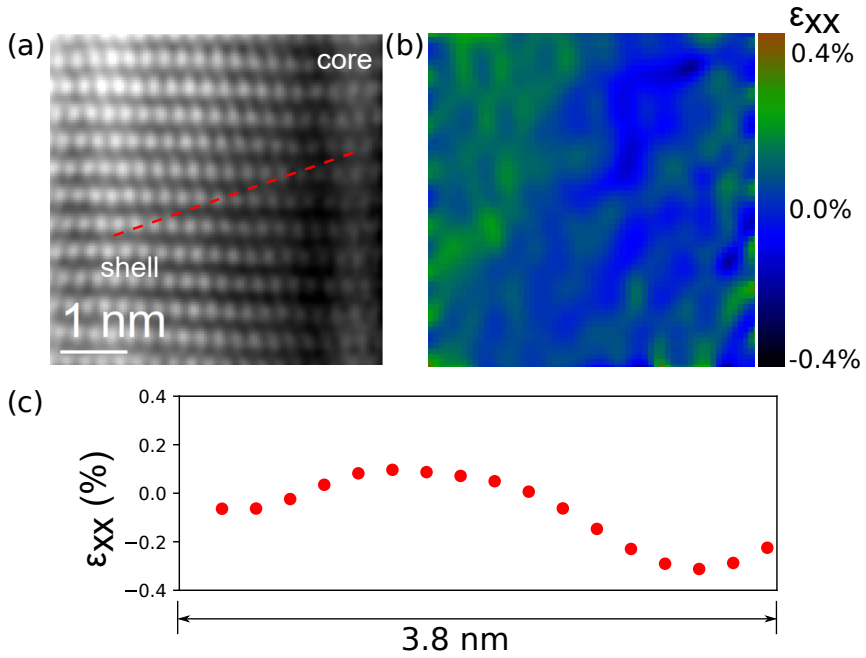

Figure 7.12: *(a) High-resolution TEM image of the core-shell interface denoted in figure 4a. (b) geometrical phase analysis (GPA) evaluation map, (c) The distribution of normal strain component ε_{xx} along the dashed line in (a).*

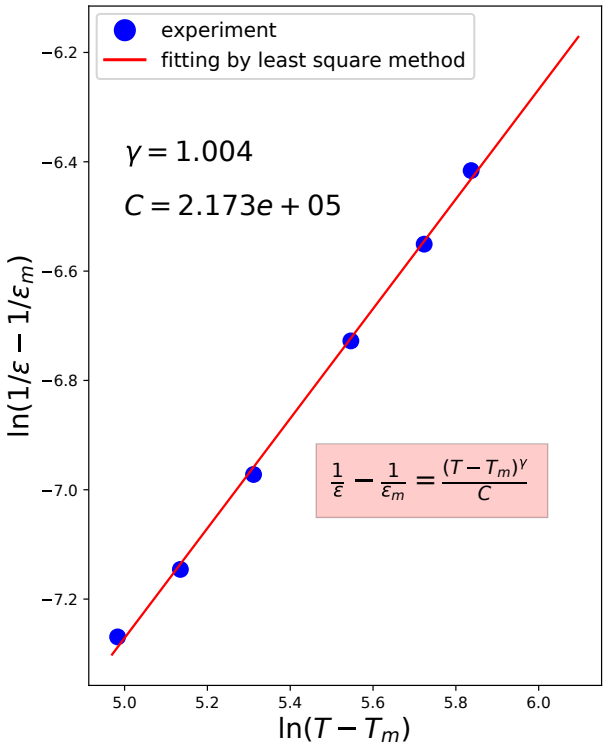

Figure 7.13: *Fitting the susceptibility as a function of temperature in logarithmic coordinates by using the modified Curie-Weiss law for BNT-25ST. Blue dot: experimental data from Jean-Richard G., et al. [222]; red line: fitting curve.*

Now consider the other Landau coefficients for BNT-ST. The coefficients α_{11} and α_{111} are related to the phase transition temperatures. At Curie temperature (Strictly speaking, there is no Curie temperature for relaxors. Here we use this terminology for convenience), the Landau energy for paraelectric phase and ferroelectric phase are the same, *i.e.*,

$$\alpha_0(T_c - T_0)P_{sc}^2 + \alpha_{11}P_{sc}^4 + \alpha_{111}P_{sc}^6 = 0 \tag{7.25}$$

where P_{sc} is the spontaneous polarization at T_c. On the other hand, at T_c,

$$\frac{\partial \mathscr{H}^{\text{sep}}}{\partial P}\Big|_{P=P_{sc}} = 2\alpha_0(T_c - T_0)P_{sc} + 4\alpha_{11}P_{sc}^3 + 6\alpha_{111}P_{sc}^5 = 0 \tag{7.26}$$

Combining the above two equations, one obtains:

$$T_c - T_0 = -\frac{\alpha_{11}^2}{2\alpha_{111}\alpha_0} \tag{7.27}$$

and

$$P_{sc}^2 = -\frac{\alpha_{11}}{2\alpha_{111}}. \tag{7.28}$$

The value of is obtained in the work by Krauss *et al.* [85]. The temperature with maximum permittivity T_m is regarded as the Curie temperature T_c. Inserting all these values to Eq. (7.27) and Eq. (7.28), one obtains $\alpha_{11} = -1.25 \times 10^{10}\,\text{C}^{-4}\text{m}^3\text{N}$ and $\alpha_{111} = 3.91 \times 10^{10}\,\text{C}^{-6}\text{m}^{10}\text{N}$. The value of α_{12} and α_{112} depends on the transition temperature between orthorhombic and tetragonal phases. For BNT-25ST, there is no such phase transition. According to Watanabe *et al.* [224], the rhombohedral-tetragonal phase transition temperature for BNT-25ST is 40°C. If one assumes that 40°C is the orthorhombic-tetragonal phase transition temperature, then:

$$\mathscr{H}^{\text{sep}}(P_1 = 0; P_2 = P_t) = \mathscr{H}^{\text{sep}}(P_1 = P_t; P_2 = 0) = \mathscr{H}^{\text{sep}}(P_1 = P_2 = P_o) \tag{7.29}$$

and

$$\frac{\partial \mathscr{H}^{\text{sep}}}{\partial P_1}\Big|_{P_1=P_2=P_o} = 2\alpha_0(T_c - T_0)P_o + 4\alpha_{11}P_o^3 + 6\alpha_{111}P_o^5 + 2\alpha_{12}P_o^3 + 6\alpha_{112}P_o^5 = 0 \tag{7.30}$$

where P_t and P_o are the components of the spontaneous polarization in one direction for the tetragonal and the orthorhombic phase, respectively. By solving these two relationships simultaneously, one obtains the value of $\alpha_{12} = 3.52{\times}10^{10}\text{C}^{-4}\text{m}^6\text{N}$ and $\alpha_{112} = -1.25{\times}10^{12}\text{C}^{-6}\text{m}^{10}\text{N}$. Till now, all the coefficients of the Landau energy up to 6th order are derived, which are listed in Table 7.2. Figure 7.14 shows the Landau energy as a function of P_1 and P_2 . The color indicates the Landau free energy $\mathscr{H}^{\text{sep}}$. Three temperatures were chosen, 100 °C (at the tetragonal phase) 200 °C (near Curie temperature) and 800 °C (the probing temperature of the experiments) for the phase-field simulations.

Coefficients	Value (T in Kelvin)
α_1 ($10^5 C^{-2} m^2 N$)	5.14(T-216)
α_{11} ($10^{10} C^{-4} m^6 N$)	-1.25
α_{12} ($10^{10} C^{-4} m^6 N$)	3.52
α_{111} ($10^{12} C^{-6} m^{10} N$)	3.91
α_{112} ($10^{12} C^{-6} m^{10} N$)	-1.250

Table 7.2: *Landau coefficients of BNT-25ST used for the phase-field simulation.*

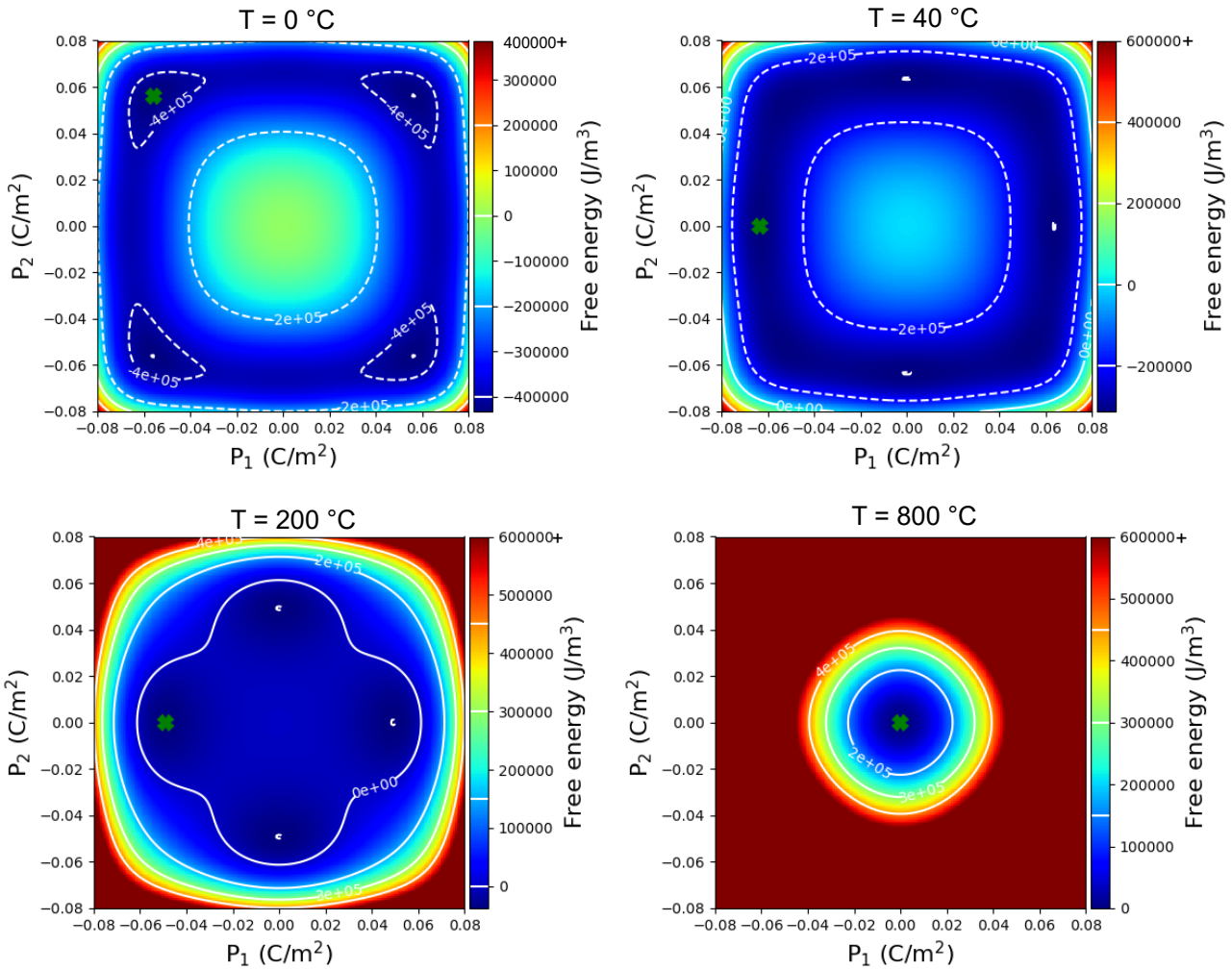

Figure 7.14: *The Landau energy as a function of the polarization by using the derived coefficients of BNT-25ST. The rhombohedral-tetragonal-cubic phase transition can be captured.*

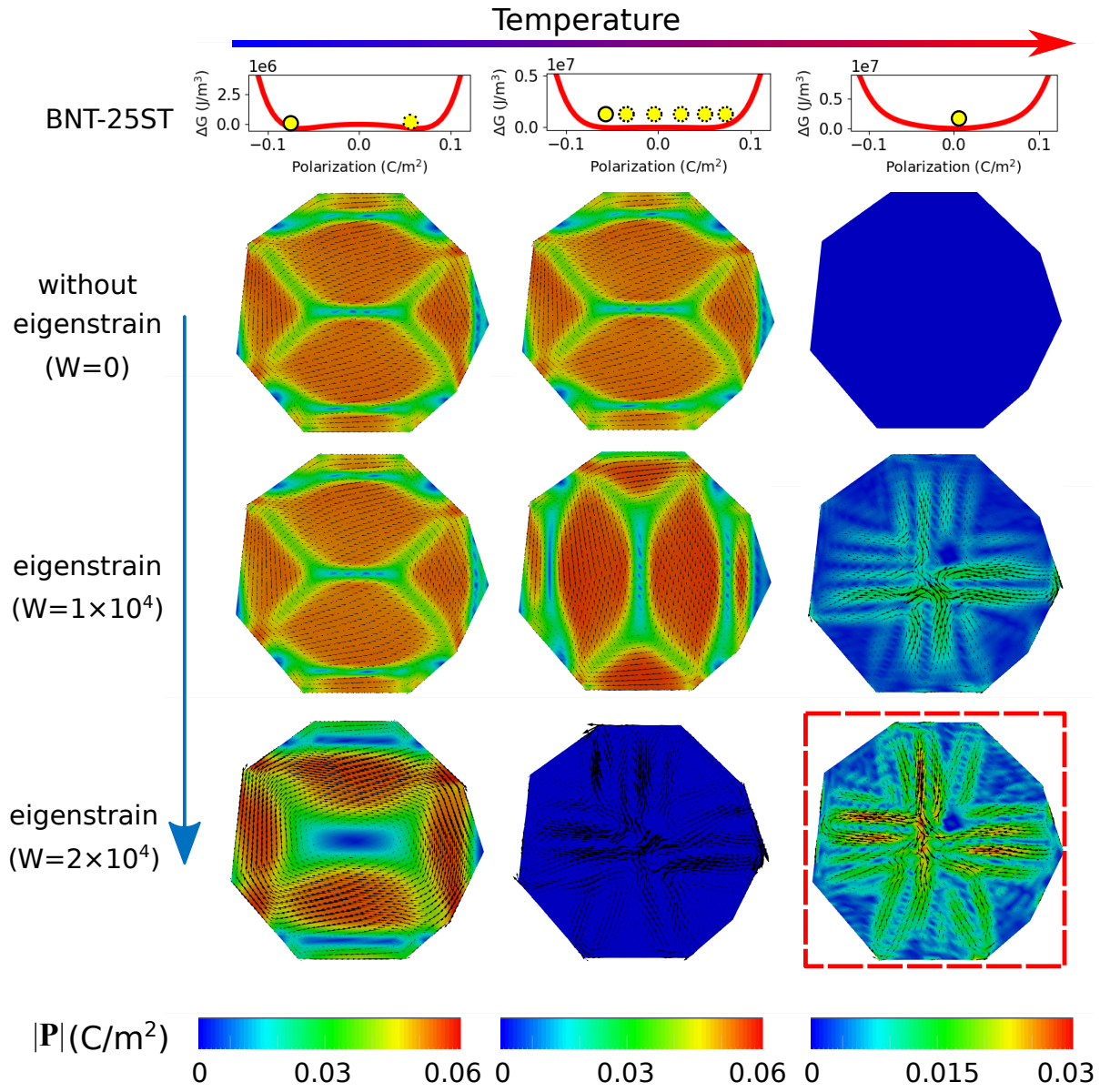

Figure 7.15: *Polarization distribution of a nanoparticle with BNT-25ST Landau coefficient at different temperatures and eigenstrain values.*

7.4.3.2 Ferroelectric-flexoelectric simulation results

In order to clarify the origin of the DLNRs shown in Fig. 7.11a, the finite element flexoelectric-ferroelectric phase-field simulations are performed. The experimentally observed shape and size of the nanoparticle was implemented in the simulation. Open-circuit [162] boundary conditions are assumed for the freestanding nanoparticle without contacting the biasing electrodes. According to the Vegard law [255], the lattice parameter is linearly changed with the constituent's concentration. The Vegard strain is treated as the eigenstrain [258, 259] in the phase-field simulation. The Sr^{2+} concentration is assumed to increase linearly from the center to the edge. Hence, the eigenstrain is set to increase from the center to the edge accordingly. The elastic energy is modified in the following form:

$$\mathscr{H}^{\text{ela}} = \frac{1}{2} c_{ijkl}(\varepsilon_{ij} - \varepsilon^0_{ij})(\varepsilon_{kl} - \varepsilon^0_{kl}), \tag{7.31}$$

and

$$\varepsilon^0_{ij} = \varepsilon^{0\text{P}}_{ij} + \varepsilon^{0-\text{ion}}_{ij} \tag{7.32}$$

where $\varepsilon^{0\text{P}}_{ij}$ is the eigenstrain induced by the spontaneous polarization and $\varepsilon^{0-\text{ion}}_{ij}$ is the eigenstrain induced from Sr^{2+} concentration. Based on the energy-dispersive X-ray spectroscopy elemental mapping shown in Fig. 7.14, Sr^{2+} concentration increases from the center to the boundary of the nanoparticle. For simulation, a linear increase of Sr^{2+} concentration is assumed. The resultant eigenstrain distribution is assumed to be:

$$\varepsilon^{0-\text{ion}}_{ij}(\mathbf{x}) = \|\mathbf{x} - \mathbf{x}^{\text{center}}\| W \delta_{ij}, \tag{7.33}$$

where $W\delta_{ij}$ describes the isotropic mismatch strain induced by the ion and takes a positive value since the radius of $Sr^{2+}$is larger than those of Bi^{3+} and Na^{+}. The symbols $\mathbf{x}$ and $\mathbf{x}^{\text{center}}$ position vector of the point under consideration and of the particle center, respectively.

With such implementation of the Vegard strain, one can simulate the polarization distribution with different eigenstrain (by tuning parameter W) at different temperature (by utilizing the temperature dependent Landau parameters). The results are shown in Fig.7.15. Three characteristic temperatures (T = 100 °C, 200 °C, and 800 °C, respectively) ranged from the tetragonal to cubic phase and three eigenstrain values are chosen for the simulation.

For the case with lower temperature and without eigenstrain, the typical domain structure is formed with both 180° and 90° domain walls. Since charge free boundary condition is set at the edge of the nanoparticle, the polarization is oriented parallel to the boundary. At higher temperature (T = 500 °C) the nanoparticle is still in the tetragonal phase and the spontaneous polarization slightly decreases compared to the case with T = 25 °C, where the energy barrier

$\mathscr{H}^{\text{barrier}}$ is lower. The domain structure remains almost the same. Above the Curie temperature (540 °C), no polarization can be seen since the energy minimum is located at P = 0 $\mathrm{C\,m^{-2}}$. When a lower eigenstrain is implemented (second row), the domain structure is modified by the heterogeneous strain. More domains are formed in the second row compared to the first row. However, in the cubic phase, since the strain increases from the core to the shell, the orientation of the strain gradient is radial-shaped. As a result, the polarization points radially and a "seastar-like" polarization pattern is generated.

When a higher eigenstrain is implemented (third row), the influence of the eigenstrain on the domain patterns at T = 25 °C is weak, while it is larger at T = 500 °C. It is mentioned above that the Landau energy barrier is lower at T = 500°C. This makes it easier to modify the domains by the external loading, *e.g.*, mechanical strain. As a result, a "seastar-like" polar nanoregion is formed. Here, a rough estimation of the flexocoupling energy for a BNT-25ST nanoparticle is given. The flexocoupling tensor f_{11} is set in the magnitude of 1 V. With the eigenstrain factor W = 2×10^4, the strain gradient is in the magnitude of $\times\ 10^5$. If the polarization is 0.06 $\mathrm{C\,m^{-2}}$, the flexocoupling energy $\mathscr{H}^{\text{flexo}} = 1 \times 10^5\,\mathrm{J\,m^{-3}}$ is in the same magnitude of $\mathscr{H}^{\text{barrier}}$. At higher temperature, the polarization distribution is the same as the one with low eigenstrain, but the magnitude of the polarization is higher.

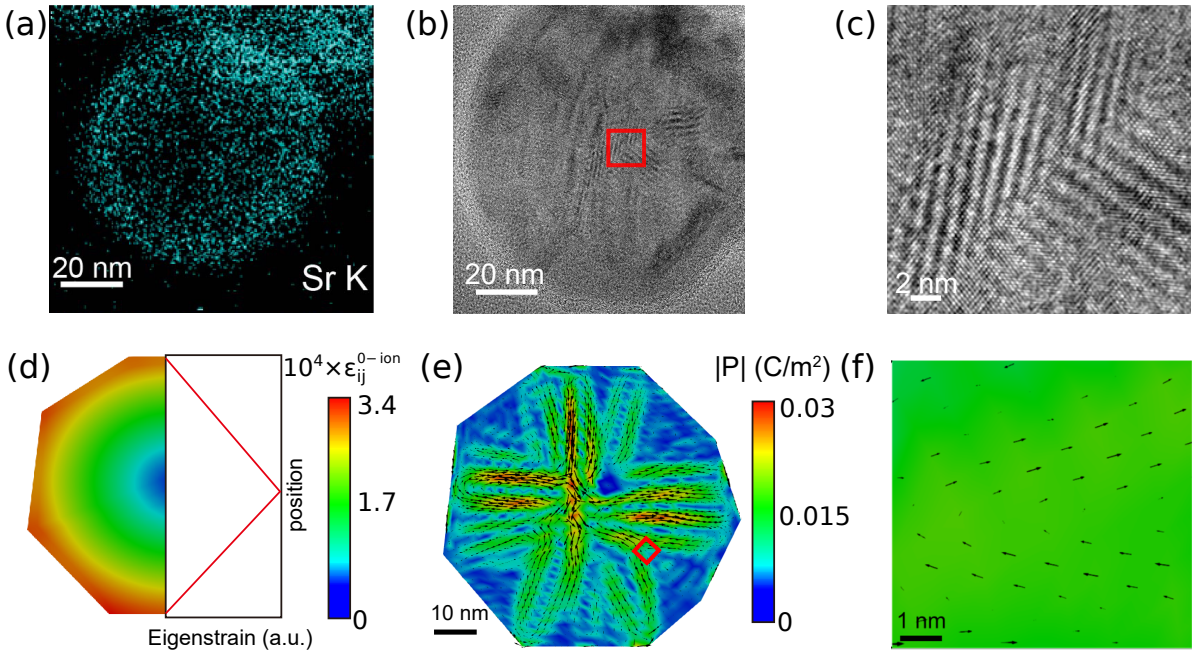

Figure 7.16: *Core-shell nanoparticle with DLNRs: (a) Elemental map showing the Sr^{2+} distribution. (b)-(c), TEM image of the core-shell nanoparticle and the enlargement of the red box region in (b). (d) The linear distribution of the eigenstrain along the radius direction according to (a). (e)-(f), Flexoelectric-ferroelectric phase-field simulation results of the polarization with its enlargement of the red box region, showing similar DLNRs as observed in the TEM images of (b) and (c).*

The strain mapping of the nanoparticle shown in Fig. 7.12 gives a rough estimate of the strain distribution and its gradient. Figure 7.10 shows that the operating temperature within the nanoparticle is around 800 °C. Therefore, the last image in Fig. 7.15 is used for the comparison with the experiments. The results are shown in Fig. 7.16.

In Fig. 7.16e, polarization vector has its highest magnitude at the center of the nanoparticle and decreases towards the edges. Multiple polarization vortices are also observed within the particles. As shown in In Fig. 7.16e, a distinct polarization configuration composed by a network of DLNRs is formed. The overall polarization configuration of the experiment and the simulation slightly differ, which may be due to the simplified strain distribution needed for the calculations. However, by comparison between the enlarged DLNRs observed in Fig. 7.16c and the polarization distribution shown in Fig. 7.16f, it is clear that they are analogous. In the phase-field simulation, Landau energy coefficients for the cubic phase were used, which indicates zero ferroelectric spontaneous polarization at the given temperature. Therefore, the DLNRs in the simulation can only be attributed to the high-order (gradient) coupling between mechanical strain and electric polarization. It should be noted that in the paraelectric phase, electrostriction still exists. The contribution of electrostriction to the polarization of the nanoparticles is two orders of magnitude lower as compared to the polarization induced by flexoelectricity. Hence, the electrostrictive effect is not responsible for the DLNRs and can be safely neglected. The phase-field simulation shows that flexoelectricity can lead to the observed DLNRs.

7.4.3.3 Field-induced polarization switching in DLNRs

To examine the origin of the DLNRs experimentally, electric field *in situ* TEM at 800 °C was performed. The core-shell structure of the *in situ* calcined BNT-25ST nanoparticle is revealed by the TEM image shown in Fig. 7.17. The image was obtained along a $[123]_{pc}$ type zone axis at 0 $kV\,mm^{-1}$ and the coherency of core and shell can be observed in the corresponding Fast Fourier Transforms (FFTs). As seen in the left inset of Fig. 7.17a, atomic resolution imaging was possible. Though not obvious in some regions in the shell, the DLNRs within the nanoparticle are observed, in which the selected regions are magnified to aid visualization in the top insets. The strain gradient across the core-shell interface denoted in Fig. 7.17a was quantified using a geometrical phase analysis (GPA). The analysis is operated in the software DigitalMicrograph™. The core and shell DLNRs are in a stable configuration at the given conditions.

While keeping the temperature constant at 800 °C, an electric field was applied in a defined direction (black arrows), as seen in the TEM images shown in Fig. 7.17b-c. The images were Wiener filtered for noise reduction [260]. The bottom insets show the corresponding FFTs of the core and shell areas, respectively. The bright spots observed in the FFT insets are analogous to Bragg spots observed in conventional electron diffraction patterns [261]. They correspond to crystallographic planes visible in the high-resolution TEM images. Variation in the FFTs can

be used to monitor the changes in the local crystal structure and related switching processes. The FFT patterns of the initial state (Fig. 7.17a) indicates that the particle is oriented along the $[1\,2\,3]_{pc}$ zone axis and features a pseudocubic crystal structure. The observed DLNRs are modified under the electric field shown in Fig. 7.17 b-c. The white arrow in the FFT inset of Fig. 7.17 marks the electric field induced splitting in the $(2\bar{2}0)$ reflex along the electric field. This indicates that there are two different polarities prevalent, *e.g.*, the dark and bright regions as shown in the top insets. The red arrow indicates a longer range ordering as expect for DLNRs. Changes in the domain-like configuration in the core and the shell become apparent at an electric field of 11.0 $kV\,mm^{-1}$ (Fig. 7.17b). Moreover, the formation of some DLNRs also occurs in the shell, as displayed in the top inset. Further increasing the electric field to 21.9 $kV\,mm^{-1}$ (Fig. 7.17c) leads to more pronounced DLNRs, as displayed in the top insets of core and shell. Besides, several DLNRs are nucleated within the shell.

In order to confirm the phenomena observed in Fig. 7.17a-c, phase-field simulations were carried out by implementing the corresponding electric field applied to the particle (Fig. 7.17d-f). The black arrows inside the simulated nanoparticle indicate the direction of the local polarization and the color scheme shows the magnitude of the polarization vector. The initial polarization configuration at zero electric field (Fig. 7.17d) changes with increasing electric field. Coalescence of nanoregions is clearly observed as the electric field increases. The evolution of the polarization under electric field can be explained by the superposition of the initial flexoelectricity-induced polarization and the one induced by the electric field. When the electric field is high enough, the polarization induced by flexoelectricity is overshadowed. This is reflected in the evolution of the FFTs. Both the experimental and simulation results suggest that the DLNRs observed at extreme temperature are polar. This implies that the flexoelectric effect is the main reason for the formation of the DLNRs. The further experiments under a reversal field prove that the process is fully reversible. The evolution and nucleation of DLNRs under bias electric field the non-polar lattice strain mismatch is not responsible for this phenomenon.

In order to critically assess our hypothesis, the samples with a different A-site doping (Bi^{3+}-deficient 75 mol % $Na_{1/2}Bi_{0.49}TiO_3$-25 mol % $SrTiO_3$) are synthesized through a conventional solid-state route. According to the work of Frömling *et al.*[249], this stoichiometry should lead to a much more homogeneous Sr^{2+} distribution within the nanoparticle rendering no core-shell structure and thus no noticeable strain gradient. The experimental setup and working environment were identical. Although some minor chemical heterogeneities can be observed (Fig. 7.18), the particles analyzed featured neither core-shell structure nor DLNRs. The lack of long-range chemical gradient in this 75 mol % $Na_{1/2}Bi_{0.49}TiO_3$-25 mol % $SrTiO_3$ results in negligible polarization.

One would argue that the role of oxygen vacancies under electric field should not be neglected. In recent work of Das *et al.* [262], controlled manipulation of oxygen vacancies in STO under mechanical loading was reported. In that case, flexoelectricity enabled the redistribution

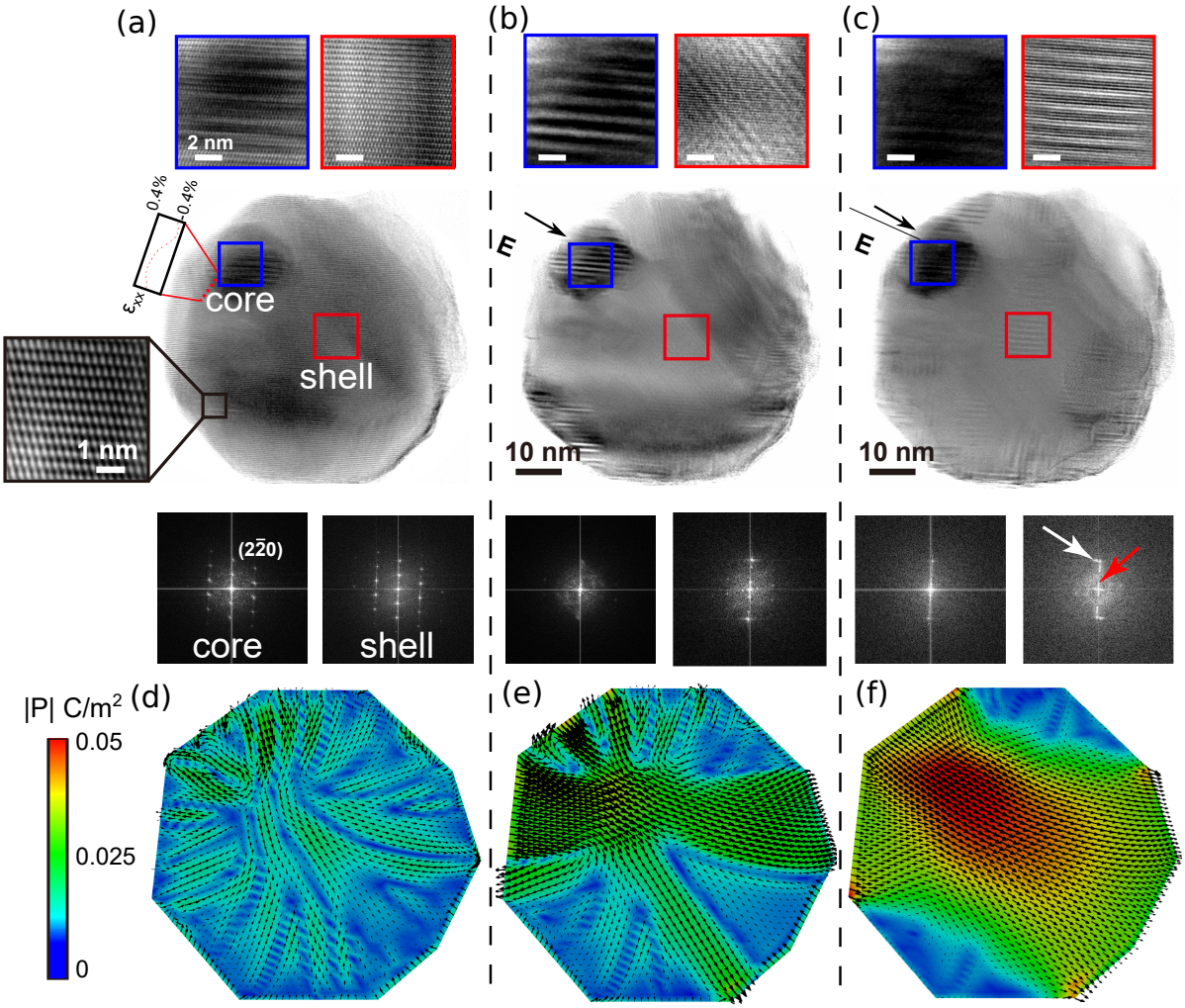

Figure 7.17: *Demonstration of switchable flexoelectric based polarization at extreme temperature: (a)-(c), TEM bright-field images taking along a* $[1\,2\,3]_{pc}$ *type zone axis, of a core-shell nanoparticle obtained at 800* °C *with electric field of 0* kV mm^{-1}*, 11.0* kV mm^{-1} *and 21.9* kV mm^{-1}*, respectively. The black arrows indicate the direction of the electric field. The local strain gradient along the core-shell interface is presented in (a). The top insets of a-c are magnifications showing DLNRs within the core and shell (a-c). The bottom insets of a-c show the Fast Fourier Transforms (FFTs) of core and shell along a* $[1\,2\,3]_{pc}$ *type zone axis. The white arrow indicates an electric field-induced splitting in the* $(2\bar{2}0)$ *reflex along the electric field indicating that there are two different polarities prevalent. The red arrow indicates a longer range ordering as expect for DLNRs. (d)-(f), Simulated domain patterns under the corresponding electric field. The color map indicates the polarization magnitude, while the black arrows the polarization vector.*

of oxygen vacancies. In our case, the oxygen vacancies may similarly influence the strain distribution and therefore the polarization by the flexoelectric effect. However, the resistivity of BNT-25BT bulk samples is relatively high even at 800 °C and it was not possible to measure the standard semi-circles expected in Nyquist plots. In situ TEM measurements of such defects with atomic resolution at 800 °C would be even more demanding. These tasks can be accomplished in the future.

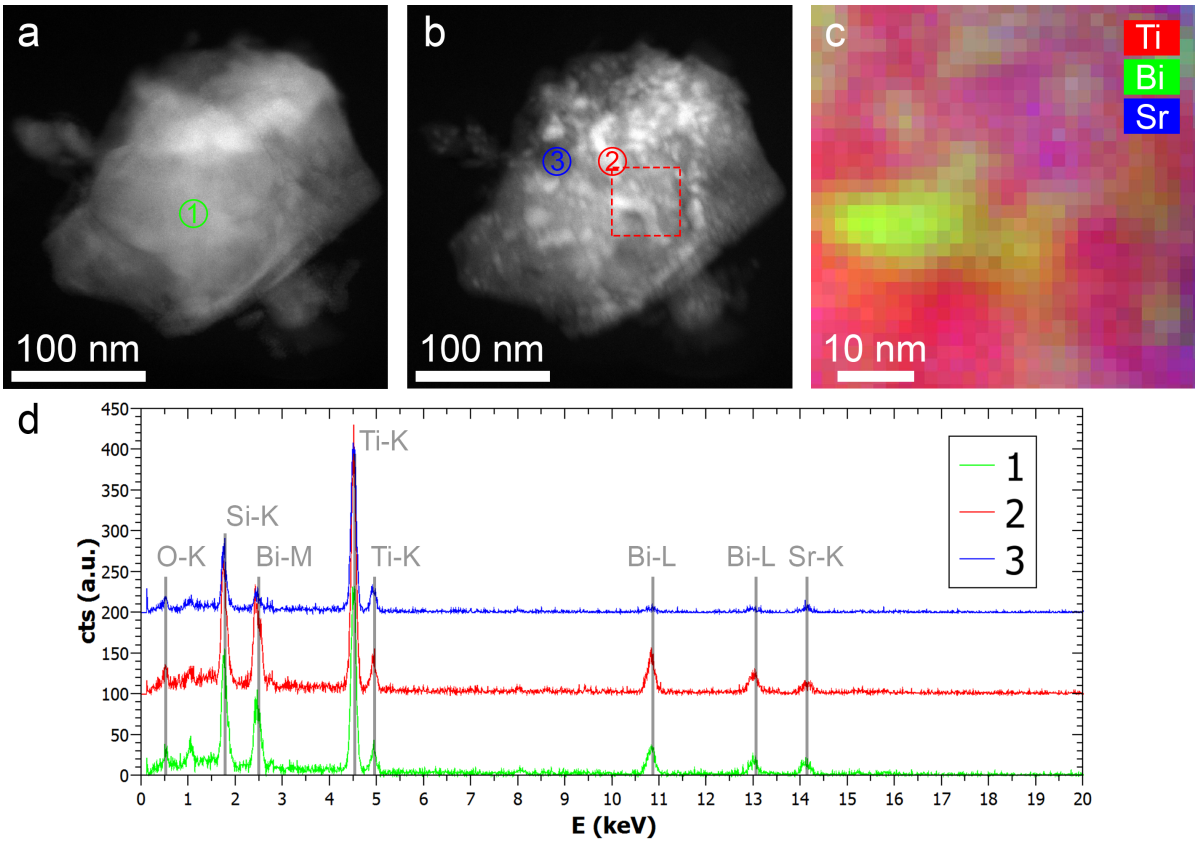

Figure 7.18: *Z-contrast STEM image of a Bi-deficient BNT-25ST nanoparticle taken (a) before heating (b) after 10 min at 800 °C. (c) RGB color map of the red box area in (b). (d) Energy-dispersive X-ray spectra at the marked points in (a) and (b).*

7.4.4 A brief summary

Through a combined experimental and phase-field modeling approach, the nanoscale flexoelectricity at extreme temperature by tuning cation diffusion is reported and explained. BNT-25ST core-shell nanoparticles with a Sr^{2+} chemical gradient were used as a model system to tune local strain by controlled ionic diffusion. The *in situ* synthesis route yielded core-shell nanoparticles that exhibit domain-like nanoregions at 800 °C and were found to be in a stable configuration. Electric field and temperature dependent *in situ* TEM together with phase-field flexoelectric simulations provide a detailed description and explanation of this phenomenon. Our results indicate that the polarization distribution is a direct consequence of nanoscale flex-

oelectricity and that it can be switched by an applied electric field. By comparing our results for samples with differing Bi deficiencies, the importance of a chemical gradient to generate strain and flexoelectric induced polarization at high temperature is affirmed. This contribution should motivate the study and the development of other high-temperature flexoelectric nanomaterials.

Chapter 8

Conclusions and Outlook

8.1 Conclusions

In this thesis, the phase-field model for relaxor ferroelectrics is built based on the random field theory. It is further utilized to reveal the properties of ferroelectric/relaxor composites, including the layered composites and the core-shell structures.

Due to the complexity of both the phenomenon and the relaxation mechanism, the phase-field models for relaxor ferroelectrics are rare. Here, inspired by Imry and Ma, the random field is introduced to the existed ferroelectric model. It was shown in Chap. 5 that the implementation of the random field can successfully reflect the short-range disorder in relaxor, and therefore some typical features found in relaxors. To be specific, the miniaturization of the domain can be captured with the implementation of the random field, and the macroscopic P-E loops are greatly influenced by it.

For the "incipient"-type relaxor, there is a nonpolar-polar phase transition under the electric field. Hence a new relaxor model is established In Chap. 6, with the modified phase-field relaxor models, it is possible to investigate the large-signal piezoelectric response in the relaxor/ferroelectric layer composites. By applying an averaging process, the parameters used for each end-member of the ferroelectric/relaxor layer composite is determined. The simulations on the trilayer composite show that the overall response of the layered composite is the combination effect of mechanical coupling and the polarization coupling. For small unipolar loading ($E_{\max} = 4\ \mathrm{kV\,mm^{-1}}$), the enhancement of large-signal response can be found at FE content of 30 %, which agrees with previous experimental observations. The further simulation with different interphase layers shows that both lateral strain coupling and charge at the interface between composite layers influence the large-signal electromechanical response in a complex manner.

In Chap. 7, the properties and functionalities of core-shell structure in relaxor ferroelectrics are investigated. The material system BNT-25ST is used as the representative research object. Two cases are studied: one at room temperature and the other at 800 °C. At room temperature, the domain structure around the core behaves differently from the normal ferroelectrics. By the poling process operated by piezoelectric force microscopy, the evolution of the polarization can be captured in real time. The phase-field simulations shown that there is a high potential

region beneath the core, which is responsible for the laterally aligned polarization in the shell around the core region. At 800 °C, the BNT-25ST nanoparticle is observed by a transmission electron microscopy. It is found that the domain-like nanoregions at such a high temperature and the nanoregions can be switched by the external field. This phenomenon is ascribed to the flexoelectric effect. To study this effect, a flexoelectric model based on the current phase-field ferroelectric framework is established. Phase-field simulation shows a similar arrangement of polarization distribution to the experiments.

The above simulations show that the phase-field model serves as an efficient tool to analysis and predict the evolution of the microstructure (domain and domain wall) in ferroelectric materials. By using the averaging process, it can also be used for the macroscopic behavior analysis, in which the electromechanical coupling effect can be intrinsically considered. The phase-field simulation can hence explain the observed phenomena, *e.g.*, domain miniaturization in relaxors (Fig. 5.3), lateral remnant domain structure around the core in BNT-25ST (Fig. 7.2), abnormal domain-like nanoregions at extreme temperature (Fig. 7.11a) *etc.*, obtain information that is difficult for the experiments, *e.g.*, the potential distribution beneath the core (Fig.7.3f), and predict the material behaviors, *e.g.*, the best ratio of FE/RE in layered composite (Fig. 6.8) and large-signal response with different interfaces (Fig. 6.11).

8.2 Outlook

The phase-field model is established and successfully adopted to help the experimenters to have a deeper understanding the material behaviors in relaxors. However, there are still plentiful of unsettled questions and challenges, deserving more intense investigations.

In the layered composite structure, the grain boundary plays an important role in the overall microscopic behavior. The material properties at the grain boundary are different from the grain, in the sense of elastic modulus, permittivity, leak voltage *etc.* Although several attempts are made in modeling the grain boundary in ferroelectrics/relaxors (*e.g.*, in the work of Choudhury *et al.* [263] the coherent interfaces are assumed between different grains, while Weng *et al.* [180] assumes that the grain boundary behaves like a dielectric with higher permittivity), a more precise and accurate description of grain boundary is needed. With such a model, many problems, such as the influence of grain size on the hysteresis, the charge effect near the grain boundary can be investigated.

The domain structure near the core-shell structure in BNT-25ST is studied. However, the connection between the laterally aligned domains and the enhancement of the piezoelectric response in such core-shell structure needs further investigation both experimentally and theoretically. One major challenge is that the behaviors of the core-shell structure can be greatly influenced by the characterization techniques. For instance, the PFM characterization of the sample will inevitably change the domain configuration. If different factors (*e.g.*, mechanical

coupling effect, strain mismatch between the core and the shell *etc.*) can be separately studied, it will help to understand the unique electromechanical response in the core-shell structure. Based on this, a better design strategy for the relaxor-type piezoceramics can be expected.

The observed domain-like nanoregions found in TEM at extreme temperature is explained by our flexoelectric-ferroelectric phase-field model. However, the oxygen vacancy is not discussed in the model. Defects, such as oxygen vacancies will have an impact on the polarization and the dielectric response. Several questions are raised here: (1) Do the oxygen vacancies exist in this diffuse process of Sr^{2+} and how are they distributed? (2) How do they change with the temperature? (3) What is the influence of the oxygen vacancy on the relaxor behaviors, such as the shifting of the peak in the permittivity curve? (4) Can we manipulate them? Either mechanically or electrically? It is an interesting topic for not only the ferroelectric community but also the whole condense matter community.

The model shown in the thesis is able to give a static response of the relaxors under external mechanical loading and electric loading. Nonetheless, one of the main features of relaxors is its relaxation process. The models developed by Refs. [17, 18] and the one shown here does not reflect such a relaxation property.

In summary, even though a lot of work has been done, more efforts should be given to gain a deeper understanding of relaxor ferroelectric. The current phase-field relaxor model can also be extended with the consideration of more influential factors, *e.g.*, thermo-fluctuations, defects, and dynamics of PNRs. The flexoelectric effect in relaxors is also a promising field to explore.

Bibliography

[1] KM Rabe, CH Ahn, and JM Triscone. *Physics of ferroelectrics: a modern perspective*. Vol. 105. Springer Science & Business Media, 2007.

[2] C Zhou and DM Newns. “Intrinsic dead layer effect and the performance of ferroelectric thin film capacitors”. In: *Journal of Applied Physics* 82.6 (1997), pp. 3081–3088.

[3] A Tombak et al. “Voltage-controlled RF filters employing thin-film barium-strontium-titanate tunable capacitors”. In: *IEEE Transactions on Microwave Theory and Techniques* 51.2 (2003), pp. 462–467.

[4] T Mikolajick et al. “FeRAM technology for high density applications”. In: *Microelectronics Reliability* 41.7 (2001), pp. 947–950.

[5] Innovative Research and Products. *Piezoelectric actuators and motors - global markets and market trends*. Tech. rep. Innovative Research and Products, 2010.

[6] European Commission. “Regulation (EC) No 1907/2006 of the European Parliament and of the Council of 18 December 2006 concerning the Registration, Evaluation, Authorisation and Restriction of Chemicals (REACH), establishing a European Chemicals Agency, amending Directive 1999/45/EC and repealing Council Regulation (EEC) No 793/93 and Commission Regulation (EC) No 1488/94 as well as Council Directive 76/769/EEC and Commission Directives 91/155/EEC, 93/67/EEC, 93/105/EC and 2000/21/EC”. In: *Off. J. Eur. Union* 396 (2006), pp. 374–375.

[7] LE Cross. “Relaxor ferroelectrics: an overview”. In: *Ferroelectrics* 151.1 (1994), pp. 305–320.

[8] CW Ahn et al. “A brief review on relaxor ferroelectrics and selected issues in lead-free relaxors”. In: *Journal of the Korean Physical Society* 68.12 (2016), pp. 1481–1494.

[9] LE Cross. “Relaxor ferroelectrics”. In: *Ferroelectrics* 76.1 (1987), pp. 241–267.

[10] Y Imry and SK Ma. “Random-field instability of the ordered state of continuous symmetry”. In: *Physical Review Letters* 35.21 (1975), p. 1399.

[11] V Westphal, W Kleemann, and MD Glinchuk. “Diffuse phase transitions and random-field-induced domain states of the "relaxor" ferroelectric $PbMg_{1/3}Nb_{2/3}O_3$”. In: *Physical Review Letters* 68.6 (1992), p. 847.

[12] D Viehland et al. “Dipolar-glass model for lead magnesium niobate”. In: *Physical Review B* 43.10 (1991), p. 8316.

[13] CM Landis. “Non-linear constitutive modeling of ferroelectrics”. In: *Current Opinion in Solid State and Materials Science* 8.1 (2004), pp. 59–69.

[14] AK Soh, YC Song, and Y Ni. “Phase Field Simulations of Hysteresis and Butterfly Loops in Ferroelectrics Subjected to Electro-Mechanical Coupled Loading”. In: *Journal of the American Ceramic Society* 89.2 (2006), pp. 652–661.

[15] BX Xu et al. “Micromechanical analysis of ferroelectric structures by a phase field method”. In: *Computational Materials Science* 45.3 (2009), pp. 832–836.

[16] N Liu, Y Su, and GJ Weng. “A phase-field study on the hysteresis behaviors and domain patterns of nanocrystalline ferroelectric polycrystals”. In: *Journal of Applied Physics* 113.20 (2013), p. 204106.

[17] D Wang et al. “Modeling Abnormal Strain States in Ferroelastic Systems: The Role of Point Defects”. In: *Physical Review Letters* 105 (20 Nov. 2010), p. 205702.

[18] F Li et al. “The origin of ultrahigh piezoelectricity in relaxor-ferroelectric solid solution crystals”. In: *Nature communications* 7 (2016), p. 13807.

[19] DE Dausch et al. “PLZT-based multilayer composite thin films, part I: Experimental investigation of composite film structures”. In: *Ferroelectrics* 177.1 (1996), pp. 221–236.

[20] DE Dausch et al. “PLZT-based multilayer composite thin films, part II: Modeling of the dielectric and hysteresis properties”. In: *Ferroelectrics* 177.1 (1996), pp. 237–253.

[21] C Groh, W Jo, and J Rödel. “Tailoring strain properties of (0.94-x) $Bi_{1/2}Na_{1/2}TiO_3$–0.06 $BaTiO_3$–x$K_{0.5}Na_{0.5}$Nb O $_3$ ferroelectric/relaxor composites”. In: *Journal of the American Ceramic Society* 97.5 (2014), pp. 1465–1470.

[22] C Groh et al. “Relaxor/Ferroelectric Composites: A Solution in the Quest for Practically Viable Lead-Free Incipient Piezoceramics”. In: *Advanced Functional Materials* 24.3 (2014), pp. 356–362.

[23] H Zhang et al. “Large strain in relaxor/ferroelectric composite lead-free piezoceramics”. In: *Advanced Electronic Materials* 1.6 (2015).

[24] A Ayrikyan et al. “Investigation of residual stress in lead-free BNT-based ceramic/ceramic composites”. In: *Acta Materialia* 148 (2018), pp. 432–441.

[25] A Ayrikyan et al. “Multilayer lead-free piezoceramic composites: Influence of co-firing on microstructure and electromechanical behavior”. In: *Journal of the American Ceramic Society* 100.8 (2017), pp. 3673–3683.

[26] BS Rawal, M Kahn, and WR Buessem. “Grain core-grain shell structure in barium titanate-based dielectrics”. In: *Advances in ceramics* 1 (1981), pp. 172–88.

[27] M Acosta, W Jo, and J Rödel. “Temperature-and Frequency-Dependent Properties of the 0.75 $Bi_{1/2}Na_{1/2}TiO_3$–0.25 $SrTiO_3$ Lead-Free Incipient Piezoceramic”. In: *Journal of the American Ceramic Society* 97.6 (2014), pp. 1937–1943.

[28] M Acosta et al. “Core–shell lead–free piezoelectric ceramics: current status and advanced characterization of the $Bi_{1/2}Na_{1/2}TiO_3$–$SrTiO_3$ system”. In: *Journal of the American Ceramic Society* 98.11 (2015), pp. 3405–3422.

[29] ME Lines and AM Glass. *Principles and applications of ferroelectrics and related materials*. Oxford university press, 1977.

[30] Y Xu. *Ferroelectric materials and their applications*. Elsevier, 2013.

[31] B Jaffe. *Piezoelectric ceramics*. Vol. 3. Elsevier, 2012.

[32] JA Gonzalo and B Jiménez. *Ferroelectricity: The Fundamentals Collection*. John Wiley & Sons, 2008.

[33] WJ Merz. “The Dielectric Behavior of $BaTiO_3$ Single-Domain Crystals”. In: *Physical Review* 75.4 (1949), p. 687.

[34] K Aizu. “Polarization, pyroelectricity, and ferroelectricity of ionic crystals”. In: *Reviews of Modern Physics* 34.3 (1962), p. 550.

[35] J Valasek. “Piezo-electric and allied phenomena in Rochelle salt”. In: *Physical review* 17.4 (1921), p. 475.

[36] B Matthias and A Von Hippel. “Domain structure and dielectric response of barium titanate single crystals”. In: *Physical Review* 73.11 (1948), p. 1378.

[37] H Blattner et al. “Domain structure of barium titanate crystals”. In: *Helvetica Physica Acta* 21 (1948), p. 207.

[38] Y Gu et al. “Flexoelectricity and ferroelectric domain wall structures: Phase-field modeling and DFT calculations”. In: *Phys. Rev. B* 89 (17 May 2014), p. 174111.

[39] SC Hwang, CS Lynch, and RM McMeeking. “Ferroelectric/ferroelastic interactions and a polarization switching model”. In: *Acta metallurgica et materialia* 43.5 (1995), pp. 2073–2084.

[40] JE Huber, NA Fleck, and RM McMeeking. “A crystal plasticity model for ferroelectrics”. In: *Ferroelectrics* 228.1 (1999), pp. 39–52.

[41] PJ Chen. “Three dimensional dynamic electromechanical constitutive relations for ferroelectric materials”. In: *International Journal of Solids and Structures* 16.12 (1980), pp. 1059–1067.

[42] E Bassiouny, AF Ghaleb, and GA Maugin. “Thermodynamical formulation for coupled electromechanical hysteresis effects - I. Basic equations”. In: *International Journal of Engineering Science* 26.12 (1988), pp. 1279–1295.

[43] M Kamlah and U Böhle. “Finite element analysis of piezoceramic components taking into account ferroelectric hysteresis behavior”. In: *International Journal of Solids and Structures* 38.4 (2001), pp. 605–633.

[44] GA Smolenskii and VA Isupov. “Ferroelectric properties of solid solution of barium strontium in barium titanate.” In: *Zhurnal Tekhnicheskoi Fiziki* 24.8 (1954), pp. 1375–1386.

[45] W Kleemann et al. “Non-linear permittivity study of the crossover from ferroelectric to relaxor and cluster glass in $BaTi_{(1-x)}Sn_xO_3$ (x=0.175–0.30)”. In: *Applied Physics Letters* 104.18 (2014), p. 182910.

[46] W Jo et al. “Giant electric-field-induced strains in lead-free ceramics for actuator applications–status and perspective”. In: *Journal of Electroceramics* 29.1 (2012), pp. 71–93.

[47] AA Bokov and ZG Ye. “Recent progress in relaxor ferroelectrics with perovskite structure”. In: *Frontiers of Ferroelectricity*. Springer, 2006, pp. 31–52.

[48] W Kleemann. “The relaxor enigma - charge disorder and random fields in ferroelectrics”. In: *Frontiers of Ferroelectricity*. Springer, 2006, pp. 129–136.

[49] GA Smolenskii and AI Agranovskaya. “Dielectric polarization and losses of some complex compounds”. In: *Zhur. Tekh. Fiz.* 28 (1958).

[50] VV Kirillov and VA Isupov. “Relaxation polarization of $PbMg_{1/3}Nb_{2/3}O_3$ (PMN)–A ferroelectric with a diffused phase transition”. In: *Ferroelectrics* 5.1 (1973), pp. 3–9.

[51] D Viehland et al. “Freezing of the polarization fluctuations in lead magnesium niobate relaxors”. In: *Journal of Applied Physics* 68.6 (1990), pp. 2916–2921.

[52] MA Akbas and PK Davies. “Domain growth in $Pb(Mg_{1/3}Ta_{2/3})O_3$ perovskite relaxor ferroelectric oxides”. In: *Journal of the American Ceramic Society* 80.11 (1997), pp. 2933–2936.

[53] ZY Cheng et al. “Dielectric behavior of lead magnesium niobate relaxors”. In: *Physical Review B* 55.13 (1997), p. 8165.

[54] R Pirc and R Blinc. “Spherical random-bond–random-field model of relaxor ferroelectrics”. In: *Physical Review B* 60.19 (1999), p. 13470.

[55] SF Edwards and PW Anderson. “Theory of spin glasses”. In: *Journal of Physics F: Metal Physics* 5.5 (1975), p. 965.

[56] N Novak et al. “High-resolution calorimetric study of $Pb(Mg_{1/3}Nb_{2/3})O_3$ single crystal”. In: *Physical Review Letters* 109.3 (2012), p. 037601.

[57] N Setter and LE Cross. “The role of B-site cation disorder in diffuse phase transition behavior of perovskite ferroelectrics”. In: *Journal of Applied Physics* 51.8 (1980), pp. 4356–4360.

[58] AK Tagantsev. “Vogel-Fulcher relationship for the dielectric permittivity of relaxor ferroelectrics”. In: *Physical Review Letters* 72.7 (1994), p. 1100.

[59] M Tachibana and E Takayama-Muromachi. “Thermal conductivity and heat capacity of the relaxor ferroelectric $[PbMg_{1/3}Nb_{2/3}O_3]_{(1-x)}[PbTiO_3]_x$”. In: *Physical Review B* 79.10 (2009), p. 100104.

[60] C Herring and C Kittel. “On the theory of spin waves in ferromagnetic media”. In: *Physical Review* 81.5 (1951), p. 869.

[61] L Leuzzi and G Parisi. “Long-range random-field Ising model: Phase transition threshold and equivalence of short and long ranges”. In: *Phys. Rev. B* 88 (22 Dec. 2013), p. 224204.

[62] D Andelman and JF Joanny. “Metastability in the random-field Ising model”. In: *Phys. Rev. B* 32 (7 Oct. 1985), pp. 4818–4821.

[63] N De Mathan et al. “Modification of the B-site order of $PbMg_{1/3}Nb_{2/3}O_3$ ceramics by thermal annealing or by La-doping”. In: *Materials research bulletin* 25.4 (1990), pp. 427–434.

[64] P Lehnen et al. “Ferroelectric nanodomains in the uniaxial relaxor system $Sr_{0.61-x}Ba_{0.39}Nb_2O_6$:$Ce_{x3+}$”. In: *Physical Review B* 64.22 (2001), p. 224109.

[65] VV Shvartsman et al. “Nanopolar structure in $Sr_xBa_{1-x}Nb_2O_6$ single crystals tuned by Sr/Ba ratio and investigated by piezoelectric force microscopy”. In: *Physical Review B* 77.5 (2008), p. 054105.

[66] VV Shvartsman and AL Kholkin. “Domain structure of $0.8Pb(Mg_{1/3}Nb_{2/3})O_3$- $0.2PbTiO_3$ studied by piezoresponse force microscopy”. In: *Physical Review B* 69.1 (2004), p. 014102.

[67] BJ Rodriguez et al. “Mapping bias-induced phase stability and random fields in relaxor ferroelectrics”. In: *Applied Physics Letters* 95.9 (2009), p. 092904.

[68] VV Shvartsman et al. “Crossover from ferroelectric to relaxor behavior in $BaTi_{1-x}Sn_xO_3$ solid solutions”. In: *Phase Transitions* 81.11-12 (2008), pp. 1013–1021.

[69] VV Shvartsman, J Zhai, and W Kleemann. “The dielectric relaxation in solid solutions $BaTi_{1-x}Zr_xO_3$”. In: *Ferroelectrics* 379.1 (2009), pp. 77–85.

[70] W Kleemann et al. “Crossover from ferroelectric to relaxor and cluster glass in $BaTi_{1-x}Zr_xO_3$(x=0.25–0.35) studied by non-linear permittivity”. In: *Applied Physics Letters* 102.23 (2013), p. 232907.

[71] YB Ma, K Albe, and BX Xu. “Lattice-based Monte Carlo simulations of the electrocaloric effect in ferroelectrics and relaxor ferroelectrics”. In: *Phys. Rev. B* 91 (18 May 2015), p. 184108.

[72] D Wang et al. “Phase diagram of polar states in doped ferroelectric systems”. In: *Phys. Rev. B* 86 (5 Aug. 2012), p. 054120.

[73] M Groeting, S Hayn, and K Albe. “Chemical order and local structure of the lead-free relaxor ferroelectric $Na_{1/2}Bi_{1/2}TiO_3$”. In: *Journal of Solid State Chemistry* 184.8 (2011), pp. 2041–2046.

[74] AR Akbarzadeh et al. “Finite-temperature properties of Ba (Zr, Ti) O_3 relaxors from first principles”. In: *Physical Review Letters* 108.25 (2012), p. 257601.

[75] Y Hinuma et al. “First-principles study on relaxor-type ferroelectric behavior without chemical inhomogeneity in $BaTaO_2N$ and $SrTaO_2N$”. In: *Chemistry of Materials* 24.22 (2012), pp. 4343–4349.

[76] J Rödel et al. “Perspective on the Development of Lead-free Piezoceramics”. In: *Journal of the American Ceramic Society* 92.6 (2009), pp. 1153–1177.

[77] VV Shvartsman and DC Lupascu. “Lead-free relaxor ferroelectrics”. In: *Journal of the American Ceramic Society* 95.1 (2012), pp. 1–26.

[78] J Rödel et al. “Transferring lead-free piezoelectric ceramics into application”. In: *Journal of the European Ceramic Society* 35.6 (2015), pp. 1659–1681.

[79] ST Zhang et al. “Giant strain in lead-free piezoceramics $Bi_{0.5}Na_{0.5}TiO_3$–BaTi O_3–$K_{0.5}Na_{0.5}NbO_3$ system”. In: *Applied Physics Letters* 91.11 (2007), p. 112906.

[80] ST Zhang et al. “Lead-free piezoceramics with giant strain in the system $Bi_{0.5}Na_{0.5}$ TiO_3–BaTi O_3–$K_{0.5}Na_{0.5}NbO_3$. I. Structure and room temperature properties”. In: *Journal of Applied Physics* 103.3 (2008), p. 034108.

[81] ST Zhang et al. “Temperature-dependent electrical properties of 0.94 $Bi_{0.5}Na_{0.5}TiO_3$–0.06 $BaTiO_3$ ceramics”. In: *Journal of the American Ceramic Society* 91.12 (2008), pp. 3950–3954.

[82] W Jo et al. “On the phase identity and its thermal evolution of lead free $(Bi_{1/2}Na_{1/2})TiO_3$-6 mol% $BaTiO_3$”. In: *Journal of Applied Physics* 110.7 (2011), p. 074106.

[83] B Noheda et al. “A monoclinic ferroelectric phase in the $Pb(Zr_{1-x}$ $Ti_x)O_3$ solid solution”. In: *Applied physics letters* 74.14 (1999), pp. 2059–2061.

[84] R Guo et al. “Origin of the high piezoelectric response in $PbZr_{1-x}Ti_xO_3$”. In: *Physical Review Letters* 84.23 (2000), p. 5423.

[85] W Krauss et al. “Piezoelectric properties and phase transition temperatures of the solid solution of (1-x)$(Bi_{0.5}Na_{0.5})$ TiO_3–x$SrTiO_3$”. In: *Journal of the European Ceramic Society* 30.8 (2010), pp. 1827–1832.

[86] B Parija et al. “Structure, microstructure and dielectric properties of 100- x $(Bi_{0.5}Na_{0.5})$ TiO_3- x [$SrTiO_3$] composites ceramics”. In: *Applied Physics A* 109.3 (2012), pp. 715–723.

[87] SI Raevskaya et al. “Lead-free niobate ceramics with relaxor-like properties”. In: *Ferroelectrics* 340.1 (2006), pp. 107–112.

[88] V Dorcet et al. “Properties of the solid solution (1-x)$Na_{0.5}Bi_{0.5}TiO_3$–(x) $BiFeO_3$”. In: *Journal of Magnetism and Magnetic Materials* 321.11 (2009), pp. 1762–1766.

[89] D Lin et al. “Piezoelectric and dielectric properties of $Bi_{0.5}Na_{0.5}TiO_3$–$Bi_{0.5}Li_{0.5}TiO_3$ lead-free ceramics”. In: *Journal of Materials Science: Materials in Electronics* 20.5 (2009), pp. 393–397.

[90] Y Hiruma, H Nagata, and T Takenaka. “Formation of morphotropic phase boundary and electrical properties of $(Bi_{1/2}Na_{1/2})TiO_3$–Ba $(Al_{1/2}Nb_{1/2})O_3$ solid solution ceramics”. In: *Japanese Journal of Applied Physics* 48.9S1 (2009), 09KC08.

[91] S Saïd and JP Mercurio. “Relaxor behaviour of low lead and lead free ferroelectric ceramics of the $Na_{0.5}Bi_{0.5}TiO_3$–PbTi O_3 and $Na_{0.5}Bi_{0.5}TiO_3$ –$K_{0.5}Bi_{0.5}TiO_3$ systems”. In: *Journal of the European Ceramic Society* 21.10-11 (2001), pp. 1333–1336.

[92] M Chandrasekhar and P Kumar. “Synthesis and characterizations of BNT–BT and BNT–BT–KNN ceramics for actuator and energy storage applications”. In: *Ceramics International* 41.4 (2015), pp. 5574–5580.

[93] H Zhang et al. “Preparation and enhanced electrical properties of grain-oriented $(Bi_{1/2}Na_{1/2})$ TiO_3-based lead-free incipient piezoceramics”. In: *Journal of the European Ceramic Society* 35.9 (2015), pp. 2501–2512.

[94] JF Trelcat et al. “Morphotropic phase boundary in the BNT–BT–BKT system”. In: *Ceramics International* 38.4 (2012), pp. 2823–2827.

[95] H Ogihara, CA Randall, and S Trolier-McKinstry. “Weakly coupled relaxor behavior of $BaTiO_3$–$BiScO_3$ ceramics”. In: *Journal of the American Ceramic Society* 92.1 (2009), pp. 110–118.

[96] E Irle and R Blachnik. “The system $KNbO_3$+ $BaTiO_3$”. In: *Thermochimica Acta* 185.2 (1991), pp. 355–357.

[97] Y Saito et al. “Lead-free piezoceramics”. In: *Nature* 432.7013 (2004), p. 84.

[98] TR Shrout and SJ Zhang. “Lead-free piezoelectric ceramics: Alternatives for PZT?” In: *Journal of Electroceramics* 19.1 (2007), pp. 113–126.

[99] W Liu and X Ren. “Large Piezoelectric Effect in Pb-Free Ceramics”. In: *Physical Review Letters* 103 (25 Dec. 2009), p. 257602.

[100] P Mishra, P Kumar, et al. “Effect of sintering temperature on dielectric, piezoelectric and ferroelectric properties of BZT–BCT 50/50 ceramics”. In: *Journal of Alloys and Compounds* 545 (2012), pp. 210–215.

[101] B Li, JE Blendell, and KJ Bowman. “Temperature-Dependent Poling Behavior of Lead-free BZT–BCT Piezoelectrics”. In: *Journal of the American Ceramic Society* 94.10 (2011), pp. 3192–3194.

[102] Y Hiruma, H Nagata, and T Takenaka. “Phase diagrams and electrical properties of $(Bi_{1/2}Na_{1/2})TiO_3$-based solid solutions”. In: *Journal of Applied Physics* 104.12 (2008), p. 124106.

[103] DS Lee et al. “Electric field-induced deformation behavior in mixed $Bi_{0.5}Na_{0.5}TiO_3$ and $Bi_{0.5}$ $(Na_{0.75}K_{0.25})_{0.5}TiO_3$-$BiAlO_3$”. In: *Applied Physics Letters* 99.6 (2011), p. 062906.

[104] KW Wagner. “Erklärung der dielektrischen nachwirkungsvorgänge auf grund maxwellscher vorstellungen”. In: *Archiv für Elektrotechnik* 2.9 (1914), pp. 371–387.

[105] DJ Bergman. “The dielectric constant of a composite material - a problem in classical physics”. In: *Physics Reports* 43.9 (1978), pp. 377–407.

[106] LA Pauer. “Flexible piezoelectric material”. In: *IEEE Int. Conv. Rec* 21 (1973), pp. 1–3.

[107] H Banno. “Theoretical equations for dielectric, piezoelectric and elastic properties of flexible composite consisting of polymer and ceramic powder of two different materials”. In: *Ferroelectrics* 95.1 (1989), pp. 111–115.

[108] J Koruza et al. “Formation of the core–shell microstructure in lead-free $Bi_{1/2}Na_{1/2}TiO_3$-SrTi O $_3$ piezoceramics and its influence on the electromechanical properties”. In: *Journal of the European Ceramic Society* 36.4 (2016), pp. 1009–1016.

[109] P Zubko, G Catalan, and AK Tagantsev. “Flexoelectric effect in solids”. In: *Annual Review of Materials Research* 43 (2013), pp. 387–421.

[110] RB Meyer. “Piezoelectric effects in liquid crystals”. In: *Physical Review Letters* 22.18 (1969), p. 918.

[111] W Ma and LE Cross. “Observation of the flexoelectric effect in relaxor Pb $(Mg_{1/3}Nb_{2/3})O_3$ ceramics”. In: *Applied Physics Letters* 78.19 (2001), pp. 2920–2921.

[112] W Ma and LE Cross. “Flexoelectricity of barium titanate”. In: *Applied Physics Letters* 88.23 (2006), p. 232902.

[113] TD Nguyen et al. “Nanoscale flexoelectricity”. In: *Advanced Materials* 25.7 (2013), pp. 946–974.

[114] SM Kogan. “Piezoelectric effect during inhomogeneous deformation and acoustic scattering of carriers in crystals”. In: *Soviet Physics-Solid State* 5.10 (1964), pp. 2069–2070.

[115] RD Mindlin and NN Eshel. “On first strain-gradient theories in linear elasticity”. In: *International Journal of Solids and Structures* 4.1 (1968), pp. 109–124.

[116] S Krichen and P Sharma. “Flexoelectricity: A perspective on an unusual electromechanical coupling”. In: *Journal of Applied Mechanics* 83.3 (2016), p. 030801.

[117] Z Suo. “Theory of dielectric elastomers”. In: *Acta Mechanica Solida Sinica* 23.6 (2010), pp. 549–578.

[118] Q Deng, L Liu, and P Sharma. “Flexoelectricity in soft materials and biological membranes”. In: *Journal of the Mechanics and Physics of Solids* 62 (2014), pp. 209–227.

[119] Alexander GP. “Electricity and mechanics of biomembrane systems: Flexoelectricity in living membranes”. In: *Analytica Chimica Acta* 568.1 (2006). Molecular Electronics and Analytical Chemistry, pp. 70–83. ISSN: 0003-2670.

[120] G Catalan et al. “Flexoelectric rotation of polarization in ferroelectric thin films”. In: *Nature materials* 10.12 (2011), p. 963.

[121] UK Bhaskar et al. “A flexoelectric microelectromechanical system on silicon”. In: *Nature nanotechnology* 11.3 (2016), p. 263.

[122] J Hong et al. “The flexoelectricity of barium and strontium titanates from first principles”. In: *Journal of Physics: Condensed Matter* 22.11 (2010), p. 112201.

[123] J Hong and D Vanderbilt. “First-principles theory of frozen-ion flexoelectricity”. In: *Physical Review B* 84.18 (2011), p. 180101.

[124] J Hong and D Vanderbilt. “First-principles theory and calculation of flexoelectricity”. In: *Physical Review B* 88.17 (2013), p. 174107.

[125] I Ponomareva, AK Tagantsev, and L Bellaiche. “Finite-temperature flexoelectricity in ferroelectric thin films from first principles”. In: *Physical Review B* 85.10 (2012), p. 104101.

[126] S Mao and PK Purohit. “Insights into flexoelectric solids from strain-gradient elasticity”. In: *Journal of Applied Mechanics* 81.8 (2014), p. 081004.

[127] S Mao and PK Purohit. “Defects in flexoelectric solids”. In: *Journal of the Mechanics and Physics of Solids* 84 (2015), pp. 95–115.

[128] S Mao, PK Purohit, and N Aravas. “Mixed finite-element formulations in piezoelectricity and flexoelectricity”. In: *Proc. R. Soc. A* 472.2190 (2016), p. 20150879.

[129] ND Sharma, CM Landis, and P Sharma. “Piezoelectric thin-film superlattices without using piezoelectric materials”. In: *Journal of Applied Physics* 108.2 (2010), p. 024304.

[130] A Abdollahi et al. “Computational evaluation of the flexoelectric effect in dielectric solids”. In: *Journal of Applied Physics* 116.9 (2014), p. 093502.

[131] HT Chen, AK Soh, and Y Ni. “Phase field modeling of flexoelectric effects in ferroelectric epitaxial thin films”. In: *Acta Mechanica* 225.4-5 (2014), pp. 1323–1333.

[132] HT Chen et al. “Phase field modeling of flexoelectricity in solid dielectrics”. In: *Journal of Applied Physics* 118.3 (2015), p. 034106.

[133] JC Maxwell. *A treatise on electricity and magnetism*. Vol. 1. Clarendon press, 1881.

[134] LD Landau and EM Lifshitz. *Mechanics and electrodynamics*. Elsevier, 2013.

[135] EM Purcell and DJ Morin. *Electricity and magnetism*. Cambridge University Press, 2013.

[136] PJ Mohr, DB Newell, and BN Taylor. “CODATA recommended values of the fundamental physical constants: 2014”. In: *Journal of Physical and Chemical Reference Data* 45.4 (2016), p. 043102.

[137] ME Gurtin, E Fried, and L Anand. *The mechanics and thermodynamics of continua*. Cambridge University Press, 2010.

[138] Yuan-cheng Fung. “A first course in continuum mechanics”. In: *Englewood Cliffs, NJ, Prentice-Hall, Inc., 1977. 351 p.* (1977).

[139] J Wang et al. “Phase-field simulations of ferroelectric/ferroelastic polarization switching”. In: *Acta Materialia* 52.3 (2004), pp. 749–764.

[140] LD Landau. “On the theory of phase transitions”. In: *Ukr. J. Phys.* 11 (1937), pp. 19–32.

[141] AF Devonshire. “XCVI. Theory of barium titanate: Part I”. In: *The London, Edinburgh, and Dublin Philosophical Magazine and Journal of Science* 40.309 (1949), pp. 1040–1063.

[142] AF Devonshire. “Theory of ferroelectrics”. In: *Advances in physics* 3.10 (1954), pp. 85–130.

[143] JW Cahn and JE Hilliard. “Free energy of a nonuniform system. I. Interfacial free energy”. In: *The Journal of chemical physics* 28.2 (1958), pp. 258–267.

[144] VA Zhirnov. “A contribution to the theory of domain walls in ferroelectrics”. In: *Sov. Phys. JETP* 35.5 (1959), pp. 822–827.

[145] Daozhi Han, Dong Sun, and Xiaoming Wang. “Two-phase flows in karstic geometry”. In: *Mathematical Methods in the Applied Sciences* 37.18 (2014), pp. 3048–3063.

[146] I Steinbach. “Phase-field models in materials science”. In: *Modelling and simulation in materials science and engineering* 17.7 (2009), p. 073001.

[147] LP Gor’kov. “Microscopic derivation of the Ginzburg-Landau equations in the theory of superconductivity”. In: *Sov. Phys. JETP* 9.6 (1959), pp. 1364–1367.

[148] LD Landau and E Lifshitz. “On the theory of the dispersion of magnetic permeability in ferromagnetic bodies”. In: *Phys. Z. Sowjet.* 8 (1935), p. 153.

[149] SM Allen and JW Cahn. “Mechanisms of phase transformations within the miscibility gap of Fe-rich Fe-Al alloys”. In: *Acta Metallurgica* 24.5 (1976), pp. 425–437.

[150] Y Hou et al. “Modeling mode I cracking failure in asphalt binder by using nonconserved phase-field model”. In: *Journal of Materials in Civil Engineering* 26.4 (2013), pp. 684–691.

[151] D Schrade et al. “Domain evolution in ferroelectric materials: A continuum phase field model and finite element implementation”. In: *Computer methods in applied mechanics and engineering* 196.41-44 (2007), pp. 4365–4374.

[152] JW Cahn and JE Hilliard. “Spinodal decomposition: A reprise”. In: *Acta Metallurgica* 19.2 (1971), pp. 151–161.

[153] P Yue et al. “A diffuse-interface method for simulating two-phase flows of complex fluids”. In: *Journal of Fluid Mechanics* 515 (2004), pp. 293–317.

[154] Y Zhao, P Stein, and BX Xu. “Isogeometric analysis of mechanically coupled Cahn–Hilliard phase segregation in hyperelastic electrodes of Li-ion batteries”. In: *Computer Methods in Applied Mechanics and Engineering* 297 (2015), pp. 325–347.

[155] W Cao and GR Barsch. “Landau-Ginzburg model of interphase boundaries in improper ferroelastic Perovskites of D_{4h}^{18} symmetry”. In: *Physical Review B* 41.7 (1990), p. 4334.

[156] W Cao and LE Cross. “Theory of tetragonal twin structures in ferroelectric perovskites with a first-order phase transition”. In: *Physical Review B* 44.1 (1991), p. 5.

[157] S Nambu and DA Sagala. “Domain formation and elastic long-range interaction in ferroelectric perovskites”. In: *Physical Review B* 50.9 (1994), p. 5838.

[158] DA Sagala and S Nambu. “Microscopic calculation of dielectric loss at microwave frequencies for complex perovskite Ba $(Zn_{1/3}Ta_{2/3})O_3$”. In: *Journal of the American Ceramic Society* 75.9 (1992), pp. 2573–2575.

[159] HL Hu and LQ Chen. “Computer simulation of 90 ferroelectric domain formation in two-dimensions”. In: *Materials Science and Engineering: A* 238.1 (1997), pp. 182–191.

[160] Y Su and CM Landis. “Continuum thermodynamics of ferroelectric domain evolution: Theory, finite element implementation, and application to domain wall pinning”. In: *Journal of the Mechanics and Physics of Solids* 55.2 (2007), pp. 280–305.

[161] YL Li et al. “Phase-field model of domain structures in ferroelectric thin films”. In: *Applied Physics Letters* 78.24 (2001), pp. 3878–3880.

[162] YL Li et al. “Effect of substrate constraint on the stability and evolution of ferroelectric domain structures in thin films”. In: *Acta materialia* 50.2 (2002), pp. 395–411.

[163] J Wang and M Kamlah. “Three-dimensional finite element modeling of polarization switching in a ferroelectric single domain with an impermeable notch”. In: *Smart Materials and Structures* 18.10 (2009), p. 104008.

[164] W Zhang and K Bhattacharya. “A computational model of ferroelectric domains. Part I: model formulation and domain switching”. In: *Acta materialia* 53.1 (2005), pp. 185–198.

[165] W Zhang and K Bhattacharya. “A computational model of ferroelectric domains. Part II: grain boundaries and defect pinning”. In: *Acta Materialia* 53.1 (2005), pp. 199–209.

[166] T Sluka et al. “Enhanced electromechanical response of ferroelectrics due to charged domain walls”. In: *Nature communications* 3 (2012), p. 748.

[167] Alexander KT. “Landau Expansion for Ferroelectrics: Which Variable to Use?” In: *Ferroelectrics* 375.1 (2008), pp. 19–27.

[168] ME Gurtin. “Generalized Ginzburg-Landau and Cahn-Hilliard equations based on a microforce balance”. In: *Physica D: Nonlinear Phenomena* 92.3-4 (1996), pp. 178–192.

[169] BP Burton et al. “First-principles-based simulations of relaxor ferroelectrics”. In: *Phase Transitions* 79.1-2 (2006), pp. 91–121.

[170] SE Park and TR Shrout. “Ultrahigh strain and piezoelectric behavior in relaxor based ferroelectric single crystals”. In: *Journal of Applied Physics* 82.4 (1997), pp. 1804–1811.

[171] TR Shrout and Fielding JJ. “Relaxor ferroelectric materials”. In: *Ultrasonics Symposium, 1990. Proceedings.* IEEE. 1990, pp. 711–720.

[172] LE Cross et al. “Large electrostrictive effects in relaxor ferroelectrics”. In: *Ferroelectrics* 23.1 (1980), pp. 187–191.

[173] MD Glinchuk and R Farhi. “A random field theory based model for ferroelectric relaxors”. In: *Journal of Physics: Condensed Matter* 8.37 (1996), pp. 6985–6996.

[174] R Blinc et al. “Local polarization distribution and Edwards-Anderson order parameter of relaxor ferroelectrics”. In: *Physical Review Letters* 83.2 (1999), pp. 424–427.

[175] LQ Chen. “Phase-field models for microstructure evolution”. In: *Annual review of materials research* 32.1 (2002), pp. 113–140.

[176] Y Xiao, VB Shenoy, and K Bhattacharya. “Depletion layers and domain walls in semiconducting ferroelectric thin films”. In: *Physical Review Letters* 95.24 (2005), p. 247603.

[177] A Kontsos and CM Landis. “Computational modeling of domain wall interactions with dislocations in ferroelectric crystals”. In: *International Journal of Solids and Structures* 46.6 (2009), pp. 1491–1498.

[178] BX Xu et al. “Phase field simulation of domain structures in cracked ferroelectrics”. In: *International Journal of Fracture* 165.2 (2010), pp. 163–173.

[179] I Münch et al. “Domain engineered ferroelectric energy harvesters on a substrate”. In: *Journal of Applied Physics* 109.10 (2011), p. 104106.

[180] Y Su, N Liu, and GJ Weng. “A phase field study of frequency dependence and grain-size effects in nanocrystalline ferroelectric polycrystals”. In: *Acta Materialia* 87 (2015), pp. 293–308.

[181] MA Keip et al. “Coordinate-invariant phase field modeling of ferro-electrics, part II: Application to composites and poly-crystals”. In: *GAMM-Mitteilungen* 38.1 (2015), pp. 115–131.

[182] D Schrade et al. “An invariant formulation for phase field models in ferroelectrics”. In: *International Journal of Solids and Structures* 51.11-12 (2014), pp. 2144–2156.

[183] D Schrade et al. “Phase field simulations of the poling behavior of $BaTiO_3$ nano-scale thin films with $SrRuO_3$ and Au electrodes”. In: *European Journal of Mechanics-A/Solids* 49 (2015), pp. 455–466.

[184] J Wang and TY Zhang. “Phase field simulations of polarization switching-induced toughening in ferroelectric ceramics”. In: *Acta materialia* 55.7 (2007), pp. 2465–2477.

[185] M Liu and J Wang. “Giant electrocaloric effect in ferroelectric nanotubes near room temperature”. In: *Scientific reports* 5 (2015).

[186] GEP Box and Muller ME. “A note on the generation of random normal deviates”. In: *Ann. Math. Stat.* 29 (1958), pp. 610–611.

[187] Y Huo and Q Jiang. “Modeling of domain switching in polycrystalline ferroelectric ceramics”. In: *Smart Materials and Structures* 6.4 (1997), p. 441.

[188] M Kamlah. “Ferroelectric and ferroelastic piezoceramics–modeling of electromechanical hysteresis phenomena”. In: *Continuum Mechanics and Thermodynamics* 13.4 (2001), pp. 219–268.

[189] D Schrade, R Müller, and D Gross. “On the physical interpretation of material parameters in phase field models for ferroelectrics”. In: *Archive of Applied Mechanics* 83.10 (2013), pp. 1393–1413.

[190] W Kleemann et al. “Uniaxial relaxor ferroelectrics: The ferroic random-field Ising model materialized at last”. In: *Europhysics Letters* 57.1 (2002), p. 14.

[191] VV Shvartsman and DC Lupascu. “Lead-Free Relaxor Ferroelectrics”. In: *Journal of the American Ceramic Society* 95.1 (2012), pp. 1–26. ISSN: 1551-2916.

[192] LQ Chen. “Phase-field method of phase transitions/domain structures in ferroelectric thin films: a review”. In: *Journal of the American Ceramic Society* 91.6 (2008), pp. 1835–1844.

[193] AJ Bell and LE Cross. “A phenomenological gibbs function for $BaTiO_3$ giving correct e field dependence of all ferroelectric phase changes”. In: *Ferroelectrics* 59.1 (1984), pp. 197–203.

[194] RL Taylor. “FEAP-finite element analysis program (2014)”. In: *URL http://www. ce. berkeley/feap* (2014).

[195] S Alatsathianos. “Experimentelle Untersuchung des Materialverhaltens von piezoelektrischen Werkstoffen”. PhD thesis. Karlsruher, 2000.

[196] W Heywang, K Lubitz, and W Wersing. *Piezoelectricity: evolution and future of a technology*. Vol. 114. Springer Science & Business Media, 2008.

[197] K Uchino. *Piezoelectric actuators and ultrasonic motors*. Vol. 1. Springer Science & Business Media, 1996.

[198] CH Hong et al. “Lead-Free Piezoceramics-Where to Move on?” In: *Journal of Materiomics* (2016).

[199] ST Zhang et al. “High-Strain Lead-free Antiferroelectric Electrostrictors”. In: *Advanced materials* 21.46 (2009), pp. 4716–4720.

[200] Y Hiruma et al. “Large electrostrain near the phase transition temperature of $(Bi_{0.5}Na_{0.5})TiO_3 - SrTiO_3$ ferroelectric ceramics”. In: *Applied Physics Letters* 92.26 (2008), p. 262904.

[201] SC Hwang and RM McMeeking. “A finite element model of ferroelectric polycrystals”. In: *Ferroelectrics* 211.1 (1998), pp. 177–194.

[202] M Kamlah and C Tsakmakis. “Phenomenological modeling of the non-linear electromechanical coupling in ferroelectrics”. In: *International Journal of Solids and Structures* 36.5 (1999), pp. 669–695.

[203] K Dayal and K Bhattacharya. “A real-space non-local phase-field model of ferroelectric domain patterns in complex geometries”. In: *Acta materialia* 55.6 (2007), pp. 1907–1917.

[204] WD Dong, DM Pisani, and CS Lynch. “A finite element based phase field model for ferroelectric domain evolution”. In: *Smart Materials and Structures* 21.9 (2012), p. 094014.

[205] F Li et al. “Local structural heterogeneity and electromechanical responses of ferroelectrics: learning from relaxor ferroelectrics”. In: *Advanced Functional Materials* (2018), p. 1801504.

[206] D Franzbach. “Field induced phase transitions in ferroelectric Materials”. PhD thesis. Darmstadt: Technische Universität, 2014.

[207] C Kittel. “Theory of antiferroelectric crystals”. In: *Physical Review* 82.5 (1951), p. 729.

[208] L Zheng et al. “Complete set of material constants of $0.95(Na_{0.5}Bi_{0.5})TiO_3 - 0.05BaTiO_3$ lead-free piezoelectric single crystal and the delineation of extrinsic contributions”. In: *Applied Physics Letters* 103.12 (2013), p. 122905.

[209] F Xue et al. “Phase field simulations of ferroelectrics domain structures in $PbZr_xTi_{1-x}O_3$ bilayers”. In: *Acta Materialia* 61.8 (2013), pp. 2909–2918.

[210] VA Stephanovich, IA Luk’yanchuk, and MG Karkut. “Domain-Enhanced Interlayer Coupling in Ferroelectric/Paraelectric Superlattices”. In: *Physical Reviel Letter* 94 (4 2005), p. 047601.

[211] R Kretschmer and K Binder. “Surface effects on phase transitions in ferroelectrics and dipolar magnets”. In: *Physical Review B* 20 (3 1979), pp. 1065–1076.

[212] W Känzig. “Space Charge Layer Near the Surface of a Ferroelectric”. In: *Phys. Rev.* 98 (2 Apr. 1955), pp. 549–550.

[213] GG Raju. *Dielectrics in electric fields*. CRC press, 2016.

[214] Y Zuo et al. “Domain wall stability in ferroelectrics with space charges”. In: *Journal of Applied Physics* 115.8 (2014), p. 084110.

[215] Y Zuo, YA Genenko, and BX Xu. “Charge compensation of head-to-head and tail-to-tail domain walls in barium titanate and its influence on conductivity”. In: *Journal of Applied Physics* 116.4 (2014), p. 044109.

[216] YA Genenko and DC Lupascu. “Drift of charged defects in local fields as aging mechanism in ferroelectrics”. In: *Physical Review B* 75.18 (2007), p. 184107.

[217] Q Qu et al. “Core–shell structure of polypyrrole grown on V_2O_5 nanoribbon as high performance anode material for supercapacitors”. In: *Advanced Energy Materials* 2.8 (2012), pp. 950–955.

[218] Y Wang et al. “The design of a $LiFePO_4$/carbon nanocomposite with a core–shell structure and its synthesis by an in situ polymerization restriction method”. In: *Angewandte Chemie* 120.39 (2008), pp. 7571–7575.

[219] W Zhao et al. “Fabrication of Uniform Magnetic Nanocomposite Spheres with a Magnetic Core/Mesoporous Silica Shell Structure”. In: *Journal of the American Chemical Society* 127.25 (2005). PMID: 15969545, pp. 8916–8917.

[220] K Sakata and Y Masuda. “Ferroelectric and antiferroelectric properties of $(Na_{0.5}Bi_{0.5})TiO_3$-$SrTiO_3$ solid solution ceramics”. In: *Ferroelectrics* 7.1 (1974), pp. 347–349.

[221] ZG Ye. “Relaxor ferroelectric $Pb(Mg_{1/3}Nb_{2/3})O_3$: Properties and present understanding”. In: *Ferroelectrics* 184.1 (1996), pp. 193–208.

[222] JR Gomah-Pettry et al. “Sodium-bismuth titanate based lead-free ferroelectric materials”. In: *Journal of the European Ceramic Society* 24.6 (2004), pp. 1165–1169.

[223] D Rout et al. “Dielectric and Raman scattering studies of phase transitions in the $(100\text{-}x)Na_{0.5}Bi_{0.5}TiO_3$ –$xSrTiO_3$ system”. In: *Journal of Applied Physics* 108.8 (2010), p. 084102.

[224] Y Watanabe et al. “Phase transition temperatures and electrical properties of divalent ions (Ca^{2+}, Sr^{2+} and Ba^{2+}) substituted $(Bi_{1/2}Na_{1/2})TiO_3$ ceramics”. In: *Ceramics International* 34.4 (2008), pp. 761–764.

[225] SE Park and KS Hong. “Variations of structure and dielectric properties on substituting A-site cations for Sr^{2+} in $(Na_{1/2}Bi_{1/2})TiO_3$”. In: *Journal of Materials Research* 12.8 (1997), pp. 2152–2157.

[226] JK Lee et al. “Phase transitions and dielectric properties in A-site ion substituted $(Na_{1/2}Bi_{1/2})$ TiO_3 ceramics (A= Pb and Sr)”. In: *Journal of Applied Physics* 91.7 (2002), pp. 4538–4542.

[227] F Weyland et al. “Electric field–temperature phase diagram of sodium bismuth titanate-based relaxor ferroelectrics”. In: *Journal of Materials Science* (2018), pp. 1–8.

[228] M Acosta. *Strain Mechanisms in Lead-Free Ferroelectrics for Actuators*. Springer, 2016.

[229] W Ma and LE Cross. “Flexoelectric polarization of barium strontium titanate in the paraelectric state”. In: *Applied Physics Letters* 81.18 (2002), pp. 3440–3442.

[230] W Ma and LE Cross. “Strain-gradient-induced electric polarization in lead zirconate titanate ceramics”. In: *Applied Physics Letters* 82.19 (2003), pp. 3293–3295.

[231] W Ma and LE Cross. “Large flexoelectric polarization in ceramic lead magnesium niobate”. In: *Applied Physics Letters* 79.26 (2001), pp. 4420–4422.

[232] Y Gu et al. “Nanoscale mechanical switching of ferroelectric polarization via flexoelectricity”. In: *Applied Physics Letters* 106.2 (2015), p. 022904.

[233] H Lu et al. “Mechanical writing of ferroelectric polarization”. In: *Science* 336.6077 (2012), pp. 59–61.

[234] VS Mashkevich and KB Tolpygo. “The interaction of vibrations of nonpolar crystals with electric fields”. In: *Soviet Physics Doklady*. Vol. 1. 1957, p. 690.

[235] ADB Woods, W Cochran, and BN Brockhouse. “Lattice Dynamics of Alkali Halide Crystals”. In: *Phys. Rev.* 119 (3 Aug. 1960), pp. 980–999.

[236] R Maranganti, ND Sharma, and P Sharma. “Electromechanical coupling in nonpiezoelectric materials due to nanoscale nonlocal size effects: Green’s function solutions and embedded inclusions”. In: *Physical Review B* 74.1 (2006), p. 014110.

[237] PV Yudin and AK Tagantsev. “Fundamentals of flexoelectricity in solids”. In: *Nanotechnology* 24.43 (2013), p. 432001.

[238] RD Mindlin. “Micro-structure in linear elasticity”. In: *Archive for Rational Mechanics and Analysis* 16.1 (1964), pp. 51–78.

[239] NA Fleck and JW Hutchinson. “Strain gradient plasticity”. In: *Advances in applied mechanics* 33 (1997), pp. 296–361.

[240] RD Mindlin. “Equations of high frequency vibrations of thermopiezoelectric crystal plates”. In: *International Journal of Solids and Structures* 10.6 (1974), pp. 625–637. ISSN: 0020-7683.

[241] F Deng et al. “Mixed Finite Elements for Flexoelectric Solids”. In: *Journal of Applied Mechanics* 84.8 (2017), p. 081004.

[242] YL Li, LE Cross, and LQ Chen. “A phenomenological thermodynamic potential for $BaTiO_3$ single crystals”. In: *Journal of Applied Physics* 98.6 (2005), p. 064101.

[243] LQ Chen. “APPENDIX A–Landau free-energy coefficients”. In: *Physics of Ferroelectrics*. Springer, 2007, pp. 363–372.

[244] R Maranganti and P Sharma. "Atomistic determination of flexoelectric properties of crystalline dielectrics". In: *Physical Review B* 80.5 (2009), p. 054109.

[245] BH Park et al. "Lanthanum-substituted bismuth titanate for use in non-volatile memories". In: *Nature* 401.6754 (1999), p. 682.

[246] JF Tressler, S Alkoy, and RE Newnham. "Piezoelectric sensors and sensor materials". In: *Journal of electroceramics* 2.4 (1998), pp. 257–272.

[247] QM Zhang et al. "An all-organic composite actuator material with a high dielectric constant". In: *Nature* 419.6904 (2002), p. 284.

[248] S Zhang et al. "Advantages and challenges of relaxor-$PbTiO_3$ ferroelectric crystals for electroacoustic transducers–A review". In: *Progress in materials science* 68 (2015), pp. 1–66.

[249] T Frömling et al. "Designing properties of $(Na_{1/2}Bi_x)$ TiO_3-based materials through A-site non-stoichiometry". In: *Journal of Materials Chemistry C* 6.4 (2018), pp. 738–744.

[250] D Yadlovker and S Berger. "Uniform orientation and size of ferroelectric domains". In: *Physical Review B* 71.18 (2005), p. 184112.

[251] B Dkhil et al. "Intermediate temperature scale T* in lead-based relaxor systems". In: *Physical Review B* 80.6 (2009), p. 064103.

[252] PM Gehring et al. "Reassessment of the Burns temperature and its relationship to the diffuse scattering, lattice dynamics, and thermal expansion in relaxor Pb $(Mg_{1/3}Nb_{2/3})O_3$". In: *Physical Review B* 79.22 (2009), p. 224109.

[253] M Vögler et al. "Temperature-dependent volume fraction of polar nanoregions in lead-free (1-x)$(Bi_{0.5}Na_{1/3})TiO_3$- x$BaTiO_3$ ceramics". In: *Physical Review B* 95.2 (2017), p. 024104.

[254] AN Morozovska et al. "Thermodynamics of electromechanically coupled mixed ionic-electronic conductors: Deformation potential, Vegard strains, and flexoelectric effect". In: *Physical Review B* 83.19 (2011), p. 195313.

[255] AN Morozovska et al. "Effect of Vegard strains on the extrinsic size effects in ferroelectric nanoparticles". In: *Physical Review B* 90.21 (2014), p. 214103.

[256] P Gao et al. "Atomic-Scale Measurement of Flexoelectric Polarization at $SrTiO_3$ Dislocations". In: *Physical Review Letters* 120.26 (2018), p. 267601.

[257] D Viehland and JF Li. "Compositional instability and the resultant charge variations in mixed B-site cation relaxer ferroelectrics". In: *Journal of applied physics* 74.6 (1993), pp. 4121–4124.

[258] KC King and T Mura. "The eigenstrain method for small defects in a lattice". In: *Journal of Physics and Chemistry of Solids* 52.8 (1991), pp. 1019–1030.

[259] W Tirry and D Schryvers. “Linking a completely three-dimensional nanostrain to a structural transformation eigenstrain”. In: *Nature materials* 8.9 (2009), p. 752.

[260] R Kilaas. “Optimal and near-optimal filters in high-resolution electron microscopy”. In: *Journal of Microscopy* 190.1-2 (1998), pp. 45–51.

[261] H Liu et al. “Temperature-dependent Evolution of Crystallographic and Domain Structures in (K,Na,Li)(Ta,Nb)O_3 Piezoelectric Single Crystals”. In: *IEEE Transactions on Ultrasonics, Ferroelectrics, and Frequency Control* (2018).

[262] S Das et al. “Controlled manipulation of oxygen vacancies using nanoscale flexoelectricity”. In: *Nature Communications* 8.1 (2017), p. 615.

[263] S Choudhury et al. “Effect of grain orientation and grain size on ferroelectric domain switching and evolution: Phase field simulations”. In: *Acta materialia* 55.4 (2007), pp. 1415–1426.

[264] F Falk. “Ginzburg-Landau theory of static domain walls in shape-memory alloys”. In: *Zeitschrift für Physik B Condensed Matter* 51.2 (1983), pp. 177–185.

[265] Z Wang. *Thermodynamics*. Peking University Press, 2014.

[266] D Berlincourt and H Jaffe. “Elastic and piezoelectric coefficients of single-crystal barium titanate”. In: *Physical Review* 111.1 (1958), p. 143.

[267] MJ Haun et al. “Thermodynamic theory of $PbTiO_3$”. In: *Journal of Applied Physics* 62.8 (1987), pp. 3331–3338.

[268] W Zhong, D Vanderbilt, and KM Rabe. “First-principles theory of ferroelectric phase transitions for perovskites: The case of $BaTiO_3$”. In: *Physical Review B* 52.9 (1995), p. 6301.

[269] A Kumar and UV Waghmare. “First-principles free energies and Ginzburg-Landau theory of domains and ferroelectric phase transitions in $BaTiO_3$”. In: *Physical Review B* 82.5 (2010), p. 054117.

[270] J Hlinka and P Marton. “Phenomenological model of a 90° domain wall in $BaTiO_3$-type ferroelectrics”. In: *Physical Review B* 74.10 (2006), p. 104104.

Publications and Presentations

Publications

I) **Wang Shuai**, Yi Min, and Xu Bai-Xiang. "A phase-field model of relaxor ferroelectrics based on random field theory." *International Journal of Solids and Structures* 83 (2016): 142-153.

II) Leopoldo Molina-Luna*, **Wang Shuai***, Pivak Yevheniy, Zintler Alexander, Pérez-Garza Hugo, Spruit Ronald, Xu Qiang, Yi Min, Xu Bai-Xiang, and Acosta Matias. "Enabling nanoscale flexoelectricity at extreme temperature by tuning cation diffusion" *Nature Communications*, 9(2018): 4445.

III) **Wang Shuai**, Ayrikyan Azatuhi, Webber Kyle G., Zhang Haibo, and Xu Bai-Xiang. "Phase-field Study of Electromechanical Coupling in Lead-free Relaxor/Ferroelectric Layered Composites" *Advanced Electronic Materials*, 2018, 1800710.

IV) Liu Na, Acosta Matias, **Wang Shuai**, Xu Bai-Xiang, Stark Robert W., and Dietz Christian. "Revealing the core-shell interaction of a giant strain relaxor ferroelectric $0.75Bi_{1/2}Na_{1/2}TiO_3$-$0.25SrTiO_3$" *Scientific reports* 6 (2016): 36910.

V) Yang Yangyiwei, **Wang Shuai**, Stein Peter, Xu Bai-Xiang, and Yang Tongqing. "Vibration-based energy harvesting with a clamped piezoelectric circular diaphragm: analysis and identification of optimal structural parameters." *Smart Materials and Structures* 26.4 (2017): 045011.

VI) Xu Bai-Xiang, **Wang Shuai**, and Yi Min. "A finite element phase field model for relaxor ferroelectrics." *Proceedings in Applied Mathematics and Mechanics* 15.1 (2015): 723-726.

VII) Chauhan Aditya, Patel Satyanarayan, **Wang Shuai**, Novak Nikola, Xu Bai-Xiang, Lv Peng, Vaish Rahul, and Lynch Cristopher S. "Enhanced performance of ferroelectric materials under hydrostatic pressure." *Journal of Applied Physics* 122.22 (2017): 224105.

*: equally contributed

Conferences with Presentations and Posters

- 4th GAMM Workshop on Phase Field Modeling, 04-05 Feb. 2016, Braunschweig

- 7th GAMM Annual Meeting, 7-11 Mar. 2016, Braunschweig
- International Symposium on the Applications of Ferroelectrics, 21-25 Aug. 2016, Darmstadt
- Materials Science and Engineering, 27-29 Sept. 2016, Darmstadt
- 13th International Symposium on Ferroic Domains and Micro- to Nano-scopic Structures, 02-06 Oct. 2016, Vancouver, Canada
- The International Meeting on Ferroelectricity, 04-08 Sept. 2017, San Antonio USA
- 4th GAMM Workshop on Phase Field Modeling, 02-03 Feb. 2017, Aachen
- 88th GAMM Annual Meeting, 6-10 Mar. 2017, Weimar
- VII International Conference on Coupled Problems in Science and Engineering, 12-14 Jun. 2017, Greece

Curriculum Vitae

Personal

Shuai Wang.
Born on December 12, 1990.
From Xiaoxian, Anhui Province, China.

Education background

Jan, 2015 - January, 2019

Fachbereich Material- und Geowissenschaften, Technische Universität Darmstadt, Germany

Graduate School of Computational Engineering, Technische Universität Darmstadt, Germany

Doctoral student.

September, 2012 - Jan, 2015

School of Aeronautic Science and Engineering, Beihang University, Beijing, China

Master of Engineering.

September, 2008 - June, 2012

School of Aeronautic Science and Engineering, Beihang University, Beijing, China

Bachelor of Engineering. Grade-Point-Average (GPA): 3.48/4.0

Honors

Outstanding scientific paper award for graduate student, Beihang University (2014)

National scholarship of people's republic of China (2014)

Aeronautic science and technology scholarship, School of Aeronautic Science and Technology, Beihang University (2010)

Appendix A

Derivation of the expression of charge, dipole, and quadrupole

For the sake of convenience, we use the tensor notation for this appendix.

Suppose there is a localized source $\varrho(\mathbf{x})$ confined to a region near the origin O. The Coulomb potential at a point $\mathrm{A}(\mathbf{x_0})$ far away from the source (See Fig. 4.1, $x = \|\mathbf{x}\| \ll \|\mathbf{x_0}\| = x_0$) is given by Eq. (4.7). Considering that

$$\|\mathbf{x_0} - \mathbf{x}\| = \sqrt{{x_0}^2 - 2\mathbf{x_0}\cdot\mathbf{x} + x^2} \quad = x_0\sqrt{1 - 2\frac{\hat{\mathbf{x}}_\mathbf{0}\cdot\mathbf{x}}{x_0} + \left(\frac{x}{x_0}\right)^2} \tag{A.1}$$

where $\hat{\mathbf{x}}_\mathbf{0} = \dfrac{\mathbf{x_0}}{\|\mathbf{x_0}\|}$, Eq. (4.7) can be reformulated by using binomial expansion,

$$\begin{aligned}
\phi(\mathbf{x}) &= \frac{1}{4\pi\epsilon_0}\int_{\mathscr{B}} \frac{\varrho(\mathbf{x})}{\|\mathbf{x_0}-\mathbf{x}\|}\mathrm{d}v. \\
&= \frac{1}{4\pi\epsilon_0 x_0}\int_{\mathscr{B}} \varrho(\mathbf{x})\left(\frac{1}{\sqrt{1 - \frac{2\hat{\mathbf{x}}_\mathbf{0}\cdot\mathbf{x}}{x_0} + \left(\frac{x}{x_0}\right)^2}}\right)\mathrm{d}v \\
&= \frac{1}{4\pi\epsilon_0 x_0}\int_{\mathscr{B}} \varrho(\mathbf{x})\left\{1 - \frac{\hat{\mathbf{x}}_\mathbf{0}\cdot\mathbf{x}}{x_0} + \frac{1}{2x_0^2}\left[3(\hat{\mathbf{x}}_\mathbf{0}\cdot\mathbf{x})^2 - x^2\right] + \mathscr{O}\left(\frac{x}{x_0}\right)\right\}\mathrm{d}v
\end{aligned} \tag{A.2}$$

Equation A.2 gives the moments of the charge distribution with a different order. The first integral represents the potential from the monopole moment or simply the net charge q of the system:

$$\phi_{mon}(\mathbf{x}) = \frac{1}{4\pi\epsilon_0 x_0}\int_{\mathscr{B}} \varrho(\mathbf{x})\mathrm{d}v = \frac{q}{4\pi\epsilon_0 x_0} \tag{A.3}$$

The second integral can be reformulated as

$$\phi_{dip}(\mathbf{x}) = \frac{1}{4\pi\epsilon_0 x_0^2}\int_{\mathscr{B}} \varrho(\mathbf{x})(\hat{\mathbf{x}}_\mathbf{0}\cdot\mathbf{x})\mathrm{d}v = \frac{\hat{\mathbf{x}}_\mathbf{0}}{4\pi\epsilon_0 x_0^2}\cdot\int_{\mathscr{B}} \varrho(\mathbf{x})\mathbf{x}\mathrm{d}v \tag{A.4}$$

The vector

$$\mathbf{p} = \int_{\mathscr{B}} \varrho(\mathbf{x})\mathbf{x}\mathrm{d}v \tag{A.5}$$

is defined as *electric dipole* and its norm $\|\mathbf{p}\|$ *dipole moment*.

The third integral can be reformulated as

$$\phi_{quad}(\mathbf{x}) = \frac{1}{8\pi\epsilon_0 x_0^3}\int_{\mathscr{B}}\left[3(\hat{\mathbf{x}}_\mathbf{0}\cdot\mathbf{x})^2 - x^2\right]\mathrm{d}v = \frac{\hat{\mathbf{x}}_\mathbf{0}\otimes\hat{\mathbf{x}}_\mathbf{0}}{8\pi\epsilon_0 x_0^3} : \int_{\mathscr{B}}\varrho(\mathbf{x})\left[3(\hat{\mathbf{x}}_\mathbf{0}\otimes\hat{\mathbf{x}}_\mathbf{0}) - \mathbf{I}x^2\right]\mathrm{d}v. \quad \text{(A.6)}$$

The second rank tensor

$$\boldsymbol{\rho} = \int_{\mathscr{B}}\varrho(\mathbf{x})\left[3(\hat{\mathbf{x}}_\mathbf{0}\otimes\hat{\mathbf{x}}_\mathbf{0}) - \mathbf{I}x^2\right]\mathrm{d}v \quad \text{(A.7)}$$

is defined as *quadrupole moment tensor*. Figure 4.2 shows the potential distribution of net charge, a dipole and a quadrupole. The solid line indicates the electric field lines of the potential field generated. Within this thesis, only charges and dipole moments are taken into account, while moments of higher order are neglected.

Appendix B

Analytical solution for 1D Ginzburg-Landau equation with 6th order bulk energy term

According to Cahn and Hilliard [143], with the bulk free energy and interface energy provided, the interface properties can be analytically obtained through a variational study. We first try to simplify the problem into a 1D problem with two domains separated by a 180° domain wall. The idea of the following calculation first comes from the work for shape memory alloy by Falk [264], in spite that the Landau energy and the boundary condition are different. The distribution of the polarization is represented by a distribution function $P(x)$, where $P(-\infty) = -P_0$, $P(-\infty) = P_0$. The bulk free energy density is assumed as a polynomial expended to the sixth order,

$$\tilde{\psi} = aP^2 + bP^4 + cP^6 = aQ + bQ^2 + cQ^3, \tag{B.1}$$

where a, b, c are the Landau coefficients. The interface energy density in 1 dimension can be represented by

$$\tilde{\psi}^{int} = \kappa(P')^2, \tag{B.2}$$

where κ is the reduced interface energy coefficient, and P' represents the spatial derivative, *i.e.*, $P' = \dfrac{\mathrm{d}P}{\mathrm{d}x}$.

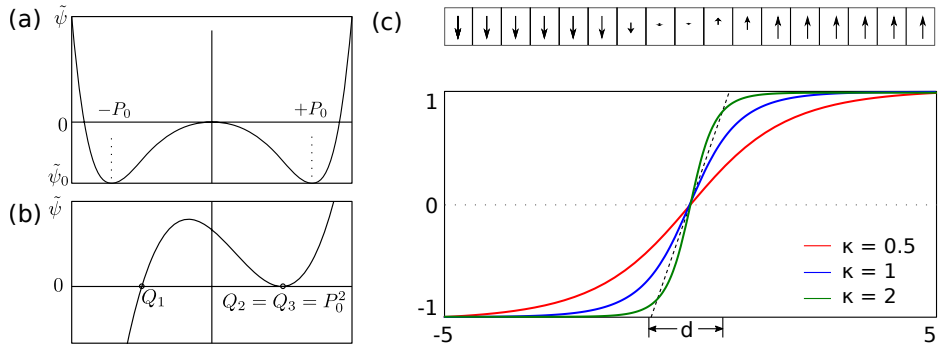

Figure B.1: *(a) and (b) Landau free energy as a function of (a) Polarization P and (b) its square $Q = P^2$, with Landau coefficients $\alpha = -1$, $\beta = -1$, $\gamma = 1$. (c) The analytical solutions for 180° domain wall with such Landau free energy. The domain wall coefficients $\kappa = 0.5$, 1 and 2 are plotted for comparison.*

One might want to find the distribution function $P(x)$, where the total free energy of the system

$$\mathscr{F}(x,P,P') = \int_{-\infty}^{+\infty} \left[aP^2 + bP^4 + cP^6 + \kappa(P')^2\right]dx \tag{B.3}$$

is minimized. This leads to solving the associated Euler-Lagrange equation:

$$\kappa P'' = aP + 2bP^3 + 3cP^5, \tag{B.4}$$

with the boundary condition

$$\lim_{x\to\pm\infty} P(x) = \pm P_0. \tag{B.5}$$

By considering that $P'' = \frac{dP'}{dP}\frac{dP}{dx}$, Eq. (B.4) is reformulated as [264]:

$$\kappa P' \frac{dP'}{dP} = aP + 2bP^3 + 3cP^5, \tag{B.6}$$

The integration of Eq. (B.6) yields,

$$\kappa(P')^2 = \tilde{\psi} - \tilde{\psi}_0. \tag{B.7}$$

where $\tilde{\psi}_0 = \tilde{\psi}(x = \pm\infty)$ (Considering that at $x = \pm\infty$, $P' = 0$). The inverse function of Eq. (B.7) is

$$x'(P) = \frac{\sqrt{\kappa}}{\sqrt{\tilde{\psi} - \tilde{\psi}_0}}. \tag{B.8}$$

The integration of Eq B.8 belongs to an indefinite ellipse integral of the first kind,

$$x(Q) = \frac{1}{2}\int \frac{\sqrt{\kappa}dQ}{\sqrt{Q(aQ + bQ^2 + cQ^3 - \tilde{\psi}_0)}} = F(\beta_Q x; k_Q). \tag{B.9}$$

where β_Q and k_Q are coefficients only related to the roots of Eq. (B.10).

For the case below the Curie temperature, the following equation

$$aQ + bQ^2 + cQ^3 - \tilde{\psi}_0 = 0 \tag{B.10}$$

has three solutions, one is negative, and two are identical (see Fig. B.1): $Q_1 < 0 < Q_2 = Q_3$. Its inverse function can be written by the Jacobian elliptic functions $\mathrm{sn}(x,k)$ and $\mathrm{cn}(x,k)$,

$$P(x) = \frac{\sqrt{-Q_1Q_2}\,\mathrm{sn}(\kappa^{-1}\beta_Q x, k_Q)}{\sqrt{Q_2\,\mathrm{cn}^2(\kappa^{-1}\beta_Q x, k_Q) - Q_1}}, \tag{B.11}$$

Fig. B.1 shows the distribution of $P(x)$ with three different κ and arbitrarily chosen Landau coefficients. Qualitatively, the width of the interface increases with the increase of κ. If the Landau energy is reduced to the fourth order:

$$\tilde{\psi} = aP^2 + bP^4 \tag{B.12}$$

The distribution of polarization will result in a simple form (This result seems to be first achieved by Cahn (1958) [143] and Zhirnov (1959) [144].):

$$P(x) = \tanh\left(x\sqrt{\frac{a}{2\kappa}}\right), \tag{B.13}$$

and the domain wall width,

$$\lambda \propto \sqrt{\frac{\kappa}{a}} \tag{B.14}$$

The energy stored at the interface (or domain wall) is

$$G = \frac{2}{3}P_0^2\sqrt{2\kappa a} \propto \sqrt{\kappa a}. \tag{B.15}$$

Appendix C

Clausius-Duhem inequality starting from Helmholtz free energy

For the derivation of the constitutive equations using Clausius-Duhem dissipation shown in Sec. 5.2.2, the electric enthalpy is used as the energy form. Here we prove that using either the electric enthalpy or the Helmholtz free energy, the same results can be reached.

For Helmholz free energy, the strain (ε_{ij}), electric field (E_i), polarization (P_i) and polarization gradient are used as the independent variable. The external work corresponding to these independent variable can be written as:

$$
\begin{aligned}
\mathscr{W}^{ext} &= \int_{\mathscr{B}} (f_i \dot{u}_i + \phi \dot{q} + \gamma_i \dot{P}_i) \mathrm{d}v + \int_{\partial \mathscr{B}} (\bar{t}_i \dot{u}_i + \phi \dot{\bar{\omega}} + \bar{\mu}_i \dot{P}_i) \mathrm{d}s \\
\text{(Neumann B.C.)} &= \int_{\mathscr{B}} (f_i \dot{u}_i + \phi \dot{q} + \gamma_i \dot{P}_i) \mathrm{d}v + \int_{\partial \mathscr{B}_u} (\sigma_{ji} n_j \dot{u}_i - \phi \dot{D}_i n_i + \xi_{ji} n_j \dot{P}_i) \mathrm{d}s \\
\text{(Gauss theorem)} &= \int_{\mathscr{B}} (f_i \dot{u}_i + \phi \dot{q} + \gamma_i \dot{P}_i) \mathrm{d}v + \int_{\mathscr{B}} \left[(\sigma_{ji} \dot{u}_i)_j - (\phi \dot{D}_i)_i + (\xi_{ji} \dot{P}_i)_j \right] \mathrm{d}v \\
&= \int_{\mathscr{B}} (f_i \dot{u}_i + \phi \dot{q} + \gamma_i \dot{P}_i) \mathrm{d}v + \\
&\quad \int_{\mathscr{B}} \left[\sigma_{ji,j} \dot{u}_i + \sigma_{ji} \dot{u}_{i,j} - (\phi \dot{D}_{i,i} + \phi_{,i} \dot{D}_i) + (\xi_{ji,j} \dot{P}_i + \xi_{ji} \dot{P}_{i,j}) \right] \mathrm{d}v \\
&= \int_{\mathscr{B}} \left[(f_i + \sigma_{ji,j}) \dot{u}_i + \phi (\dot{q} - \dot{D}_{i,i}) + (\gamma_i + \xi_{ji,j}) \dot{P}_i \right] \mathrm{d}v + \\
&\quad \int_{\mathscr{B}} \left[\sigma_{ji} \dot{u}_{i,j} - \phi_{,i} \dot{D}_i + \xi_{ji} \dot{P}_{i,j} \right] \mathrm{d}s \\
&= \int_{\mathscr{B}} (-\pi_i \dot{P}_i + \sigma_{ji} \dot{u}_{i,j} - \phi_{,i} \dot{D}_i + \xi_{ji} \dot{P}_{i,j}) \mathrm{d}v \\
&= \int_{\mathscr{B}} (-\pi_i \dot{P}_i + \sigma_{ji} \dot{u}_{i,j} + E_i \dot{D}_i + \xi_{ji} \dot{P}_{i,j}) \mathrm{d}v
\end{aligned}
\tag{C.1}
$$

By the Clausius-Duham inequality:

$$
\mathscr{W}^{ext} \geq \int_{\mathscr{B}} \dot{\mathscr{H}}(\varepsilon_{ij}, D_i, P_i, P_{i,j}) \mathrm{d}v, \tag{C.2}
$$

where $\mathscr{H}$ is Helmholtz free energy density. By utilizing the Legendre transformation:

$$\dot{\mathscr{H}}(\varepsilon_{ij}, D_i, P_i, P_{i,j}) = \dot{\mathscr{H}}_2(\varepsilon_{ij}, E_i, P_i, P_{i,j}) + \dot{E}_i D_i + \dot{D}_i E_i \tag{C.3}$$

Inserting Eq. (C.1) and Eq. (C.3) into the inequality C.2, we have:

$$\int_{\mathscr{B}} \left[(-\pi_i \dot{P}_i + \sigma_{ji}\dot{\varepsilon}_{ij} + E_i \dot{D}_i + \xi_{ji}\dot{P}_{i,j}) - (\dot{\mathscr{H}}_2 + \dot{E}_i D_i + E_i \dot{D}_i)\right] \mathrm{d}v \geq 0 \tag{C.4}$$

$$\int_{\mathscr{B}} (-\pi_i \dot{P}_i + \sigma_{ji}\dot{\varepsilon}_{ij} + \xi_{ji}\dot{P}_{i,j} - \dot{\mathscr{H}}_2 - \dot{E}_i D_i) \mathrm{d}v \geq 0 \tag{C.5}$$

Considering that

$$\dot{\mathscr{H}}_2 = \frac{\partial \mathscr{H}_2}{\partial \varepsilon_{ij}}\dot{\varepsilon}_{ij} + \frac{\partial \mathscr{H}_2}{\partial E_i}\dot{E}_i + \frac{\partial \mathscr{H}_2}{\partial P_i}\dot{P}_i + \frac{\partial \mathscr{H}_2}{\partial P_{i,j}}\dot{P}_{i,j} \tag{C.6}$$

one obtains:

$$\int_{\mathscr{B}} \left[-\frac{\partial \mathscr{H}_2}{\partial P_i}\dot{P}_i - \pi_i \dot{P}_i + \left(\sigma_{ij} - \frac{\partial \mathscr{H}_2}{\partial \varepsilon_{ij}}\right)\dot{\varepsilon_{ij}} + \left(\xi_{ij} - \frac{\partial \mathscr{H}_2}{\partial P_{i,j}}\right)\dot{P}_{i,j} - \left(D_i + \frac{\partial \mathscr{H}_2}{\partial E_i}\right)\dot{E}_i \right] \mathrm{d}v \geq 0. \tag{C.7}$$

Clausius-Duhem inequality starting from the electric enthalpy

For electric enthalpy ($\mathscr{H}_2$) free energy, the strain (ε_{ij}), electric displacement (D_i), polarization (P_i) and polarization gradient are used as the independent variable. The external work corresponding to these independent variables can be written as:

$$\begin{aligned}
\mathscr{W}_2^{ext} &= \int_{\mathscr{B}} (f_i \dot{u}_i - \dot{\phi} q + \gamma_i \dot{P}_i)\mathrm{d}v + \int_{\partial\mathscr{B}} (\bar{t}_i \dot{u}_i - \dot{\phi}\bar{\omega} + \bar{\mu}_i \dot{P}_i)\mathrm{d}s \\
&= \int_{\mathscr{B}} (f_i \dot{u}_i - \dot{\phi} q + \gamma_i \dot{P}_i)\mathrm{d}v + \int_{\partial\mathscr{B}_u} (\sigma_{ji} n_j \dot{u}_i + \dot{\phi} D_i n_i + \xi_{ji} n_j \dot{P}_i)\mathrm{d}s \\
&= \int_{\mathscr{B}} (f_i \dot{u}_i - \dot{\phi} q + \gamma_i \dot{P}_i)\mathrm{d}v + \int_{\mathscr{B}} \left[(\sigma_{ji}\dot{u}_i)_j + (\dot{\phi} D_i)_i + (\xi_{ji}\dot{P}_i)_j\right]\mathrm{d}v \\
&= \int_{\mathscr{B}} (f_i \dot{u}_i - \dot{\phi} q + \gamma_i \dot{P}_i)\mathrm{d}v + \\
&\quad \int_{\mathscr{B}} \left[\sigma_{ji,j}\dot{u}_i + \sigma_{ji}\dot{u}_{i,j} + (\dot{\phi} D_{i,i} + \dot{\phi}_{,i} D_i) + (\xi_{ji,j}\dot{P}_i + \xi_{ji}\dot{P}_{i,j})\right]\mathrm{d}v \\
&= \int_{\mathscr{B}} \left[(f_i + \sigma_{ji,j})\dot{u}_i - \dot{\phi}(q - D_{i,i}) + (\gamma_i + \xi_{ji,j})\dot{P}_i\right]\mathrm{d}v + \\
&\quad \int_{\mathscr{B}} \left[\sigma_{ji}\dot{u}_{i,j} + \dot{\phi}_i D_i + \xi_{ji}\dot{P}_{i,j}\right]\mathrm{d}v \\
&= \int_{\mathscr{B}} (-\pi_i \dot{P}_i + \sigma_{ji}\dot{u}_{i,j} + \dot{\phi}_i D_i + \xi_{ji}\dot{P}_{i,j})\mathrm{d}v \\
&= \int_{\mathscr{B}} (-\pi_i \dot{P}_i + \sigma_{ji}\dot{u}_{i,j} - \dot{E}_i D_i + \xi_{ji}\dot{P}_{i,j})\mathrm{d}v
\end{aligned} \tag{C.8}$$

By Clausius-Duham inequality:

$$\mathscr{W}_2^{ext} \geq \int_{\mathscr{B}} \dot{\mathscr{H}}_2(\varepsilon_{ij}, E_i, P_i, P_{i,j}) \mathrm{d}v, \tag{C.9}$$

where $\mathscr{H}_2$ is the electric enthalpy.

Inserting Eq. (C.8) into the inequality (C.9), we have:

$$\int_{\mathscr{B}} \left[(-\pi_i \dot{P}_i + \sigma_{ji} \dot{\varepsilon}_{ij} - E_i \dot{D}_i + \xi_{ji} \dot{P}_{i,j}) - \dot{\mathscr{H}}_2 \mathrm{d}v \geq 0 \right. \tag{C.10}$$

Considering that

$$\dot{\mathscr{H}}_2 = \frac{\partial \mathscr{H}_2}{\partial \varepsilon_{ij}} \dot{\varepsilon}_{ij} + \frac{\partial \mathscr{H}_2}{\partial D_i} \dot{D}_i + \frac{\partial \mathscr{H}_2}{\partial P_i} \dot{P}_i + \frac{\partial \mathscr{H}_2}{\partial P_{i,j}} \dot{P}_{i,j} \tag{C.11}$$

one obtains:

$$\int_{\mathscr{B}} \left[-\frac{\partial \mathscr{H}_2}{\partial P_i} \dot{P}_i - \pi_i \dot{P}_i + \left(\sigma_{ij} - \frac{\partial \mathscr{H}_2}{\partial \varepsilon_{ij}}\right) \dot{\varepsilon_{ij}} + \left(\xi_{ij} - \frac{\partial \mathscr{H}_2}{\partial P_{i,j}}\right) \dot{P}_{i,j} - \left(D_i + \frac{\partial \mathscr{H}_2}{\partial D_i}\right) \dot{E}_i \right] \mathrm{d}v \geq 0. \tag{C.12}$$

One finds that both Eq. (C.7) and Eq. (C.12) lead to the same form of the constitutive relations and evolution equation to Eq. (5.25).

Appendix D

Some comments on the electric enthalpy of a ferroelectric system

In Chap. 5, the electric enthalpy [265] or phase-field potential is assumed to depend on the strain, the electric field, the spontaneous polarization, and the polarization gradient. It consists of five parts,

$$\mathscr{H}_2 = \mathscr{H}^{ela} + \mathscr{H}^{ele} + \mathscr{H}^{piezo} + \mathscr{H}^{sep} + \mathscr{H}^{grad}, \tag{D.1}$$

in which $\mathscr{H}^{ela}$, $\mathscr{H}^{ele}$, $\mathscr{H}^{piezo}$, $\mathscr{H}^{sep}$, and $\mathscr{H}^{grad}$ represent elastic energy density, electric energy density, piezoelectric coupling energy density, domain separation energy density and gradient energy density, respectively. The domain separation energy density resembles the Landau-Devonshire free energy and the interface energy density describes the energy stored in the domain wall by a function of the gradient of the order parameter. These energy terms take the following specific form:

$$\begin{cases} \mathscr{H}^{ela} = \dfrac{1}{2} c_{ijkl} \varepsilon^e_{ij} \varepsilon^e_{kl}, & \text{(D.2a)} \\ \mathscr{H}^{ele} = -\dfrac{1}{2} k_{ij} E_i E_j - P_i E_i, & \text{(D.2b)} \\ \mathscr{H}^{coup} = -b_{ijk} \varepsilon_{ij} E_k, & \text{(D.2c)} \\ \mathscr{H}^{sep} = \beta_1 \dfrac{G}{\lambda} \psi(P_i), & \text{(D.2d)} \\ \mathscr{H}^{grad} = \beta_2 G \lambda P_{i,j} P_{i,j}. & \text{(D.2e)} \end{cases}$$

In the following, we give some comments additionally to Chap. 5 for each of the five terms. Equation D.2a represents the elastic energy where only the elastic strain contributes to this term. For a poled ferroelectric single crystal, there is always an eigenstrain accompanied. The eigenstrain highly depends on the spontaneous polarization. Since experimental findings indicate that changes of the macroscopic strain state due to domain switching are volume preserving, we constructed the spontaneous strain such that it yields a pure deviatoric strain state in the direction of the spontaneous polarization. According to [43],

$$\varepsilon^0_{ij}(\boldsymbol{P}) = \frac{3}{2} \varepsilon_0 \frac{\|\mathbf{P}\|}{P_0} \Big(n_i n_j - \frac{1}{3} \delta_{ij} \Big), \tag{D.3}$$

where n_i is the unit vector along $\boldsymbol{P}$. P_0 is the equilibrium polarization for zero applied loading. Note that the spontaneous polarization P_i slightly changes with the applied loading, *e.g.*, electric field. In such case, the change of electric displacement D_i has two contributions, the one directly related to the electric field, *i.e.*, $\epsilon_{ij}E_j$, and the one related to the change of the spontaneous polarization. In contrast to that, P_0 is rather a material related parameter which is invariant under different loading. The symbol ε_0 is the normal strain for the poled state at a null field with respect to the paraelectric phase (or cubic phase). The value of ε_0 can be obtained directly from the calculation of lattice parameter, which is assumed only dependent on temperature. The elastic strain is thus the difference between the strain calculated in Eq. (4.31) and the eigenstrain:

$$\varepsilon_{ij}^{ela} = \varepsilon_{ij}^{tot} - \varepsilon_{ij}^{0}. \tag{D.4}$$

The first term in Eq. (D.2b) represents the electric energy density stored in the material if ϵ_{ij} represents the material permittivity rather than vacuum permittivity. If the polarization is aligned with the same direction to the applied field, the energy will be reduced. Hence the second terms in Eq. (D.2b) is introduced. It represents the interaction between the local polarization and the electric field. In some works (*e.g.*, Ref. [139]), the dipole-dipole interaction is considered within a finite difference scheme. Different from that model, the distribution of **E** in Eq. (D.2b) is rather from the global energy minimization.

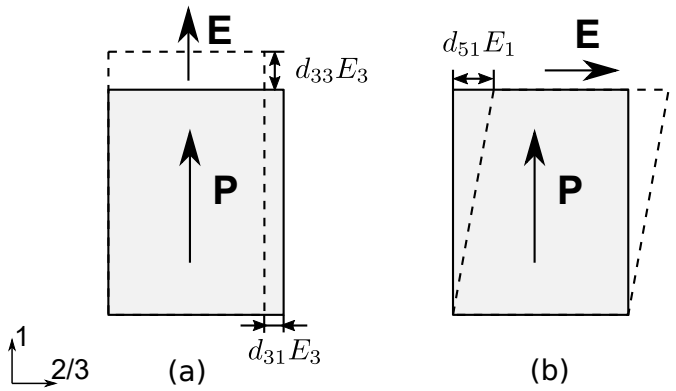

Figure D.1: *Schematic graph of the strain under different electric field loading of a transverse isotropic material poled in the 1-direction. (a) The electric field is parallel to the spontaneous polarization. (b) The electric field is perpendicular to the spontaneous polarization.*

Equation D.2c represents the electromechanical coupling energy with only piezoelectric contribution considered. The eigenstrain does not contribute to the piezoelectric effect, thus it is excluded from Eq. (D.2c). The piezoelectric constant $\mathbb{e}$ is highly dependent on the spontaneous polarization. At the poled state, piezoelectricity is transversely isotropic, where the plane of anisotropy is perpendicular to the poling direction. We used the representation [43],

$$e_{kij}(\boldsymbol{P}) = \frac{\|\boldsymbol{P}\|}{P_0}\Big\{e_{33}n_in_jn_k + e_{31}(\delta_{ij} - n_in_j)n_k + \frac{1}{2}e_{15}\big[(\delta_{ki} - n_kn_i)n_j + (\delta_{kj} - n_kn_j)n_i\big]\Big\}, \tag{D.5}$$

in which e_{33}, e_{31}, e_{15} are linear piezoelectric constants at the poled state, and $e_{kij} = (\mathbb{e})_{kij}$. Suppose the crystal is poled in the 1-direction, only the following components are non-zero:

$$e_{333} = e_{33} \quad e_{311} = e_{322} = e_{31} \quad e_{113} = e_{223} = e_{131} = e_{232} = \frac{1}{2} e_{51}. \tag{D.6}$$

The application of the electric field in the 1-direction will result in the deformation shown in Fig. D.1, where we ignore the influence of the electric field to polarization.

Equation D.2d represents the phase separation energy (or bulk free energy [143]). Schrade *et al.* [151, 182] used an artificial six-order polynomial, which is constructed to be invariant at equivalent ferroelectric state to allow different domain structures. This bulk free energy can also be measured/derived from experiments [193, 242, 266, 267] or from first principle calculation [268, 269]. Fig. 2.2 is an example of the bulk free energy of barium titanium with the Landau coefficients from Li *et al.* [242]. The bulk free energy, in general, take the following form:

$$\psi = a_0 + a_{ij} P_i P_j + a_{ijkl} P_i P_j P_k P_l + a_{ijklmn} P_i P_j P_k P_l P_m P_n + \cdots \tag{D.7}$$

Equation D.2e represents the gradient energy or interface energy [143]. Here, the gradient energy only refers to the gradient of the order parameter $\mathbf{P}$. The gradient energy from strain gradient belongs to the topic of strain gradient elasticity theory (SGE), which is out of the scope. The variable β_1 and β_2 are used to calibrate the phase separation energy and the gradient energy.

The coefficients G and λ can be identified as the domain wall energy and domain wall width, respectively. Theoretically, the domain wall energy can be quantified by the integration over the interface region. In some other phase field models, instead of physical parameters like domain wall energy G and domain wall width λ, the parameters with simple Taylor expansion are used. (See Sec. 4.5) Cao and Cross first attempt to obtain the coefficients κ and Landau coefficients (See Eq.(4.19) and Eq.(5.1) in [156]) in an analytical way, by calculating energy for 90° and 180° domain walls. Hlinka *et al.* [270] calculated the coefficient κ by soft-mode theory. Moreover, the DFT calculations have been used to get these gradient parameters. There are divergences between the values obtained through different methods.

Appendix E

Tangent matrix for the random field relaxor model

The stiffness tangent matrices used in Chap. 5 have the following form:

$$\underline{\boldsymbol{S}} = \begin{bmatrix} \underline{\boldsymbol{S}}^{11} & \underline{\boldsymbol{S}}^{12} & \underline{\boldsymbol{S}}^{13} & \underline{\boldsymbol{S}}^{14} \\ \underline{\boldsymbol{S}}^{21} & \underline{\boldsymbol{S}}^{22} & \underline{\boldsymbol{S}}^{23} & \underline{\boldsymbol{S}}^{24} \\ \underline{\boldsymbol{S}}^{31} & \underline{\boldsymbol{S}}^{32} & \underline{\boldsymbol{S}}^{33} & \underline{\boldsymbol{S}}^{34} \\ \underline{\boldsymbol{S}}^{41} & \underline{\boldsymbol{S}}^{42} & \underline{\boldsymbol{S}}^{43} & \underline{\boldsymbol{S}}^{44} \end{bmatrix}. \tag{E.1}$$

In each component in $\underline{\boldsymbol{S}}^{IJ}$,

$$\underline{\boldsymbol{S}}^{IJ} = \begin{bmatrix} \underline{\boldsymbol{S}}^{IJ}_{uu} & \underline{\boldsymbol{S}}^{IJ}_{u\phi} & \underline{\boldsymbol{S}}^{IJ}_{uP} \\ \underline{\boldsymbol{S}}^{IJ}_{\phi u} & S^{IJ}_{\phi\phi} & \underline{\boldsymbol{S}}^{IJ}_{\phi P} \\ \underline{\boldsymbol{S}}^{IJ}_{Pu} & \underline{\boldsymbol{S}}^{IJ}_{P\phi} & \underline{\boldsymbol{S}}^{IJ}_{PP} \end{bmatrix} = \begin{bmatrix} \underline{\boldsymbol{K}}^{IJ}_{uu} & \underline{\boldsymbol{K}}^{IJ}_{u\phi} & \underline{\boldsymbol{K}}^{IJ}_{uP} \\ \underline{\boldsymbol{K}}^{IJ}_{\phi u} & K^{IJ}_{\phi\phi} & \underline{\boldsymbol{K}}^{IJ}_{\phi P} \\ \underline{\boldsymbol{K}}^{IJ}_{Pu} & \underline{\boldsymbol{K}}^{IJ}_{P\phi} & \underline{\boldsymbol{K}}^{IJ}_{PP} + \frac{1}{\tau}\underline{\boldsymbol{D}}^{IJ}_{PP} \end{bmatrix}. \tag{E.2}$$

For each tangent matrix:

$$\underline{\boldsymbol{S}}^{IJ}_{uu} = \int_{\mathscr{B}^e} \underline{\boldsymbol{B}}^{I\,T}_{u}\, \underline{\boldsymbol{C}}\, \underline{\boldsymbol{B}}^{J}_{u} \mathrm{d}v \tag{E.3}$$

$$\underline{\boldsymbol{S}}^{IJ}_{u\phi} = \int_{\mathscr{B}^e} \underline{\boldsymbol{B}}^{I\,T}_{u}\, \underline{\mathbb{e}}^{T}\, \underline{\boldsymbol{B}}^{J}_{\phi} \mathrm{d}v \tag{E.4}$$

$$\underline{\boldsymbol{S}}^{IJ}_{uP} = -\int_{\mathscr{B}^e} \underline{\boldsymbol{B}}^{I\,T}_{u} \left(\underline{\boldsymbol{C}} \frac{\partial \underline{\boldsymbol{\varepsilon}}^{0}}{\partial \underline{\boldsymbol{P}}^{J}} + \frac{\partial \underline{\boldsymbol{b}}^{T}}{\partial \underline{\boldsymbol{P}}^{J}} (\underline{\boldsymbol{E}}^{\phi} + \underline{\boldsymbol{E}}^{rand})^{T} \right) \mathrm{d}v \tag{E.5}$$

$$\underline{\boldsymbol{S}}^{IJ}_{\phi u} = \int_{\mathscr{B}^e} \underline{\boldsymbol{B}}^{I\,T}_{\phi}\, \underline{\mathbb{e}}\, \underline{\boldsymbol{B}}^{J}_{u} \mathrm{d}v \tag{E.6}$$

$$\boldsymbol{S}^{IJ}_{\phi\phi} = -\int_{\mathscr{B}^e} \underline{\boldsymbol{B}}^{I\,T}_{\phi}\, \underline{\boldsymbol{\epsilon}}\, \underline{\boldsymbol{B}}^{J}_{\phi} \mathrm{d}v \tag{E.7}$$

$$\boldsymbol{S}_{\phi P}^{IJ} = \int_{\mathscr{B}^e} \underline{\boldsymbol{B}}_{\phi}^{I\,T} \left(\frac{\partial \underline{\mathbb{e}}}{\partial \underline{\boldsymbol{P}}^J} \underline{\boldsymbol{\varepsilon}}^e + \underline{\mathbb{e}} \frac{\partial \underline{\boldsymbol{\varepsilon}}^e}{\partial \underline{\boldsymbol{P}}^J} + \underline{\mathbf{1}} N^J \right) \mathrm{d}v \tag{E.8}$$

$$\underline{\boldsymbol{S}}_{Pu}^{IJ} = -\int_{\mathscr{B}^e} N^I \left(\frac{\partial \underline{\boldsymbol{\varepsilon}}^{0\,T}}{\partial \underline{\boldsymbol{P}}} \underline{\boldsymbol{C}} + (\underline{\boldsymbol{E}}^{\phi} + \underline{\boldsymbol{E}}^{rand}) \frac{\partial \underline{\mathbb{e}}}{\partial \underline{\boldsymbol{P}}} \right) \underline{\boldsymbol{B}}_u^{J\,T} \mathrm{d}v \tag{E.9}$$

$$\boldsymbol{S}_{P\phi}^{IJ} = \int_{\mathscr{B}^e} N^I \left(\underline{\boldsymbol{\varepsilon}}^{e\,T} \frac{\partial \underline{\mathbb{e}}^T}{\partial \underline{\boldsymbol{P}}} + \frac{\partial \underline{\boldsymbol{\varepsilon}}^{e\,T}}{\partial \underline{\boldsymbol{P}}} \underline{\mathbb{e}}^T + \underline{\mathbf{1}} \right) \underline{\boldsymbol{B}}_{\phi}^J \mathrm{d}v \tag{E.10}$$

$$\boldsymbol{S}_{P\phi}^{IJ} = -\int_{\mathscr{B}^e} \Bigg\{ \Bigg[N^I \left(\frac{\partial^2 \underline{\boldsymbol{\varepsilon}}^{0\,T}}{\partial \underline{\boldsymbol{P}} \partial \underline{\boldsymbol{P}}^J} - \frac{\partial \underline{\boldsymbol{\varepsilon}}^{0\,T}}{\partial \underline{\boldsymbol{P}}} \frac{\partial \underline{\boldsymbol{\sigma}}^T}{\partial \underline{\boldsymbol{P}}^J} \right) - N^I \left(\frac{\partial \underline{\boldsymbol{\varepsilon}}^{e\,T}}{\partial \underline{\boldsymbol{P}}^J} \frac{\partial \underline{\mathbb{e}}^T}{\partial \underline{\boldsymbol{P}}} + \underline{\boldsymbol{\varepsilon}}^{e\,T} \frac{\partial^2 \underline{\mathbb{e}}^T}{\partial \underline{\boldsymbol{P}} \partial \underline{\boldsymbol{P}}^J} \right) (\underline{\boldsymbol{E}}^{\phi} + \underline{\boldsymbol{E}}^{rand})^T \tag{E.11}$$

$$+ \beta_1 N^I \frac{\partial^2 \psi}{\partial \underline{\boldsymbol{P}} \partial \underline{\boldsymbol{P}}^J} + \beta_2 \underline{\boldsymbol{B}}_P^{I\,T} \underline{\boldsymbol{B}}_P^J \Bigg] - \frac{\beta}{\tau} N^I \underline{\mathbf{1}} N^J \Bigg\} \mathrm{d}v. \tag{E.12}$$